The Electronic and Magnetic Effects of $3d$ Transition Metal Impurities in Semiconductors

Author:

Brett

Leedahl

A Thesis Submitted to the College of Graduate and Postdoctoral Studies in Partial Fulfillment of the Requirements for the Degree of Doctor of Philosophy in the Department of Physics and Engineering Physics University of Saskatchewan Saskatoon

PERMISSION TO USE

In presenting this thesis in partial fulfillment of the requirements for a Postgraduate degree from the University of Saskatchewan, I agree that the Libraries of this University may make it freely available for inspection. I further agree that permission for copying of this thesis in any manner, in whole or in part, for scholarly purposes may be granted by the professor or professors who supervised my thesis work or, in their absence, by the Head of the Department or the Dean of the College in which my thesis work was done. It is understood that any copying or publication or use of this thesis or parts thereof for financial gain shall not be allowed without my written permission. It is also understood that due recognition shall be given to me and to the University of Saskatchewan in any scholarly use which may be made of any material in my thesis. Requests for permission to copy or to make other use of material in this thesis in whole or part should be addressed to:

Head of the Department of Physics and Engineering Physics 163 Physics Building
116 Science Place
University of Saskatchewan
Saskatoon, Saskatchewan, Canada, S7N 5E2

Dean
College of Graduate and Postdoctoral Studies
University of Saskatchewan
116 Thorvaldson Building, 110 Science Place
Saskatoon, Saskatchewan, Canada, S7N 5C9

ABSTRACT

The subject of this dissertation is concerned almost exclusively with soft x-ray spectroscopy of the $3d$ transition metals. These relatively common metals, owing to their widespread availability, are already used in all facets of technology. Stainless steel is largely chromium, iron, and nickel; copper wires transmit nearly all of our electricity; nickel is used in the making of margarine. Their wide range of electronic properties, strength, and usefulness in chemical reactions underpins their versatility to the point where they are used in essentially everything we manufacture. Key to this thesis is their ability to induce magnetism. If realized, spintronic technologies would harness the semiconducting electronic properties of a material, while also utilizing the induced magnetic properties to transport spin polarized charge. The ability to advance digital logic (0s and 1s) from its current state as on/off switches controlled solely via current, to the spintronic method of flipping spins to an up or down state, would have vast consequences for the computing world. Heat dissipation and cooling issues would largely vanish, and computing speed would show large improvements, while being non-volatile when power is lost.

Succinctly put, the broad goal of my studies focused on how transition metal impurities doped into host semiconductors in small proportions can influence the host material's electronic and magnetic properties. This was accomplished primarily through modelling experimental spectra with theoretical calculations, and then extracting information through their agreement. In doing this, it is possible to determine fundamental quantitative properties of for each $3d$ ion, and how each ion situates itself within the host lattice. This information can then be linked back to known properties of the material in order to determine which $3d$ ions, host materials, and synthesis conditions show promise for spintronic or other related

technologies.

For the study concerning Bi_2Te_3 it was shown that the various transition metals Cr, Mn, Fe, Co, Ni, and Cu each integrate themselves into the host crystal in a particular fashion. Manganese atoms substitute cleanly into Bi sites; chromium atoms are not absorbed into the bulk, but only the surface; iron prefers a mixture of oxidation states; and for cobalt and nickel a mixture of configurations was found. Similarly, with host materials TiO_2 and ZnO, DFT calculations predicted that the probability of substitution by a transition metal atom into a Zn or Ti site decreased in probability as the atomic number of the dopant metal atom increases, with a greater chance of metallic clustering in TiO_2. Spectroscopic measurements, along with crystal field calculations confirmed these trends though modelling and direct comparison of calculation and experiment. This allowed us to extract real physical properties of the system, such as oxidation state, local symmetry, and effects *d*-orbital energies, via the calculation parameters.

In the ferromagnetic compound $NiFe_2O_4$, the Fe atoms are responsible for the magnetism, but are in three different unique sites of various oxidation states and symmetries. By theoretically modelling x-ray magnetic circular dichroism experiments I have shown how these three sites can be readily distinguished, and how the interplay between their individual contributions to the magnetism are necessary to understand how the bulk magnetism arises. Furthermore, only through modelling the experimental XMCD with calculations can it be understood how aluminum alloying affects the overall magnetism. As more non-magnetic aluminum atoms replace magnetic iron atoms, the overall strength of the magnetism does not continuously decrease, but in fact begins to increase again at a certain point; this unexpected and unintuitive result can only be explained using the methodology described above.

Structural changes in regular white TiO_2 occur under a high pressure atmosphere that cause it to turn black, as a result of mid band gap states forming. I was able to adapt a generally hard x-ray technique (EXAFS) to the soft x-ray regime using the capabilities of the REIXS beamline at the Canadian Light Source to probe the change in interatomic distances between the white and black materials and observe the undergone structural changes. The shift in atomic distances were then compared to distorted structures of the nominal material

and a distortion in the vicinity of an oxygen vacancy were able to solve the dilemma of the nature of the distortion.

The Chelyabinsk meteorite had a thermomagnetic analysis performed on it to determine the various Curie temperatures of the magnetic materials contained in it, which consists of nickel and iron. Through comparisons with magnetic phase charts, we showed that the meteorite contains an iron-nickel alloy, which is quite common. But the breakthrough finding that had not been observed before was the discovery of an extremely pure form of iron, which hadn't ever been observed to occur naturally before.

ACKNOWLEDGEMENTS

Firstly, I would like to thank my supervisor Professor Alex Moewes, for initially taking me on as part of his group in 2013, and supporting me for the last five years. He has always been a wise source for scientific direction and input, but has found the artful balance of also allowing me the flexibility and freedom to pursue my own scientific interests. His experience in the field has afforded his graduate students the opportunities that few others get—the chance to use world-class research labs (the Advanced Light Source in Berkeley, California and the Canadian Light Source in Saskatoon, Saskatchewan), and largely independently perform their own experiments. In conjunction with this, Alex has always brought in quality students as part of his BeamTeam, and I thank all past member that have overlapped with me in the group for the dialogue over the years.

The other individual that deserves distinct recognition throughout my graduate studies is Professor Robert Green, without whom, my current level of knowledge in the research field would not be anything near what it is today. The ability to pick his brain over the years has been a valuable source of information that no internet search or textbook could replace.

As all projects were large collaborative efforts, and none could have been accomplished without my coauthors, I would like to thank all coauthors, specifically Ernst Kurmaev who was a valuable source for initial drafts of manuscripts in those he is authored on. These were specifically instrumental early in my scientific career, effectively allowing me to jumpstart my production and hit the ground running.

Beamline scientist Wanli Yang at Beamline 8 at the Advanced Light Source has been essential to all experimental data taken therein. At the Canadian Light Source I would like to mention beamline scientist Tom Regier for all work done at the SGM beamline, and David

Muir in my initial years at REIXS. In my latter graduate school years, discussions with Teak Boyko at REIXS have always proved fruitful for my knowledge.

Financially, I would like to thank Alex for contributions from his funding, and NSERC for initially supporting me as a summer student in 2012, allowing to get my foot in the door in Alex's group. The Department of Physics and Engineering Physics, along with the College of Graduate Studies and Research has also supported me for years. The Saskatchewan Innovation and Opportunity Scholarship provided me with two years of funding, for which I am extremely grateful. And lastly, but perhaps most importantly the funding from the Dr. Gerhard Herzberg Memorial Scholarship in Physics has provided me with my final year of funding, affording me the time to complete my studies stress free.

CONTENTS

PERMISSION TO USE . . . . . **i**

ABSTRACT . . . . . **ii**

ACKNOWLEDGEMENTS . . . . . **v**

CONTENTS . . . . . **vii**

LIST OF TABLES . . . . . **xiii**

LIST OF FIGURES . . . . . **xiv**

LIST OF ABBREVIATIONS . . . . . **xvii**

CHAPTER ONE
INTRODUCTION **1**

1.1 Spintronics 3

CHAPTER TWO
3D TRANSITION METALS **8**

2.1 Magnetism 10

2.2 Ferromagnetism 11

2.3 Multiplet Effects 14

2.3.1 Atomic Multiplets 15

2.3.2 Term Symbols . . . 15
2.3.3 Hund's Rules . . . 18
2.3.4 X-ray Absorption in the Atomic Model . . . 21
2.3.5 Crystal Field Multiplets . . . 24
2.3.6 Tanabe-Sugano Diagrams . . . 28
2.3.7 Crystal Field Charge/Hole Densities . . . 31
2.3.8 Charge Transfer Multiplets . . . 33

CHAPTER THREE

EXPERIMENTAL TECHNIQUES . . . 40

3.1 X-ray Absorption Spectroscopy . . . 40
3.2 X-ray Magnetic Circular Dichroism . . . 44
3.2.1 Experimental Considerations . . . 49
3.2.2 Sum Rules . . . 50
3.3 Extended X-ray Absorption Fine Structure . . . 51
3.4 X-ray Emission Spectroscopy . . . 55
3.4.1 RIXS . . . 57
3.4.2 NXES . . . 60
3.4.3 Band Gap Determination . . . 62
3.5 X-ray Photoemission Spectroscopy . . . 64
3.6 Ion Implantation . . . 66

CHAPTER FOUR

DATA ANALYSIS AND SOFTWARE . . . 68

4.1 Image Correction for XES Spectra . . . 68
4.2 Energy Calibration . . . 70
4.3 Maximum Entropy Deconvolution . . . 73

CHAPTER FIVE

TiO_2:Fe . . . 77

5.1 Introduction . . . 78

5.2 Experimental and Calculation Details . . . 79
5.2.1 Sample Preparation . . . 79
5.2.2 Ion Implantation . . . 80
5.2.3 XPS Measurements . . . 81
5.2.4 XES and XAS Measurements . . . 81
5.2.5 DFT Calculations . . . 82
5.3 Results and Discussion . . . 84
5.3.1 XPS Measurements . . . 84
5.3.2 XAS and RXES Measurements . . . 85
5.3.3 DFT Calculations . . . 89
5.4 Conclusion . . . 92

CHAPTER SIX

Cr, Mn, Fe, Co, Ni, and Cu Doped ZnO and TiO_2 . . . 94

6.1 Introduction . . . 96
6.2 Experimental and Calculational Details . . . 97
6.2.1 Sample Preparation . . . 97
6.2.2 Ion Implantation . . . 98
6.2.3 Spectroscopic Measurements . . . 98
6.2.4 Calculations . . . 99
6.3 Results and Discussion . . . 101
6.3.1 XPS Survey Measurements . . . 101
6.3.2 Chromium . . . 102
6.3.3 Iron . . . 105
6.3.4 Manganese . . . 107
6.3.5 Cobalt . . . 109
6.3.6 Nickel . . . 111
6.3.7 Copper . . . 112
6.3.8 Valence XPS . . . 114
6.4 Conclusion . . . 117

CHAPTER SEVEN

The Chelyabinsk Meteorite 118

7.1 Introduction 119

7.2 Experimental Details 121

7.3 Magnetic Measurements 122

7.3.1 Thermomagnetic Analysis 122

7.3.2 Curie-Weiss Law 126

7.4 Spectroscopic Measurements 128

7.4.1 X-ray Emission Measurements 128

7.4.2 X-ray Absorption Measurements 130

7.4.3 XPS Measurements 131

7.5 Ab-initio Theoretical Analysis 134

7.6 Conclusion 136

7.7 Acknowledgements 136

CHAPTER EIGHT

Ferromagnetism in Nickel Ferrite 138

8.1 Introduction 139

8.2 Experiment and Calculation Details 141

8.3 Results and Discussion 142

8.4 Conclusion 147

8.5 Acknowledgements 147

8.6 Supporting Material 148

8.6.1 Oxygen XAS and XES – The Band Gap of $NiFe_2O_4$ 148

8.6.2 Fe and Ni XAS 149

8.6.3 Fe and Ni XES 151

CHAPTER NINE

$3d$ Doped Topological Insulator Bi_2Te_3 154

9.1 Introduction 156

9.2 Experiment and Calculation Details . . . 157
9.3 XPS Measurements . . . 160
9.4 X-ray Absorption and Emission . . . 162
9.4.1 Cobalt . . . 162
9.4.2 Chromium . . . 163
9.4.3 Nickel . . . 164
9.4.4 Manganese . . . 164
9.4.5 Copper . . . 164
9.4.6 Iron . . . 165
9.5 Conclusion . . . 168
9.6 Acknowledgements . . . 168

CHAPTER TEN

TiO_2 EXAFS . . . 169

10.1 Introduction . . . 170
10.2 Experiment and Calculation Details . . . 172
10.3 Results and Discussion . . . 174
10.3.1 Rutile and Anatase TiO_2 . . . 174
10.3.2 Black Titania . . . 176
10.4 Conclusion . . . 180
10.5 Acknowledgements . . . 180
10.6 Supplemental Material . . . 181

BIBLIOGRAPHY . . . 183

APPENDICES . . . 214

APPENDIX A

AUTHORED PUBLICATIONS . . . 214

APPENDIX B

COPYRIGHT AGREEMENTS 217

B.1 American Physical Society 217

B.2 American Chemical Society 219

B.3 American Institute of Physics 221

B.4 Royal Society of Chemisty 223

B.5 Nature Publishing Group 224

LIST OF TABLES

2.1 a/r Ratios 13
2.2 Quantum Numbers 16
2.3 Atomic Electron Configurations 17
2.4 Dipole Allowed $3d^n \rightarrow 3d^{n+1}$ Transitions in the Atomic Model 23
2.5 $3d$ orbital energy in terms of Dq, Ds, and Dt values. 27
2.6 Ligand Field Model Parameters 34
2.7 Ligand Field Model Calculation Parameters 38

5.1 Formation Energies for $3d$ Impurities in in TiO_2 91

6.1 TiO_2 Impurity Formation Energies 102
6.2 ZnO Impurity Formation Energies 102

7.1 Integrated $I(L_2)/I(L_3)$ NXES Ratios 129
7.2 Surface Composition of Chelyabinsk Meteorite 133

9.1 $3d$ Ion Fractions in Bi_2Te_3 161
9.2 Crystal Field Parameters for $3d$ Ions in Bi_2Te_3 166

10.1 Black Titania Interatomic Distances 178

LIST OF FIGURES

1.1 Moore's Law 2
1.2 Spin Transistors 5

2.1 Radiual Wave Functions 9
2.2 Atomic XAS 22
2.3 $3d$ Electron Orbitals 25
2.4 $3d$ Orbital Energies and Symmetries 26
2.5 Tanabe-Sugano Diagram of a $3d^2$ System 29
2.6 Crystal Field Parameters 30
2.7 Charge Densities 32
2.8 Charge Transfer Multiplets 35
2.9 Ligand Field Charge Densities 36
2.10 Charge Transfer Experiment and Calculation 38

3.1 XAS Edges & Cross Sections 41
3.2 XAS Techniques 43
3.3 XMCD Transitions 46
3.4 Clebsch-Gordon Table 47
3.5 XMCD Sum Rules 51
3.6 EXAFS Diagram 53
3.7 Manganese EXAFS 55
3.8 RIXS 58

3.9 NXES and Band Gap Determindation 63
3.10 XPS Survey and Electron Mean Free Paths 65
3.11 Ion Implantation Depth Profile of Co in ZnO 67

4.1 Image Correction 69
4.2 Pixel to Energy Calibration 71
4.3 Maximum Entropy Deconvolution 75

5.1 XPS Survey of pure and Fe-implanted TiO_2 83
5.2 Fe XAS & XES of TiO_2:Fe 87
5.3 Oxygen XAS & XES of TiO_2:Fe 89

6.1 TiO_2 XPS Survey 103
6.2 ZnO XPS Survey 104
6.3 Cr in ZnO and TiO_2 105
6.4 Fe in ZnO and TiO_2 106
6.5 Mn in ZnO and TiO_2 108
6.6 Co in ZnO and TiO_2 109
6.7 Ni in ZnO and TiO_2 111
6.8 Cu in ZnO and TiO_2 113
6.9 TiO_2 Valence Band XPS 115
6.10 ZnO Valence Band XPS 116

7.1 Temperature Dependance of Magnetization 123
7.2 Fe-Ni Alloy Phase Diagram 124
7.3 Curie-Weiss Law 127
7.4 Fe $L_{2,3}$ XES of Chelyabinsk Meteorite 129
7.5 Fe $L_{2,3}$ XAS of Chelyabinsk Meteorite 130
7.6 XPS Survery of Chelyabinsk Meteorite 132
7.7 Fe $2p$ XPS of Chelyabinsk Meteorite 134
7.8 DMFT Calculated Fe and Ni Density of States 135

8.1 XMCD Schematic 142
8.2 $NiFe_2O_4$ XMCD Results 144
8.3 Band Gap Determination for $NiFe_2O_4$ 149
8.4 O K-edge Spectra for $NiFe_2O_4$ 150
8.5 Fe and Ni $L_{2,3}$ XAS 151
8.6 Fe and Ni $L_{2,3}$ RXES 152

9.1 Bi_2Te_3 X-ray Diffraction Pattern 157
9.2 Proposed Defect Structures in Bi_2Te_3 158
9.3 3d Ion XPS Spectra in Bi_2Te_3 159
9.4 3d Ion XAS and RXES in Bi_2Te_3 167

10.1 2D Color Map of TiO_2 Anatase Spectrum Recorded by SDD 172
10.2 SDD Emission Spectrum of TiO_2 173
10.3 TiO_2 EXAFS and Fourier Transforms 175
10.4 Proposed Black Titania Structure 177
10.5 Raw PFY Spectra Recorded by SDD 181
10.6 Magnified PFY Spectra 181
10.7 Components of Fourier Transform for Black Titania 182

LIST OF ABBREVIATIONS

(ALS) Advanced Light Source

(CB) conduction band

(CLS) Canadian Light Source

(CPS+DMFT) coherent potential approximation in combination with dynamical mean-field theory

(CPU) central processing unit

(DFT) density functional theory

(DOS) density of states

(DMS) dilute magnetic semiconductors

(EXAFS) extended x-ray absorption fine structure

(GGA) generalized gradient approximation

(GMR) giant magnetoresistive effect

(IPFY) inverse partial fluorescence yield

(NXES) non-resonant x-ray emission spectroscopy

(PFY) partial fluorescence yield

(VES) valence electron states

(RAM) random access memory

(REIXS) resonant elastic and inelastic x-ray scattering beamline at the CLS

(RIXS) resonant inelastic x-ray scattering

(RXES) resonant x-ray emission spectroscopy

(SDD) silicon drift detector

(SGM) spherical grating monochromator beamline at the CLS

(TEY) total electron yield

(TFY) total fluorescence yield

(TM) transition metal

(TMA) thermal magnetic analysis

(VB) valence band

(XAS) x-ray absorption spectroscopy

(XES) x-ray emission spectroscopy

(XMCD) x-ray magnetic circular dichroism

(XPS) x-ray photoemission spectroscopy

(XRD) x-ray diffraction

CHAPTER

ONE

INTRODUCTION

Semiconductor technologies have become so prominent in the developed world such that many of us take them for granted, and no longer notice the large role they play in every minute of our lives. They are arguably the single most influential technological breakthrough in the history of our planet. Semiconducting materials are needed as the building blocks for computational logic; simply stated, this is the ability to be turned on or off, which is the fundamental principle that has led to the creation of nearly all our electronic technology we see today.

The most rudimentary semiconducting device is the diode, typically formed from a single p-n junction—two connected materials, one with excess electrons and one with excess holes. This material is usually silicon, or a metal oxide doped with very small amounts of another element to provide the excess (or depleted) electron regions. By providing a voltage to either end of the material it can be either forward biased or reverse biased if the voltage is higher at the p end or n end, respectively. The effect is that conduction is high and current will readily flow if forward biased, while very little current will flow when reverse biased. This simple fundamental process is behind every computer we have ever seen.

Then, in 1947 at Bell Labs, physicists John Bardeen, Walter Brattain, and William Shockley took the next logical step and created the transistor—a device using multiple p-n junctions that can be used as either an on-off switch or an amplifier—they were awarded

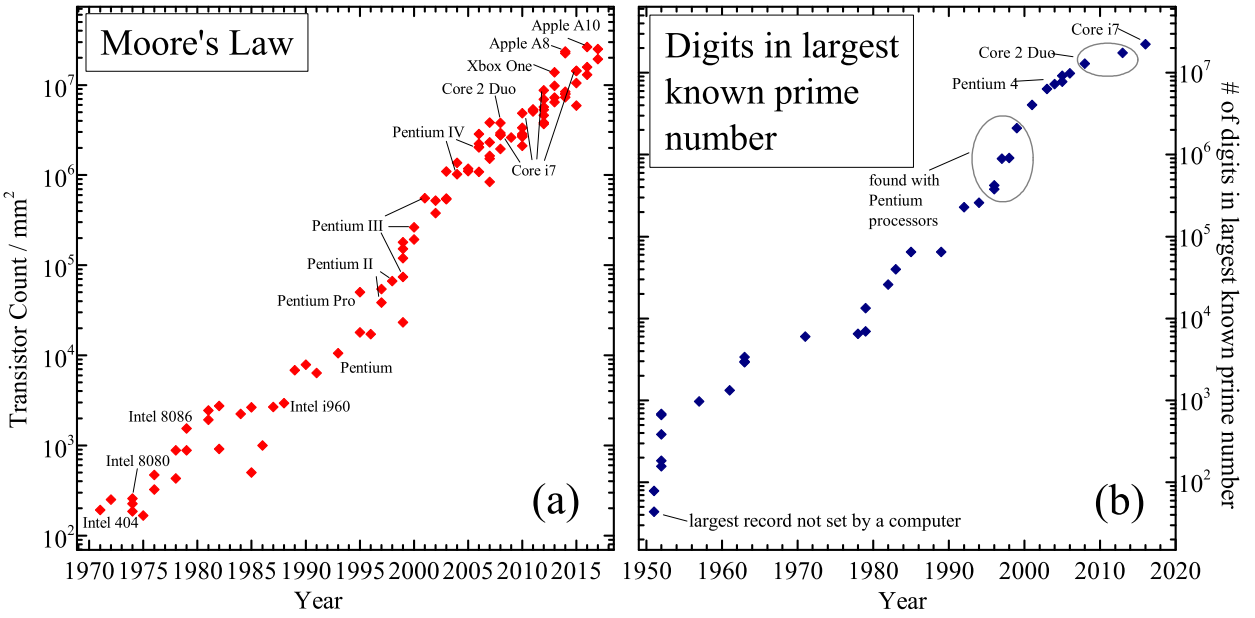

Figure 1.1: Moore's Law. Left Panel: Since Gordon Moore's seminal 1965 and 1975 papers, his exponential law has maintained its pace without folly. Plotted are the number of transitors per square millimeter, with some select processors labelled. Right Panel: A metric for mapping the increase in computing power is the constant discovery of the largest prime number known. Plotted is the number of digits in the largest known prime since computers started searching for them in 1951. Data adapted from Refs. [1] and [2].

the Nobel Prize in 1956 for this discovery. Currently all computer processors are made from intricately fabricated transistors that are wired together in such a way as to allow us to perform calculations, or "compute". The size of transistors on integrated circuits has diminished to the point that their dimensions are now on the scale of a dozen or so nanometers, and still shrinking. Given that atoms in solids are typically separated by about 0.2 nm, this implies that transistors are now made up of only a few hundred or so atoms. It is clear that this miniaturization we have become so accustomed to cannot continue forever.

In fact, in two seminal papers a decade apart (1965 and 1975) by Gordon Moore, co-founder of Intel, predicted the exponential relationship that the density of electronic components on a circuit would double every two years.[3, 4] This has since become the widely popularized *Moore's Law*. In Figure 1.1(a) I have plotted the transistor density count of the most widely used computer processors since 1970 on a logarithmic scale. The near linear

nature of the data indicates that this law has unequivocally stood the test of time. A valid and relatively simple proxy for actually computational performance can be found in Figure 1.1(b); this plot shows the largest prime number known to date as a function of year. Euclid proved that there is no largest prime number, and as such many people (and their computers) still search for a new spot atop the prime number totem pole. As can be seen in Figure 1.1(b), a new largest number is found almost yearly. As the search becomes greater and more expansive as the most recent and powerful computers are used to find the next largest prime number, it is a useful metric for evaluating Moore's Law, and has indeed followed the exponential trend for many decades. However, as foreshadowed in the previous paragraph, this cannot continue forever, and new technologies will need to replace silicon computing in the near future.

The astounding progress in the semiconductor industry has even simulated the neural complexity of brains, as complex as mammals such as cats, using the IBM Blue Gene supercomputer.[5] However, at some point in the near future quantum tunnelling effects will halt the progress of increasing transistor density, as well as the obvious limit that a transistor cannot be made smaller than a few atoms in size. In reality, some exponential trends—such as the energy dissipation of switching events at logic gates, leading to heat issues—associated with Moore's Law have already begun to show clear signs of slowing.[6] Specifically, with miniaturization occurring rapidly, while operating voltages are only declining slowly, a breaking point will be reached where progress can no longer be made, or can only be made very slowly. Furthermore, with Holy Grails such as quantum computing seemingly, at the very least, several decades away, a new feasible technology that is rapidly progressing and could be relatively easily integrated into the existing world of computing is known as *spintronics*.

1.1 Spintronics

As the sustainability of silicon technologically has been called into question at ever increasing frequency over the last two decades, spintronics has risen as the premier technology to overcome many of the hurdles presented above. The source of electron spin is rooted in

the angular momentum that an electron inherently carries; it is the fundamental source of magnetism. Hence, spintronics (spin electronics) effectively comprises the large and quickly evolving field of magnetic electronics. At the heart of spintronics is the *giant magnetoresistive effect* (GMR), first reported in 1988,[7] which showed that the electric resistance of a material could be changed significantly when a magnetic field is applied. The 2007 Nobel Prize in physics was given to Albert Fert and Peter Grünberg for the discovery of GMR. The phenomena was quickly commercialized, and within ten years was being applied as the read head for hard drive disks in computers.

Essentially what was created was a spin valve, in which current could flow easily through a non-magnetic electrical contact sandwiched between two ferromagnetic layers if their magnetic fields are parallel (low resistance), or alternatively, if their magnetic fields are anti-parallel, the electrical resistance would be high. Hence, bits are able to be read as on or off (0 or 1) as the spin valve records the magnetic polarization of the disk. Thus, as the magnetic recording medium (hard drive) spins beneath the read head, the spin valve acts as a sensor to the magnetic field, recording the presence or absence of electric current.[8] This method has constantly been improved on over the last two decades, leading to enormous increases in information storage density. Even today our hard drives make use of a version of GMR—the tunnelling magnetoresistance effect—in which the metal between the magnetic layers is replaced by an insulation layer. The ultimate effect is similar, and the probability of an electron tunnelling through the insulating layer is much higher when the magnetic contacts are parallel.

The next step in computing is to harness the spin of an electron to act as a switch. All existing computer processors (made up of transistors) utilize only the charge of an electron to control logic gates. The idea is to replace silicon transistors with that of a magnetic material in which the spin of electrons being up or down can replace the flow of electronic charge to switch logic gates. The natural question to then ask is: what advantages does controlling the spin of electrons have over only manipulating their charges? Of course, the improvements are plentiful:

1. The energy required to flip spins (i.e. change logic states) is a minute fraction of

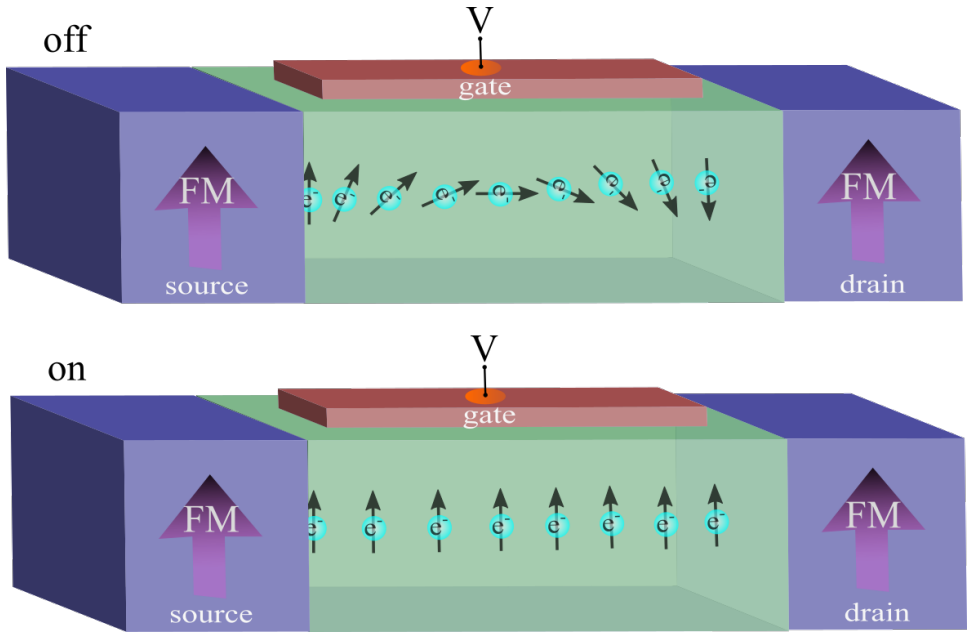

Figure 1.2: A spin transistor requires ferrormagnetic contacts to both inject and detect spin. A smaller gate voltage than in conventional transistors can then take advantage of the Rashba effect, which is a phenomenon that can use an electric field to rotate the spin to be accepted (parallel) or rejected (antiparallel) at the other contact, allowing high and low resistance states. This allows digital on/off logic in a faster more energy efficient manner.

what is required to move electrons. This sidesteps many of the issues regarding heat dissipation in conventional semiconductors, and also has the advantage that spin flips occur on a much shorter timescale, which would lead to faster computers.

2. Spin states can be detected and switched without requiring the flow of the involved electrons. This has the advantage of allowing devices to be smaller, more sensitive, and consume less energy.

3. Spin remains when power is lost. Therefore, random access memory (RAM)—which contains all the data that is being processed by the central processing unit (CPU)—in our computers today is lost when power is lost (nonvolatile), can be replaced by low power consumption magnetic random access memory (MRAM), which would allow semi-permanent storage of memory.[9]

Even more attractive than MRAM technologies is the potential for nonvolatile logic gates in computer processors.[10] The analog of a conventional transistor used for logic in spintronics is a spin transistor, a schematic of which is shown in Figure 1.2. It consists of a ferromagnetic source and drain, and a channel between the two that allows electrons to flow effectively as a two-dimensional gas. The idea was first proposed in 1989, and utilizes the Rashba effect, in which electron spin can be controlled by use of an electric field.[11] In most semiconductors, like silicon, the effect is very small and the electrons are required to travel long distances at very low temperatures in order for a spin flip to occur. However, it has recently been shown that topological insulators Bi_2Te_3 and Bi_2Se_3 also display this effect, but an order of magnitude stronger, and at temperatures exceeding 100°C.[12]

The basic operation of a spin transistor is that an external gate voltage is applied that causes the spins injected at the source to be flipped by the time they reach the drain. A ferromagnetic contact at the source is required to inject spin polarized electrons into the channel. In the ON state the spins do not precess and spin matching is realized at the drain and current is allowed to flow. In the OFF state the gate voltage causes the spins to precess such that they are not aligned at the drain and electrical resistance is high. Essentially, the ferromagnet at the drain acts as a spin detector. Hence, the need for a material that is both semiconducting and ferromagnetic at room temperatures is of the utmost importance for spintronic devices. In fact, contrary to conventional transistors, spin transistors can be manufactured to perform Boolean operations such as AND, NAND, and OR all within a single spin transistor, which is quicker, smaller, and more energy efficient.[13] The application of this programmable logic employing the ability to flip spins is where the true potential of spintronics lies.

There are still several hurdles faced by the spintronic community. Much effort has been given to improving the spin injection and detection efficiencies. Because of this low efficiency, the leakage current in the OFF state is significant, up to one third of that in the ON case. It is essential to have the ability to fully control the injection, detection, as well as their transportation in a nonmagnetic semiconducting channel in order to realize a functional spin transistor. In addition to this, conductivity mismatches at the interfaces between source,

channel, and drain also lead to energy consumption issues.[14]

Despite the successes to date, our understanding of how magnetism arises is far from complete. In general, today, when fabricating a material with some desired properties, one has to employ an educated guess and check method based on the knowledge of the properties of well known materials. The goal of synthesizing a material with electronic and magnetic properties engineered to be precisely as desired requires an understanding of how dopant atoms impact the existing properties of the host semiconductor. A fundamental step in this understanding requires a firm grasp on how dopant magnetic atoms situate themselves within a host semiconductor, and how their presence affects the existing properties. Many experimental findings have emerged over the previous twenty years, but the field is still in its infancy from a technological standpoint.[15]

The typical approach to discovering materials that may be relevant for spintronic materials has been to dope a known semiconductor with some $3d$ transition metal impurity at small concentrations in order to induce magnetism while retaining the desirable semiconducting properties. Since appropriate materials still need to be discovered to overcome the obstacles mentioned above, my research has focused on some of the potentially useful materials, and specifically how the dopant metal atoms interact and influence the host semiconductor. The goal of my work has been to determine the tenability of some of these materials, while addressing issues raised by earlier studies using complementary techniques in order to elicit a deeper understanding of what is taking place at an atomic level.

CHAPTER

TWO

3D TRANSITION METALS

The $3d$ transition metals refer to the row in the periodic table wherein the $3d$ electron shell is partially, and increasingly filled as atomic number increases. The electrons in this shell are known as the valence electrons, and they are the most important from a scientific and technological point of view. In fact, nearly every property of a solid is determined by its valence electron states, including its conductivity, hardness, colour, chemical reactivity, magnetism, thermal, and luminescing properties to name a few. Hence, solid state physics is essentially the study of valence electrons and how they give rise to the properties we observe.

The spatial distribution of electron density is described by its wavefunction $\psi(r, \theta, \phi)$; the square of this function multiplied by some volume dv then gives the probability of finding an electron in the volume dv. For a given orbital ψ_{nlm}—which is defined by its three quantum numbers n, l, and m for principal, angular, and magnetic quantum numbers, respectively—one can separate the radial and angular parts such that $\psi_{nlm}(r, \theta, \phi) = R_{nl}(r)A_{lm}(\theta, \phi)$. The (normalized) radial parts of the wavefunction R_{nl} for the first ten combinations of n and l are plotted in Figure 2.1. What makes the row of $3d$ metals so unique is that the radial part of the electron density for its valence electrons is quite near to the nucleus of the atom, and hence overlaps significantly with the core electrons. Also due to this localization, is that the $3d$ electrons generally become lower in energy than the $4s$ electrons and so the (very slightly) higher energy $4s$ electrons are generally lost first upon ionization; this is

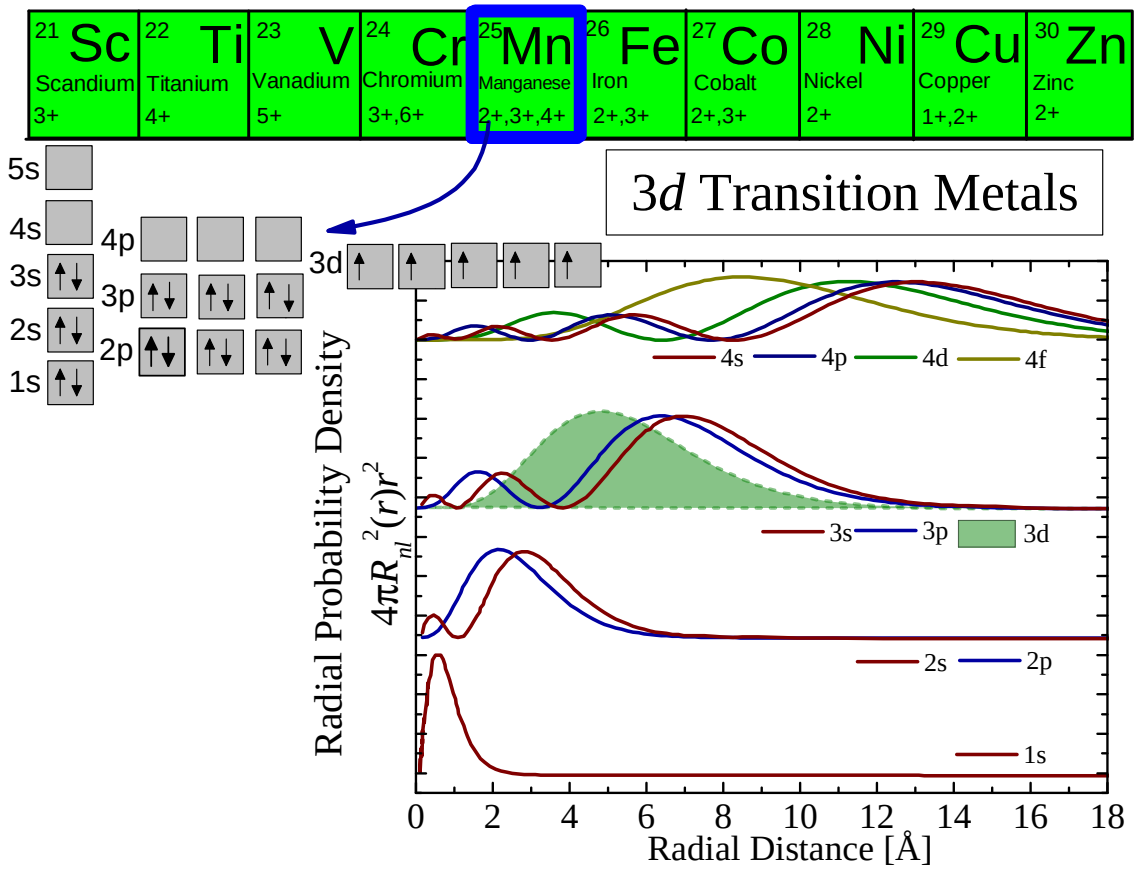

Figure 2.1: Shown are the ten 3d *metals along with their commonly found oxidation states. The spin-up and spin-down filled electron shells are shown for* Mn^{2+}*. The plot shows the radial probability density for electron shells up to* $n = 4$ *that I calculated using Quanty. Of note is the relatively localized nature of the* 3d *valence orbital, which results in a strong overlap with the core electron's wavefunctions, and the emergence of useful electrical and magnetic properties.*

contrary to commonly taught method of filling electrons across the periodic table in the order $1s^2 2s^2 2p^6 3s^2 3p^6 4s^2 3d^{10}$ et cetera. Because the valence electrons are very sensitive to the solid state in which they find themselves, if one can observe them by some means then all the properties and their sources can be elucidated.

The vast majority of the physics in this thesis relies on the localized nature of 3*d* electrons, their overlap with the core 2*p* electrons, and our ability to probe exactly these states. This overlap leads to what are known as *multiplet effects* (discussed at length in Section 2.3), which is essentially a splitting of degenerate electron energies due to the solid state.[16]

2.1 Magnetism

In 1929, Paul Dirac said in his paper *Quantum Mechanics of Many-Electron Systems*, "The underlying physical laws necessary for the mathematical theory of a large part of physics and the whole of chemistry are thus completely known, and the difficulty is only the exact application of these laws leads to equations much too complicated to be soluble."[17] While it is clear that this claim was slightly premature, it is even more clear that the search for applications has been daunting, but also astonishingly fruitful. Nonetheless, even today we lack a complete understanding of the sources of magnetism and the conditions necessary for its appearance. This explains the extensive search for magnetic semiconductors over the last two decades; one cannot synthesize a material with the properties desired if one does not grasp the fundamentals. Despite this, magnetism has been the quintessential example over the previous century of how technological progress can be made despite lacking a complete picture. Even the Earth's magnetic field, one of the oldest known magnets to humankind is imperfectly understood and we still cannot predict its future. A major goal of my research has been to contribute to the vast body of knowledge in understanding its fundamental source, with the ultimate goal of predicting magnetism.

Strictly speaking, all materials are magnetic, and they are classified according to their response from an externally applied magnetic field. Diamagnetism is a property of *all* materials, when an external magnetic field is applied, small current loops are induced in the atoms of that material, which is diamagnetism. However, in accordance with Lenz's law, these current loops create a magnetic field that directly opposed the very field that created it. The types of materials where this effect dominates are repelled from magnetic fields, although in reality the effect is always very small, even with some of the strongest diamagnetic materials, like bismuth.

Paramagnetism is much more common, and generally stronger than the diamagnetic effects in nearly all compounds. When the dominating effect is that the magnetism of a material can be measured to be proportional to the magnetic field it resides in, the material is classified as paramagnetic. The external magnetic field causes some of the electrons in the

material to align in the same direction as itself, and a net magnetic moment in the material is created in this direction; the material is then said to be magnetized. As the external field is shut off, thermal fluctuations take over and no overall net magnetic moment can be detected as the spins once again become scrambled.[18]

For the purposes of this thesis, we are concerned with permanent magnets—magnets whose magnetization remains even after the external field is shut off. These materials are known as *ferromagnets*, and they are what we commonly refer to when we speak of "magnets" in our everyday lexicon. Even these types of magnets lose their permanent magnetism if exposed to high temperatures—known as the Curie temperature—where the thermal jostling of atoms can overpower the force that causes the spins to align. Hence, the bulk of spintronic research is devoted to finding materials in which the Curie temperature is sufficiently above room temperature and ferromagnetism can be maintained, so devices will continue working even as they heat up. The 3d elements iron, cobalt, and nickel are the only three elements in the periodic table to display ferromagnetism at room temperature (gadolinium is close with a Curie temperature of 293 K). Not coincidentally, these are the three most commonly used dopant atoms in known semiconductors used in attempts to induce ferromagnetism.

2.2 Ferromagnetism

On a macroscopic scale we know that electrical currents induce a magnetic field in accordance with Maxwell's equations. It seems reasonable that magnetism on an atomic scale results from tiny current loops of the electrons within an atom. Indeed this is true up to the point in which one can envision classical analogs within the framework of quantum mechanics. It is more accurate to say that magnetism is a result of the angular momentum of an electron, which can be separated into its spin and orbital angular momenta. Whereas orbital angular momentum has its classical analog in a current loop around an atom that induces magnetism, there is no classical analog to electron spin.

Ferromagnetism arises when the summed angular momentum of all the electrons in a materials are aligned together, on average, in the same direction. Clearly, this is quite rare,

as very few materials are ferromagnetic, there must be *something*—a force or interaction—causing electrons to align such that their spins are antiparallel or completely scrambled, and thus cancel out. This apparent force arises from Pauli's exclusion principle. It states that no two electrons can occupy the same quantum state, i.e. they cannot have the same quantum numbers. Another way to state this is to say that two electrons cannot occupy the same place if they have the same spin. For example, if two electrons are orbiting a helium atom, they prefer to be in the lowest energy state. Two electrons with opposite spins in the lowest energy 1s shell is much more energetically favourable (because of their proximity to the nucleus) than having two parallel (or antiparallel) spins with one in each the 1s and 2s shells. The law of nature that it is against the rules to have parallel spins, unless the electrons stay away from one another, explains the absence of magnetism in virtually every material. Of course, this then raises the question of why ferromagnetism appears at all.

In 1907 Weiss first proposed a material dependent "internal molecular field" to explain the phenomenon of spin alignment in some materials,[19] and though it explained a wide range of ferromagnetic phenomena, it did little to explain *why* this field exists at all. The next major breakthrough was made in 1928 by Heisenberg. He introduced what is known as an *exchange interaction* into the Hamiltonian.[20] Mathematically, it is proportional to what is called the exchange integral J_{ex} and the negative of the dot product of adjacent spins $\propto -J_{ex}\mathbf{S}_i \cdot \mathbf{S}_j$. Hence, if J_{ex} is positive, this energy is lowest when the spins are aligned ($\mathbf{S}_i \cdot \mathbf{S}_j = S^2$), leading to ferromagnetism; if J_{ex} is negative the energy is lowest when the spins are antiparallel ($\mathbf{S}_i \cdot \mathbf{S}_j = -S^2$).

Two years later Slater added to this, noting that the exchange integral J_{ex} could be determined experimentally as a function of the ratio of the interatomic spacing a to the unfilled shell radius r (the 3d shell in most cases).[21] He found that if this ratio was greater than 3 (shown in Table 2.1), the exchange integral would be positive and ferromagnetism would be present. What this also suggested was that Mn could perhaps be made ferromagnetic if this ratio could be slightly tweaked, which is exactly what was discovered in ferromagnetic Mn alloys such as Mn-As, Cu-Mn, and Mn-Sb.[22]

This exchange interaction can manifest itself in several forms, however the most common

Element	Cr	Mn	Fe	Co	Ni	Gd
a/r ratio	2.60	2.94	3.26	3.64	3.94	3.10

Table 2.1: Interatomic spacing (a) to unfilled shell radius (r) ratios for some TMs. A ratio greater than 3.0 was found in cases where ferromagnetism is present.

is itinerant exchange, which is what occurs in Fe, Co, and Ni. In itinerant magnetism the electrons responsible for the magnetism are also responsible for conduction; they are delocalized–they belong to no specific atom. This is epitomized by the non-integer values of magnetic moment for Fe = $2.2\mu_B$, Co = $1.7\mu_B$, and Ni = $0.6\mu_B$, where μ_B is the Bohr magneton and is essentially the magnetic moment carried by a single free electron.

Loosely speaking from a qualitative perspective, one can say that an unpaired localized electron has influence on the conduction electrons as they become spatially near. They have a tendency to align their spins opposite in accordance with the exclusion principle. This conduction electron then carries its spin inclination to the next unpaired electron and influences that electron to become opposite to itself, and the net effect is that two nearby electrons are aligned. All there needs to be is very slight predilection for conduction electrons to align successive localized electrons in the same direction for ferromagnetism to exist.[23] Hence, there is an exchange interaction (this where the term originates from) between localized and delocalized conduction electrons that can result in a net overall spin polarization, which we observe macroscopically as ferromagnetism. Of course, this says nothing about why this occurs in some metals and not others.

A more complete picture can be understood in terms of band theory.[24] The result that was found is known as the *Stoner criterion* for itinerant ferromagnetism. Stoner found that there is a critical point at $UD(E_F) > 1$ where U is the intra-atomic Coulomb interaction energy, which is roughly constant for 3d metals, and $D(E_F)$ is the density of states (DOS) at the Fermi level (note: DOS has units of inverse energy). When this condition is met, the paramagnetic state is unstable. In other words, what it essentially says is that the ferromagnetic state is stable if the energy gained from the Coulumb interaction resulting from aligned spins overcomes the band energy loss ($U > 1/D(E_F)$).[25] Therefore, ferromagnetic

metals and alloys all have a large peak in their DOS at the Fermi level.

2.3 Multiplet Effects

Since the electric, magnetic, and thermal properties of solids are determined by the valence electrons, we must have a method of observing these electrons that allows us to extract physics from the system. The technologically relevant materials studied herein have a large degree of electron correlation—that is, strong electron-electron interactions due to the core and valence overlapping wavefunctions (see Figure 2.1). This overlap also occurs in the ground state, but only in the presence of a core hole does the strong overlap of wavefunctions manifest itself experimentally. Materials in which the electrons interact very strongly with one another to determine the properties of that material are commonly referred to as strongly correlated materials.

Since we are exciting electrons into the unoccupied density of states when performing an XAS measurement, intuitively one would expect that the spectral XAS shape would resemble the unoccupied density of states in accordance with Fermi's golden rule for absorption. And indeed there is very good agreement between the calculated density of states and experimental spectra for transition metal, oxygen, nitrogen, and carbon K-edges.[26] However, for the $L_{2,3}$-edges ($2p$ electrons) of the $3d$ metals, the agreement is very poor. The discrepancy at the $L_{2,3}$-edge arises because one does not actually observe the density of states in experiment, not because the density of states is calculated incorrectly.

What one actually observes in experiment is that $L_{2,3}$ XAS spectral shapes are nearly entirely determined by multiplet effects. Thus, x-ray spectroscopic studies of strongly correlated systems can establish the source, on an atomic scale, of the macroscopic properties of a material by observing the perturbed valence electrons.[27] The various arrangements of the valence electrons (with various energies) are referred to as multiplets. In order to extract information from strongly correlated systems, an understanding of multiplets and how they arise must be gained. Herein I will focus on such effects in the context of $3d$ transition metals, although most of the discussion also applies to rare earth $4f$ elements as well.

Throughout this thesis, all calculations that I performed were done using a multiplet software written by Robert Green, or a similar code called Quanty written by M. Haverkort, Y. Li, S. Macke, and R. Green.[28, 29, 30, 31]

2.3.1 Atomic Multiplets

In the atomic model, no influences from the solid state are included, and all effects originate within the atom. The Hamiltonian contains four terms: the kinetic energy of the electrons, Coulomb interaction with the nucleus, electron-electron Coulomb repulsion, and a spin-orbit coupling term:

$$H_{atomic} = \sum_i \frac{p_i^2}{2m} + \sum_i \frac{-Ze^2}{r_i} + \sum_{pairs} \frac{e^2}{r_{ij}} + \sum_i \zeta(r_i) l_i \cdot s_i \tag{2.1}$$

The first two terms are the same for all electrons in a given atomic configuration (for example, a $3d^5$ system), and alone give the average energy of the system. The latter two terms are the source of the relative energy differences between different electron configurations within a given atomic configuration.

2.3.2 Term Symbols

The notation we use to identify all possible states for a given electron configuration is known as term symbol notation. Here it is valuable to review quantum numbers, and their possible values as displayed in Table 2.2. Both L and S (total orbital and spin angular momenta) are vectors and their minimum and maximum possible values arise from the fact that their constituent l and s components can be added to reinforce one another, or cancel each other out. For example, in a two electron configuration (each with spin $\frac{1}{2}$) S must be either $s_1 + s_2 = 1$ or $s_1 - s_2 = 0$. A given electron can be identified with its term symbol given by ${}^{2S+1}L_J$, where $L = S, P, D, F, G, H$ and so on for $L = 0, 1, 2, 3, 4, 5$, respectively. If there is no spin-orbit coupling then all terms with the same values of L and S have the same energy, which is $(2L+1)(2S+1)$-fold degenerate. Here, $(2S+1)$ is the spin multiplicity and is called singlet, doublet, triplet, etc. for $S = 0, 1/2, 1, 3/2$ etcetera, and represents the number of

Name	Symbol	**Single electron** Values (min & max)		**Multi-electron** Values (min & max)	
Principal q.n.	n	$n = 1$	$n = \infty$	$n = 1$	$n = \infty$
Orbital angular momentum q.n.	l or L	$l = 0$	$l = n - 1$	$L = \|l_1 - l_2\|$	$L = l_1 + l_2$
Magnetic q.n.	m_L or M_L	$m_L = -l$	$m_L = l$	$M_L = -L$	$M_L = L$
Spin angular momentum q.n.	s or S	$s = 1/2$	$s = 1/2$	$S = \|s_1 - s_2\|$	$S = s_1 + s_2$
Spin magnetic q.n.	m_s or M_s	$m_s = -1/2$	$m_s = 1/2$	$M_s = -S$	$M_s = S$
Total angular momentum q.n.	j or J	$j = l - 1/2$	$j = l + 1/2$	$J = \|L - S\|$	$J = L + S$
Total magnetic q.n.	m_j or M_j	$m_j = -j$	$m_j = j$	$M_J = -J$	$M_J = J$

Table 2.2: A list of quantum numbers and their respective nomenclature. Note that in a multi-electron system the sums shown in the table are for only two electrons, but can be generalized to an arbitrary amount of electrons. There will then be additional terms in the sums since S and L are vectors and can be superimposed, or added. Similarly, to obtain J values, L and S cannot be added arbitraryly oriented with respect to one another, but must be added such that the different possible values of their vector sums have integer differences. Also, all values between minimum and maximum values must be in integer steps.

possible orientations of the total spin vector. When spin-orbit coupling is included the terms split according to their J values, which are then each $(2J + 1)$ degenerate.

For example, a single s electron has $l = 0$, $s = 1/2$, and $j = 1/2$. The only term symbol possible is $^2S_{1/2}$. Similarly, a single p electron has $l = 1$, $s = 1/2$, and $j = 1/2, 3/2$; or equivalently terms symbols $^2P_{1/2}$ and $^2P_{3/2}$. With the degeneracy of $2J + 1$ we see that the $^2P_{3/2}$ is twice as degenerate as the $^2P_{1/2}$ state. This is commonly seen in the ratio of L_3 and L_2 absorption edges in transition metals, where the L_3 edge jump in an XAS spectrum is approximately twice as large.

In the case of a more complex system, for example, if we have a $3d^1 4d^1$ configuration, which is a two electron configuration with possible values of $L = 0, 1, 2, 3,$ or 4 and $S = 0 or 1$, i.e. integer steps between $2 - 2 \leq L \leq 2 + 2$ and $1/2 - 1/2 \leq S \leq 1/2 + 1/2$). The corresponding term symbols for all possible combinations here are ^1S, ^1P, ^1D, ^1F, ^1G, ^3S, ^3P, ^3D, ^3F, and ^3G. In accordance with the $(2L + 1)(2S + 1)$ degeneracy, it can easily be

	m_l						
	+2	+1	0	-1	-2	M_L	M_S
All spin-up	↑	↑				3	1
	↑		↑			2	1
	↑			↑		1	1
	↑				↑	0	1
		↑	↑			1	1
		↑		↑		0	1
		↑			↑	-1	1
			↑	↑		-1	1
			↑		↑	-2	1
				↑	↑	-3	1

Table 2.3: All possible 2-electron spin-up states shown for a $3d^2$ system. An all spin-down table could be shown that would be exactly the same except the spins would be down and $M_S = -1$. And a mixture of spin-up and spin-down table would also be nearly the same except with one spin-up and one spin-down, and then vice versa. The remaining five states would show both electrons with the same value for m_l but opposite spins. The total number of microstates is 45.

shown that the degeneracy of the $3d^1 4d^1$ configuration is 100. In the case of a $3d^2$ system, this number is reduced to 45 because of the Pauli exclusion principle; there can't be two spin-up or two spin-down electrons with the same quantum numbers. Each microstate can be written explicitly as shown in Table 2.3. For size considerations, only all possible micro states for both electrons being spin-up are shown. A similar table for all spin-down combinations ($M_S = -1$) could be made, as well as one for one spin-up and one spin-down electron ($M_S = 0$) and one would find 45 total possibilities. The general formula to determine the degeneracy of a $3d^N$ configuration can be written as

$$\binom{10}{N} = \frac{10!}{(10-N)!N!} \tag{2.2}$$

One could then write down all 45 of these term symbols and verify that their respective term symbol degeneracies are indeed $(2S+1)(2L+1)$. For example, the top line in Table 2.3 corresponds to possible term symbols with $L = 3, 4$ and $S = 1$, since $M_L = 3$ and $M_S = 1$

(to be consistent with allowed quantum numbers in Table 2.2). But $L = 4$ is not allowed for 2 spin-up electrons (due to Pauli's exclusion principle that requires two opposite spin electrons both with $m_L = +2$ for $L = 4$), thus the term symbol for the top line configuration of Table 2.3 must be ${}^3F$, and you would find a degeneracy of $(2 * 1 + 1)(2 * 3 + 1) = 21$ for that term symbol if all 45 possibilities were written out. Similarly if an up and a down spin are in the $m_l = +2$ position then $S = 0$ (the spins "cancel") then $L = 4$ since $M_L = 4$ and the term symbol is ${}^1G$ with a 9-fold degeneracy. If J values are included, then all possible term symbols turn out to be: ${}^3F_2$, ${}^3F_3$, ${}^3F_4$, ${}^3P_0$, ${}^3P_1$, ${}^3P_2$, ${}^1G_4$, ${}^1D_2$, and ${}^1S_0$, each with their own respective degeneracy.

Things can quickly become very complicated in the presence of a core hole. For a $2p \rightarrow 3d$ transition one wishes to consider configurations of the kind $2p^5 3d^{N+1}$. Because of the six possible configurations of the five $2p$ electrons, the number of possible microstates for a $2p^5 3d^{N+1}$ is six times as that of a $3d^{N+1}$ configuration. For example, a $2p^5 3d^5$ configuration has 1512 possible microstates that can be split up into 205 term symbols, although some of these transitions may be dipole forbidden. So even in the simple, but necessary atomic model, the splitting of the energy levels due to various arrangements of the d electrons can become quite numerous. Often, the most important of all these configurations is the ground state—the lowest energy state that the atom prefers to reside in—which can be determined using Hund's Rules.

2.3.3 Hund's Rules

To determine the term symbol that corresponds to the ground state of an atom one must apply Hund's rules. The rules find the term with the lowest energy (ground state); they can be succinctly stated as follows:

1. The term with the largest S is lowest in energy.

2. Within these, the term with the largest L is lowest in energy.

3. Within these, the smallest J and largest J have the lowest energy if the shell is less than half full and more than half full, respectively.

The first rule of maximum spin can be understood in terms of Pauli's exclusion principle: the more parallel spins there are, the larger the distances the electrons will be from one another due to their repulsion, thus lowering the overall energy. Rarely, this rule can be broken if the crystal field splitting is sufficiently large and it is more energy efficient to have an opposite spin electron occupy the same orbital instead of a parallel spin in a much higher energy orbital.

Within this subset, the term with the largest orbital angular momentum has the lowest energy. This rule can also be interpreted in terms of minimizing electron repulsion. The classical analogy is that with a larger orbital angular momentum the electrons are orbiting the nucleus in roughly the same direction and effectively stay farther apart on average. Whereas with less orbital angular momentum, the electrons must pass by each other frequently, and thus their separation is on average smaller, and therefore exist in a higher energy state.

Finally, within this smaller subset, if the shell is half filled or less the lowest energy is the term symbol with the lowest total angular momentum, and if more than half full the ground state corresponds to the largest total angular momentum. This stems from the fact that the product $S \cdot L$ is negative in the Hamiltonian if the spin and orbital angular momentum are in opposite directions. For lowest energy we would like it to be negative, and so the smallest value of $L + S = J$ is the lowest energy term. Due to the symmetry of holes and electrons, this rule is reversed for shells that are more than half full.

Note that the rules are only strictly valid for determining the ground state energy. Beyond that they can be used as a first approximation for the ordering of term symbols, but will often give incorrect results for the exact ordering. Given the above rules and terms symbols for the $3d^2$ configuration in the example above, the ground state term is ${}^3F_2$.

To quantitatively calculate the energies for the term symbols within the atomic model one must compute the Slater integrals F^k and G^k, which physically represent the degree of intra-atomic Coulomb and exchange interaction between electrons. They are in units of energy and take the form[32]

$$F^k = \underbrace{\int d\mathbf{r_1} \int d\mathbf{r_2}}_{\text{integrate over all possible electron locations}} \underbrace{\frac{2r_<^k}{r_>^{k+1}}}_{\text{Coulomb repulsion b/w electrons at } r_1 \text{ and } r_2} \underbrace{P_i^*(\mathbf{r_1})P_i(\mathbf{r_1})}_{\text{probability electron 1 in orbital i is located at } r_1} \underbrace{P_j^*(\mathbf{r_2})P_j(\mathbf{r_2})}_{\text{probability electron 2 in orbital j is located at } r_2} \tag{2.3}$$

$$G^k = \int d\mathbf{r_1} \int d\mathbf{r_2} \frac{2r_<^k}{r_>^{k+1}} \underbrace{P_i^*(\mathbf{r_1})P_j(\mathbf{r_1})P_j^*(\mathbf{r_2})P_i(\mathbf{r_2})}_{\text{exchange integrals}} \tag{2.4}$$

where $r_<$ amd $r_>$ are the smallest and largest radius vectors between the electrons, i and j represent the orbitals (p and d orbitals for all intents and purposes), and the multiplication of a wavefunction by its complex conjugate (PP^*) represent the probability of finding the electron at the location $\mathbf{r}$. Note the indices i and j for G_k are "exchanged", and hence this is known as the exchange integral, while the F^k integral physically represents only Coulomb interaction within a given orbital. The calculation of these integrals is very involved, generally requiring computers to solve them numerically within the Hartree-Fock approximation.[33] However, for most values of k the integrals are zero, and one only needs to compute F^k's for even k up to $2l$ for the orbital being calculated ($2l = 4$ for d-orbitals and $2l = 2$ for p-orbitals), and odd G^k's up to one less the above; in every case only non-full orbitals need to be calculated. With subscripts representing the orbitals of the two interacting electrons, F^0_{dd}, F^2_{dd}, and F^4_{dd} are the only relevant integrals in the initial non-core hole state, and then F^0_{dd}, F^2_{dd}, F^4_{dd}, F^0_{pd}, F^2_{pd}, G^1_{pd}, and G^3_{pd} are all relevant in the presence of a p core hole and unfilled valence d shell. These values have been computed, and $F^2_{dd} \approx 10$ eV for 3d transition metals with F^4_{dd} being about 0.62 times that amount.

In practical calculations of spectra however, the Hartree-Fock values of the Slater integrals often overestimate the interactions that occurs in real solid state materials because of screening effects. By scaling down these integrals to some percentage (usually around 60-80%) of their Hartree-Fock values, we are reducing the energy of these intra-atomic interactions. When hybridization of orbitals is present—as it always is to some degree—there is a small delocalization of the 3d electrons, and this effectively lowers the energy of the intra-atomic interactions. So by reducing these interactions further we can account, to some

degree, for the 2p (ligand)-3d (metal) hybridization of orbitals, which we often call *covalent bonding*.

2.3.4 X-ray Absorption in the Atomic Model

If considering only intra-atomic effects, neglecting the solid state, we can use the term symbols to roughly calculate x-ray absorption spectra (XAS). To show this I will stick to the simplest of all $2p \rightarrow 3d$ transitions. A single atom of Ti^{4+} in its ground state $2p^6 3d^0$ configuration has quantum numbers $L = 0, S = 0, J = 0$, or $^1S_0$. When a 2p electron is excited, the atom resides in the $2p^5 3d^1$ state, which has many term symbols, and can be written down individually similar to what was shown above. In this case there are 12 term symbols in the final state: $^1P_1$, $^1D_2$, $^1F_3$, $^3P_{0,1,2}$, $^3D_{1,2,3}$ and $^3F_{2,3,4}$. That is, there are 12 possible transitions that could occur in this excitation. Whether or not these transitions are seen or not in the XAS spectrum depends largely on electric dipole selection rules, which I will reproduce here for single electrons:

1. Δn is not constrained
2. $\Delta s = 0$ but can be ± 1 in the case of appreciable spin-orbit coupling [34, 35]
3. $\Delta l = -1, +1$ but can be 0 or ± 2 if $\Delta s = \pm 1$
4. $\Delta j = -1, 0, +1$ — but not a $0 \rightarrow 0$ transition
5. $\Delta m_j = -1, 0, +1$ — but not a $0 \rightarrow 0$ transition if $\Delta j = 0$

If we restrict ourselves to the hard rule that always holds, $\Delta j = 0, \pm 1, 0 \not\rightarrow 0$ we are left with the three term symbols. $^1P_1$, $^3P_1$, and $^3D_1$, and thus three allowed transitions. Indeed, this is exactly what is seen if we calculate a $2p \rightarrow 3d$ transition for a Ti^{4+} atom as seen in Figure 2.2 (c).[36] There are three discrete transitions (shown by the "sticks"); they have been convolved to show something that actually resembles a spectrum.

This example can be extended to all $2p \rightarrow 3d$ transitions to give the number of observed transitions in the atomic state. Writing down all the term symbols would be quite laborious,

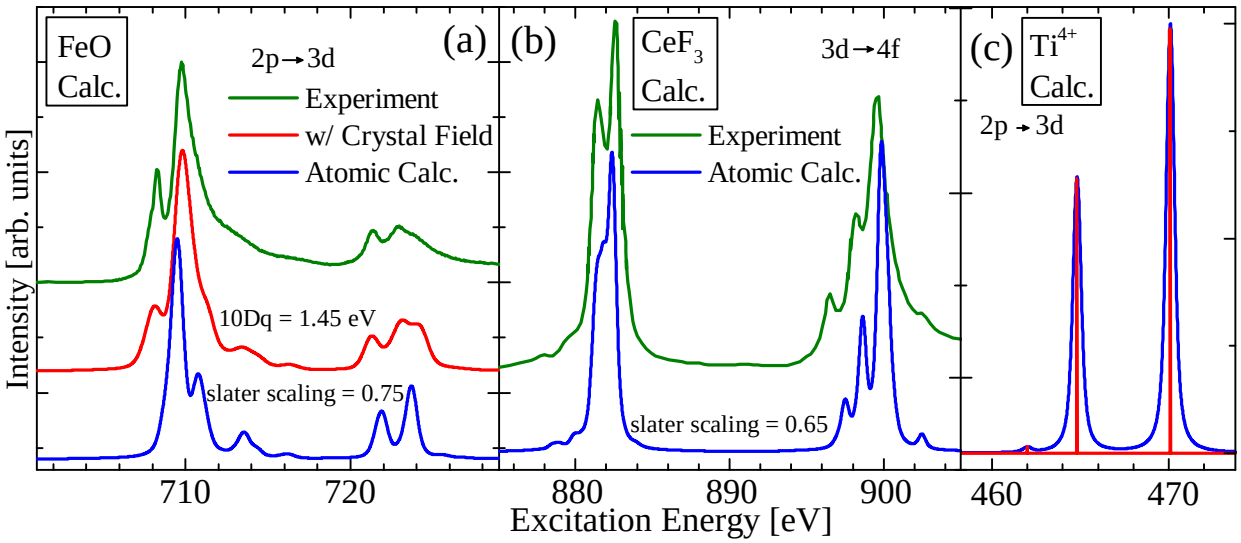

Figure 2.2: (a) Atomic multiplet calculation of Fe^{2+} $2p^6 3d^6 \rightarrow 2p^5 3d^7$ *transition. The atomic model (blue calc.) alone is generally inadequate (but necessary) when considering the* 3d *transition metals as it does not account for the surrounding environment. The calculation in red includes a crystal field that further splits the energies of the electrons. (b)* 4f *metals are very atomic-like due to their even more localized* 4f *orbitals, and usually an atomic calculation alone is sufficient to reproduce experimental spectra. (c)* Ti^{4+} *atomic XAS calculation shows three peaks, in accordance with what is predicted from the term symbols.*

so I have summarized the number of transitions and term symbols in Table 2.4. Another relatively simple case that can be seen in Table 2.4 is that only one transition is allowed to the $3d^{10}$ state, implying the intensity of the L_2 peak is zero, which is what is observed in Cu and Zn XAS spectra. In addition, the above discussion applies quite readily to the 4f orbitals of rare earth metals as well, because these electrons display a similarly large localization as that of 3d electrons, and symmetry (crystal field) effects play an even smaller role. Therefore, these 4f solids can be calculated quite well with only an atomic model.

If atomic calculations are compared to real experimental spectra in the case of 3d ions, very poor agreement is found. This is because the effects of neighbouring atoms is significant and must be considered. In Figure 2.2 (a) I display an FeO $L_{2,3}$ XAS spectrum from experiment, an atomic calculation, and one that also includes the effect of the crystal field. It is clear that the atomic calculation, no matter the scaling of the Slater integrals, is insufficient to model the spectrum. However, upon the introduction of a crystal field splitting (discussed

Transition	Ground State	Transitions	Term Symbols
$2p^6 3d^0 \rightarrow 2p^5 3d^1$	$^1S_0$	3	12
$2p^6 3d^1 \rightarrow 2p^5 3d^2$	$^2D_{3/2}$	29	45
$2p^6 3d^2 \rightarrow 2p^5 3d^3$	$^3F_2$	68	110
$2p^6 3d^3 \rightarrow 2p^5 3d^4$	$^4F_{3/2}$	95	180
$2p^6 3d^4 \rightarrow 2p^5 3d^5$	$^5D_0$	32	205
$2p^6 3d^5 \rightarrow 2p^5 3d^6$	$^6S_{5/2}$	110	180
$2p^6 3d^6 \rightarrow 2p^5 3d^7$	$^5D_2$	68	110
$2p^6 3d^7 \rightarrow 2p^5 3d^8$	$^4F_{9/2}$	16	45
$2p^6 3d^8 \rightarrow 2p^5 3d^9$	$^3F_4$	4	12
$2p^6 3d^9 \rightarrow 2p^5 3d^{10}$	$^2D_{5/2}$	1	2

Table 2.4: The number of available transitions for $3d^n \rightarrow 3d^{n+1}$ transitions in the atomic model determined by writing down all term symbols and applying dipole selection rule $\Delta J = 0, \pm 1$ to get the number of available transitions.

in the next section), good agreement is found. This trend of the necessity of the crystal field, and insufficiency of using only atomic effects is found throughout all of the 3d transition metals.

Predictably, the atomic model has its limitations, as the valence electrons in real solids do not behave as they would in isolated atoms. The effect of the solid state is of the utmost importance for most materials, especially 3d metals. However, it is still very important to include all the above atomic effects in more complex models, because as limited as the atomic model is on its own, it is still necessary. On the other hand, the atomic model is quite sufficient when calculating 4f spectra of rare earth metals as shown in Figure 2.2 (b). Because, like the 3d orbitals, the 4f orbitals also contain no radial nodes, and are extremely localized to the atom (Figure 2.1), but the crystal field splitting for 4f ions is very small. So much so that these elements, even in the solid state, can be adequately described using only the atomic model.[37] To form a more complete model that takes in account the solid state, we must also consider the effect of the crystal field and the additional multiplets that arise in its presence.

2.3.5 Crystal Field Multiplets

Crystal field multiplets arise from the Coulomb interaction between the 3d electrons themselves, and between the 2p core hole and 3d electrons. The net result is that the surrounding crystal lattice influences the relative energy levels of the d orbitals. So instead of seeing two featureless spin orbit peaks when exciting the $2p_{3/2}$ (L_3) and $2p_{1/2}$ (L_2) electrons of the 3d TMs, we instead observe that very rich spectra emerge.[38]

The mathematical concepts of the crystal field are very much related to group theory and its applications to real systems are well developed and have been used for decades. Effectively what happens is that the term symbols discussed above branch apart, degeneracies are broken, and more available states emerge.[39] The simplistic description of the crystal field model is still to consider the atom as isolated, but with a charge distribution around it that approximates the charges of the surrounding ligands in the real solid. In effect, the crystal field is treated as a perturbation to the atomic model. In fact, the Hamiltonian written above simply has another term added to it.

$$H_{ligand} = H_{atomic} + (-e\phi(r,\theta)) \tag{2.5}$$

where e is the electron charge and ϕ is the surrounding potential of the ligands. This potential is generally written as a series expansion of spherical harmonics.

If one considers a transition metal in a gas phase it will have have five 3d orbitals, all degenerate in energy. But once condensed to a solid state there will be a splitting of these energy levels. This is evident in Figure 2.3, which shows the lobes (probability distributions) for the five d orbitals for an atom. Mathematically, these orbitals are spherical harmonics, or sums of spherical harmonics. However, an intuitive explanation for their shapes can be obtained by considering nodes. Beginning with a classical vibrating string secured at both ends, we know that the lowest energy vibration has zero nodes, the next available energy state is the first harmonic with one node in the centre of the string, the 2nd harmonic has two nodes 1/3rd and 2/3rds the distance across the string, and so on to further harmonics. Atomic orbitals, and their shapes, can be thought of similarly by adding nodes, except in three dimensions with a sphere. Zero nodes correspond to s orbitals, which are simply

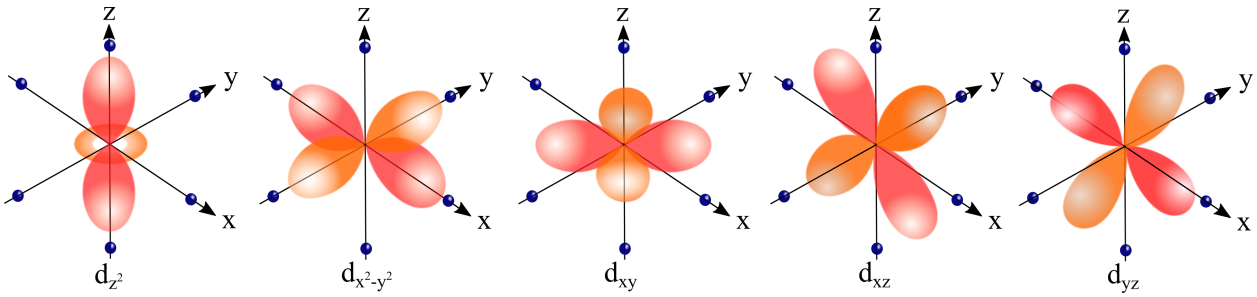

Figure 2.3: The five d-orbitals are shown in a surrounding ligand field of octahedral geometry (O_h). The spatial distance from these orbitals to the ligands determines the degree to which they interact, and therefore their respective energies as well. The spatial distance of the orbitals to the ligands also plays a large role in the degree to which each orbital is hybridized with the neighbouring ligand atoms; this is considered in charge transfer models.

spheres. By slicing the sphere with a plane through the centre, a node is created. Hence, p orbitals are essentially spheres wherein a node is created by a plane slicing through a sphere. That is, they are *not* the figure eight shape they are nearly always portrayed as, but instead more akin to a halved sphere folded in on itself. Nodal planes can be added in three orthogonal ways, which give rise to the p_x, p_y, and p_z orbitals. Finally, d orbitals are then "spheres" in which there are two nodes. These are formed by slicing the sphere with two planes and folding the resulting quarter spheres in on themselves such that they are smooth. The unique looking d_{z^2} orbital is formed by slicing a sphere with two conical shaped surfaces, with one inverted such that their apexes both pass through the centre of the sphere. Thus, it is possible to understand the origin of atomic orbital shapes qualitatively without the use of spherical harmonics; this method can also be used to predict the shape of exotic g and h orbitals.

In octahedral symmetry, the d_{z^2} and $d_{x^2-y^2}$ orbitals are spatially near that of the surrounding ligands, and hence higher in energy. The remaining three orbitals consist of electron locations that are between the ligands and are therefore in a lower energy state because of a smaller Coulomb repulsion. This effect is reversed in the case that the metal ion is in tetrahedral symmetry. Changes in the geometry of the surrounding ligand atoms have profound influences on these energy levels,[40] which can be indirectly detected experimentally in the

form of multiplets. Indeed, all the calculations in this thesis consider exactly this effect on the orbitals, and the multiplets in the spectra that result.

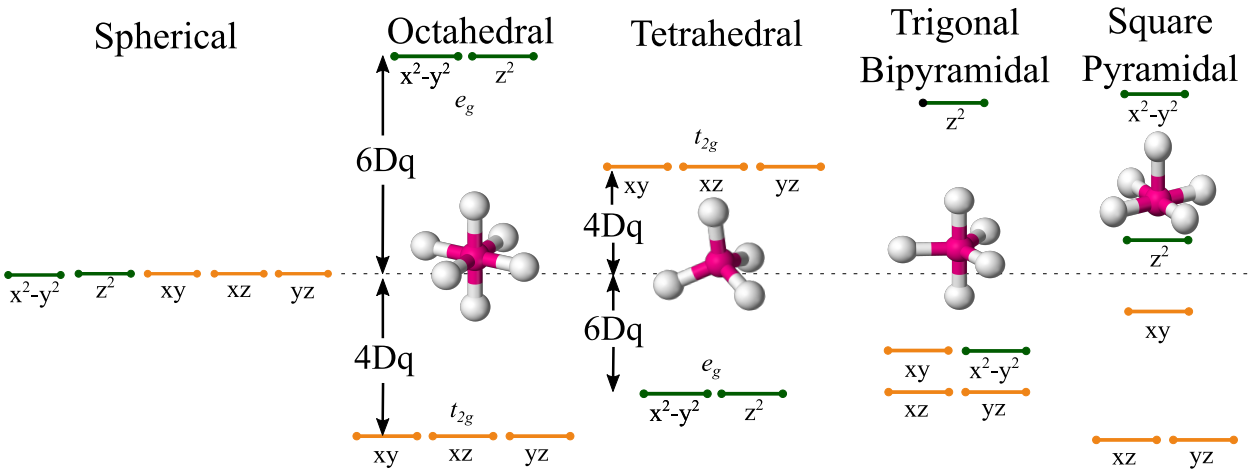

Figure 2.4: An illustration showing the relative energies of the five d-orbitals in various crystal fields, and the physical role of the $10Dq$ *value. The d-orbital energies are extremely sensitive to the ligand atoms surrounding the central metal atom. This sensitivity allows us to extract local symmetry information of the real system from the agreement achieved through comparisons with crystal field calculations.*

In Figure 2.4 I have plotted a schematic of the splitting of the d-orbitals for a few select crystal field symmetries. The energy splitting between the e_g and t_{2g} orbitals is given by the $10Dq$ value, and is generally on the order of $\sim$1 eV. Note that this orbital notation refers to Mulliken symbols: $e \Rightarrow$ doubly degenerate orbital, $t \Rightarrow$ triply degenerate orbital. The g and 2 subscripts refer to inversion symmetry $(x, y, z) \rightarrow (-x, -y, -z)$, and anti-symmetry (sign change of the wavefunction) with respect to a secondary C_2 axis that is perpendicular to the principal axis (z-axis here). In symmetries other than octahedral and tetrahedral, a single $10Dq$ value is not sufficient to describe the energy differences of the d-orbitals. In this case additional parameters Ds and Dt are used to describe the energy splittings, and in even lower symmetries, further parameters Du and Dv are required. The orbitals and their energies in terms of these parameters are summarized in Table 2.5. One can see that if $Ds = Dt = 0$, the energy splitting reduces to the $10Dq$ value between e_g and t_{2g} orbitals.

For completeness, a brief overview of point group symmetry notation should be included. A complete description with many figures can be found at Ref. [41]. The following is a not

Orbital	Energy [eV]
$3d_{xy}$	$-4Dq + 2Ds - 1Dt$
$3d_{xz}$, $3d_{yz}$	$-4Dq - 1Ds + 4Dt$
$3d_{z^2}$	$6Dq - 2Ds - 6Dt$
$3d_{x^2-y^2}$	$6Dq + 2Ds - 1Dt$

Table 2.5: 3d orbital energy in terms of Dq, Ds, and Dt values.

an exhaustive list, but should be sufficient for the scope of this thesis. The *principal axis* is always the axis with the highest degree of rotational symmetry (most commonly things are oriented such that this is the z-axis). The notation used for point groups in this thesis is Schoenflies notation.[42]

1. $C_n \Rightarrow$ cyclic groups, a crystal that has only a single n-fold rotation axis; anti-clockwise rotations of $2\pi/n$ are symmetric.

2. $D_n \Rightarrow$ dihedral groups, a crystal that has a single n-fold rotation axis, but also n secondary axes perpendicular to the principal axis such that symmetry remains through π rotations about the secondary axes.

3. $T \Rightarrow$ tetrahedral point groups are characterized by the presence of four C_3 principal axes and three C_2 axes.

4. $O \Rightarrow$ octahedral point groups feature three C_4 principal axes, four C_3 axes as well as multiple C_2 axes.

5. subscripts v and $h \Rightarrow$ correspond to crystal environments having vertical or horizontal mirror planes, respectively.

All calculations performed herein are done within a given point group, such that through comparison with experiment, the point group of the real system can be determined.

2.3.6 Tanabe-Sugano Diagrams

A Tanabe-Sugano diagram is a valuable tool to understand how the crystal field affects the energy levels in contrast to the atomic model.[43] They are often used in conjunction with UV/visible spectra to determine the crystal field splitting energy ($10Dq$) of octahedral and tetrahedral complexes.[44] The field produced by the ligands around the metal cation creates a potential that causes a shift in energy of the d-orbitals. As the ligands and d electrons of the metal ions approach one another, the electron clouds of the various orbitals each experience differing Coulomb repulsions, and the energy degeneracy of these orbitals is broken.

The Tanabe-Sugano diagram of Figure 2.5 is for a $3d^2$ system in an octahedral geometry. It can be interpreted such that the x-axis is the $10Dq$ value, and the y-axis is the energy of the electronic transition. The first thing to notice is the consistency with the atomic model and term symbols described in Section 2.3.2; if $10Dq = 0$ then we see the ground state is ^3F as predicted, and that there are four other states described by the term symbols ^3P, ^1G, ^1D, and ^1S. It is of note that all transitions are shown, but some may not be observable in experiment due to the spin flip $\Delta s = 0$ dipole selection rule. As the crystal field splitting energy increases, the term symbols of the ground state begin to split, allowing significantly more electronic transitions to occur. The origin of crystal field multiplets is a result of this splitting.

To illustrate the practical effect of the changes in calculated $L_{2,3}$ absorption spectra for varying Slater integral and $10Dq$ values (while holding all other variables constant), I have plotted calculated spectra at step intervals of the parameters for Fe^{2+} and displayed them in Figure 2.6. In panels (a) and (b) I have plotted calculations of XAS and RIXS spectra, respectively, for various $10Dq$ values at 0.4 eV increments. As the crystal field splitting takes on different intensities, the spectral shapes gradually change. If an experimental spectrum matches that of a positive value of $10Dq$, it would signify that the measured sample contains metal atoms in an O_h point group.

The right panel shows the effect of varying the scalar by which the nominal Slater integral values are multiplied, i.e. the intra-atomic electron interaction strength. At the minimum

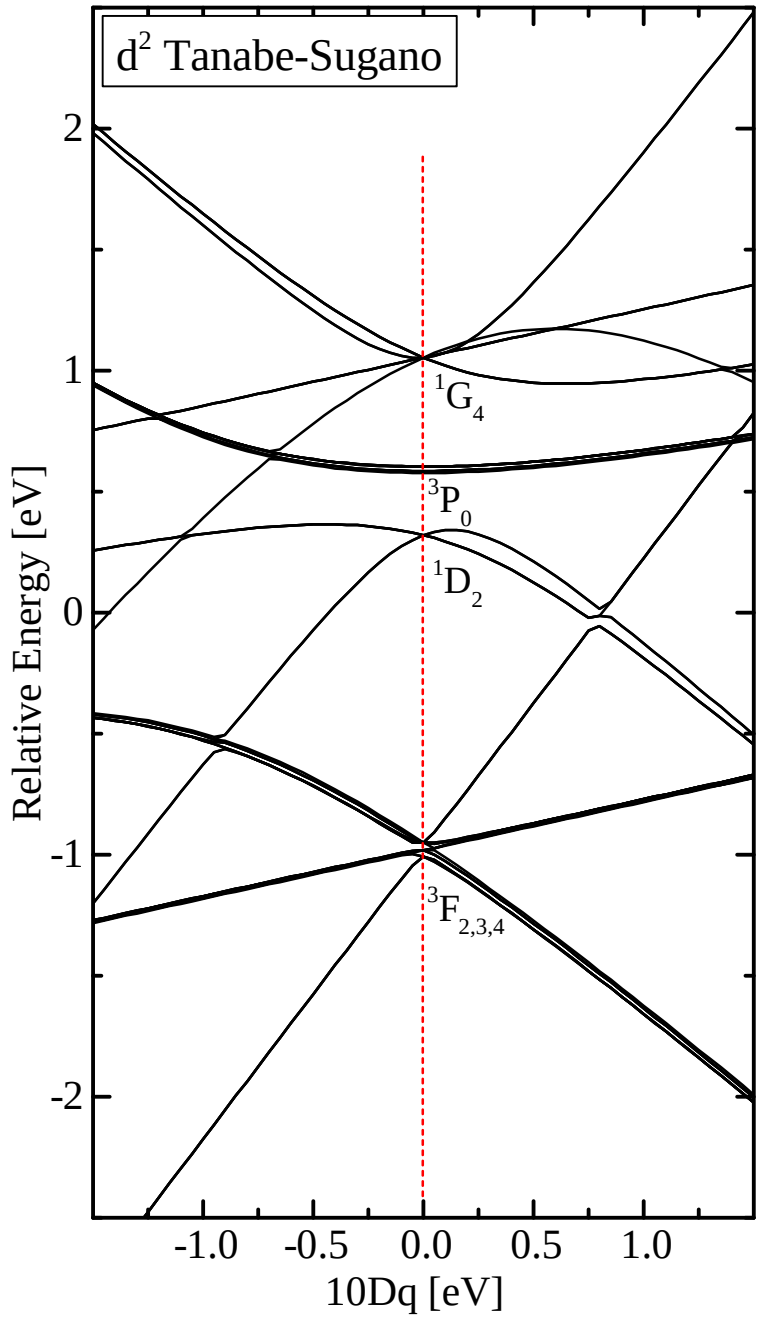

Figure 2.5: A Tanabe-Sugano diagram of a $3d^2$ system. The x-axis shows the 10Dq crystal field parameter, while the y-axis displays the relative energy of the states. A vertical line from anywhere on the x-axis can be drawn to see the energy of states for that value of $10Dq$. One can see that in these high symmetry states (O_h for positive 10Dq and T_d for negative 10Dq) the term symbols displayed for $10Dq = 0$ split as the strength of the field is varied. By comparing the relative energies of these states to experiment, the true crystal field parameters of the system can be deduced.

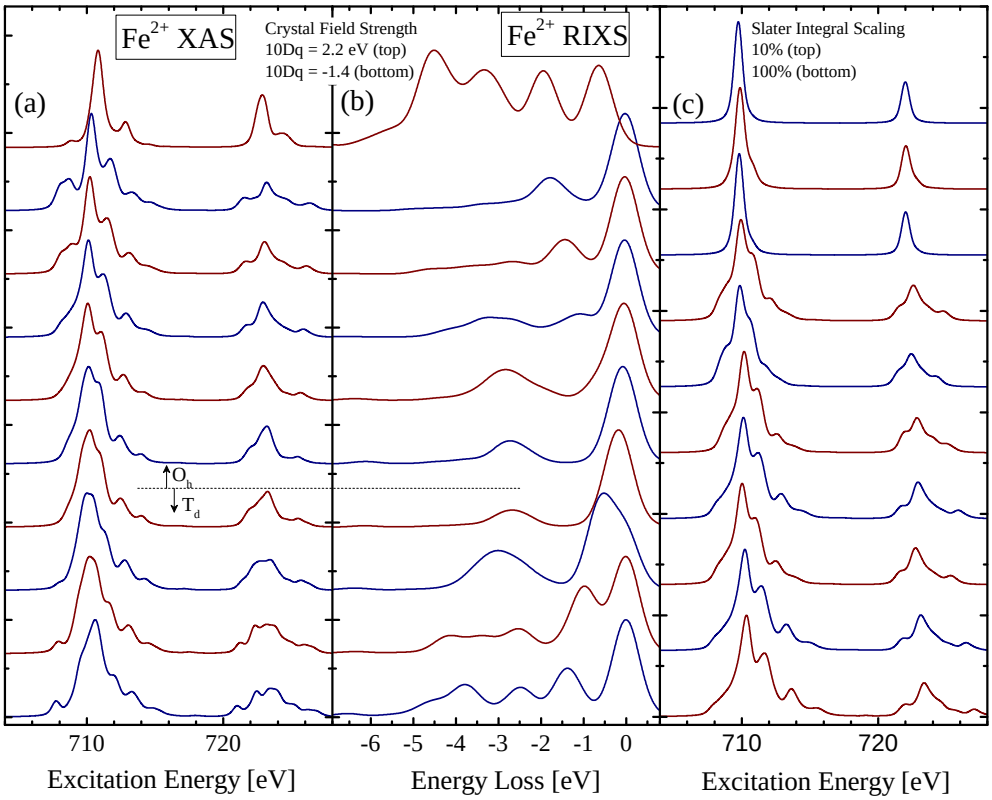

Figure 2.6: Calculated Fe^{2+} spectra. (a) The left panel shows the effect of adjusting the $10Dq$ value at 0.4 eV increments (while holding the Slater integral scaling constant at 80%). (b) Shows the same effect, except on the calculated RIXS taken at 710.2 eV, near the L_3 maximum. (c) The right panel shows the effect of scaling the Slater integrals, or qualitatively speaking, the intra-atomic electron-electron interactions.

shown, there is little overlap between the $2p$ core hole and the $3d$ electron wave functions, as well as between the $3d$ electrons themselves, and only two peaks are observed. As this interaction becomes stronger, a multiplet structure begins to emerge as more intra-atomic electronic transitions become available due to the increasing wave function overlap.

In practice, if one wishes to determine the crystal field parameters, one usually employs an educated guess and check method, taking into account past knowledge of similar systems. This requires that many hundreds of calculations are performed, with each one to be carefully compared to experimental results. As such, very good agreement can generally be found between calculated and experimental $L_{2,3}$ absorption and emission spectra using the crystal field model.[45]

Often a better method for determining a starting point for the crystal field parameters is to approximate the crystal as an infinite point charge distribution centred on the ion of interest. This requires only the input of the space group, fractional atomic coordinates, and lattice parameters. The Madelung potential on the central atom due to the point charges (other atoms) can then be calculated using the code of M. W. Haverkort's thesis.[46] While this approximation is quite crude, it can tell us the relative strength of the crystal field parameters relative to one another. This can be quite useful when considering low symmetry crystals, or modelling the effect that a ligand vacancy has on the crystal field parameters. For instance, if the input is the perfect octahedral coordination of NiO, it calculates the potentials due to all surrounding Ni and O atoms on a central Ni atom, and we can validate the illustration in Figure 2.4, which shows that $10Dq$ has some positive value, while the other crystal field parameters $Ds = Dt = Du = Dv = 0$.

If, however, we wish to perform a calculation that simulates an octahedral structure with a single ligand vacancy surrounding the metal ion, then it is not obvious what crystal field parameters should be used. With the aforementioned code, it can be determined that the ratio of the five parameters should be such that $10Dq : Ds : Dt : Du : Dv$ are $1.0 : 0.44 : 0.03 : 0 : 0$. These values are then all scaled by a single constant to adjust for the overall crystal field strength of the material. This method has been successfully employed to explain the origin of room temperature magnetism in $(In_{1-x}Fe_x)_2O_3$,[47] and I have further expanded it to be the default method for determining crystal field parameters, as it greatly reduces the computational time required while also leading to more quantitative conclusions.

2.3.7 Crystal Field Charge/Hole Densities

It is often useful to plot the resulting wavefunctions that arise from the filling of the d-orbitals by n electrons. However, a multielectron wavefunction depends on $3n$ coordinates $\psi(r_{11}, r_{12}r_{13}, r_{21}...r_{n3})$, which is far too cumbersome to compute in practice. Alternatively, we can plot the charge (or hole) density from the occupied (unoccupied) d-orbitals. In Figure 2.7 I have performed calculations with Quanty and plotted a few special circumstances along with the corresponding electron filling of the e_g and t_{2g} orbitals. NiO and MnO are very

ionic compounds and are therefore very well described by crystal field theory alone. That is, MnO is nearly entirely d^5, containing very little $d^6\underline{L}$ character, where $\underline{L}$ corresponds to a ligand hole. In this way, each of the five d-orbitals are equally occupied by one electron, and so each of the orbitals displayed in Figure 2.3 contribute equally to the charge density. With each of the d-orbitals being a combination of spherical harmonics—functions defined on the surface of a sphere—the sum of all five in equal amounts is an overall perfectly spherical charge (and hole) density for MnO. Also illustrative is the low spin d^5 scenario shown in Figure 2.7, which occurs when the crystal field splitting is sufficiently large that it is more energetically favourable to insert down-spin electrons into the t_{2g} orbitals than to overcome the energy cost associated with the crystal field splitting. Under these circumstances the charge distribution takes on a more complicated shape, but is still a combination of the occupied orbitals.

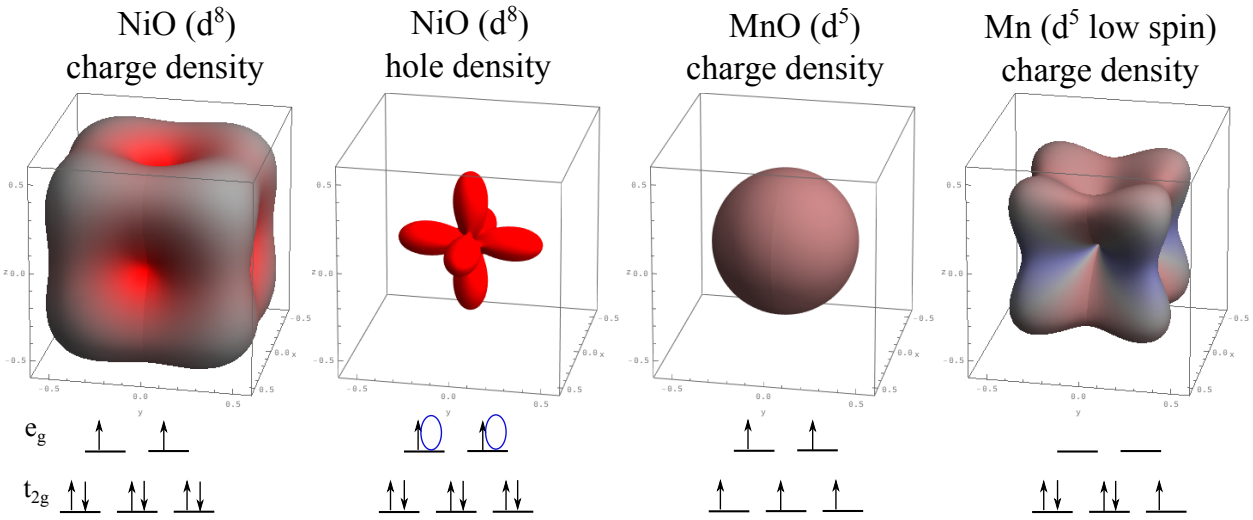

Figure 2.7: With ionic compounds such as NiO and MnO, orbital charge and hole densities can be calculated very accurately within the crystal field model because the covalency is very low (very little $d^{n+1}\underline{L}$ character). The NiO hole density is then the combined $d_{x^2-y^2}$ and d_{z^2} orbitals, and its charge density is the combination of the rest of the filled orbitals. MnO has each of the five d-orbitals equally filled and has a spherical charge density. In Mn^{2+} compounds that have a large crystal field, a low spin d^5 case arises that leads to a more complex charge density.

In the case of NiO, because it is d^8 with completely filled t_{2g} orbitals, it is convenient

to look at the hole density. And because there is a hole in each of the d orbitals, the hole density is exactly the combination of those two orbitals, as expected. The charge density, also shown, is then a perfect sphere minus the shape of the NiO hole density, which takes an unfamiliar shape, but is an accurate representation of real NiO.

Furthermore, many real solids are not in octahedral symmetry as in the examples just described. The energetic degeneracy of the five d-orbitals would then be broken and the filling of the electrons would then occur in various orders, starting from the lowest available energies. But, as depicted above, if the crystal field splitting is sufficiently large, electrons will organize themselves to create a low spin situation. The point to recognize is that charge distributions can vary greatly depending on the host environment, and that we can calculate them quite accurately.

2.3.8 Charge Transfer Multiplets

Despite the large degree of success the crystal field model has in describing experimental spectra, there are many scenarios in which the bonding (i.e. ligand field effects) plays a significant role in determining the spectral shapes, and hence a more thorough theory is required. The natural step to take is to then include the effects of hybridization due to the bonding of the metal ion with the surrounding nearest neighbour ligands.[48] In practice what is done is that further configurations (i.e. various arrangements of the electrons) are included, as well as the available electronic transitions between them, henceforth known as the ligand field model. These configurations simulate the charge fluctuations between initial and final states—the possibility of electrons hopping between the 3d orbitals of the metal and the 2p band of the surrounding ligands. Physically, this hopping can largely be attributed to the various electronegativities of the elements—the tendency for various elements to attract electrons. To this extent, a multitude of energy configurations emerge; it is these so-called charge transfer effects that are allowed for in this model.

Figure 2.8 illustrates some of the various configurations for XPS, XAS, and RIXS core level spectroscopies, with descriptions of the calculation parameters shown in Table 2.6. Within the framework of the ligand field model, higher energy states above the ground

Parameter	Description
Δ	Charge transfer energy, the average energy separation between individual configurations.
U_{dd}	Coulomb repulsion between 3d electrons (due to the addition electron that hopped from the ligand) at a given site leads to an overall increase in energy of that state by U_{dd}.
U_{cd}	The potential of the core hole in the final state acting on a 3d electron leads to an energy reduction of U_{cd}.
V_x	Value of the hopping integrals for electrons of symmetry $x = e_g, t_{2g}, b_{1g}, b_{2g}$, which can be regarded as the hybridization strength.

Table 2.6: Description of parameters used in the charge transfer model.

state exist wherein an electron hops from the surrounding ligands to the metal site. In an XAS process, the first excited state after exciting a 2p electron would be $\underline{c}3d^{n+1}$ where $\underline{c}$ represents the core hole. Including charge transfer effects, there are further configurations above this $\underline{c}3d^{n+2}\underline{L}$, $\underline{c}3d^{n+3}\underline{L}^2$, and so on, where $\underline{L}$ represents a ligand hole. Usually only the first set of configurations where there is just one ligand hole is sufficient to describe experimental spectra. The electron hopping from a ligand site to a metal site comes at an energy cost known as the charge transfer energy Δ, and is usually on the order of about 5 eV, but this can vary widely and in some cases can even be negative. Additional energy considerations are then the on-site Coulomb repulsion due to the extra d electron, and the core hole potential acting on that electron. Therefore, the first excited charge transfer state is an energy $\Delta + U_{dd} - U_{cd}$ above the lowest level excited state, as depicted in Figure 2.8. However, it is important to remember that this energy is actually a band of energies spanned by the density of states of the ligand atoms. Hence, the ligand excitations in an experimental metal $L_{2,3}$ RIXS measurement can actually give us information on the density of electronic states of the ligand atoms.

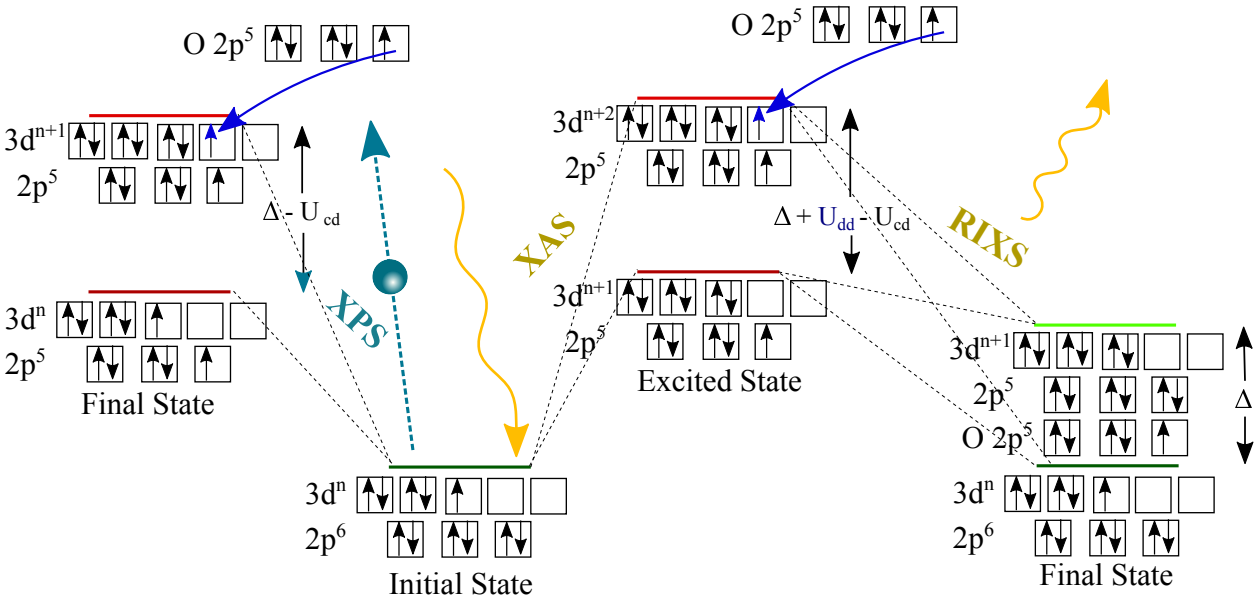

Figure 2.8: The figure shows possible configurations included in the ligand field model. The ligand atom's (usually oxygen) valence 2p electrons form a band several eV wide, the 2p valence electrons can hop to transition metal 3d sites at a charge transfer energy cost Δ. In this case there is an additional on-site coloumb repulsion energy between d electrons U_{dd}, as well as the attraction energy between core hole and the additional d electron U_{cd}. We can denote such a transition as $3d^n \rightarrow c3d^{n+1}\underline{L}$, where $\underline{c}$ and $\underline{L}$ denote the core and ligand holes, respectively. Dotted lines represent possible dipole transitions due to incident x-rays from the initial state to the final state for XPS, XAS, and RIXS techniques. In the XPS process a 2p electron is ejected from the system.

We can also directly see the effect of including charge transfer excitations by calculating the charge and hole densities as was done in Figure 2.7. An example that well illustrates this effect of covalency is to compare the calculated spherical charge distribution of ionic MnO in Figure 2.7 to a more covalent Mn^{2+} compound. In a significantly more covalent compound, there is much more $d^6\underline{L}$ in the ground state. This causes a significant deviation from the spherical charge and hole distributions, which I have calculated and plotted in Figure 2.9. A good way to quantify this is by calculating the expectation value of the number of d electrons in the lowest energy wavefunctions (ground state). This value deviates from $\langle N_d \rangle \approx 5.08$ in MnO, up to $\langle N_d \rangle \approx 5.4$ for the example shown in Figure 2.7.

The essential parameters that determine the degree to which electrons are "allowed" to

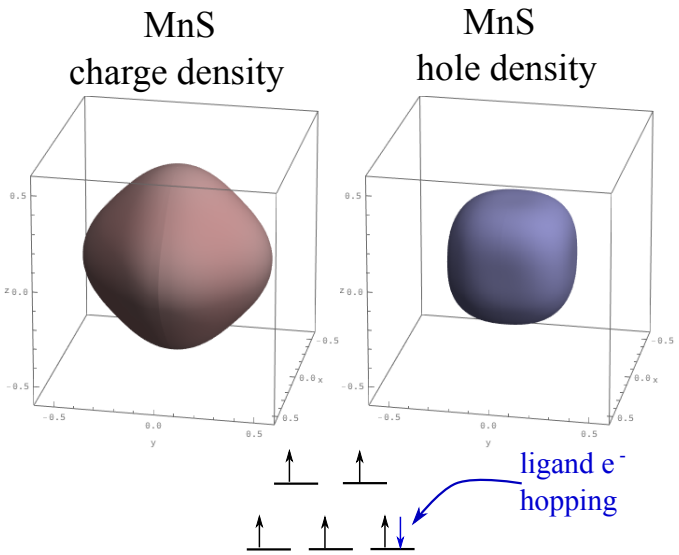

Figure 2.9: In more convalent compounds such as MnS, the character of the ground state includes more ligand hole character, which can be seen directly through a calculation of the charge and hole densities. This $d^6\underline{L}$ character should be contrasted to that of ionic compound MnO in Figure 2.7, which is also nominally d^5, but has a spherical charge distribution due to its much large charge transfer energy and small hopping integral energies.

hop, as listed in Table 2.6, are the charge transfer and hopping integrals. In O_h symmetry, the hopping integrals b_{1g}, a_{1g} (corresponding to $d_{x^2-y^2}$ and d_{z^2} orbitals) are usually roughly twice as large as the e_g and b_{2g} integrals, given their closer proximity to the ligands. This means that electron hopping is twice as likely to the $d_{x^2-y^2}$ and d_{z^2} orbitals. Conversely, the smaller the charge transfer energy, the easier it is for electrons to hop between sites.

To show how it is possible to extract the ligand's density of states by considering the charge transfer effects I have plotted a comparison of O K-edge NXES and V L-edge RXES in Figure 2.10 (a). The red spectra show maximum entropy deconvolutions (see Section 4.3) of the experimental data, which is a computational process that removes the effects of experimental broadening such that spectral features are more readily observable. There is a resemblance between the O and V spectra, with spectral features being nearly perfectly energetically aligned (note that the V RXES spectrum was shifted in energy to be aligned with the O emission energy so the two could be compared on a single axis). I will show that the V RXES is a reliable mapping of the O VB density of states, and in this case, should be

favoured over the O NXES.

In spectroscopy experiments such as these, the O K-edge NXES has been universally adopted as the tool for mapping the VB DOS.[49, 50] However, in this case the O emission photons are at energies that coincide with the V $L_{2,3}$ absorption edge at resonance (grey background spectrum in Figure 2.10 (a)), and so are actively reabsorbed by the material, but in a manner that is very energy sensitive. At 525 eV there is a peak in the V XAS spectrum, which will result in a large distortion in the O NXES such that its intensity will be greatly reduced in energy ranges where the V atoms in the sample reabsorb strongly. This explains the discepancy between the two spectra, for which there is much less intensity in the O NXES around 525 eV. Therefore, the accepted method of mapping the VB DOS needs to be scaled by the intensity of the V $L_{2,3}$ XAS spectrum, which is not a trivial task, and so it is the V RXES data that ought to be accepted as the preferred method of experimentally determining the O DOS. This example is a case study showing how it is not only relevant, and complementary information that is gained by considering the metal edge charge transfer features, but also advantageous in some scenarios.

Note that in Figure 2.10 (a), the true energy of the plotted V RXES spectrum has the elastic peak centred at 518.9 eV (but plotted at 534.5 eV so it could be plotted on the same axis as the O NXES), energetically distant from any absorption edges, and so the emitted photons will not suffer any meaningful distortion due to reabsorption. We can then conclude that the electronic transitions as depicted in Figure 2.8 wherein an O 2*p* electron transfers from its band to the metal site, accurately reflects the true VB DOS. We can be quite confident in this because at other edges where self-absorption is not an issue, there is generally even stronger agreement than seen here.[53] In fact, if one does the reverse and uses exactly the O K-edge NXES as the band shape when calculating spectra within the ligand field model, improved agreement is always found.[54] This reverse engineering is further evidence that we can deduce the electronic structure of the ligand atoms through measurements of metal edges.

Furthermore, in Figure 2.10 (b) I have plotted ligand field model calculations for V^{4+} and V^{5+} and compared them to the experimental spectrum of exf-$Sr_xV_2O_5$—where the notation

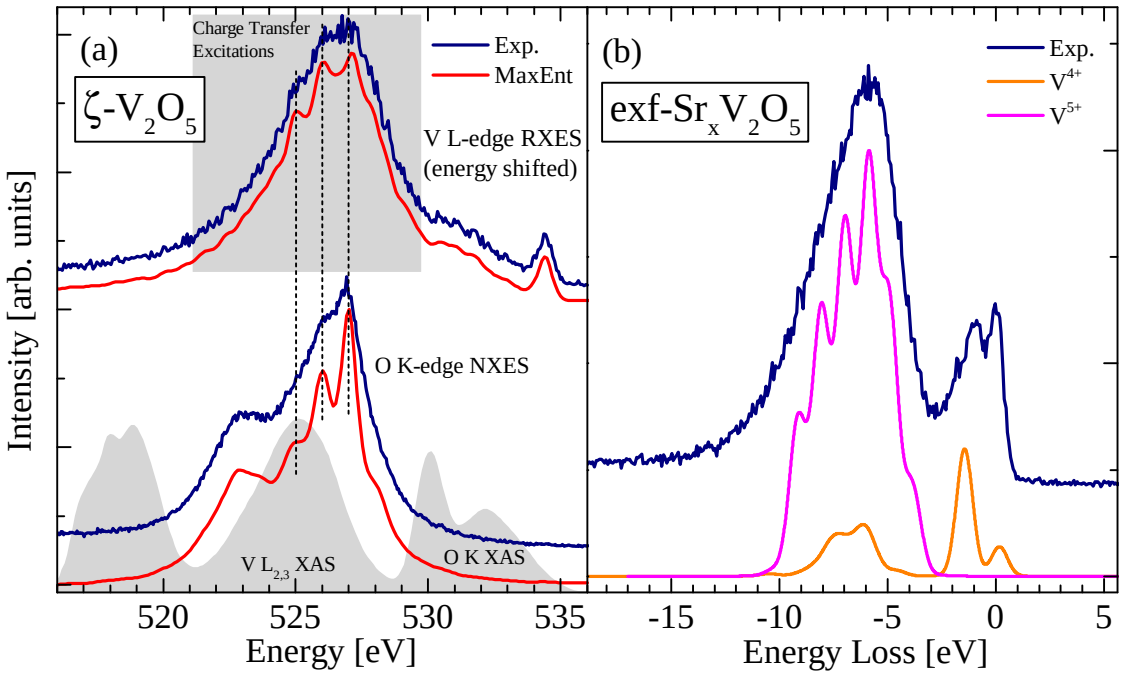

Figure 2.10: (a) Comparison of experimental O K-edge NXES (blue, bottom) and V L-edge RXES (blue, top), along with corresponding maximum entropy deconvolutions (red) to elucidate the underlying spectral structure blurred by experimental broadening. The charge transfer peak features in the vanadium RXES spectrum agree well with the oxygen spectrum, which is generally regarded as a map of the oxygen valence band density of states. Note that differences between the two can be attributed to considerable self-absorption by the V $L_{2,3}$ − edge (grey) affecting the oxygen spectrum, leading us to conclude that the V charge transfer region can, in this case, be regarded as a more reliable mapping of the O DOS. (b) Calculations including charge transfer effects can distinguish between the V^{4+} and V^{5+} sites, and how each contributes to both the overall covalent bonding, as well as the lower energy loss dd excitations, from which structural information can be extracted. Data adapted from calculations I performed in Refs. [51] and [52], with permission.

State	$10Dq$	Ds	Dt	Δ	U_{dd}	U_{cd}	V_{b1g}	V_{a1g}	V_{b2g}	V_{eg}	W	β
V^{5+}	3.5	-0.05	0.10	6.0	6.0	8.0	2.3	2.0	0.9	1.2	5.5	0.75
V^{4+}	1.7	-0.10	0.10	9.0	6.0	8.0	2.3	2.0	0.9	1.2	7.0	0.85

Table 2.7: Calculation parameters for the V^{4+} and V^{5+} spectra in Figure 2.10 (b). All parameters are in units of eV except β, which is the scaling of the intra-atomic Slater integrals.

refers to an exfoliated sample in which layers were removed from the surface to stabilize a few-layered nanosheet of the material.[55] From these calculations it was deduced that the

various vanadium oxidation states play significantly different roles in the electronic structure of this compound. We corroborated past finding and determined that vanadium in 4+ and 5+ states occur in roughly equal number densities.[56] However, the electron hopping from ligand oxygen sites to vanadium occurs almost completely to V^{5+} sites, as indicated by its substantially larger intensity and smaller charge transfer energy Δ. This reveals that covalent bonding plays a strong role in this material, such that about half the contribution to the ground state is due to the $3d^1\underline{L}$ (V^{5+} with a ligand hole) configuration. On the other hand, the dd excitations at less than ≈ 4 eV energy loss, are centred entirely on V^{4+} sites. Hence, the parameters used in the calculations (Table 2.7) can be used to extract real physical parameters from the system, and clarify what is responsible for the electronic properties of the material.

CHAPTER

THREE

EXPERIMENTAL TECHNIQUES

3.1 X-ray Absorption Spectroscopy

The fundamental first order process used in every experiment in this thesis involves the use of ionizing x-ray radiation, which is shined on some compound and absorbed by its core level electrons. Every further technique discussed is in some sense a derivative of this basic process. The binding energy of an electron that does the absorbing is unique for every core level and element, and can be further shifted in energy by the exact compound being studied. If the x-ray energy is tuned in the vicinity of the binding energy of a core level electron, an abrupt increase in the absorption cross section will be found. Figure 3.1 (b) shows the sudden increase in absorption cross section for all the Mn edges as well as the L-edge for several transition metals. If the absorption intensity as a function of the incident energy is then plotted, a fingerprint that is unique for that material, element, and edge will be obtained.[57]

The energy of all K ($1s$), $L_{2,3}$ ($2p$), and $M_{4,5}$ ($3d$) edges are plotted in Figure 3.1 (a) as a function of atomic number. The wealth of information across this spectrum of edges is so plentiful that only a small subset can be concentrated on by any given person or experiment. The edges I have primarily worked with are the $L_{2,3}$-edges for Z from 22-29 and K edges for $Z = 6, 7, 8$. As discussed in Section 2.3 it is these L-edges that contain the most physics

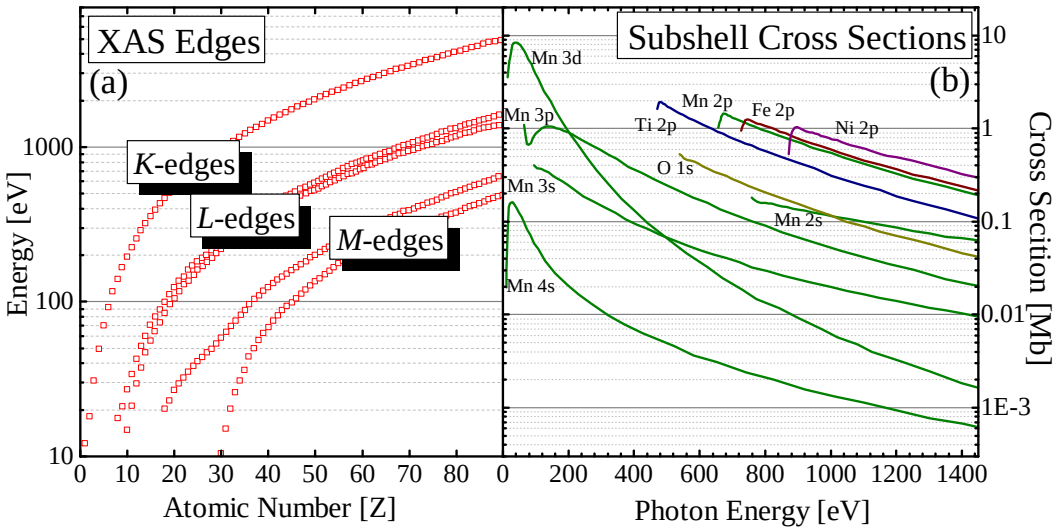

Figure 3.1: (a) Plotted on a logarithmic energy scale are the various absorption edges as a function of atomic number. The entire focus of this thesis is a very small subset of about a dozen of these. (b) Cross sections data from Ref. [58] show all Mn edges in green; the total absorption cross section is then the sum of all these. For comparison, I have also plotted several other edges to get a sense of atomic number versus absorption energy and edge.

due to the multiplet effects observed in XAS experiments.

In practice there are several ways to measure the absorption coefficient. Probably the best, and most direct way of doing this is through transmission—passing x-rays directly through the sample. This intuitive method requires only placing a sample in the path of an x-ray source and measuring the intensity both before and after it. The decrease in intensity (number of photons) can be expressed via the Beer-Lambert law:

$$N(\omega) = N_0(w)e^{-\mu(\omega)d} \tag{3.1}$$

where ω is the x-ray energy, N_0 is the incident number of photons, N is the detected number of photons after the sample, d is the sample thickness, and μ is the linear attenuation coefficient (which is nearly identical to the absorption coefficient in the soft x-ray regime) we are actually trying to measure. The issue with this technique is that if $\mu(\omega)d \gg 1$ the photons will not sufficiently penetrate the sample to obtain any meaningful signal. This is especially an issue in the soft x-ray regime where the x-ray attenuation length (distance

through a sample wherein the number of photons drops to $1/e = 36.8\%$ of its original intensity) is usually ~ 500 nm for most solids. Because synthesizing a freestanding sample on this thickness scale is not practical, we must resort to indirect techniques of measuring $\mu(\omega)$.

Therefore, the two practical methods in the soft x-ray regime for measuring XAS depend on the detection of decay products: electrons or photons. Total electron yield relies on indirectly detecting the Auger decay products (as opposed to primary electrons directly ejected from the sample) discussed in Section 3.4 by electrically connecting the sample to ground and measuring the current flowing out of the sample as electrons are ejected from it. Fluorescence techniques require one to measure the outgoing photons from the sample. The number of outgoing photons should be proportional to the number of core holes created; that is, the degree to which the sample absorbs photons, and hence $\mu(\omega)$.

However, there is a method that is vastly superior to the aforementioned ones: inverse partial fluorescence yield (IPFY). The primary issue with the above techniques is that self-absorption effects can introduce spurious peak heights into the recorded measurement. When the induced fluorescence photons leave the sample, some fraction of them are reabsorbed, so we do not actually detect the full signal. The effect is more pronounced on more intense features, and peak height ratios in the spectrum can be heavily distorted.[59] That is, the measured spectrum becomes not only dependent on the sample, but also on the photon penetration and escape depth. As an absorption edge is encountered and photons are strongly absorbed, the penetration depth (and hence interaction volume) of the sample changes; taking care that this effect does not lead to dubious conclusions is of the utmost importance in XAS. Electron yield may also suffer saturation effects, but also has its own unique issues. As a surface sensitive technique the measurements are sensitive to any inhomogeneity that may exist in the first few atomic layers, but not in the bulk—often due to exposure to air. And because it relies on the free flow of electrons to the sample, high conductivity is required or sample charging effects will drastically distort the spectrum.

With IPFY the non-resonant x-ray fluorescence from an element that is different from the edge we are actually interested in (but lower in energy), is measured. When this is done, self-

absorption effects can be circumvented. Essentially what happens is that new decay pathways open up as one tunes the energy across an absorption edge, which results in the decrease of fluorescence intensity from the lower energy edge. The integrated intensity of photons from the lower energy edge (partial fluorescence yield), when inverted, is theoretically proportional to the absorption cross section.[60] This is only strictly valid if the sample is infinitely thick (i.e. all photons are absorbed), however, the approximation is usually valid as samples are generally sufficiently thick as to not allow the transmission of a significant fraction of photons.

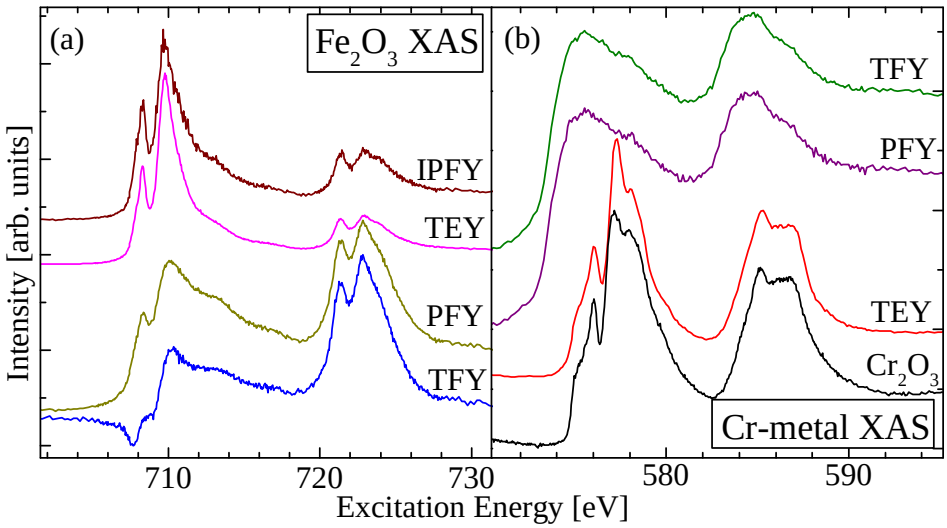

Figure 3.2: (a) In the case of Fe_2O_3 powder, which is essentially rust, it will not further oxidize and so TEY yields a spectrum that agrees with the IPFY, which we know to be the true spectrum. Both PFY and TFY suffer from anomolies that are not true representations of $\mu(\omega)$. (b) For metallic Cr, the surface layer oxidizes and so TEY measurements produce something akin to Cr_2O_3 and other Cr oxides. The PFY and TFY are closer to the true absorption coefficient, but still suffer from self-absorption. IPFY measurements are not possible because the bulk has no oxygen.

In Figure 3.2 I have plotted XAS for two samples. I wish to illustrate how the best technique to accept as your measurement for $\mu(\omega)$ varies depending on the situation and sample. In both cases, all techniques were performed simultaneously, as should always be the case if possible because each contains its own unique information. The TFY for Fe_2O_3 has a dip at the L_3-edge stemming from the fact that as we count all fluorescence photons,

the oxygen emission drops as we encounter the edge, but by a greater amount than the Fe emission photons increase, which we observe as a dip. This is basically a superposition of the IPFY from the oxygen, plus the PFY from the iron. The PFY has an abnormally large L_2 peak because the detector was windowed off to count all photons from both the L_2- and L_3-edges, such that as we scan energies across the L_2 edge, we are accepting also non-resonant L_3 photons, leading to a distortion from the true absorption. However, in this case, the TEY agrees very well with the IPFY, which we know to be the true absorption coefficient, except the TEY will always be significantly less noisy. Therefore, in this situation, the TEY measurement is the preferred result.

In contrast to this, in Figure 3.2 (b) I have plotted TEY, PFY, and TFY for metallic Cr, which shows that the TEY is heavily distorted due to surface oxidation. The TFY and PFY agree with one another, so we can be confident that they are correct, but suffer from self-absorption. On the other hand, IPFY was not possible because there are no oxygen atoms in the bulk to observe fluorescence from. In this situation, the only possible way to obtain the true absorption coefficient is to do some post-processing correction for the self-absorption in the PFY or TFY spectra, which is possible if necessary.[61]

3.2 X-ray Magnetic Circular Dichroism

X-ray magnetic circular dichroism is an experimental technique in which one measures the difference in the absorptive part of the refractive index for left and right circularly polarized x-rays. Circularly polarized light has a rotating electric field vector that carries a unit of angular momentum of $\pm\hbar$. Whether we deem right or left circularly polarized light as positive or negative is a matter of convention and is not important. It is one of the very few methods of separating the spin and orbital magnetic moment per atom for a given element in a material. And, as I will show in Chapter 8, it is also possible to separate the magnetic contributions from unique sites of a given element due to their differing local symmetries, even in a compound that may contain several elements.

XMCD was first observed in 1986 after being predicted just a year earlier;[62, 63] the

corresponding sum rules from which the spin and orbital angular momenta can be calculated were then derived in 1992.[64] Thus, it has become a powerful technique for discovering the origin of magnetism on an atomic level due to its non-destructive elemental and orbital specificity, and simplified sum rules. The femtosecond time scale on which x-ray transitions occur is much faster than the time the valence $3d$ electrons take to rearrange and relax. Therefore, calculations can be done that are in the limit of a sudden approximation and are sensitive to the $3d$ orbitals, whose energies are sensitive to the local symmetry.[65]

The dichroic signal we observe with circularly polarized light comes from the slight alteration to the dipole selection rules. Whereas with linearly polarized light we had $\Delta m_j = 0$, the rules now become

$$\Delta j = 0, \pm 1 \quad \Delta s = 0 \quad \Delta l = \pm 1 \quad \Delta m_j = +1(\text{right}),\text{-}1(\text{left}) \tag{3.2}$$

The XMCD signal is defined as the difference between the XAS spectra of left and right circularly polarized light. Qualitatively this can be understood if one considers the $2p$ electrons being excited; they are split into $j = l + s = 3/2$ (L_3-edge) and $j = l - s = 1/2$ states (L_2-edge), corresponding to spin and orbital momenta being coupled parallel and antiparallel, respectively. As a consequence of the conservation of angular momentum, the angular momentum of the photon is entirely transferred to the orbital momentum of the absorbing electron, and only to the spin indirectly through spin-orbit coupling.[66] The result is that right circularly polarized light (carrying $+\hbar$ momentum) preferentially excites spin-up electrons at the L_3-edge where the orbital and spin angular momenta are parallel. Whereas at the L_2-edge, right circularly polarized light will preferentially excite spin-down electrons since the spin and orbital angular momenta are antiparallel. Left circularly polarized light will do the opposite. This will occur in any sample whether it is ferromagnetic or not.

Shown in Figure 3.3 is a schematic of all possible transitions from the $2p$ orbital. The magnetic quantum numbers m_l and m_s are shown for each of the electrons corresponding to each transition. In cases where there are two possible combinations of orbital and spin quantum numbers, Clebsch-Gordon coefficients are used to determine their relative probabilities (see Figure 3.4). For example, a $2p_{1/2}$ (i.e. $j = 1/2$) electron may either be in one of two states $|m_l, m_s\rangle = |1, -1/2\rangle$ or $|0, 1/2\rangle$, where $m_j = m_l + m_s$.

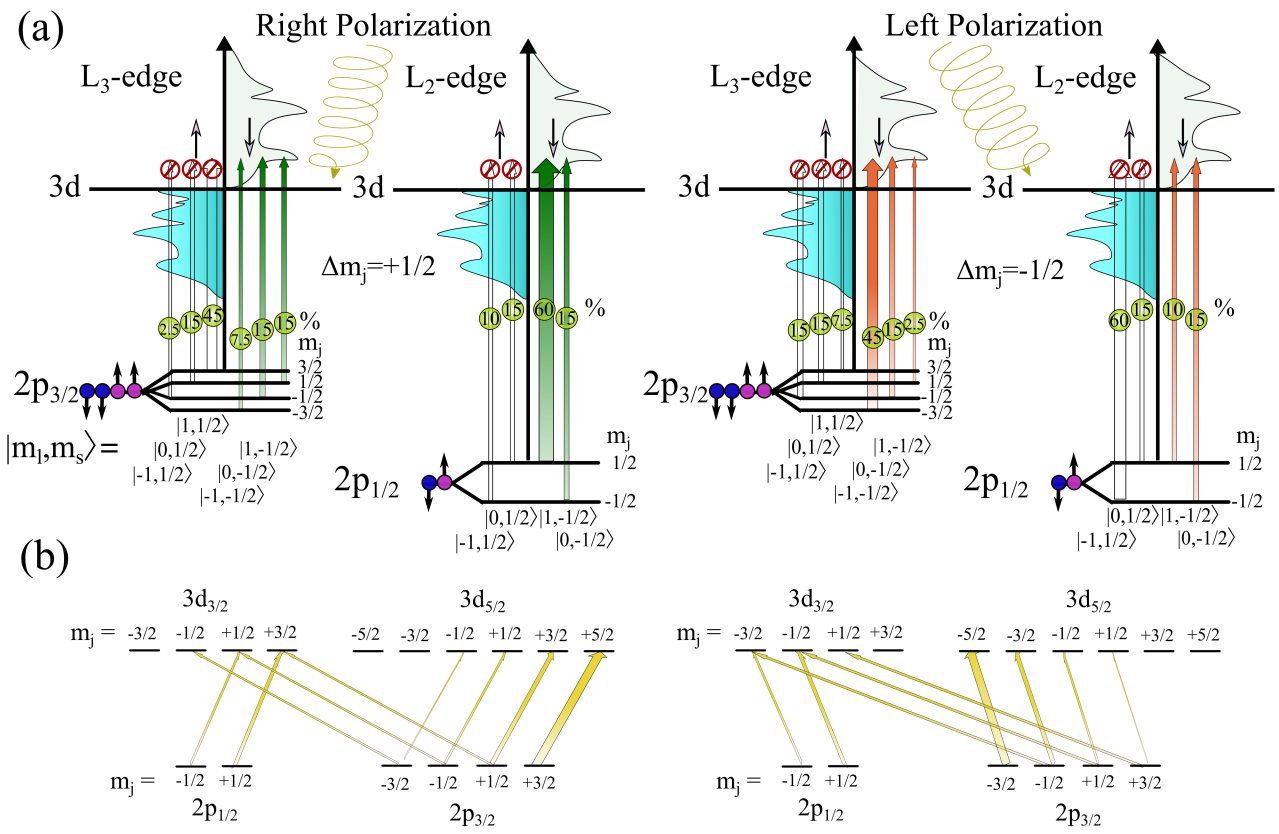

Figure 3.3: (a) Possible electron transitions when exciting with circularly polarized light such that the selection rule for the magnetic quantum number is $\Delta m_j = \pm 1$. In this hypothetical material the 3d band has a very large exchange splitting such that the spin-up band is completely full below the Fermi level and there are no spin-up states available above it, and the spin-down band is completely empty above the Fermi level. For each transition the $|m_l m_s\rangle$ quantum numbers are given for the initial state, and the percentage shown is that transition's fraction of the total absorption cross section for the corresponding polarization and edge, as calculated in the main text. In such a ferromagnetic material, the exchange splitting causes an imbalance in available states for the spin polarized photoelectrons. Hence, excitations of spin-up electrons are forbidden in this picture due to the lack of available states. If we just look at the L_2-edge transition probabilities, we can see that they are much more probable for right circularly polarized photons (75% of overall cross section) as opposed to left circularly polarized photons (25% of overall cross section). It is this difference that we call magnetic dichroism, which allows us to measure the magnetic properties of ferromagnets. In practice, the total absorption cross section is scaled not only by the transition matrix elements calculated here, but also by the density of states available in the 3d band. (b) A schematic showing dipole allowed $2p \rightarrow 3d$ transitions such that $\Delta m_j = +1$ for right polarized photons and -1 for left polarized photons, while retaining the $j = 0, \pm 1$ selection rule. The thickness of the arrows is roughly proportional to the transition probability. This illustrates how the additional selection rule imposed by the use of circularly polarized light alters the relative transition probabilities as compared to linearly polarized light. Note that dipole allowed $\rightarrow 4s$ transitions are not accounted for in this sketch as these transitions are generally about two orders of magnitude less likely.

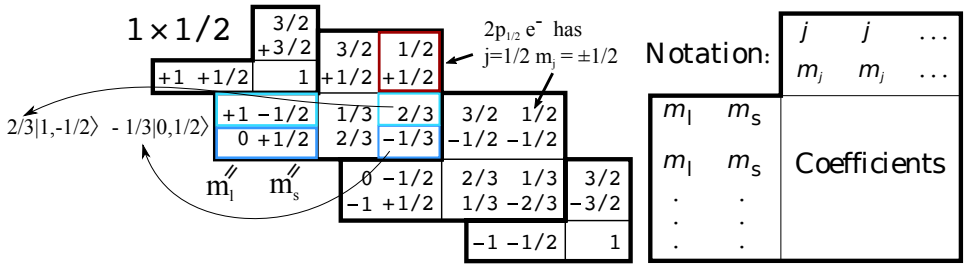

Figure 3.4: Clebsch-Gordon coefficents are used for adding angular momentum values and determining their relative probabilites. For our purposes, we want to determine the relative probabilites of finding 2p electrons with some orbital and spin magnetic angular momenta for a given total angular momentum. This example illustrates how this is done for a $2p_{1/2}$ electron ($j = 1/2, m_j = \pm 1/2$). For $m_j = 1/2$ there are two possible combinations of m_l and m_s such that $m_l + m_s = m_j$, these are $m_l = 1$, $m_j = -1/2$, and $m_l = 0, m_j = 1/2$. To calculate their relative probabilities begin at the red box above ($j = 1/2, m_j = +1/2$). The light blue box on the left indicates that for $|m_l m_s\rangle = |+1 \frac{-1}{2}\rangle$ its relative probability is 2/3 while for the state $|0\frac{1}{2}\rangle$, the relative probability is 1/3. These values are then weighted against the transition matrix elements for transitions to an empty 3d band.

What we can also see from Figure 3.3 (b) is why certain transitions are not allowed. With linearly polarized light, transitions from $2p_{1/2}$ to $3d_{3/2}$ would be allowed as long as $\Delta m_j = 0$, but the $\Delta m_j = \pm 1$ selection rule for circularly polarized light imposes a restriction that forbids this transition to the $3d_{3/2}$ orbital, i.e. one cannot observe an electron dipole transition from $2p_{1/2\ m_j=1/2} \rightarrow 3d_{3/2\ m_j=1/2}$ unless linear polarized light is used to excite the photoelectron. And a transition such as $2p_{1/2\ m_j=1/2} \rightarrow 3d_{3/2\ m_j=3/2}$ is only possible if the electron is excited using a right circularly polarized photon carrying $+\hbar$ angular momentum.

The numerical values shown in Figure 3.3 are a result of the transition probabilities calculated in the transition matrix elements from Fermi's golden rule for x-ray absorption, which are then weighted by the Clebsch-Gordon coefficients above. Fermi's golden rule for absorption is

$$\mu_{abs}^{\pm} \propto M_{if}^2 \cdot \rho^{\pm}(E) \tag{3.3}$$

where M_{if} is the dipole transition matrix element, and $\rho^{\pm}$ is the density of states for up and down spin electrons. The dipole transition matrix elements can be separated into radial and

angular parts

$$M_{if} = \sqrt{\frac{4\pi}{3}}\delta(m_{sf}, m_{si}) \langle n_f l_f | r | n_i l_i \rangle \langle l m_{lf} | \mathbf{e} | l_i m_{li} \rangle \tag{3.4}$$

where the subscripts i and f refer to initial and final states, n is the principal quantum number, the delta function ensures that spin is conserved, and $\mathbf{e}$ is the electric field vector of the light, which is rotating for circularly polarized light, stemming from the helically rotating electrons as they pass through an undulator and emit polarized photons. Conveniently, the radial part has no dependence on polarization, since circular polarization changes only m_l. For right and left circularly polarized light, this term becomes

$$\begin{aligned} \langle l_i + 1 \quad m_{li} + 1 | C^{(1)}_{+1} | l_i m_{li} \rangle &= \sqrt{\frac{(l_i + m_{li} + 2)(l_i + m_{li} + 1)}{2(2m_{li} + 3)(2m_{li} + 1)}} \\ \langle l_i + 1 \quad m_{li} - 1 | C^{(1)}_{-1} | l_i m_{li} \rangle &= \sqrt{\frac{(l_i - m_{li} + 2)(l_i - m_{li} + 1)}{2(2m_{li} + 3)(2m_{li} + 1)}} \end{aligned} \tag{3.5}$$

where $C^{(1)}_{\pm 1}$ are Racah's spherical operators for cicularly polarized light. Thus, by substituting in $l_i = 1$ for p electrons, and $m_{li} = -1, 0, 1$, multiplying by the $\sqrt{4\pi/3}$ constant in M_{if}, ignoring the radial part, and then squaring we get $M^2_{if} \approx 0.28, 0.81$, and 1.66 for right circularly polarized light, and $M^2_{if} \approx 1.66, 0.81$, and 0.28 for left circularly polarized light, for $m_{li} = -1, 0, 1$, respectively. Next, these values must be weighted against their respective Clebsch-Gordon coefficients and then we obtain the total percentages of overall cross section as shown in Figure 3.3.

For illustrative purposes, in Figure 3.3 (a) I have drawn a hypothetical exchange band splitting such that the majority spin-up band is completely filled, and only transitions to the minority band are allowed. For simplicity, the calculated transition probabilities were summed over all possible transitions into an empty $3d$ shell. In reality, the relative transition probabilities would also have to be multiplied by the integrated unoccupied density of states as in equation (3.3), which is proportional to the number of holes in the $3d$ band per atom.[67]

The second step of the process is driven by the magnetic properties of the sample. The excited electron needs to find a place in the $3d$ valence band, and in a ferromagnetic material there will be an imbalance of unoccupied spin-up and spin-down available states due to an exchange interaction (see Section 2.2). This imbalances creates a spin-dependent transition

probability for the excited electrons. The final state, as determined by selection rules, essentially acts as a spin detector. An XMCD spectrum reflects the difference in density of states for difference spin and orbital moments. That is, the excited photoelectron carries with it a spin and orbital momentum, and any imbalance in the unoccupied density of states for said momenta will lead to a dichroic effect. This effect is quite strong, and therefore measurable because the transitions involved are electric dipole transitions as opposed to magnetic dipole transitions.

3.2.1 Experimental Considerations

In practice, one needs to measure the absorption coefficient as a function of energy for both helicities of circularly polarized light while the sample is mounted on a magnet that saturates its magnetism. This is possible using a 0.5 T magnet at the REIXS beamline at the Canadian Light Source, where I have performed my XMCD measurements. One must scan across an energy range that corresponds to the $2p$ electron binding energies of the element of interest, and record either fluorescence photons or the current flowing from the sample to ground as a proxy for the absorption coefficient. While it is true that performing transmission mode absorption experiments is the most natural and reliable method of obtaining the energy dependent absorption coefficient, it is not practical in the soft x-ray regime where the penetration depth of photons is on the order of 100 nm. Therefore, often the best way to record XMCD spectra is through total electron yield (TEY), which is inherently much less noisy than observing fluorescence photons because the decay method to fill the $2p$ core hole is between one and two orders magnitude more likely to produce an Auger electron than a photon. Hence, by indirectly measuring the emitted Auger electrons one can record a spectrum with nearly no noise.

Performing high quality XMCD experiments can be quite difficult due to difficulties in obtaining left and right polarized spectra simultaneously; large uncertainties can easily creep into the quantitative results.[68]. In order to account for beamline parameters that change over time, such as beam intensity decay due to the decrease in current in the storage ring, several spectra are recorded in the order left, right, right, left and so on, and then averaged

for each polarization. Lastly, since XMCD results are very sensitive to small changes in peak intensities, it is also good practice to record spectra in alternative absorption modes partial and inverse partial fluorescence yield, which will be much noisier, but can still be qualitatively compared to ensure that the TEY spectrum is a reliable measurements of absorption. Once all spectra are averaged they are normalized such that the pre-edge and post-edge backgrounds are identical.

3.2.2 Sum Rules

Sum rules can then used be to obtain quantifiable data from an analysis of the measured spectra. While the derivation of the sum rules is far from straightforward, requiring several approximations along the way, their final result is quite condensed and can be easily applied to experimental spectra.[69] The equations for the orbital and spin magnetic moment per atom in units of bohr magnetons is

$$\mu_{orb} = \frac{-4q}{3rP\cos\theta} n_H \tag{3.6}$$

$$\mu_{spin} = \frac{-(6p-4q)}{rP\cos\theta} n_H + \frac{7}{2}\langle T_z \rangle \tag{3.7}$$

where p, q, and r are the integrals shown in Figure 3.5, P is the degree of circular polarization of the photons (≈ 0.95 at REIXS), θ is the angle between the direction of incident light and magnetic field, and n_H is the number of $3d$ holes per atom of the element being probed. $\langle T_z \rangle$ is the magnetic dipole term, and is generally sufficiently close to zero at room temperature that it can be neglected.[70] The number of holes per atom n_H is the largest unknown that must be estimated as it varies with the degree of covalency. However, there are fairly reliable methods of quantitatively estimating the degree of covalency such that the error in the sum rules remains tolerable.[71] By comparing the integrated intensity over the entire $L_{2,3}$-edge to that of a known sample, one can extract a good estimate for the number of available holes. For example, in NiO this method was used to find that the number of holes is 1.45 per atom. This change of about -0.5 holes per atom from the nominal value of 2, due to the effects of covalency, is a good estimate for transition metal oxides. [72]

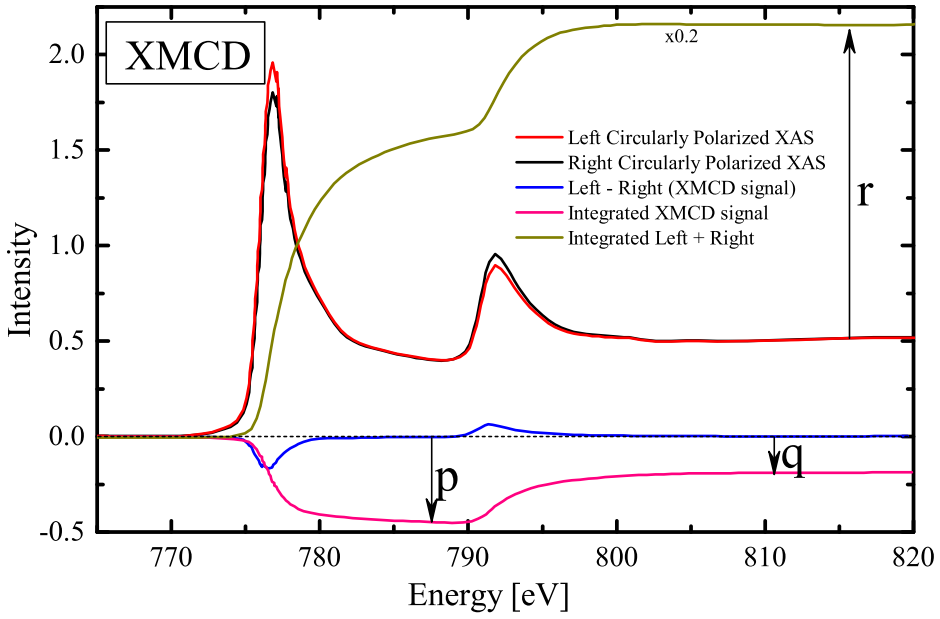

Figure 3.5: XAS spectra at the Co $L_{2,3}$-edge are shown for left and right circularly polarized light. Also shown is their difference (XMCD signal), and its integration curve from which the values p, q, and r are extracted for use in the sum rules in equations 3.6 and 3.7. Figure adapted from data in Reference [73].

3.3 Extended X-ray Absorption Fine Structure

Yet another method in which XAS can be harnessed to gather essential information is by extending the range of the collected absorption spectrum several hundred eV beyond the absorption edge of interest. This is known as extended x-ray absorption fine structure (EXAFS), and the governing equations date back to 1971.[74] By extending the range of data collection, oscillations in the spectrum become visible and, if properly analyzed, will contain valuable structural information on the sample. The oscillations that arise in the XAS are, of course, due to changes in the absorption coefficient of the material. This arises when a core level electron is excited to create a photoelectron—with some wavelength that depends on the energy of the exciting photon—that backscatters off a neighbouring atom. The photoelectron then returns to the absorbing atom and interferes with the original emitted photoelectron wave. If they are in phase, they constructively interfere, and the final state wavefunction is increased, which we observe as an increase in the absorption. Similarly,

destructive interference occurs if they are out of phase. The progression of constructive and destructive interference as a function of energy appears as oscillations in the spectrum. A sketch of the EXAFS process is shown in Figure 3.6.

In essence, the final state wave function is a combination of both the lone atom absorption, plus a part that is affected by the neighbouring atoms because the photoelectron can "see" them, $\mu(E) = \mu_0(E)[1 + \chi(E)]$ where $\chi = \mu - \mu_0/\mu_0$. The isolated atom's absorption coefficient is μ_0, and the term containing χ is a correction factor that is necessary to include because of the presence of neighbouring atoms. Frequently, χ is referred to as "the EXAFS", as it contains all the oscillations that we focus on for our analysis. If we write the absorption coefficient as in Fermi's golden rule between the initial $\langle i|$ state with a core electron and final $|f\rangle$ state with a photoelectron, and the interaction Hamiltonian between electromagnetic field and electrons $\mathcal{H}$ we have

$$\mu(E) \propto |\langle i|\,\mathcal{H}\,|f\rangle|^2 \tag{3.8}$$

In a single photon interaction picture $\mathcal{H} \propto \hat{\epsilon} \cdot \mathbf{r}e^{ikr}$, where $\hat{\epsilon}$, $\mathbf{r}$, and k are the x-ray's polarization vector, electron position vector, and wavenumber. But, as mentioned, the final state can be interpreted in two parts: the lone atom contribution $|f_0\rangle$ and the contribution from surrounding neighbours $|\Delta f\rangle$

$$|f\rangle = |f_0\rangle + |\Delta f\rangle \tag{3.9}$$

so that the fine structure that we are interested in can be expressed as

$$\chi(E) \propto \langle i|\,\mathcal{H}\,|\Delta f\rangle \tag{3.10}$$

Since the initial state is a tightly bound core electron, we can approximate it as a delta function. This is because the approximate radius for a $1s$ electron is a_0/Z where a_0 is the Bohr radius = 0.529 Å and Z is the atomic number. The change in the final state wavefunction $|\Delta f\rangle$ is also just the wavefunction of the scattered photoelectron. This allows us to solve the above integral quite easily.

$$\chi(E) \propto \int dr\delta(r)e^{ikr}\hat{\epsilon} \cdot \mathbf{r}\psi_{scatt}(r) = \psi_{scatt}(0) \tag{3.11}$$

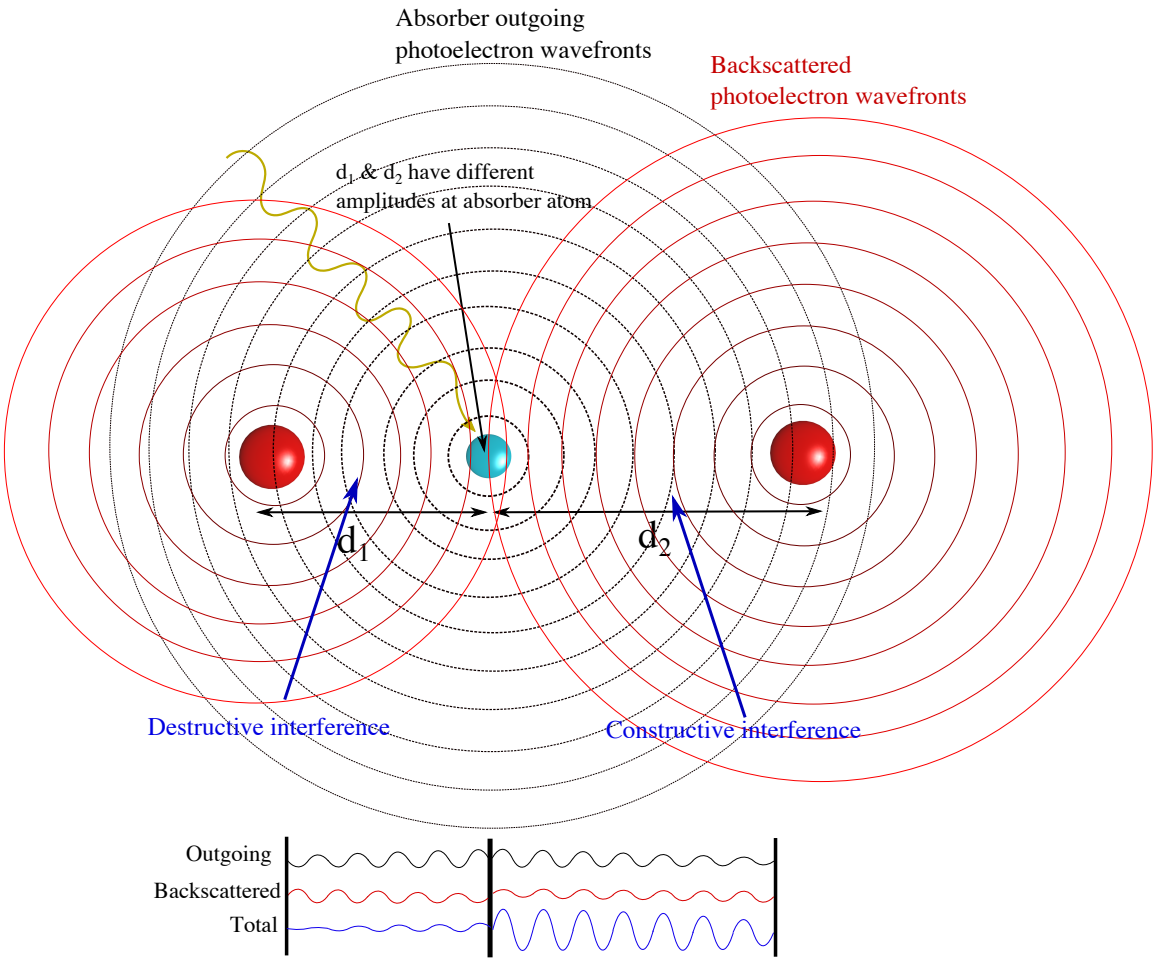

Figure 3.6: In a simplified picture we can treat the outgoing photoelectron (black circles) as travelling spherical waves whose amplitudes decay with the square of the distance from the source. At distances d_1 and d_2 they are backscattered (with some phase-shift) and eventually return to the emitting atom with some phase and amplitude. In the above sketch, the waves arriving from the atom at d_1 are out of phase with the originally emitted photoelectron, and so destructive interference occurs, and in turn, a drop in the overall absorption coefficient μ. The opposite occurs from the atom at d_2, where constructive interference between the outgoing and backscattered photoelectron waves takes place.

This equation states that the EXAFS is proportional to the amplitude of the scattered photoelectron at the absorbing atom $r = 0$.

However, we would like a workable equation such that we can model our experimental spectra by adjusting the parameters therein. The EXAFS equation allows us to do this, so we can extract real physical parameters by obtaining an adequate fit to the experimental

data. The EXAFS equation and a description of its parameters:

$$\chi(k) = S_0^2 \sum_i N_i \frac{f_i(k)}{kR_i^2} e^{-2\sigma_i^2 k^2} e^{-2R_i/\lambda(k)} \sin\left(2kR_i + 2\delta_i + 2\phi_i\right) \tag{3.12}$$

- N_i is the number of scattering atoms of type i
- R_i is the distance from the absorbing atom to the backscattering atom
- S_0^2 is an amplitude scaling factor
- $e^{-2\sigma_i^2 k^2}$ contains the Debye-Waller factor σ^2, which is the root mean squared deviation of the backscattering atom from its mean position and accounts for the thermal disorder of atoms
- $e^{-2R_i/\lambda(k)}$ is a damping factor taking into account that photoelectron waves are only scattered elastically over short distances, where λ is the mean free path
- $f_i(k)$ is the scattering amplitude at backscattering atom i
- δ_i is the phase-shift of the photoelectron that occurs at the absorbing atom
- ϕ_i is the phase-shift undergone by the photoelectron as it backscatters off atom i

To illustrate the sensitivity of EXAFS I have plotted four manganese oxide compounds EXAFS signals and their Fourier transforms in Figure 3.7. It is very clear that these similar compounds can easily be distinguished via their EXAFS fingerprints, and that accurate interatomic distances can be determined via fitting using Equation 3.12. The mean free paths, scattering amplitudes, and phases are all calculated using FEFF,[75] which is an *ab initio* code that performs a fast calculation accounting for the most important phenomena: it reformulates the plane-wave single scattering picture as a curve-wave multiple scattering effective scattering parameter f_{eff} (where its name is derived from). The number of scattering atoms of a given type N_i can often be known with a high degree of certainty from previous knowledge of the sample at hand. The Debye-Waller factor σ^2 has the effect of damping oscillations in the EXAFS signal due to thermal vibrations; in practice, it is allowed to vary

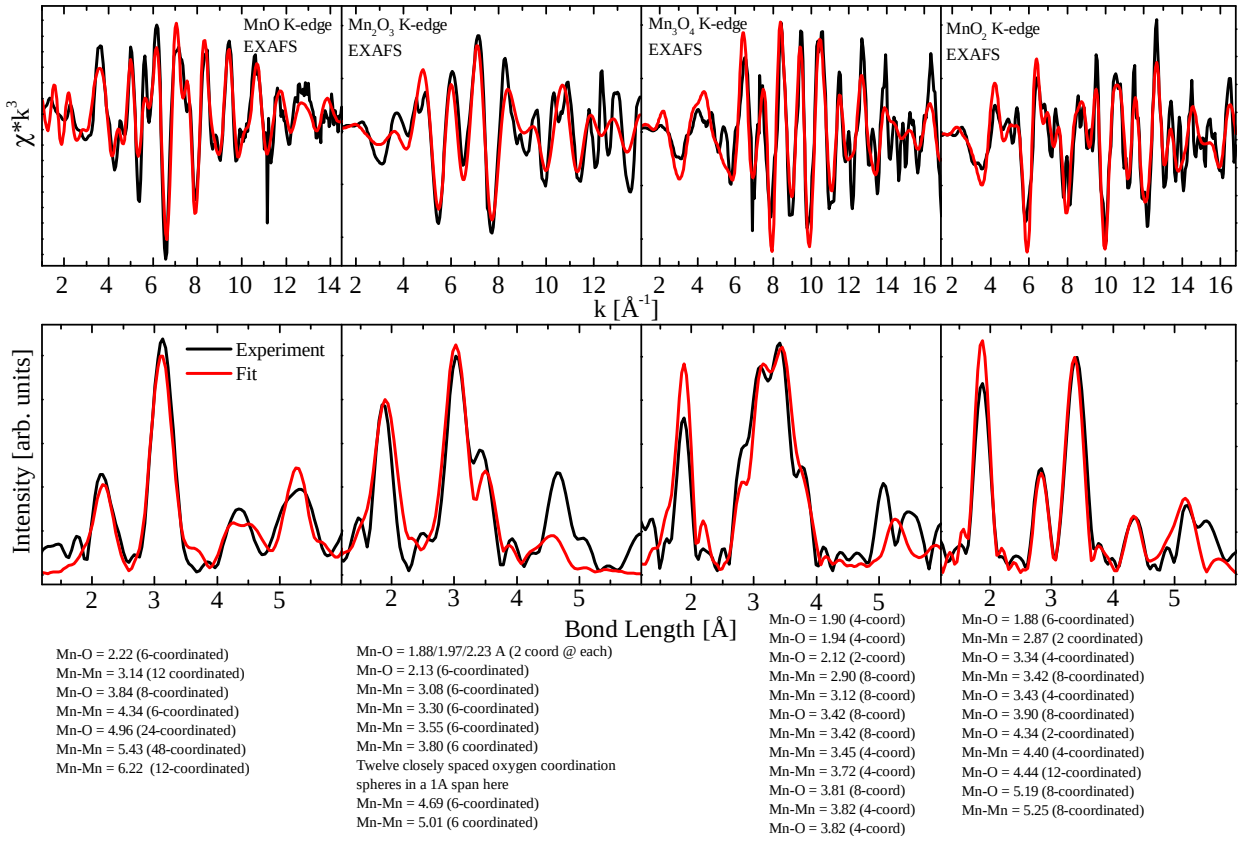

Figure 3.7: The four standard Mn oxides MnO, Mn_2O_3, Mn_3O_4, and MnO_2 have their experimental EXAFS curves displayed along with fits I obtained by varying the parameters in Equation 3.12. The interatomic distances used to obtain these fits are displayed beneath each panel. The results compare favourably with previously established results. The post-experiment analysis was performed by myself from Mn K-edge spectra courtesy of Graham George (Department of Geological Sciences, University of Saskatchewan).

within a reasonable range, but is always on the order of 0.005 Å. Lastly, the most important parameter, the interatomic distances R_i are allowed to vary freely to produce the best quality fit with the experimental spectrum such that real bond lengths can be determined.

3.4 X-ray Emission Spectroscopy

Emission spectroscopy is a term that covers a wide variety of techniques, but they all share the idea that photons are emitted from a material upon the excitation and the ensuing de-excitation of an electron. As such, in contrast to absorption spectroscopy, it is a second

order process. The insights and information that can be gained from such spectra are therefore much greater because one can directly probe specific intermediate states by tuning the incident photon energy. For the purposes of this thesis, all excitations involve an incident soft x-ray in the range of 150-1000 eV exciting a core level electron—$2p$ electrons in the case of the $3d$ metals, and $1s$ in the case of oxygen, nitrogen, or carbon measurements. The core level is then filled by a valence electron, or an electron in a higher energy core level, and sometimes a photon is emitted to conserve the overall energy.

The question of whether or not a photon is emitted is a very complex one, depending on the relative probabilities of radiative and non-radiative transitions. As it turns out, in the soft-x-ray regime with which we are concerned, non-radiative Auger and Coster-Kronig processes dominate.[76] Auger emission occurs when an electron is ejected from the system with some kinetic energy in order to compensate for the energy lost in the de-excitation of the excited electron. Qualitatively, the likelihood of Auger electron emission steadily increases as the energy difference between states in a given electron shell decreases. Thus, lighter elements, and edges in the soft x-ray regime are much more likely to emit Auger electrons rather than photons. A Coster-Kronig transition involves an electron from the same shell as the initially created hole, being filled by an electron in the same shell, coinciding with the emission of an Auger electron from a higher shell. An example would be an L_2 electron filling an initial L_1 hole, with the emission of an M_1 electron (LLM Auger). Given that all experiments herein involve soft x-rays, this creates experimental challenges and the need for brilliant synchrotron sources and highly efficient detectors.

There are two main variations on emission spectroscopy that I will be concerned with here: the resonant and non-resonant cases. In non-resonant x-ray emission spectroscopy (NXES) the incident photon is tuned in energy well above the absorption edge of interest. RIXS refers to resonant inelastic x-ray scattering in which the incident photon is tuned to be on resonance with some feature in the corresponding XAS.

3.4.1 RIXS

By tuning the incident photon energy to a specific feature in a transition metal $L_{2,3}$ XAS spectrum, the inelastic scattering cross section can be substantially enhanced. As a photon-in photon-out process, the change in the emitted photon from the incident photon (energy and momentum are transferred to the material) contains information regarding the fundamental intrinsic excitations (see Section 2.3 on multiplets) that occur within the sample.[77] By detecting these excitations for a single element, which are unique for a given material, valuable information regarding its role in the function of that material can be extracted. Often this means structural information, as well as the electronic and magnetic role of an individual element, the understanding of which is crucial for the technological applications. In this sense RIXS is truly an experimental technique probing fundamental science.

The RIXS process can be described by the following sequence of events: an electron in the system absorbs an x-ray that was tuned to be coincident with the absorption edge of an element in the material (herein, because of the low momentum transfer with soft x-rays, we are only concerned with dipole allowed transitions $p \rightarrow d$ and $s \rightarrow p$), this leaves the system in an unstable, highly energetic state. This process leaves behind a core hole that wishes to be filled in order to return the atom to a lower energy state; this is the intermediate state. Then, within $\approx$ 1 to 2 femtoseconds the core hole is filled via one of the radiative or non-radiative processes mentioned above; for RIXS we are only interested in the radiative cases wherein the core hole is filled by an electron from a different valence state and a photon of a lower energy is instantly emitted. The overall net result is an excited state in which there is a hole in the previously filled valence band, and an electron in the previously unfilled valence band; this is an electron-hole excited state (see Figure 3.8a).

Since a photon of lower energy and different momentum is emitted from the sample, there exists some scattering mechanism that transfers the momentum change and lost energy to the sample. Due to the conservation of these quantities, the electron-hole excited state must carry with it the energy $\hbar\omega = \hbar\omega_{in} - \hbar\omega_{out}$ and momentum $\hbar\mathbf{q} = \hbar\mathbf{k}_{in} - \hbar\mathbf{k}_{out}$, where the incident and outgoing photons carry energy $\hbar\omega_{in}$ and $\hbar\omega_{out}$, and momentum $\hbar\mathbf{k}_{in}$ and

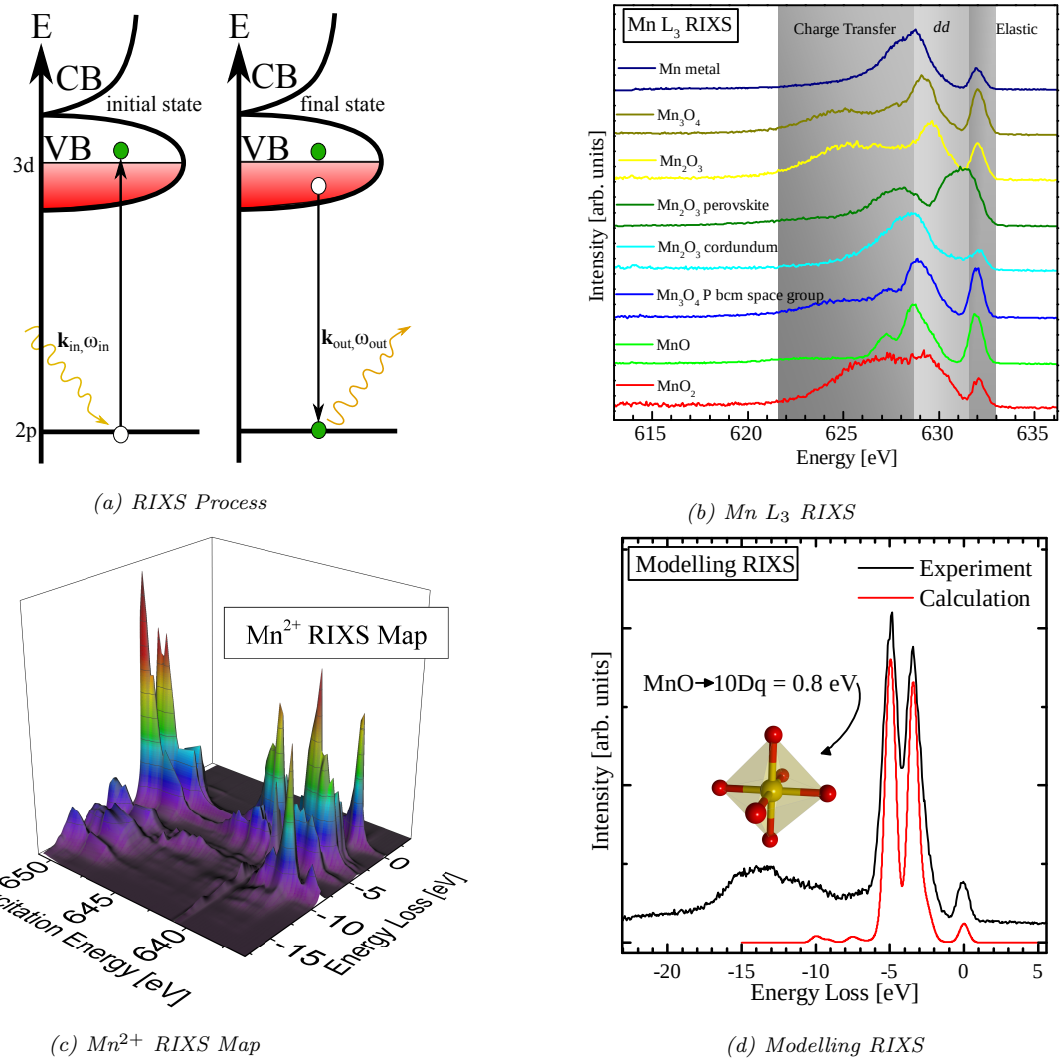

(a) RIXS Process

(b) Mn L_3 RIXS

(c) Mn^{2+} RIXS Map

(d) Modelling RIXS

Figure 3.8: (a) Illustration of the photon in-photon out RIXS process. (b)Mn L_2 RIXS data taken at identical excitation energies for various compounds, displaying the chemical sensitivity of the technique. The charge transfer, dd, and elastic regions of the spectra are highlighted. (c) The richness of information contained in a complete $L_{2,3}$ RIXS map is displayed. For each excitation energy, various intermediate excited states can be accessed, which contain information regarding fundamental excitations in the sample. (d) A RIXS spectrum can be modelled by varying crystal field parameters, which link directly to the way the transition metal resides in the crystal.

$\hbar\mathbf{k}_{out}$, respectively. Mathematically, the intensity of a RIXS spectrum is contained within

the scattering amplitude $\mathcal{F}_{fg}$

$$I(\omega, \mathbf{k}_{in}, \mathbf{k}_{out}, \boldsymbol{\epsilon}_{in}, \boldsymbol{\epsilon}_{out}) = \sum_f |\mathcal{F}_{fg}(\mathbf{k}_{in}, \mathbf{k}_{out}, \boldsymbol{\epsilon}_{in}, \boldsymbol{\epsilon}_{out}, \omega_{in}, \omega_{out})|^2 \delta(E_f - E_g + \hbar\omega_{out} - \hbar\omega_{in}) \tag{3.13}$$

where $\boldsymbol{\epsilon_{in}}$ and $\boldsymbol{\epsilon_{out}}$ are the polarization vector in the incoming and outgoing photons, and E_g and E_f are the energies of the ground and final states of the system, respectively. From this, the Kramers-Heisenberg formula can be derived to compute RIXS intensities.[78, 79] The result is that the scattering amplitude is given by

$$\mathcal{F}_{fg} = \sum_n \frac{\langle f | \mathcal{D}'^{\dagger} | n \rangle \langle n | \mathcal{D} | i \rangle}{E_g + \hbar\omega_{in} - E_n + i\Gamma_n} \tag{3.14}$$

where i, n, and f are the initial, intermediate, and final states of the system, Γ_n is the HWHM of the lifetime induced Lorentzian broadening, and $\mathcal{D}$ is the relevant transition operator, which in the dipole limit is

$$\mathcal{D} = \frac{1}{im_e\omega_{in}} \sum_{n=1}^{N} e^{i\mathbf{k}\cdot\mathbf{R}_n} \boldsymbol{\epsilon} \cdot \mathbf{r}_n \tag{3.15}$$

where $\mathbf{R}_n$ indicates the position vector for the atom to which the nth electron is bound, $\mathbf{r}_n$ is the electron position, and m_e is the electron mass. Note that in experiments we generally do not detect the polarization of scattered photons, and so the individual intensities of orthogonal polarizations are summed. When simulating spectra one needs to take a given Hamiltonian and compute the eigenvectors $|i\rangle$ and $|f\rangle$ and eigenvalues (energy levels) E_i and E_f by solving the Schroedinger equation. The issue is that the basis sets can be very large and exact eigenstate solutions may not be possible to practically compute. However, using approximate model Hamiltonians, satisfactory eigensolutions can be obtained. In addition to this, by only storing portions of the large matrices required (which often contain many zeros), computational memory can be saved that allows spectra in even very complex impurity models to be computed in a reasonable amount of time.

In most cases, the RIXS spectrum contains valuable information in two regions of the spectrum. These are the charge transfer and *dd* excitation regions as shown in Figure 3.8b. As can be seen, for several Mn compounds, these regions are quite different, indicating the

difference in fundamental excitations within them. For practical purposes, there are two main methods through which we can extract information from experimental RIXS. (1) Through comparison with theoretically calculated spectra using the models described previously. The parameters that are used to compute the spectra can then be extracted as real physical quantities that are present in the real-world material (see Figure 3.8d). By doing this it is possible to understand the material properties from a very fundamental perspective. (2) To augment the theoretical findings, often comparisons to well known materials can be made. If a Ni RIXS spectrum strongly resembles that of NiO, we can form the conclusion that the Ni in that material shares many of the same characteristics as Ni in NiO, and then it is the role of other relevant information, in addition to theoretical calculations to explain any differences present. To illustrate the richness in a RIXS map, I have plotted a calculated one in Figure 3.8c. The wealth of information in a single RIXS map allows the possibility for extremely detailed analysis. Contrast this to XAS experiments, in which there is just one spectrum per edge per element. Certainly, the RIXS experimenter can extract an abundance of knowledge that is not afforded to the XAS experimenter.

3.4.2 NXES

In the situation where the sample is bombarded with x-rays that do not correspond to the energy of a specific resonant electronic transition, it is said to be of the non-resonant type. A characteristic feature of these measurements is that the fluorescence that is detected is of constant energy and intensity, regardless of the incident energy chosen, as long as it is sufficiently above a given absorption edge. The NXES measurements performed herein can be separated into two classes: NXES above the metal $L_{2,3}$-edges, and above the ligand K-edge, which is usually oxygen, nitrogen, or carbon.

NXES probes the occupied density of states in a manner similar to that of XAS probing the unoccupied density of states. In this situation a photoexcited electron is ejected to the continuum with energy commensurate with that of the incoming photon energy minus that of the binding energy. The core hole left behind is then filled by a previously excited electron, or an electron from a higher occupied state and may emit a photon as described

in Section 3.4. However, with NXES we use a spectrometer to detect, in an energy selective manner, only photons that result from the decay of electrons from valence occupied states. Therefore, we have an experimental method of directly measuring the occupied density of states of a material, and in the case of ligand K-edges it is a very close representation of the true DOS.[80] In fact, Equations 3.13-3.15 can be shown to reduce to an expression that is proportional to the occupied density of states, only broadened by lifetime effects.

This can be readily understood by considering the presence of electron states near the Fermi level, which in the case of transition metal oxides consists of metal $3d$ and oxygen $2p$ states. In insulating or wide band gap transition metal oxides, the top of the valence band will either be dominated by mainly $2p$ (charge transfer type) or $3d$ (Mott-Hubbard type) states depending on the energy costs associated with charge transport within the material. The energy cost of moving an electron from one metal site to another is the Mott-Hubbard energy U, and in a material with d^n electrons, with E being the energy of that configuration, we have a corresponding Mott-Hubbard energy of

$$U = E(d^{n-1}) + E(d^{n+1}) - 2E(d^n) \tag{3.16}$$

where the band gap, and whether a material is insulating, is directly related to this energy cost.[81, 82] However, this is not the only effect that one must consider when determining the insulating nature of a material; one must also consider charge transfer fluctuations. In a charge transfer type insulator, the Mott-Hubbard energy is large enough to push the occupied $3d$ states lower in the valence band, such that the valence band becomes dominated by ligand $2p$ character. Whether a material has a Mott-Hubbard or charge transfer type band gap is determined by the lesser of the two energies: the energy gained from an electron hopping between metal sites (Mott-Hubbard), or the amount gained through ligand to metal electron hopping (charge transfer). The upshot that we can take advantage of with NXES, is that no matter what the dominant character at the top of the valence band, hybridization will to some extent mix the $2p$ and $3d$ states such that there is always some $2p$ character at the top of the valence band. Therefore, in transition metal oxides the oxygen NXES will appear as $2p \rightarrow 1s$ electron transitions from the generally fully occupied $2p$ band, and will hence provide us with the shape of the occupied valence band states, including its energetic onset,

which is crucial for band gap determination.

Aside from ligand K-edge NXES, metal L-edge NXES also contains relevant spectroscopic information. The underlying process as previously described is the same, except the spectral shape conveys different information. Because of the large overlap of transition metal $2p$ and $3d$ wavefunctions, the approximation that the NXES spectrum is the occupied density of states loses its validity. One would expect occupied valence band transitions from $3d/4s \rightarrow 2p_{1/2,3/2}$ to appear in exactly a $I(L_2)$:$I(L_3)$ ratio of 1:2, corresponding to the $2j+1$ degeneracy of the core states (there are two $p_{1/2}$ and four $p_{3/2}$ electrons) across the transition metal series. However, large deviations from this ratio are found via experiment.[83, 84] Radiationless $L_2L_3M_{4,5}$ Coster-Kronig transitions are primarily responsible for this deviation from 1:2. This means that an L_2 hole is filled by an L_3 electron, with the subsequent ejection of an $M_{4,5}$ electron. Generally, the peak intensity depends most strongly on the stoichiometry and oxidation state of the sample. Through comparisons of the $I(L_2)$:$I(L_3)$ ratio to known compounds, a reasonable estimate of these values can be obtained.

3.4.3 Band Gap Determination

Given that the top of the valence will have some ligand $2p$ character mixed in due to hybridization of orbitals, and the bottom of the conduction band generally consists of d states mixed with ligand p states, the difference between probes of these onsets will provide us with the band gap. Strictly speaking there should be no empty $2p$ states for an O^{2-} ligand. As mentioned above, there are two types of band gaps, depending on whether the top of the valence band is dominated by metal d states (Mott-Hubbard), or ligand p states (charge transfer). However, in both cases the band gap is a function of the energy of electron transitions between the metal d states at the bottom of the conduction band and whatever states dominate the top of the valence band.

Shown in Figure 3.9 (b) is the O K-edge XAS and NXES for NbO_2. The two main peaks in the XAS correspond to the $4d$ Nb states at the bottom of the conduction band, mixed with some O $2p$ character; the intensity in the XAS at higher energies is due to O $2p$ states with Nb $5s$ and $5p$ states mixed in (hybridized). Taking the second derivatives of

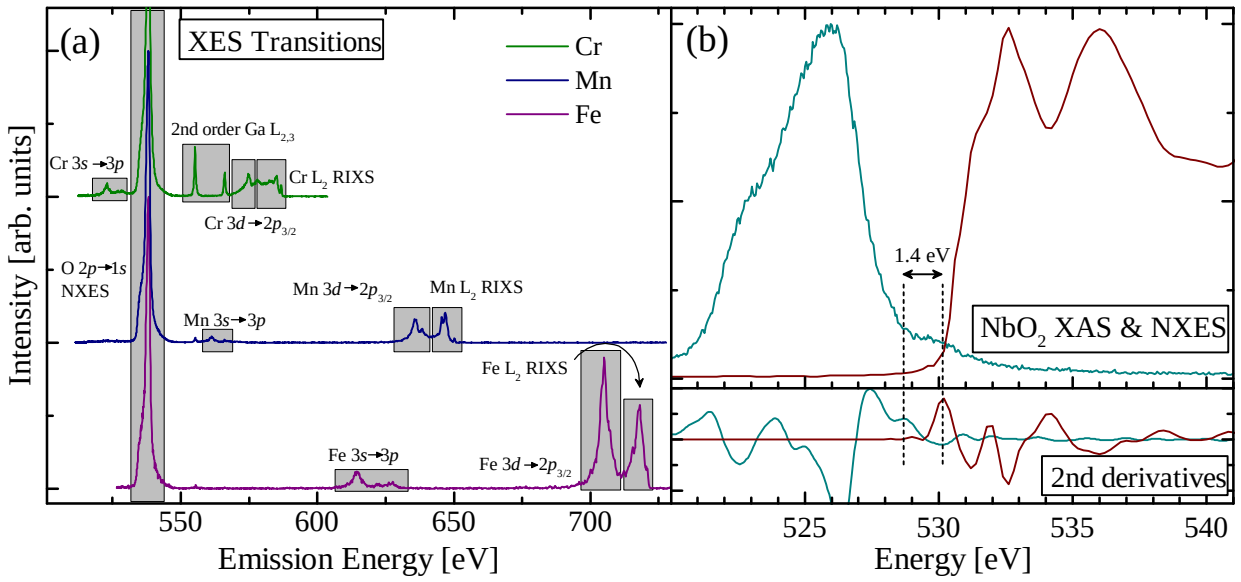

Figure 3.9: (a) Shown are three RIXS spectra at the Cr, Mn, and Fe L_2-edges. However, all electronic transitions lower in energy are simultaneously accessible as non-resonant excitations. Sometimes it is even possible to see higher energy excitations due to second order light from the monochromator (exciting Ga 2p electrons here). These are then detectable as second order peaks from the diffraction gratings that separate the light into its constituent energies before the spectrometer. In this figure the Ga $L_{2,3}$ emission lines are readily observable, despite formally being at ≈ 1100 eV. (b) As the NXES spectra of ligands atoms such as oxygen provide a picture of the occupied DOS, we can use the difference between it and the unoccupied DOS obtained from XAS to obtain the electronic band gap of a material. Here, the second derivatives of the spectra are used to unambiguously determine the onset of the electronic states.

both spectra is a simple way to reproducibly and unambiguosly determine the onset of the actual electronic states, which are experimentally blurred due to broadening effects. I found that the energetic difference between the first peak above the level of the noise in the two derivatives is 1.4 eV, which is within the range of reported values in the literature.[85, 86] Having said this, it is important to remember that with XAS we are probing the unoccupied DOS in the presence of a core hole. The good news is that the effect on the overall shape of the DOS is usually small, and the energetic shift of the onset of electronic states is often on the order of 0.1 eV,[50] and can be compensated for by calculating the core hole shift with density functional theory, and adding its value to the measurement.

Using x-ray techniques XAS and NXES to determine the electronic band gap of a material

is useful because it provides a complementary method to the more frequently used optical or reflectance techniques.[87, 88] Each technique probes a different depth and interaction volume within the sample, and so exact agreement is often no expected. No one method is better or more valid than the others, and the need for several means of measuring the band gap is obvious when one considers the frequent disagreement on the value of the band gap of common materials across several studies.[89]

3.5 X-ray Photoemission Spectroscopy

XPS involves holding the incident photon energy fixed at an energy several hundred eV above the edge of interest. This will result in the ejection of electrons from the material with a kinetic energy equal to the photon energy minus the electron's binding energy. In an XPS experiment, because the photon energy is fixed, and we are detecting ejected electrons, an integrated XPS spectrum is actually just a single data point in an XAS spectrum. Generally the key information that one wishes to gain from an XPS experiment is the binding energy of a certain electron shell.

The actual measurement of the electron's kinetic energy is accomplished by applying a magnetic field, which the electrons will circle around, with the more energetic electrons having a larger radius. Thus, by detecting the radius of the pile up of electrons on a detector, the binding energies can be indirectly determined. Since XPS relies on the ejection of electrons from the sample, it is a quite surface sensitive technique, especially in the soft x-ray regime.[90] This is because, in contrast to photons, the mean free path of electrons in a solid is much shorter, generally on the order of a nanometre for electrons under 1000 eV. For the XPS measurements in the publications concerning TiO_2 in Chapters 5 and 6, the kinetic energy of the ejected electrons is 1486 eV (excitation energy, Al $K\alpha$ photons) minus the $3d$ ion's $2p$ binding energy. This corresponds to electron ejection energies from $\approx$ 912 eV for chromium to $\approx$ 534 eV for copper. Given TiO_2 mean free path tables (also plotted in Figure 3.10 (b)), this can be translated to a mean free path range between 1.4 and 0.8 nm.[91] Since in most solids, the atoms are separated by a distance very close to 0.2 nm,

we can conclude that the XPS measurement performed herein probe between four and seven atomic layers deep, and are thus very surface sensitive.

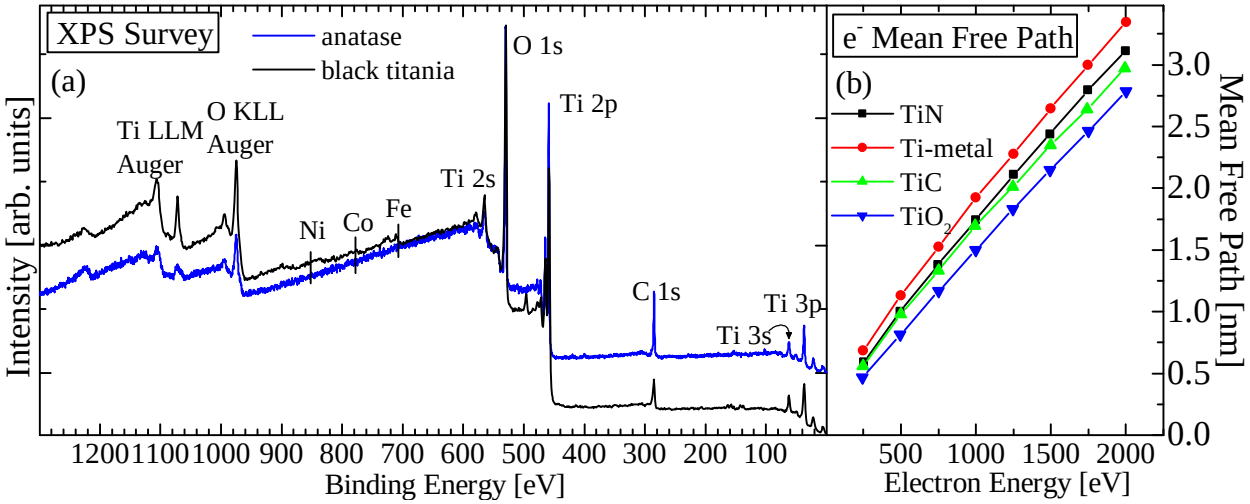

Figure 3.10: (a) An XPS Survey spectrum is an overview of all elements present in a sample, with quantitative sensitivity down to as much as tenths of a percent with good data and careful practices.[92] The binding energies of all elements present and also several secondary Auger transitions are clearly visible. (b) The electron mean free paths for several Ti compounds illustrates the surface sensitivity of XPS. Mean free path data from Ref. [91].

While the main power of XPS is measuring the binding energies of electrons as shown in Figure 3.10 (a), the physical phenomenon that allows us to actually extract useful information from this is the chemical shift of the binding energies in various solids. The chemistry of the bond between atoms is a function of the spatial distribution of the atoms and their valence electrons, and the interactions between them. In covalent bonding the electrons are shared between atoms, whereas in ionic bonds electrons are transferred between atoms. However, real world solids always exist somewhere between the two extremes of purely covalent or purely ionic. For example, in general oxygen $1s$ electrons will have binding energies around 543 eV, but can differ by several eV depending on its local bonding environment.[93] It is primarily this difference (the chemical shift) that can be harnessed to extract information from an XPS spectrum.

The XPS analysis performed herein is focused on peak fitting, where a single peak (say

oxygen $1s$) is composed of several component peaks superimposed on top of one another, but slightly separated in energy. By fitting the overall peak with various components we suspect to comprise our material, information on the chemical proportion of various compounds can be gained by integration of the fitted components, which then need to we weighted by relative sensitivity factors for the corresponding elements and edges.[94] The other fitting procedure that can be done involves determining the oxidation states, and their relative proportion, that exist in a given material. For example, Mn-metal, Mn^{2+}, Mn^{3+}, and Mn^{4+} will all display slightly different chemical shifts for the same edge. By performing a weighted sum of these to match a sample of interest, a good approximation to their relative proportions in the real sample can be determined.

3.6 Ion Implantation

Although not performed by me, all doped thin film samples in the publications contained herein were doped via ion implantation. Therefore, it is necessary to give a brief overview of the modelling of the process I have done. Ion implantation is a process in which ions of one element are accelerated into another such that a beam of atoms bombards and penetrates the surface. This will alter the chemical make-up of the material, with the general goal of tuning the host material's electronic and/or magnetic properties through doping.

Figure 3.11 shows a calculation of the ion depth profile using Stopping Range in Matter (SRIM) calculations [95]. The 3D profile displays the relative Co ion concentration for ions incident normal to the surface from a point source. However, the source is more akin to a beam, so the horizontal ion profile here would be more widely distributed over the sample surface. The vertical scale is for the shaded area on the right, which shows the Co depth profile. The peak Co density is at 15.9 nm depth where it is 2.5×10^{22} atoms/cm^3. Because of such high concentrations here, the term "dopant" is somewhat of a misnomer, as the concentrations reach 26% in terms of atomic percentage.

Given the widely variable depth profile, it is apparent that whether we choose photon-out or electron-out techniques, we are inherently measuring a fundamentally different material.

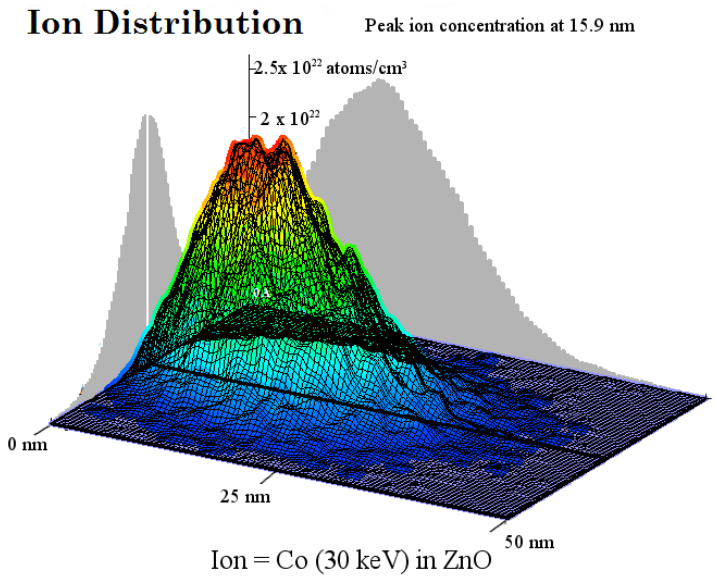

Figure 3.11: 3D plot of the depth profile of the dopant atom Co, in ZnO, given the implantation conditions. The maximum cobalt density is at a depth of 15.9 nm, and the penetration of Co ions reaches a maximum depth of ≈45 nm. Note that the figure assumes implantation occured at a single point on the sample surface, and the horizontal profile is due to ion scattering. Plotted using the software The Stopping and Range of Ions in Matter (SRIM) in Ref. [95].

As previously discussed in Section 3.5, the probing depth of XPS and TEY is only a few nanometres, where the concentration is in the range of ≈2%. And, for any x-ray-in x-ray-out technique where the penetration and probing are depth are ∼150 nm, the average cobalt concentration varies widely over from its peak value to effectively zero. However, with the larger penetration of x-ray we can measure at grazing incidences to the sample surface to systematically control the probing depth. In fact, using the fact that one can obtain the absolute value of the absorption coefficient μ using IPFY, and by taking a series of measurements at various angles, it is in principle possible to experimentally map the ion implantation depth concentration.

CHAPTER

FOUR

DATA ANALYSIS AND SOFTWARE

All software written by me throughout the course of my graduate studies was written using MATLAB. This not only includes the algorithms discussed below, but also several scripts on calculation-experiment matching for XAS and RIXS, quantitative linear summing used in my publications, IPFY and PFY analysis, and EXAFS analysis. The Quanty code used to do calculations was written in Lua programming language, which I frequently modified for specialized tasks. Lastly, I did not write or perform any of the DFT calculations in the published work, which was done by collaborators.

4.1 Image Correction for XES Spectra

When collecting emission spectra we are observing photons that are emitted from our sample at a 90° angle from the incident light. This light is then partitioned into spectral lines by a grating that diffracts the radiation into its component energies. The optical design of the detector in the spectrometer is such that when photons impinge on it a curved image appears. This is due to photons of equal energies landing on different vertical pixels despite having identical energies, depending on their horizontal position across the detector. We observe this effect as a curved two dimensional image (Figure 4.1a). As shown in Figure 4.1c, if the pixels were summed horizontally and plotted on the raw pixel scale we record, we would

suffer not only a loss in resolution, but also have incorrect energy separations for features in our spectra—a stretching or compressing of the image. The XES work in this thesis was done using three different spectrometers: (1) CLS REIXS beamline post-2016 spectra required image correction as shown in Figure 4.1, (2) ALS Beamline 8.0.1 mid-2016 and earlier required severe image correction as the curvature was quite large, (3) ALS Beamline 8.0.1 mid-2016 and later had a CCD camera installed such that the image correction is negligible.

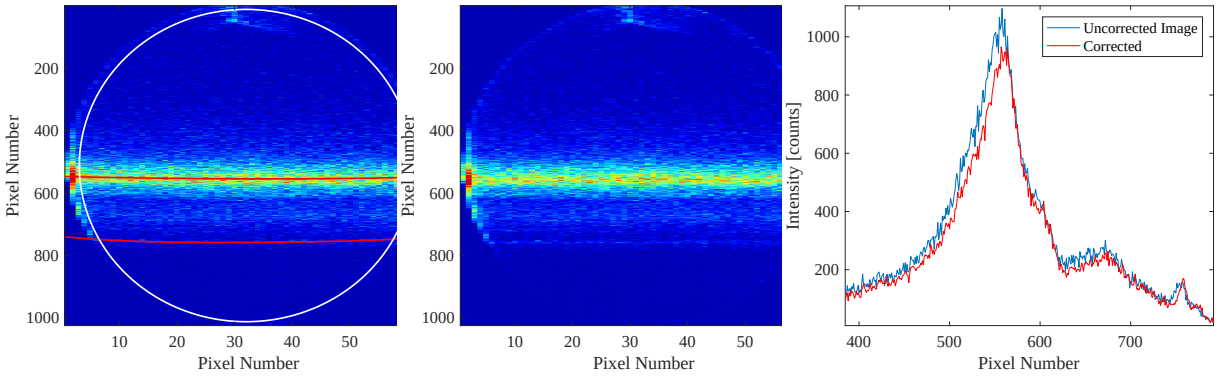

(a) Uncorrected Image *(b) Corrected Image* *(c) Resulting Spectra*

Figure 4.1: (a) The raw recorded 2D image contains a curvature that is not constant across the detector. (b) After the treatment described in the text the image appears straight, such that horizontal rows can be summed to produce the corrected spectrum in (c), which is contrasted to the result had the image correction not been carried out.

In practice, to adjust for the curvature of the image one must develop an algorithm that logically rearranges the counts on the detector without losing the total number of counts. As a decent first approximation, one could simply shift each of the 64 columns up or down an integer number of pixels manually until a sufficiently straight horizontal line across the detector for some feature is seen. However, this will lead to the loss of counts near the detector edges, and does not account for the change in curvature across the detector. To achieve the greatest improvement it is necessary to detect the curvature of at least two spectral features. In Figure 4.1a the two red lines show polynomial functions that track an intense spectral feature across the detector, and the weaker elastic peak (both of which we know to be at a constant energy). The polynomial functions were created by fitting a gaussian curve within

a given pixel range (depending on which single feature we are attempting to track) for each of the 64 columns. Then noting all of the gaussian's centre positions, a polynomial of a chosen order is fit to the centre positions of those gaussians. Thus, there are 64 data points to fit our polynomials to.

For each column there is then two data points corresponding to each polynomials value. A straight line is fit to these data points, which will be different for each column. Essentially, the slope of this line tells us how the counts on each pixel need to be rearranged as we go from the top to the bottom of the image, and this will be different for each column. The value of the straight line evaluated for every one of the 64×1024 pixels will correspond to new pixel number where the original counts should be placed. However, it is always the case that some fractional pixel is arrived at (we cannot place the counts from pixel #537 into pixel #558.33). This allows us one last step to further improve the image quality: fractional pixel shifts. If a result like the above occurs, then we redistribute 33% of the original pixels in pixel #559 and 67% of the original pixels into pixel #558. Of course, one cannot take 67% of a whole number of counts most of the time, but any further rounding of fractions of fractions of counts beyond this is negligible. Lastly, to avoid edge effects on the detector, an ellipse is fit to it (as shown in Figure 4.1a), and only counts within the ellipse are included in the final spectrum. This is the reason that the total integrated counts in Figure 4.1c appears to be slightly less after the image correction process. The result is that spectral features are sharper and shifted from their original pixels, which in turn will create an energy axis shift once the pixels are converted to absolute energies, and that the noise is slightly reduced by performing non-integer shifts.

4.2 Energy Calibration

Once a quality spectrum is obtained such that its shape and noise level can be maximally optimized via handling of the raw two dimensional data, care must be taken to convert the pixels numbers to an energy axis, representing the actual energies of emitted photons. To do this we must assume that the monochromator of the beamline can very accurately

change energies. That is, we assume the ΔE changes of energy (not the absolute energy E) are extremely precise. We know this is a valid assumption because beamline scientists take a lot of care to ensure reproducibility of the data across well known materials that have been measured countless times all around the world (XAS spectra would look stretched or compressed if ΔE moves were off). Given this assumption, elastic peaks in a RIXS spectrum with known energy spacings and pixel numbers can be used to convert the pixel scale to an energy scale.

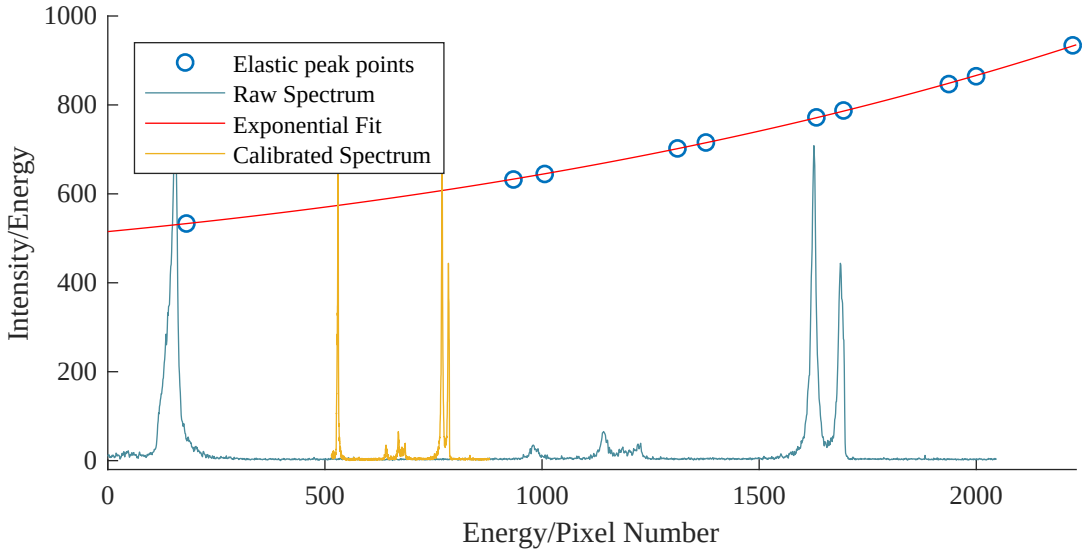

Figure 4.2: There are two x/y axes shown here: Pixel Number (x-axis)/Energy (y-axis) maps the raw spectrum (blue) via the calibration curve (red) from the pixel scale (x-axis) to the energy scale (y-axis). The secondary axes, Energy (x-axis)/Intensity (y-axis) scale has the calibrated curve (yellow) plotted on it after the conversion to energy has been done.

The process is shown for the ALS Beamline 8.0.1 CCD spectrometer in Figure 4.2. This spectrometer has an energy range that is dependent on the energy you wish to detect. The grating before the CCD camera is held fixed and the camera is on a 1.5 m arm that rotates in a circle, so depending on the angle of rotation, a specific energy range of photons can be detected. This range is quite large at the higher end of the soft x-ray range, and is ≈ 400 eV in this example, detecting emission photons from the oxygen K-edge up to the nickel L-edge. The blue circles in Figure 4.2 are the key to calibration, each one represents the energy and

pixel of an elastic peak from a single $3d$ metal spectrum. By fitting an exponential function to these points of known energy and pixel, a universal calibration curve can be developed that maps every pixel to an energy value. That is, in Figure 4.2, the value of the red line for any pixel will map directly to an energy in eV. The essential feature of the line is not that it exactly passes through every single point perfectly, but that the slope of the line in the vicinity of the points is accurate. This is because the slope of the line serves as the energy spacing per pixel, which varies widely depending on the energy. To get a sense of this it goes from 0.30 eV/pixel at the Cu L-edge to 0.11 eV/pixel at the O K-edge, down to 0.085 eV/pixel at the N K-edge. Therefore, our resolution is mostly pixel limited for higher energy Co, Ni, and Cu RIXS. This, plus the limits of the diffraction gratings before the detector combine to produce the overall resolving power.

The universality of the curve can be adopted to any spectrometer angle single because the angle of rotation is exactly constant per pixel. Every pixel (or energy spacing) corresponds to exactly some angle of rotation. This is what allows me in Figure 4.2 to use an elastic peak in the Cu energy range (highest pixel blue dot) even though this is outside the 2048 pixel window of the detector. It is essential to have a wide spread of elastic peak points on either side of the detector, or outside the detector window to ensure proper energy calibration. Essentially this means that we will interpolate data between the points, but will not fall into the trap of extrapolating data outside the recorded points, ensuring proper energy calibration.

Lastly, a constant energy shift of the RIXS spectrum needs to be performed. This process is straightforward, and only requires us to have previously done a proper constant energy shift with the corresponding XAS spectrum, which is done by aligning it to previously published standardized spectra. Then we align our known elastic peaks to the same energy as in the XAS spectrum that we know we excited at.

It is of note that the first two steps in calibrating a RIXS spectrum are of the utmost importance, as they result in the stretching/compressing of spectral features. Our analysis, calculations, and eventual conclusions rely heavily (often solely) on the energy separation of peaks in the spectra. On the other hand, the constant energy shift at the end is of little

importance as it contains no physics, and energy shift discrepancies of several eV for common oxides is not uncommon in the literature.[96, 97]

4.3 Maximum Entropy Deconvolution

A deconvolution algorithm serves the purpose of removing some function (here a Gaussian) that has been convolved with some other function (here the spectra) with the intent of viewing the spectrum in the absence of the convolution. Essentially this means reducing broadening effects from the experimental data to better resolve features. There are several ways of doing this, but certainly the most elegant is through maximizing information entropy.[98] In 1982 Jaynes stated the principle quite eloquently, "The MaxEnt principle, stated most briefly, is: When we make inferences based on incomplete information, we should draw them from the probability distribution that has the maximum entropy permitted by the information we do have. Essentially all of the known results of statistical mechanics are derivable consequences of this principle".[99] Information entropy quantifies the information content, or equivalently, the uncertainty of a system. That is, an increase in entropy is analogous to an *increase* in uncertainty or a *decrease* in information. I have used this algorithm to improve spectra in two publications to date, seen in Refs. [51] and [100].

A simple argument leading to the definition of entropy is as follows: say we have two machines, one of which produces any of 24 of the Greek letters at random with equal probability, the other produces any of the 26 English letters randomly. We would like our measure of entropy to have the property that it is additive, that is, if we receive two symbols, it is twice as much information as receiving one symbol. Logarithms naturally lend themselves as a choice for our definition, where we could say entropy is S = log(N), where N is the number of equally probable choices. The amount of entropy in our system is then $\log 24 + \log 26 = \log 624$. In this way we can add entropy instead of multiplying the number of choices available. This can be rewritten as $S = \log N = -\log P$ where $P = 1/N$ is the probability of a given choice. For a group of many machines, scenarios, pixels, etc. this can be written as $-\sum_{i=1}^{N} \log P_i$.

This must be generalized for the case where all probabilities are not equal (of course they must always sum to unity, $\sum_{i=1}^{N} P_i = 1$). If the English letter producing machine spits out one letter with $P = 1$ and the rest with P = 0 then the entropy (uncertainty) is at a minimum, $\log 1 = 0$; likewise if the probabilities are all equal the uncertainty is maximum. The reason all terms in the sum with P = 0 are ignored is because $\lim_{p\to 0} P \log P = 0$. The natural, and as it turns out, correct choice, is to take a weighted sum of the distribution by introducing a factor of P_i. This leads to the well known formulation of entropy $S = -\sum_{i=1}^{N} P_i \log P_i$. It can then readily be seen that this is of the same form as thermodynamic entropy, $S = -k_B - \sum_{i=1}^{N} P_i \ln P_i$, hence why the term entropy was adopted.

The key point to be taken is that in the same way that an increase in thermodynamic entropy implies an increased probability of the system being in that state, the identical proposition holds true for information entropy. A concise way to state this in general is that a larger entropy is equivalent to a larger multiplicity, and therefore it can be realized in more ways, and consequently is the most reasonable choice to be observed. For example, when we roll two dice there are 36 possible outcomes with 11 different totals, the outcome where the two dice sum to 7 has the highest multiplicity (6), the highest entropy, and accordingly, is the most probable outcome. Out of the distribution of possible outcomes, the one to be preferred over all others is the one with the highest information entropy.

I took the general algorithm set forth in Ref. [101] and wrote and applied it to 2-dimensional image reconstruction (spectra). It has been independently used in spectroscopy in recent years, but is certainly not common practice, despite the obvious benefits.[102, 103, 104, 105] As it is also inherently a smoothing algorithm, and the smoothing of data is pervasive across science, it should without a doubt be the standardized method of doing so.

In terms of image reconstruction, the underlying problem is that we have some recorded data D which is the convolution of the ideal signal f and some broadening function R (point spread function), $D = R * f$. Observe here that D, R, and f are vectors and the symbol $*$ represents convolution, in discrete form the nth index is defined as $(R * f)[n] = \sum_{n=0}^{\infty} R[n] f[m - n]$. Note that this is equivalent to $(R * f) = R_{jk} f$ where R_{jk} is a square matrix in Toeplitz form containing the response function and f is a vector. A Toeplitz

matrix is a symmetric matrix where the value along every diagonal (from upper left to lower right) is the same. The entire problem including noise (σ) can then be stated as $D_k = \sum_{j=1}^{N} R_{kj} f_j + \sigma_k$. The point is that we want to recover the true signal f and the problem is that there are many solutions which fit this criterion due to noise in the image and R^{-1} not being unique.

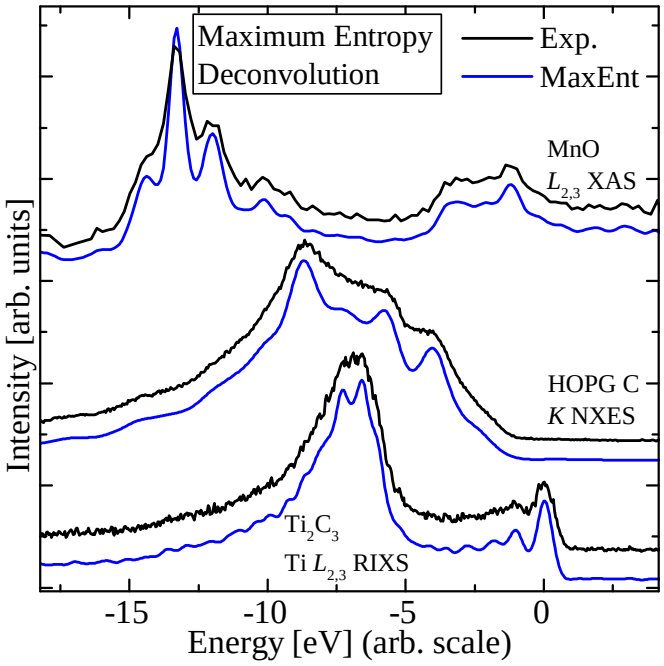

Figure 4.3: Shown are three examples of the MaxEnt deconvolution algorithm for three different techniques: XAS, NXES, and RIXS. In all cases the spectra are smoothed, but also the spectral features are significantly more elucidated.

The goal then is to seek the image with the maximum entropy, or minimum information by searching in image-space. The procedure is to start with an unbiased flat spectrum and update it iteratively until a satisfactory solution is reached. The solution obtained, once broadened, must fit the experimental data to within noise levels. A simple chi-squared consistency test is done to ensure this is the case, $\chi^2 = \sum[(R * f)_k - D_k]^2/\sigma_k^2$; this is just a comparison of the raw data with the convolved solution. To find a solution three search directions are used: the gradient of the entropy (∇S), the gradient of the consistency test ($\nabla \chi^2$), and third direction which is a more complicated combination of the first two. The

solution is then updated after each iteration where the latest solution is $f_{new} = f_{last} + x_\mu e_\mu$; here e_μ's are the search direction vectors weighted by constants x_μ (Einstein notation used). The true maximum entropy solution has been reached when the vectors ∇S and $\nabla \chi^2$ are anti-parallel, a check is done for this after every iteration and when they have become sufficiently anti-parallel a satisfactory solution is said to have been obtained.

To show the algorithm in action I have plotted some examples in Figure 4.3. In each of the three example shown, features that are not clear, or not present at all, appear in the treated spectrum. It is certainly advantageous to use over any smoothing algorithm as it presents the results more clearly with "added" information.

CHAPTER

FIVE

Background Information

This paper was published in the Journal of Applied Physics in February 2014. It can be accessed online with doi 10.1063/1.4864748. The reference to it is: Journal of Applied Physics 115, 053711 (2014). My contribution to this manuscript includes: performing all RXES, XAS, and XES measurements along with R. A. Green and J. A. McLeod; doing the bulk of the scientific analysis of all data and crystal field calculations therein; and re-writing the initial draft by E. Z. Kurmaev.

Structural defects induced by Fe-ion implantation in TiO_2

B. Leedahl,[1] D. A. Zatsepin,[2] D. W. Boukhvalov,[3] R. J. Green,[1] J. A. McLeod,[1] S. S. Kim,[4] E. Z. Kurmaev,[5] I. S. Zhidkov,[2] N. V. Gavrilov,[6] S. O. Cholakh,[7] and A. Moewes[1]

[1] Department of Physics and Engineering Physics, University of Saskatchewan, 116 Science Place, Saskatoon, Saskatchewan, Canada, S7N 5E2

[2] Ural Federal University, 19 Mira Str., 620002 Yekaterinburg, Russia

[3] School of Computational Sciences, Korea Institute for Advanced Study (KIAS) Hoegiro

87, Dongdaemun-Gu, Seoul, 130-722, Korean Republic

[4] School of Materials Science and Engineering, Inha University,Incheon 402-751, Republic of Korea

[5] Institute of Metal Physics, Russian Academy of Sciences-Ural Division, 620990 Yekaterinburg, Russia

[6] Institute of Electrophysics, Russian Academy of Sciences-Ural Division, 620016 Yekaterinburg, Russia

Abstract

X-ray photoelectron spectroscopy (XPS) and resonant x-ray emission spectroscopy (RXES) measurements of pellet and thin film forms of TiO_2 with implanted Fe ions are presented and discussed. The findings indicate that Fe-implantation in a TiO_2 pellet sample induces heterovalent cation substitution ($Fe^{2+} \rightarrow Ti^{4+}$) beneath the surface region. But in thin film samples, the clustering of Fe atoms is primarily detected. In addition to this, significant amounts of secondary phases of Fe^{3+} are detected on the surface of all doped samples due to oxygen exposure. These experimental findings are compared with density functional theory (DFT) calculations of formation energies for different configurations of structural defects in the implanted TiO_2:Fe system. According to our calculations, the clustering of Fe-atoms in TiO_2:Fe thin films can be attributed to the formation of combined substitutional and interstitial defects. Further, the differences due to Fe doping in pellet and thin film samples can ultimately be attributed to different surface to volume ratios.

5.1 Introduction

Enormous efforts have been put forth in the last several years to study TiO_2-based materials; these materials have been shown to display many promising technological applications in a wide variety of fields. This includes areas such as photovoltaics,[106] photocatalysis,[107,

108, 109] photo/electrochromics,[110] and spintronics.[111, 112] The electronic properties of the TiO_2 host material, and therefore the specific technological application as well, depend on the modifications to the sample (for example, by ordinary chemical doping, precise cation-anion site substitutions, etc.). In addition to this, the interactions between the TiO_2-based materials and their surrounding environment play an active role in the properties of such materials, and should therefore also be considered when studying these materials.[113]

Among the aforementioned modifications to the TiO_2 matrix, cation doping with $3d$-transition metals is of particular interest. This is because $3d$ transition metal doping is often linked with the appearance of ferromagnetism in dilute magnetic semiconductors, since ferromagnetism can be induced by the exchange interaction of magnetic $3d$-ions mediated by carriers.[114, 115] A second point of interest is that by filling the mid-gap states in TiO_2 with d^n-states, the band gap ($\sim$3.03 eV for rutile TiO_2),[116] which is too large for absorption in the visible part of solar spectrum, will be reduced. The system would then be more viable for established photocatalysis use in the visible region of the electromagnetic spectrum.[117]

Doping of TiO_2 with Fe, Co and Ni occurs only by heterovalent substitution, this is because these $3d$-elements do not easily maintain a 4+ oxidation state. This induces the formation of different structural defects (vacancies, interstitials, precipitates), which can affect the electronic structure, and hence, the magnetic and electrical properties of doped materials.

In the present paper we have studied the local structure of Fe impurity atoms in TiO_2 pellet and thin films using x-ray photoelectron spectroscopy (XPS) and resonant x-ray emission spectroscopy (RXES). Based on these measurements, the structural models of TiO_2:Fe are discussed and compared with our DFT-calculations.

5.2 Experimental and Calculation Details

5.2.1 Sample Preparation

TiO_2 coating sols were prepared by a sol-gel chemical process, where titanium-isopropoxide, nitric acid, and anhydrous ethanol were used as the precursor, catalyst, and solvent, respec-

tively. Deionized water was also supplied for the hydrolysis of TIPP and all of the chemicals were used as received without any further purification. Using the prepared coating sols, TiO_2 films were deposited on Si wafers (100) by a dip-coating process.[118] The withdrawal rate of the substrate was 4 mm/s. The as-prepared films were dried at room temperature and then kept in an oven at 60°C for 1 day to remove the remaining solvents completely, and finally they were annealed at 100°C for 2 hours. The obtained films were ∼200 nm thick and characterized by field emission scanning electron microscopy and atomic force microscopy.

Samples of ceramic TiO_2 powder were obtained by electrical explosion of wires,[119] they were made in molds of 15 mm diameter at 7×10^4 N force. They were then sintered for one hour at a temperature of 1040°C. The final dimensions when compact were on average: 12.8 mm in diameter, 1.8 mm in height, and a density of 4.25 g/cm^3. The phase composition was verified by an x-ray diffractometer (XRD), and the compact material was found to be nearly all single phase rutile (99.85%). The parameters of its tetragonal lattice were: a = b = 4.592 Å, c = 2.960 Å, and the average crystallite size was determined to be $>$ 200 nm. This sample will be referred to herein as the "pellet" sample.

5.2.2 Ion Implantation

The implantation of Fe ions in pellet and thin film TiO_2 samples was carried out in vacuum, the chamber was evacuated to a residual pressure of 3×10^{-3} Pa. An ion beam with an energy of 30 keV was then generated by the source based on a cathodic vacuum arc. The arc was initiated with an auxiliary discharge in an argon atmosphere, by doing this the gas pressure in the chamber increased to 1.5×10^{-2} Pa. The processing was carried out in a pulsed mode with a repetition rate of 25 Hz and a pulse duration of 0.4 ms with a pulse current density of 0.7 mA/cm^2. The duration of exposure for which the fluence reached 1×10^{17} cm^{-2} was 38 minutes. The samples were mounted on a massive water-cooled collector in order to prevent overheating. The initial temperature of the samples prior to irradiation was 20°C. After implantation, the samples were cooled under vacuum for 20 minutes. Stopping range of ions in matter (SRIM) simulations were performed to determine the approximate distribution and concentration of implanted ions.[95] The average

concentration of Fe ions was found to be ∼23% (by atomic %) to a maximum depth of ∼45nm.

5.2.3 XPS Measurements

XPS core-level and valence-band measurements were made using a PHI XPS Versaprobe 5000 spectrometer (ULVAC-Physical Electronics, USA) based on the classic x-ray optic scheme with a hemispherical quartz monochromator and an energy analyzer working in the range of binding energies from 0 to 1500 eV. This system uses electrostatic focusing and magnetic screening to achieve an energy resolution of $\Delta E \leq 0.5$ eV for Al $K\alpha$ excitations (1486.6 eV). All samples under study were introduced to vacuum (10^{-7} Pa) for 24 hours prior to measurement, and only samples whose surfaces were free from micro-impurities were measured and reported herein. The XPS spectra were recorded using Al $K\alpha$ x-ray emission; the spot size was 100 μm, and the x-ray power load on the sample was kept below 25 watts. Typical signal to noise ratios were above 10000:3. The spectra were processed using ULVAC-PHI MultiPak Software 9.3 and the residual background was removed using the Tougaard method.[120] XPS spectra were calibrated using a reference energy of 285.0 eV for the carbon 1s level.[121]

5.2.4 XES and XAS Measurements

The x-ray emission spectroscopy (XES) and x-ray absorption spectroscopy (XAS) measurements taken at the Fe L-edge were performed using Beamline 8.0.1 [122] at the Advanced Light Source (ALS) at the Lawrence Berkeley National Laboratory. The beamline uses a Rowland circle geometry grating spectrometer with spherical gratings. The photons emitted from the sample were detected at an angle of 90° with respect to the incident photons, and the incident photons were 30° to the sample surface normal with a linear polarization in the horizontal scattering plane. All of the experiments were performed in a vacuum chamber at $\sim 10^{-5}$ Pa. The XAS resolving power ($E/\Delta E$) was ∼2000, while the XES resolving power was ∼1000.

The Fe L-edge XAS spectra were calibrated using a reference energy of 708.4 eV for the first peak in the L_3 absorption edge and a reference splitting of 13.5 eV between the L_3 and

L_2 absorption lines of metallic iron; the XES spectra were then calibrated with respect to the elastic scattering peaks from incident x-rays with energies resonant with the L_2 and L_3 absorption lines. The O K-edge XES and XAS spectra were calibrated using a reference energy of 526.0 eV and 532.7 eV for the O K emission line and absorption edge of $Bi_4Ge_3O_{12}$, respectively. Inverse partial fluorescence yield (IPFY)[60] measurements were made using the SGM beamline at the Canadian Light Source.[123] In IPFY, the edge of interest is resonantly excited over a a range of energies, but regular partial fluorescence yield (PFY) measurements are taken with the detector at some other lower energy edge of a *different* element in the sample. As the resonantly excited (Fe $L_{2,3}$ is the edge of interest herein) edge begins absorbing photons, it reduces the amount absorbed at the lower energy edge (O K-edge herein), when inverted, this lower energy PFY spectra is proportional to the true x-ray absorption coefficient, but free of saturation and self-absorption effects.

5.2.5 DFT Calculations

The density-functional theory (DFT) calculations were performed using the SIESTA pseudopotential code,[124] as has previously been utilized with success for related studies of impurities in semiconductors.[125] All calculations were made using the Perdew-Burke-Ernzerhof variant of the generalized gradient approximation (GGA-PBE)[126] for the exchange-correlation potential. A full optimization of the atomic positions was done, during which the electronic ground state was consistently found using norm-conserving pseudopotentials for the cores and a double-ξ plus polarization basis of localized orbitals for Fe, Ti, and O. Optimizations of the force and total energy were performed with an accuracy of 0.04 eV/Å and 1.0 meV, respectively. For the atomic structure calculations, a Ti pseudopotential was employed with Ti $3d$ electrons treated as localized core states. The calculations of the formation energies (E_{form}) were performed using the standard method described in detail in Ref. [125]. As a host for the studied defects, a TiO_2 supercell consisting of 96 atoms was used. Taking into account our previous modelling of transition metal impurities in semiconductors,[125] we have calculated various combinations of substitutional (S) and interstitial (I) Fe impurities.

GGA-PBE was chosen as opposed to more complex approaches such as using a hybrid

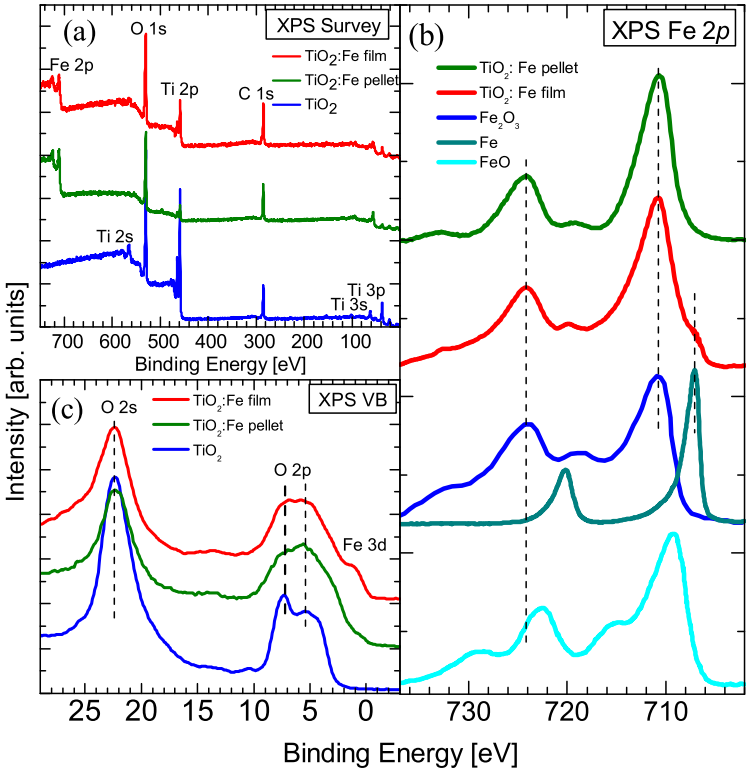

Figure 5.1: (Color online) XPS data. (a) XPS Survery of pure and Fe-implanted TiO_2. The Fe 2p signal is strong in doped samples while the carbon content is relatively low, there is also no indication of impurites other than Fe. (b) Fe 2p XPS spectra of doped and reference samples are shown. Both doped samples show a strong similarity to Fe_2O_3 in both pellet and thin film TiO_2 samples, indicating the presence of primarily Fe^{3+} on the surface. In addition to this, a clear Fe metal signal can be seen in the thin film sample due to the clustering of Fe atoms. (c) Valence band spectra show that Fe doping introduces Fe 3d states near the Fermi level as compared to pure $TiO2_2$, indicated a reduction in the band gap upon doping with Fe.

functional or on-site Hubbard U because GGA-PBE is computationally much simpler than other approaches, and GGA-PBE adequately reproduces the electronic structure of TM-doped DMS systems.[125] Indeed, in past studies the more complex approaches provided virtually identical results in terms of defect structures and exchange interactions.[127, 128]

5.3 Results and Discussion

By using core level XPS to probe the occupied density of states (DOS), the local environment of the absorbing atom can be determined due to the final state interaction between the core hole and the valence band electrons. In addition to this, XPS is also useful for profiling the occupied DOS in the valence band. The nature of XPS allows for a probing depth of only ≈5 nm, due to the inelastic mean free path of excited electrons in TiO_2, and is thus a very surface sensitive technique.[91] Based on the aforementioned SRIM calculations for ion implantation, the Fe content in this region is significantly less than in the bulk (1-2% as compared to ≈23% on average). In XAS, transitions are governed by dipole selection rules in which the absorption cross section is measured across a range of excitation energies. Hence, an electron is excited from a core level state to an empty valence or conduction band state and the total unoccupied DOS is probed. RXES is also governed by dipole selection rules, in this case an excitation energy is chosen to resonate with a peak in the corresponding XAS spectrum. In RXES, an incident x-ray excites an electron to produce an elementary transition in the sample, which will subsequently decay to a lower energy, with the emission of an x-ray. It is these emitted x-ray which are detected as a function of energy. By choosing an appropriate excitation energy RXES can probe specific transitions such as $d-d$, charge transfer, and even magnetic excitations.

5.3.1 XPS Measurements

The XPS survey spectra of pure and Fe-implanted TiO_2 (pellet and thin films) are presented in Figure 5.1 (a). The samples show a relatively low carbon content, and do not contain any impurities other than Fe, as can be seen by the Fe $2p$ signal in the doped samples.

In Figure 5.1 (b) XPS Fe $2p$-core level spectra of doped samples are shown along with spectra of reference samples FeO (Fe^{2+}), Fe_2O_3 (Fe^{3+}), and Fe-metal taken from Refs. [129] and [130]. From this comparison, we see that the XPS Fe $2p$ spectrum of TiO_2:Fe is similar to that of Fe_2O_3, which suggests that heterovalent substitution $Fe^{3+} \rightarrow Ti^{4+}$ takes place for both pellet and thin film materials. This was a foreseeable result because Fe on the surface

of the sample will oxidize quite easily in the presence of an oxygen rich atmosphere, and XPS measurements will be quite sensitive to this within its probing depth. On the other hand, one can see the contribution of the metallic peaks in the TiO_2 thin film XPS signal at ≈707 eV and ≈720 eV, this is strong evidence of Fe-clustering near the surface of the thin film sample.

XPS valence band spectra of pure and Fe doped TiO_2 are presented in Figure 5.1 (c). O 2*s*-states are concentrated (≈22.3 eV) at the bottom of the valence band, whereas O 2*p*-states prevail at the top of the valence band. Fe-doping induces Fe 3*d*-states near the Fermi level as expected, as indicated by the appearance of a shoulder in the doped spectra as compared to the pure TiO_2 sample. For TiO_2:Fe (film), the Fe 3*d*-states are more pronounced and form a peak that is located at ≈1.5 eV, whereas in the pellet sample the Fe 3*d* peak is rather smeared. The presence of Fe 3*d*-states near the mid-gap states is consistent with the general strategy of band gap engineering TiO_2-based photocatalysts where the d^0 states are substituted by d^n-states. [131] But note that the presence of Fe^{3+} states in the vicinity of the Fermi level is usually considered to be the main reason for the appearance of Fe^{3+} induced ferromagnetism in thin film TiO_2:Fe.[132] For completeness, it should also be stated that core level Ti 2*p* XPS spectra were investigated for all samples, but contributed very little to the conclusions posed herein. This is due to the high degree of similarity between the samples in the very weakly doped surface regions to which XPS is sensitive.

5.3.2 XAS and RXES Measurements

The measurements of Fe 2*p* XAS spectra (as shown in Figure 5.2 (a,b)) show a significant difference between TiO_2:Fe (pellet) and TiO_2:Fe (film) samples. The Fe 2*p* TEY XAS of TiO_2:Fe (pellet) is nearly identical to Fe_2O_3 XAS with typical multiplet splitting.[133] This is in agreement with the aforementioned XPS data which also show that the overwhelming majority of Fe near the sample surface was in the 3+ oxidation state. Quite to the contrary, the more bulk sensitive TFY XAS shows significantly more pronounced FeO characteristics. This would suggest that in the pellet sample, $Fe^{2+} \rightarrow Ti^{4+}$ substitution occurs beneath the surface where oxidizing effects are less prominent, but when exposed to oxygen, the sample

soon after forms secondary phases.

On the other hand, the intensity of the first peak in the L_3 region of the TiO_2:Fe (film) (Figure 5.2 (b)) is increased due to contributions from Fe-metal atoms as can be seen clearly when compared with the Fe metal TEY spectrum. Note that the pure Fe metal would have suffered surface oxidation effects as well, and thus it will include some contributions from FeO and Fe_2O_3, that is, the signal with not be pure Fe metal on the surface. But the marked similarity between the TEY spectra of the thin film sample and the pure Fe metal is strong evidence of primarily Fe atom clustering in the the film. The gradual 'trailing off' of the L_2 and L_3 peaks in the TFY thin film spectrum is also indicative of the metallic clustering of atoms.

In Figure 5.2 (c, d), Fe $L_{2,3}$ RXES spectra for TiO_2:Fe (pellet) and TiO_2:Fe (film) are compared to reference samples. Note that the vertical lines in all spectra correspond to excitation energies a, b, and c as shown in the XAS spectra above. At excitation energy a (L_3 peak), the pellet sample is very much akin to that of the FeO reference sample, supporting the conclusions of the XAS data that it is indeed Fe^{2+} substitution below the sample surface.

The TiO_2 thin film RXES spectra in Figure 5.2 (d) nearly exactly reproduce the Fe metal spectra at all excitation energies. This is convincing evidence that Fe atoms aggregate, and along with the XPS and XAS data, it can be firmly concluded that in the thin film there is an overwhelming tendency for the Fe atoms to cluster together under the conditions of sample fabrication presented herein.

The relative I(L_2)/I(L_3) intensity ratio of the TiO_2:Fe (film) sample excited at the L_2 threshold (point c at 721.0 eV) is much smaller than that of the TiO_2:Fe (pellet) sample. This intensity ratio is similar to that of FeO/Fe_2O_3 and Fe metal (Figure 5.2). The I(L_2)/I(L_3) intensity ratio is usually related to the probability of non-radiative $L_2L_3M_{4,5}$ Coster-Kronig (C−K) transitions (in which an electron transitions from within the same shell, for example $2p \rightarrow 2s$), and also to the ratio of total photo absorption coefficients (μ_3/μ_2) for excitation energies at the L_2 and L_3 absorption threshold.[83] Since the ratio of total photon absorption coefficients depends only on the excitation energy, the I(L_2)/I(L_3) intensity ratio of RXES

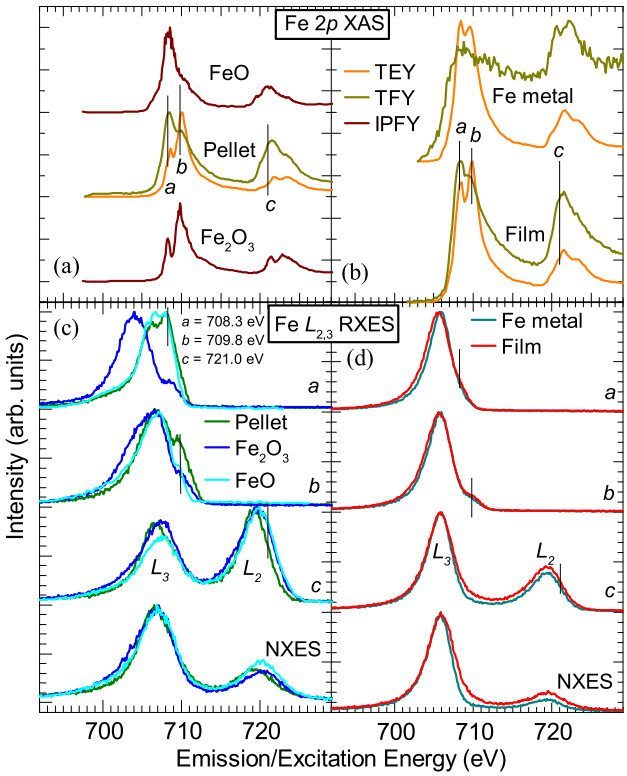

Figure 5.2: (Color online) Comparison of Fe 2p XAS and XES spectra for TiO_2:Fe (pellet), TiO_2:Fe (film), Fe_2O_3, and Fe-metal. (a) The pellet sample shows a clear similarity to Fe_2O_3 and FeO in the surface sensitive TEY and bulk sensitive TFY data, respectively. (b) The thin film doped samples shows clear characteristics of Fe metal, but note that both will have suffered surface oxidation effects, and will therefore show contribitions due to the formation of Fe^{2+} and Fe^{3+} in what should be pure metallic Fe. (c) $L_{2,3}$ RXES spectra of the pellet sample indicates that it is indeed $Fe^{2+} \rightarrow Ti^{4+}$ substitution that occurs beneath the surface layer. This is evident at excitation energy a wherein the pellet spectrum is nearly identical to the FeO spectrum, but quite different from that of Fe_2O_3. (d) Thin film RXES data is essentially identical to that of Fe metal, implying that Fe clustering also occurs beneath the surface layer.

spectra taken at the same excitation energy is determined by the C−K transitions alone, which are in turn governed by the number of free *d*-electrons around the target atom. The I(L_2)/I(L_3) ratio of Fe atoms in the mixed Fe^{3+} + Fe^0 state (as in the film) should be suppressed in comparison with Fe atoms in the Fe^{2+} + Fe^{3+} state (as in the pellet sample). Therefore, Fe L_2 RXES measurements confirm the existence of Fe^{3+} species in both pellet and thin film TiO_2:Fe samples. In addition to this, there is strong suppression of the I(L_2)/I(L_3)

ratio in the thin film sample due to the additional clustering of Fe-atoms (i.e. Fe^0 atoms have more free d-electrons and therefore a suppressed I(L_2)/I(L_3) ratio). Both RXES and XAS spectra indicate the clustering of Fe-atoms in TiO_2:Fe (film), which is in good agreement with the more surface sensitive XPS Fe 2p-measurements (Figure 5.1).

Figure 5.3 shows XAS and non-resonant XES oxygen K-edge spectra for both pellet and thin film Fe doped TiO_2 samples, pure TiO_2, and reference samples FeO and Fe_2O_3. Oxygen XES spectra vary between the samples due to the differing crystal structures, and the Fe-coordination level. The shift of the main peak in the XES data of the doped samples to lower energies can be attributed to Fe doping. This can be seen by looking at the main O peak in FeO and Fe_2O_3 and noting that they are noticeably lower than that of pure TiO_2.

The O K-edge TFY spectra of the pellet sample is nearly identical to that of the pure TiO_2 sample because, as noted earlier, the maximum depth of implantation of Fe ions was 45 nm, while TFY probes on the order of ∼150-200 nm. This means that fluorescence yield is largely obtained from the pure TiO_2, beneath the level of ion implantation (likely less than 25% of the signal is from the actual implantation region). Whereas the film TFY data show a significant suppression of the first two peaks in comparison with pure TiO_2. This is likely due to an oxide layer of SiO_2 forming at the substrate-film boundary, and it is this O K signal showing through the TiO_2. This is clear if one compares it to the onset of the O K-edge of SiO_2 in Ref. [134], in which there are no electronic states in the suppressed region.

The surface sensitive TEY data show clear shifts to lower energies of the onset of the O K-edge (similar to that of reference samples), again indicating the expected formation of secondary phases on the sample surfaces. This shifting to lower energies of the onset of the conduction band signifies that Fe doping decreases the band gap on the sample surface, in agreement with the XPS VB data of Figure 5.1. The onset of O K-edge XAS is very close to the true ground state conduction band, this is because the O 1s core hole only leads to a very minor perturbation on the energy of the unoccupied states.[135] This is in contrast to the Fe L-edge spectra (which would offer the most direct probe of the electronic structure in the vicinity of the dopants), because the Fe 2p core hole will considerably perturb the onset

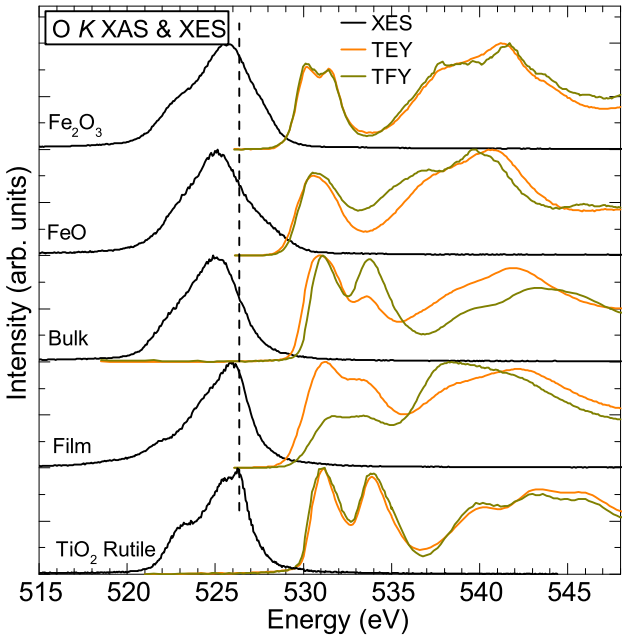

Figure 5.3: (Color online) O K XAS and XES. Doping of TiO_2 with Fe in pellet and thin film indicate that there are contributions from secondary phases due to oxidation on the surface of both samples. This is clear from the large suppression of the second main peak in the surface sensitive TEY data, in the same energy region in which FeO and Fe_2O_3 show a weak signal. TFY spectra largely probe beneath the implantation depth, and is therefore very much like pure TiO_2 in the pellet sample, and show evidence of the Si substrate in the thin film. XES data suggests that Fe doping shifts the main O peak to lower energies, as in FeO and Fe_2O_3 reference samples.

of the L-edge from the true ground state conduction band.

The TEY spectra of the doped samples also show a large suppression of the second main peak as compared to the pure TiO_2 sample. This is in the same energy range as the large dips in intensity of the reference samples, again indicating that secondary phases of Fe are prevalent in the surface region.

5.3.3 DFT Calculations

The x-ray spectroscopy measurements shown in the previous section indicates that Fe-doping in the pellet TiO_2 rutile sample induces Fe^{2+} substitution at Ti^{4+} sites beneath the surface layer; and that Fe^{3+} substitution occurs near the surface (note that both XAS in TEY mode

and XPS have a probe depth of only ∼5nm). Therefore, we have spectroscopic data to test the validity of our DFT structural optimizations and electronic structure calculations, these calculations can then be used to obtain a better understanding of the influence of Fe-doping in TiO_2.

The calculations of the formation energy for iron impurities in both anatase and rutile TiO_2 are shown in Table 5.1. As the criterion for the observed oxidation states, it is possible to map a given impurity to the observed phase of the implanted Fe atoms. A single substitutional (S) impurity (i.e. an Fe atom replacing a Ti atom) corresponds to FeO_2. This is a very unstable 4+ oxidation state for iron, and it is therefore not surprising that it is not observed in our experimental data, and not favoured in the calculations. Similarly, an $S + I$ (substitution and nearby interstitial Fe atom) corresponds to a 2+ oxidation state, due to the favourable formation of local Fe-O bonding in the form of Fe(S)O and Fe(I)O. And $2S + I$ can be regarded as the favourable formation of a combination of Fe_2O_3 (Fe^{3+}) and Fe_3O_4 (both Fe^{2+} and Fe^{3+}), in the form of 2Fe(S)Fe(I)O4. Note that this mapping provides a crude, but logical way of relating the DFT calculations to the observed valencies; and the actual formation of a given oxidation state or phase of iron will be a complex process depending upon many factors that we cannot explicitly account for. Nevertheless, the calculations provide valuable information in understanding the cause of the observed oxidation states.

The first thing to notice is the near identical formation energies of all defects on the surfaces of both samples. This is in agreement with our highly surface sensitive spectroscopic XPS and TEY data, both of which indicated a strong Fe^{3+} signal. But consider that the formation energies for $S + I$ and $2S + I$ on the surface of anatase are more closely spaced, and less in energy as compared to the rutile sample (0.62 eV and 0.92 eV compared to 0.68 eV and 1.01 eV, respectively). This is likely the cause of a largely metallic Fe signal on the surface of our anatase sample, as it could lead to the formation of several nearby $S + I$ and $2S + I$ defects. The formation of neighbouring $2S + I$ and $S + I$ impurities can generally be considered as the aggregation of Fe atoms, and it is this aggregation that is observed as a metallic signal in our data. The reason for this is because in anatase TiO_2

Sample	Dopant Location	S	$S+I$	$2S+I$
Anatase	Surface	1.58	0.62	0.92
	Bulk	2.09	1.59	0.67
Rutile	Surface	1.58	0.68	1.01
	Bulk	1.86	0.72	0.88

Table 5.1: The calculated formation energies (in eV) for 3d-impurity atoms for substitutional (S) impurities and their various combinations with interstitial (I) defects ($S+I$ and $2S+I$) in TiO_2 rutile and antase phases.

the distance between impurity atoms in cation (substitutional) sites and interstitial sites is ∼2.67 Å, and in pure Fe metal the atomic spacing is ∼2.47 Å. That is, the distance between substitutional and interstitial sites is comparable to the distance between metallic Fe atoms. We can therefore conclude that an arrangement of adjacent $S+I$ and $2S+I$ Fe-impurities can be related to the formation of iron clusters in TiO_2:Fe thin films, in agreement with the observations in XPS, XAS, and XES measurements. This is in contrast to the ion implantation in SiO_2 and ZnO thin film hosts, wherein substitution below the surface layer was energetically favourable and the clustering of metallic atoms was not observed (see our previous work regarding Pb and Sn in SiO_2 [136] and Fe in ZnO[137]). It was also calculated that 3+ substitutional iron impurities in TiO_2 have a magnetic moment of 3.21 μB for single impurities, and 3.28 μB for a pair of nearest neighbours.

DFT calculations for rutile show that $S+I$ (and therefore Fe^{2+}) impurities are the most favourable configuration (0.72 eV) below the surface region, this is in agreement with the spectroscopic data of the previous sections. On the other hand, it was calculated that $2S+I$ impurities come at only a slightly higher energy cost (0.88 eV), and thus we may expect to see an Fe^{3+} signal in our pellet sample (which we do not). To explain this we argue that the formation of Fe^{2+} substitutional impurities in the pellet sample can be justified in terms of the thin film versus pellet geometry, rather than the differences between rutile and anatase crystal phases. Our main motivation for this claim is that the polycrystalline thin film was synthesized with crystallites of ∼5 nm in size, while in the pellet sample the crystallites

were ∼200 nm. The surface to volume ratio scales as $1/r$, and therefore there is a large difference in effective surface to volume ratio inherent in the samples ($200/5 = 40$ times the effective surface area in the thin film). If we assume oxygen can only reach the surface or penetrate between crystallites, we can then conclude that there is a significant relative deficiency of oxygen in the pellet samples, and thus is highly conducive to the formation of Fe^{2+} as opposed to Fe^{3+}.

For conventional transition metal doped semiconductors, the observed configurations of impurities and their relation to the methods of samples fabrication (sol-gel, molecular beam epitaxy, etc.) can be explained by the kinetics of the material's formation.[125] But in our case, the insertion of impurities occurs *after* the fabrication of the samples, this is in contrast to previously used methods wherein impurities were introduced to the host during the fabrication process.[138, 139, 140, 141]

Differences between the configurations of impurities in pellet and thin film samples has previously been discussed in terms of different surface to volume ratios.[137] To examine the effect on the surface, we have calculated formation energies for $1S$ and $1S + 1I$ defects on the hydrogen passivated surface of TiO_2. The obtained energies for these two defects were +0.17 eV/Fe and -0.97 eV/Fe, respectively. We can therefore say that the formation of a $1S + 1I$ defect is more energetically favourable in the vicinity of the surface than in the bulk as compared to only substitution ($1S$). Therefore, ultimately we can explain different amounts of Fe clustering in pellet and thin films samples in terms of different surface to volume ratios.

5.4 Conclusion

To conclude, we have studied the formation of structural defects induced by Fe-ion implantation of TiO_2 pellet and thin films with XPS, XAS and RXES analytical techniques. The results were compared with DFT calculations of the formation energies for different configurations of structural defects. It was found that $Fe^{2+} \rightarrow Ti^{4+}$ heterovalent substitution takes place in pellet TiO_2:Fe samples below the surface layer, which is prone to oxidation effects

and thus Fe^{3+} is largely detected on the sample surface. In thin film TiO_2:Fe samples, in addition to Fe^{3+} on the surface, primarily the clustering of Fe-atoms was observed. This suggests that under Fe-ion implantation, the controlled and reproducible data can be obtained only for the pellet TiO_2:Fe material.

Acknowledgments

We gratefully acknowledge support from the Natural Sciences and Engineering Research Council of Canada (NSERC) and the Canada Research Chair program. This work was done with partial support of Ural Division of Russian Academy of Sciences (Project 12-I-2-2040), Ministry of Science and Education of Russian Federation (GK No.16.513.11.3007) and Russian Foundation for Basic Research (Project 13-08-00059).

CHAPTER

SIX

Background Information

Reproduced with permission from Journal of Physical Chemistry C 118, (48) 28143-28151. Copyright December 2014 American Chemical Society. It can be accessed online with doi:10.1021/jp509761c. My contributions to this manuscript were the following: I performed all XES and XAS experiments along with R. J. Green; I performed all crystal field calculations; I did the vast majority of the scientific analysis, especially concerning the spectra I took; I created all figures; and lastly I rewrote the manuscript from the initial draft provided by E. Z. Kurmaev.

Study of the structural characteristics of 3d metals Cr, Mn, Fe, Co, Ni, and Cu implanted in ZnO and TiO_2 – Experiment and Theory

B. Leedahl,[1] D. A. Zatsepin,[2,4] D. W. Boukhvalov,[3,7] E. Z. Kurmaev,[4] R. J. Green,[1] I. S. Zhidkov,[2] S. S. Kim,[5] N. V. Gavrilov,[6] S. O. Cholakh,[7] and A. Moewes[1]

[1] Department of Physics and Engineering Physics, University of Saskatchewan, 116 Science Place, Saskatoon, Saskatchewan, Canada, S7N 5E2

[2] Ural Federal University, 19 Mira Str., 620002 Yekaterinburg, Russia

[3] School of Computational Sciences, Korea Institute for Advanced Study (KIAS) Hoegiro 87, Dongdaemun-Gu, Seoul, 130-722, Korean Republic

[4] Institute of Metal Physics, Russian Academy of Sciences-Ural Division, 620990 Yekaterinburg, Russia

[5] School of Materials Science and Engineering, Inha University,Incheon 402-751, Republic of Korea

[6] Institute of Electrophysics, Russian Academy of Sciences-Ural Division, 620016 Yekaterinburg, Russia

[7] Department of Chemistry, Hanyang University, 17 Haengdang-dong, Seongdong-gu, Seoul 133-791, Republic of Korea

Abstract

Herein we systematically study a range of dopants (Cr, Mn, Fe, Co, Ni and Cu) in ZnO and TiO_2 using several x-ray spectroscopic techniques. We identify the dopant's local environment and interaction with the host lattice by employing crystal field multiplet calculations, and hence clarify their potential applicability for spintronic technologies. Our density functional theory (DFT) calculations predict a decreasing probability of direct cation (Zn/Ti) substitution by dopant atoms as atomic number increases; as well as a much greater likelihood of metallic clustering in TiO_2. Our spectroscopic measurements confirm that in all cases, except Mn, metallic clusters of dopant atoms form in the TiO_2 crystal lattice, thus making it unfit for spintronic capabilities. On the other hand, in ZnO, the dopants substitute directly into zinc sites, which is promising for spintronic tech-

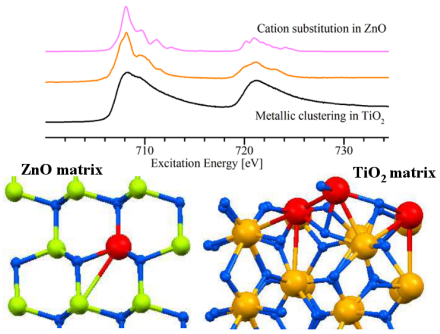

nologies.

6.1 Introduction

The paper of Dietl et al. [142] has stimulated great interest in dilute magnetic oxides (DMO). In these materials it is predicted that a ferromagnetic state with high Curie temperatures can be induced by doping them with magnetic impurities at levels below the percolation threshold for nearest neighbour cation interactions, this comes at the expense of the indirect exchange interaction of magnetic $3d$-ions mediated by carriers. Indeed, the first experimental studies of anatase TiO_2-based thin films doped with 7% Co show a fixed Curie temperature above 400 K,[143] this was the catalyst for an enormous amount of activity in the search for ferromagnetism in different DMO systems.[144] On the other hand, the metallic clustering of Co atoms was found in TiO_2:Co,[145] this led to an alternative explanation for the appearance of ferromagnetism in this system: direct Co-Co exchange interactions. It was soon recognized that the structural and magnetic properties of $3d$-doped oxide films are extremely sensitive to the sample preparation and thermal processing methods due to the formation of different structural defects. [146, 147] All available methods (ion implantation, pulsed laser deposition, reactive magnetron sputtering, etc.) produce imperfect films, which are far from the thermodynamic equilibrium. These materials are unstable against various heterogeneities,[148, 149] namely, precipitation of other crystallographic phases, phase separation in the host material, spinodal decomposition of dopant, inhomogeneities, diffusion, etc. In connection with this, the question, "Oxide diluted magnetic semiconductors – fact or fiction?" [144] is legitimate and reflects the current state of dilute magnetic oxide research.

In the present paper, the possibility of cation substitution and clustering of impurity atoms in $3d$-doped (Cr, Mn, Fe, Co, Ni and Cu) ZnO with a wurtzite structure and TiO_2 with an anatase structure are estimated using density functional theory (DFT) calculations of formation energies for different structural defects. The obtained results are then compared with spectroscopic measurements (XPS, XAS, and XES) of $3d$-ion implanted ZnO and TiO_2 thin films. Ultimately, crystal field multiplet calculations of these spectra are also performed

to give additional and complementary information regarding their electronic properties.

6.2 Experimental and Calculational Details

6.2.1 Sample Preparation

TiO_2 coating solutions were prepared by a sol-gel chemical method, wherein titanium isopropoxide (97%), nitric acid (60%), and anhydrous ethanol were used as the precursor, the catalyst, and the solvent, respectively. Deionized water was used for the hydrolysis of the precursor, and all of the chemicals were used as received without any further purification.

Using the prepared coating sols, TiO_2 films were deposited on Si wafers (100) by a dip-coating process,[118] and 1-butanol was added to the coating sols to control the wettability and the viscosity. The substrates were ultrasonically cleaned for 30 minutes in acetone and ethanol in sequence, and then washed with deionized water. The withdrawal rate of the substrate was 4 mm/s. Finally, the as-prepared films were dried at room temperature and kept in an oven at 60°C for 1 day to remove the remaining solvents completely, they were then annealed at 100°C for 2 hours. The obtained films were characterized by field emission scanning electron microscopy and atomic force microscopy to confirm high quality films were indeed produced.

To deposit the ZnO thin films, a sapphire substrate (100) was ultrasonically cleaned in acetone and alcohol for 10 minutes, then rinsed in deionized water, and finally dried in N_2. The sapphire substrates were held at a temperature of 250°C for 90 minutes during deposition, and the deposition was carried out at a working pressure of 2 Pa after pre-sputtering with Ar for 10 minutes. When the chamber pressure was stabilized, the radio frequency generator was set to 100 W. The growth rate of ZnO thin films was 3.4 nm/min and the typical thin film thickness was 302 nm. The polycrystalline ZnO samples had a hexagonal structure with lattice parameters a = 3.250 Å and c = 5.207 Å. Further details regarding sample preparation are available in the synthesis publication.[150]

6.2.2 Ion Implantation

The implantation of ions in ZnO and TiO_2 thin film samples was carried out in a vacuum chamber that was evacuated to a residual pressure of 3×10^{-3} Pa. An ion beam with an energy of 30 keV was used to irradiate the sample, this process caused the gas pressure in the chamber during irradiation to increase to 1.5×10^{-2} Pa. The implantation was carried out in a pulsed mode with a repetition rate of 25 Hz and the pulse duration of 0.4 ms with a pulse current density of 0.7 mA/cm^2. After 38 minutes of exposure the sample had an ion fluence (integrated flux over time) of 1×10^{17} cm^{-2}. After implantation, the samples were cooled in vacuum for 20 minutes. It should be noted that the initial temperature of the samples prior to irradiation was 20°C. For ion implantation we used Cr, Fe, Ni and Cu metals, and a $Mn_{0.5}Co_{0.5}$ alloy.

6.2.3 Spectroscopic Measurements

The x-ray absorption spectroscopy (XAS) measurements were taken at the Spherical Grating Monochromator (SGM) beamline at the Canadian Light Source.[151] At this beamline we are able to record XAS using several techniques: total fluorescence yield (TFY), partial fluorescence yield (PFY), inverse partial fluorescence yield (IPFY), and total electron yield (TEY). The goal of each technique is to measure the true absorption cross section, but in practice there are limitations of each, depending on the sample and edge of interest. TEY is very surface sensitive (a few atomic layers), and is thus included to show surface effects. IPFY is the most reliable measure of the true absorption due to the lack of saturation and self-absorption effects that plague fluorescence yield techniques.[60] Indeed some of our fluorescence yield spectra suffer from these effects, but it is not critical to our qualitative analysis. But, unfortunately IPFY can only be performed if there is an edge in the sample at a lower energy than the edge of interest, and even with this restraint the spectra may be too noisy to be used anyway. While IPFY is still the best choice we have for measuring absorption, it is only theoretically perfect if you have an infinitely thick, uniform sample. In our case, the implanted ions will have a nonuniform distribution peaking at a depth less

than that of the incident x-ray attenuation length. While this is not absolutely critical, it will lead to some distortions in the IPFY spectra as compared to the "true" absorption cross section. Herein the most appropriate absorption spectra are included in the figures and labelled as such, although *all* techniques were performed for all samples, many are redundant or unusable.

X-ray emission (XES) measurements were performed at Beamline 8.0.1 and the Advanced Light Source.[122] The incident x-rays were 30° to the sample surface normal, and the angle between the incident x-rays and the x-rays detected by the spectrometer was 90°.

XPS core-level and valence-band spectra measurements were made using a PHI XPS Versaprobe 5000 spectrometer which is based on the classic x-ray optic scheme with a hemispherical quartz monochromator and an energy analyzer working in the range of binding energies from 0 to 1500 eV. The energy resolution was $\Delta E \leq 0.5$ eV for the Al $K\alpha$ excitations (1486.6 eV) used herein. It is important to note that the probing depth of the XPS is ~5 Å due to the short mean free path of excited electrons, and it is thus quite surface sensitive, similar to that of TEY absorption measurements.

The spectra were processed using ULVAC-PHI MultiPak Software 9.3 and the residual background noise was removed using the Tougaard method.[120] All spectra were calibrated using the reference energy value of the carbon core-level energy (C $1s$) = 285.0 eV.[121]

6.2.4 Calculations

The density-functional theory (DFT) calculations were performed using the SIESTA pseudopotential code,[152, 153] as has previously been utilized with success for related studies of impurities in semiconductors.[125] All calculations were made using the Perdew-Burke-Ernzerhof variant of the generalized gradient approximation (GGA-PBE)[126] for the exchange-correlation potential. A full optimization of the atomic positions was done, during which the electronic ground state was consistently found using norm-conserving pseudopotentials for the cores and a double-ξ plus polarization basis of localized orbitals for the $3d$ dopants, Zn, Ti, and O. The forces and total energies were optimized with an accuracy of 0.04 eV/Å and 1.0 meV, respectively. For the atomic structure calculations, we employed

Zn and Ti pseudopotentials with $3d$ electrons treated as localized core states. The calculations of the formation energies (E_{form}) were performed by considering the supercell both with and without a given defect.[125] As a host for the studied defects, ZnO and TiO_2 supercells consisting of 96 and 108 atoms, respectively, were used. Taking into account our previous modelling of transition metal impurities in semiconductors,[125] we have calculated various combinations of structural defects including substitutional ($1S$) $3d$-impurities and their combinations with interstitial (I) impurities ($S + I$ and $2S + I$).

Tables 6.1 and 6.2 show the formation energies for the above defects. The first point that should be noted from the first column of Tables 6.1 and 6.2, is that the formation energy generally increases with atomic number. This tells us that there is roughly a decreasing probability of the formation of substitutional impurities in the Zn/Ti sites from Cr to Cu dopants. Another general feature of the TiO_2 anatase lattice is that there is a relatively large amount of "empty" space, this, as we will see, is at least in part responsible for the large amount of dopants residing in interstitial sites that we see in our TiO_2 data.

As a rough criterion, we can map a given defect to the formation of a specific oxidation state. For example, we may interpret a low formation energy for S defects as the criterion for the direct substitution of a Zn/Ti atom by the transition metal dopant. Then, the formation of $S+I$ defects in TiO_2 is used as the criterion for the formation of a metal oxide (MO) with the metal being in a 2+ oxidation state; the reason being that the formation of an $S + I$ defect can be considered as the replacement of a TiO_2 molecule with two dopant atoms (one substitutional and one interstitial), forming 2(MO). Similarly, in ZnO a favourable $S + I$ defect would be considered as the likely formation of a oxide in the form of M_2O. Finally, when $S+I$ and $2S+I$ configurations are similarly favourable, we can interpret this as the criterion for clustering, the reason for such a definition is related to the crystal structures of the pure transition metals and TiO_2. For all transition metal dopants used, the distance between atoms (M-M) is ∼2.5 Å in the pure metals,[154] whereas in TiO_2 with an anatase structure the distance between impurity atoms in cation sites and interstitial sites is ∼2.67 Å. That is, the distance between substitutional and interstitial sites is comparable to the metal-metal distance in the pure metal, and therefore the location of impurity atoms in many nearby

$S+I$ and $2S+I$ positions can indicate a large probability of metallic clustering.[155] This is far from an exhaustive list of defects (for example, there may be Zn/Ti or oxygen vacancies and several combinations with S and I defects) but for our purposes the DFT calculations herein prove to be sufficient.

The crystal field multiplet calculations in this work use the code produced by Cowan, Butler, and Thole.[156] The adjustable parameters include the crystal field strength and symmetry, and the scaling of the intra-atomic Coulomb and exchange (Slater) integrals, which can be thought of as scaling the intensity of intra-atomic electron interactions. The dipole transition matrix elements calculated by this code are then used in the Kramer-Heisenberg equation to simulate XES spectra. All spectra are then broadened by convolutions with a lorentzian function (to simulate lifetime broadening), and a gaussian function (to simulate experimental broadening) to match experimental conditions.

6.3 Results and Discussion

6.3.1 XPS Survey Measurements

The XPS spectra of pure and doped TiO_2 and ZnO are shown in Figs. 6.1 and 6.2, respectively. As can be seen, the host thin films consist of Ti and Zn $2p$, and O $1s$ lines without any uncontrolled impurities and a relatively low C $1s$ signal, the thin films are therefore of high quality. In the XPS spectra of doped films, the transition metal $2p$-lines appear, which indicates the successful integration of $3d$-ions into the target samples.

Of note regarding Figs. 6.3-6.8: the XPS spectra of reference samples are taken from the literature.[157, 158, 159, 129]. And all mention of ionic radii values are cited from reference textbooks.[154, 160] Vertical lines labelled in the XAS panels correspond to the excitation energies used in the respective figure's RXES panel, all reference samples are coloured black or grey while the samples of interest are not, and the calculations are always shown in pink.

	S	$S+I$	$2S+I$
TiO_2:Cr	+0.17	-2.85	-2.71
TiO_2:Mn	+1.88	+1.12	+2.26
TiO_2:Fe	+2.09	+1.59	+0.67
TiO_2:Co	+2.98	+1.41	+1.23
TiO_2:Ni	+4.75	+0.52	+0.63
TiO_2:Cu	+6.06	+2.33	+3.13

Table 6.1: The calculated formation energies (in eV) for 3d-impurity atoms for substitutional (S) impurities and their various combinations with interstitial (I) defects ($S+I$ and $2S+I$) in the bulk of TiO_2.

	S	$S+I$	$2S+I$
ZnO:Cr	-2.04	-0.97	-1.45
ZnO:Mn	-1.22	+0.22	+0.65
ZnO:Fe	+0.66	+1.92	+1.96
ZnO:Co	+0.03	+1.37	+1.22
ZnO:Ni	+0.91	+2.02	+1.63
ZnO:Cu	+2.11	+1.46	+2.17

Table 6.2: The calculated formation energies (in eV) for 3d-impurity atoms for substitutional (S and S surface) and various combinations ($S+I$ and $2S+I$) in the bulk of ZnO.

6.3.2 Chromium

We start with chromium as the dopant, shown in Figure 6.3 (a), the binding energies of both doped samples closely resemble that of Cr_2O_3 and *not* CrO_2. This theme of the dopants on the sample surface being found in their most stable oxidation state is a common one throughout this manuscript. Because, when exposed to atmosphere over time, the transition metal elements tend towards their most stable state, even when incorporated into the host lattice of TiO_2 or ZnO. This largely 3+ signal is suggestive of direct cation substitution occurring on the surface, that is, Zn^{2+}/Ti^{4+} cations are substituted by Cr^{3+} dopant atoms

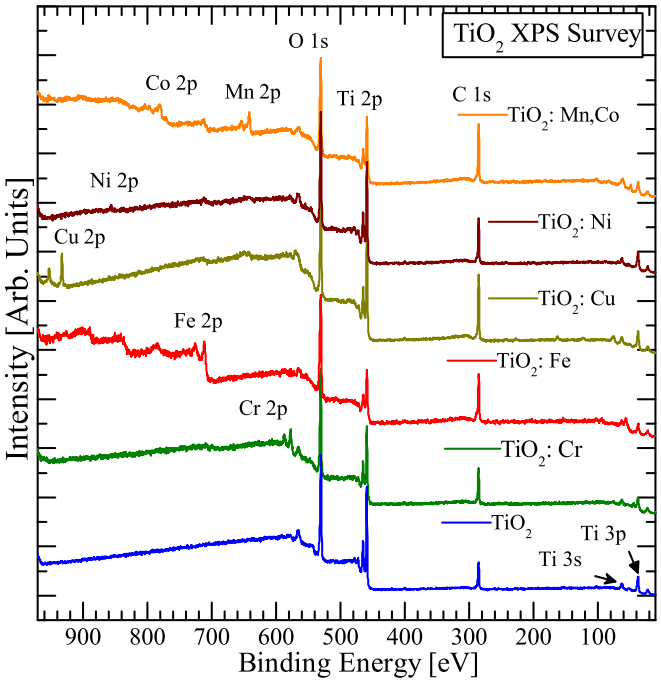

Figure 6.1: (Color online.) XPS survey of doped TiO_2 thin films shows relatively low carbon content and no evidence of uncrontrolled impurities. This, in addition to microscopy measurements ensure that the film are of high quality.

within the first few atomic layers. On the other hand, TiO_2:Cr $2p$ XPS spectra have additional low energy features which are energetically close to the main peaks of the pure metal, and therefore indicate an aggregation of dopant atoms near the surface, which we will see is more prevalent in the bulk of the TiO_2 sample.

The XAS spectra in panel (b) show an obvious similarity between Cr in ZnO and Cr_2O_3. But it should be anticipated that there will be differences due to the Cr in Cr_2O_3 being in a different environment than the Cr in ZnO. Panel (c) shows RXES spectra of doped and reference samples with the excitation energy indicated by the dashed line in the absorption spectra. The bulk sensitive x-ray emission shows the resemblance between ZnO:Cr and Cr_2O_3, supporting the XPS results of $Cr^{3+} \rightarrow Zn^{2+}$ substitution. However, multiplet calculations indicate that the Cr is in a slightly warped octahedral environment, with a crystal field splitting value of $10Dq = 1.6$ eV, $Ds = -0.1$ eV, and $Dt = -0.1$ eV, with the Slater integrals scaled to 70% of their Hartree-Fock values. This result is somewhat surprising, as we would

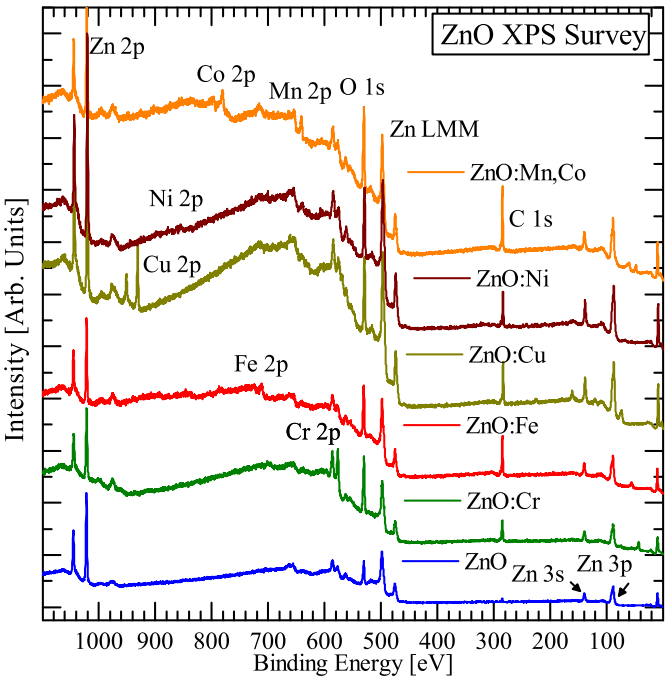

Figure 6.2: (Color online.) XPS survey of doped ZnO thin films shows relatively low carbon content and no evidence of uncrontrolled impurities. This, in addition to microscopy measurements ensure that the film are of high quality.

expect the Cr to substitute directly into Zn sites and therefore be in a 4-coordinated tetrahedral environment. Furthermore, compounds with Cr in a 3+ oxidation state while being 4-coordinated in a tetrahedral structure are *extremely* rare. Because of this, the presence of distorted octahedral sites is not totally unexpected here, and in fact is likely required in order to incorporate the Cr dopants. The DFT calculations in Table 6.2 are in agreement with what our spectroscopic data suggests as well, Cr substitution of Zn atoms is the most heavily favoured impurity as it has the lowest formation energy.

When the XAS and RXES spectra for TiO_2 are examined, they confirm what the XPS spectra proposed, unambiguously the clustering of Cr atoms in the bulk, as can be seen in the PFY and RXES spectral shape's similarity to the pure metal. This indicates that Cr^{3+} substitution is primarily a surface effect *or* the simpler, more likely result that it is pure Cr being exposed to atmosphere and oxidizing. The formation of metallic Cr in the bulk is also confirmed by DFT calculations. That is, the impurities $S + I$ and $2S + I$ have similarly

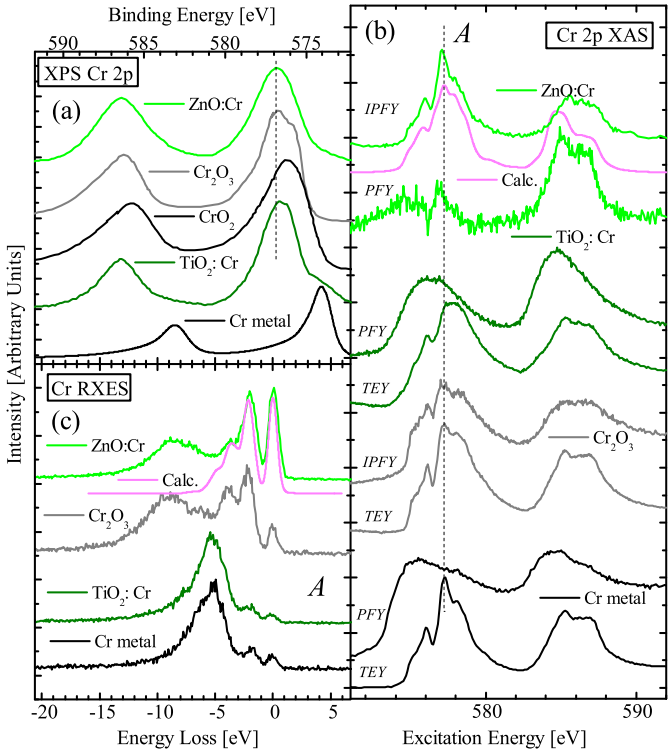

Figure 6.3: (Color online.) Cr dopant in TiO_2 and ZnO. (a) Cr dopant in TiO_2 shows primarily Cr^{3+} in surface sensitive XPS. (b) and (c) In the bulk sensitive XAS and RXES it is clear that the clustering of Cr atoms is the dominate process in TiO_2. To the contrary, in ZnO:Cr the data show that $Cr^{3+} \rightarrow Zn^{2+}$ substitution is the main process.

low formation energies (-2.85 and -2.71 eV), and therefore suggest that these will form in clusters, leading to the observed chromium atoms aggregated together (metallic Cr).

6.3.3 Iron

The XPS measurements for Fe are presented in Figure 6.4 (a). The data show similar results to Cr: both doped samples show primarily Fe^{3+} near the surface, as can be seen by their similarity in binding energy to Fe_2O_3. This is consistent with the oxidation tending towards iron's most stable valency when exposed to air. As was the case with Cr, the appearance of the metallic peaks in the TiO_2:Fe sample suggests some metallic clustering near the surface that has not been oxidized.

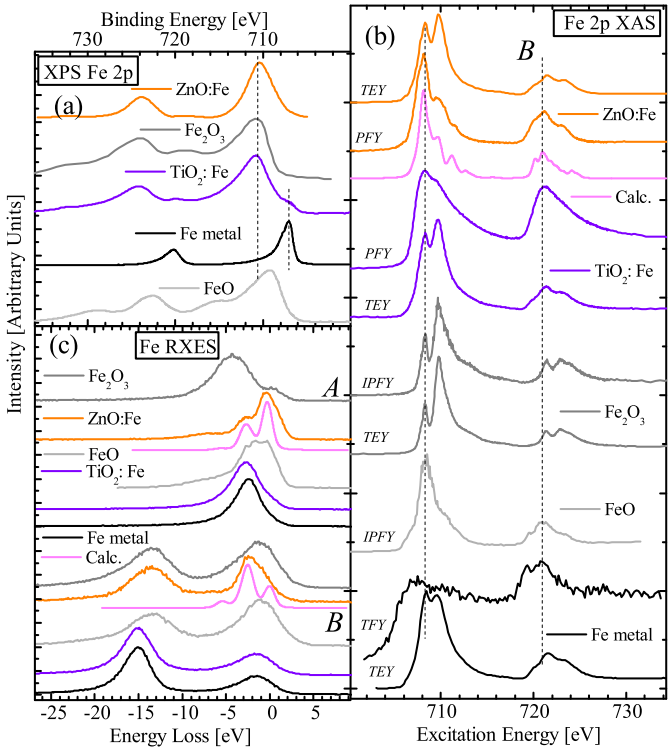

Figure 6.4: (Color online.) Fe dopant in TiO_2 and ZnO. (a) XPS spectra show primarily Fe^{3+} in the surface sensitive data, with some metallic Fe signal in TiO_2. (b) XAS for ZnO:Fe agree well with multiplet calculations for Fe^{2+} a strong indicator of direct $Fe^{2+} \rightarrow Zn^{2+}$ substitution. The TiO_2:Fe sample is clearly mainly metallic iron, with the surface (TEY) being oxidized as expected (showing a combination of Fe^{2+} and Fe^{3+}). (c) RXES taken at excitation energies shown in panel (b) confirm the results of XAS.

ZnO:Fe XAS L-edge measurements are compared with crystal field multiplet calculations for Fe^{2+} in Figure 6.4 (b). A crystal field splitting $10Dq$ value of -0.5 eV was used, and Slater integrals were scaled to 80% of their Hartree-Fock values, which is indicative of tetrahedral coordination. The large degree of agreement suggests that the existence of Fe^{3+} is a surface effect (also confirmed by the TEY) whereas Fe^{2+} substitution occurs in the bulk. XAS measurements for TiO_2 suggest that there is nearly entirely metallic iron in this doped sample beneath the first few nanometers. This conclusion is strongly supported in Figure 6.4 (c), where the L-edge RXES show a remarkable similarity to the Fe metal. The RXES multiplet calculations of panel (c) correctly reproduce the *dd* excitations in iron doped ZnO, with this additional evidence we can be confident that the iron substitutes Zn, and is tetrahedrally

coordinated. Note that charge transfer excitations and non-resonant fluorescence at energy losses of $\sim$ 15 eV in panel (c), excitation energy B and to a lesser degree A, are not explicitly accounted for by the crystal field calculations in this manuscript, and therefore we will not expect features to be reproduced by our calculations in these areas.

The DFT calculations in Tables 6.1 and 6.2 for Fe in TiO_2 show a large favouritism for $2S + I$ impurities, consistent with our rough criterion for the appearance of metallic iron in the bulk. The more interesting ZnO:Fe calculations agree exactly with our spectroscopic data in that Fe$\rightarrow$Zn substitution occurs, as it is the most energetically favourable, with respect to pure ZnO.

6.3.4 Manganese

The nearly identical binding energies of MnO and Mn_2O_3 of Figure 6.5, with both doped samples make it difficult to distinguish which is the more prevalent oxidation state on our sample's surfaces. But the higher energy satellite feature at $\sim$646 eV present in both doped samples, but only in the MnO reference sample is evidence of mainly Mn^{2+} in both doped samples. Along with the fact the TEY XAS is also very much akin to Mn^{2+} (from comparison with calculations), and that the most stable oxidation state for Mn is 2+, this result is rather expected.

We can confidently conclude that Mn^{2+} substitution occurs from the comparison of the XAS and RXES spectra with calculations shown in Figure 6.5 (b) and (c). For the calculations, a 2+ oxidation state, $10Dq$ value of -0.4 eV, and a Slater integral scaling of 70% were used for the ZnO sample; while for the TiO_2 sample the values used were $10Dq = +0.4$ eV and the Slater integrals were scaled to 66%. The relatively small absolute values of $10Dq$ tell us that the complexes, in both symmetries, are in their *high spin* state. Meaning that the crystal field splitting energy is less than the spin pairing energy. While the XAS calculations under different symmetries (positive versus negative values of $10Dq$) are actually very similar, the RXES spectra, particularly at excitation energy A, confirm that the differences are significant enough to produce distinct RXES spectra.

DFT calculations for manganese in TiO_2 imply that $S + I$ impurities are much more

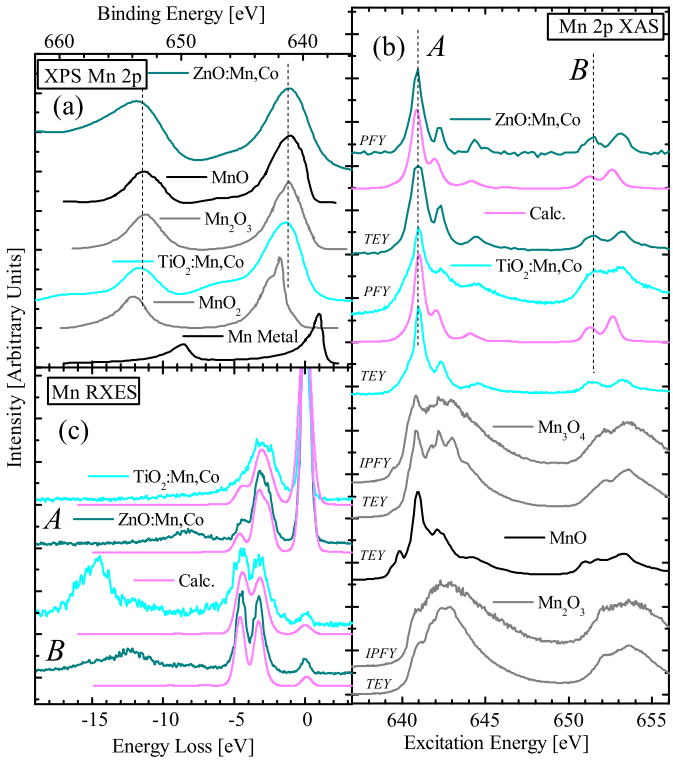

Figure 6.5: (Color online.) Mn dopant in TiO_2:Mn,Co and ZnO:Mn,Co. (a) the feature at ∼646 eV is the largest indicator of Mn^{2+} in both samples. (b) The XAS spectra agree well with multiplet calculations for Mn^{2+}, the calculation parameters are indicated in the main text. (c) Agreement between RXES experimental data and calculations also show that Mn^{2+} substitution occurs in both doped samples.

favourable than other defects. In this configuration we can say that the S impurity takes the place of a Ti atom and bonds with an oxygen atom, and the interstitial Mn atom bonds with the remaining nearby oxygen atom. We therefore expect this to produce largely 2+ Mn atoms, in agreement with our spectroscopic information. Additionally, a $10Dq$ value of 0.4 eV is relatively small for O_h bonding in the TiO_2 lattice. This is additional evidence of Mn in interstitial locations, as these atoms would reside in a more spacious location, and thus the crystal field strength is lessened. The broader nature of the TiO_2:Mn XAS and RXES as compared to ZnO:Mn could also support the view multiple Mn sites (substitutional and interstitial) in TiO_2. The formation energy for a simple substitutional impurity in ZnO is most favoured in our calculations, in accordance with the $Mn^{2+} \rightarrow Zn^{2+}$ conclusion of the previous paragraph.

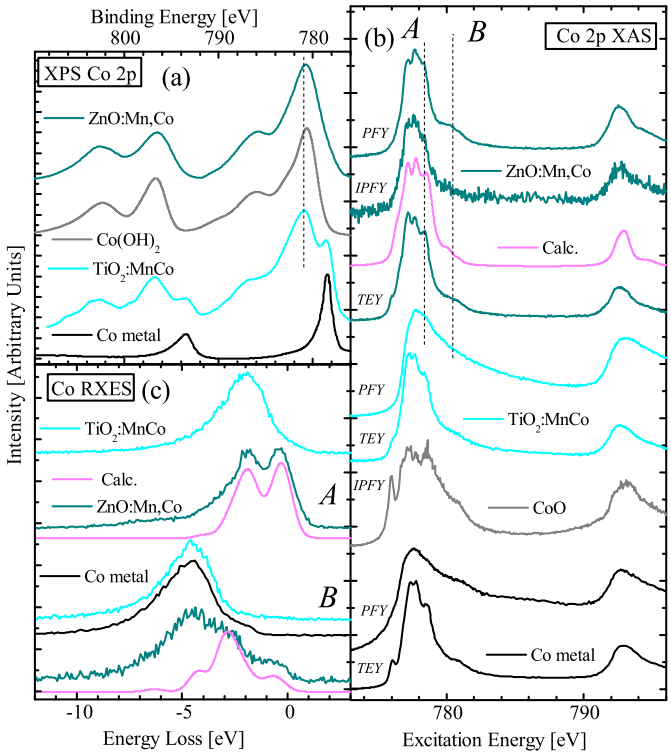

Figure 6.6: (Color online.) Co dopant in TiO_2 and ZnO. (a) XPS data show largely Co^{2+} on the sample's surfaces, with metallic clusters forming in TiO_2. (b) and (c) XAS and RXES experimental spectra agree well with multiplet calculations for Co^{2+} in the ZnO sample, indicating Co→Zn substitution is occurring. Co metal reference spectra closely resemble Co in TiO_2:Mn,Co, indicating that large amounts of metallic cobalt form below the surface.

6.3.5 Cobalt

The 2+ oxidation state of cobalt is easily its most common, and we therefore expect the results of Figure 6.6 (a), i.e. the binding energies of Co on the sample surface are nearly identical to that of $Co(OH)_2$. Although, as in the case of previously mentioned dopants, the Co 2*p*-spectra in TiO_2 display the signal of metallic Co atoms as well. The tendency of Co clustering in dilute magnetic oxides has already been observed in TiO_2:Co,[145] in this study it was found that the Co atoms prefer to be in a "close" geometry, and thus form metallic clusters.[161, 162] In contrast to this, Co in ZnO shows no sign of surface clustering and very closely resembles the Co^{2+} spectrum of $Co(OH)_2$.

The XAS and RXES support the conclusions above, except now in the bulk, the spectra in panels (b) and (c) were calculated with values of $10Dq = -0.45$ eV, $Ds = 0.0$ eV, $Dt = -0.10$, a 2+ oxidation state, and Slater integral scaling of 65%. Once again a large degree of agreement is seen, indicating that $Co^{2+} \rightarrow Zn^{2+}$ substitution is the primary process. While the negative $10Dq$ value would suggest a tetrahedral symmetry, the need for a small value of Dt can have a large impact on the actual d-orbital energies. We can therefore conclude that cobalt due to the ion implantation process significantly distorts the ZnO wurtzite lattice. The need for a nonzero Dt value stems from the distortion in the lattice due to damage in the ion implantation process, and the fact that Co atoms replacing Zn atoms have different ionic radii. The value for 4-coordinated Zn is 0.60 Å (as we would roughly expect in pristine ZnO), and 0.56 Å for 4-coordinated Co^{2+}. But as we have shown in our crystal field calculations, the cobalt is only *approximately* in a tetrahedral environment (and therefore only roughly 4-coordinated as well). The other main conclusion that can be extracted from our multiplet calculations is the relatively large scaling down of the Slater integrals to 65%, which is a means of artificially reducing intra-atomic electron-electron interactions normally taken into account by the more detailed charge transfer theory, which includes hybridization. This significant degree of hybridization of Co atoms with the surrounding oxygen ligands is supported in the RXES spectrum at excitation energy B. Here, a large proportion of charge transfer excitations are probed, and the fact that the multiplet calculations can only reproduce the *dd* excitations at low energy losses, indicates that charge transfer process are indeed important here. In the case of TiO_2 the results are mundane, the bulk sensitive XAS and RXES show that it is very metallic-like with no indication of multiplet splitting, therefore the Co atoms tend to form metallic clusters and this is the source of any observed magnetism.

The DFT calculations also support the above conclusions in that pure Co→Zn substitution is easily the most favoured defect in terms of formation energies, as expected. And $2S + I$ are most favourable in the TiO_2 sample, with $S + I$ slightly less desirable, which is again in line with our criterion for the formation of metallic clusters.

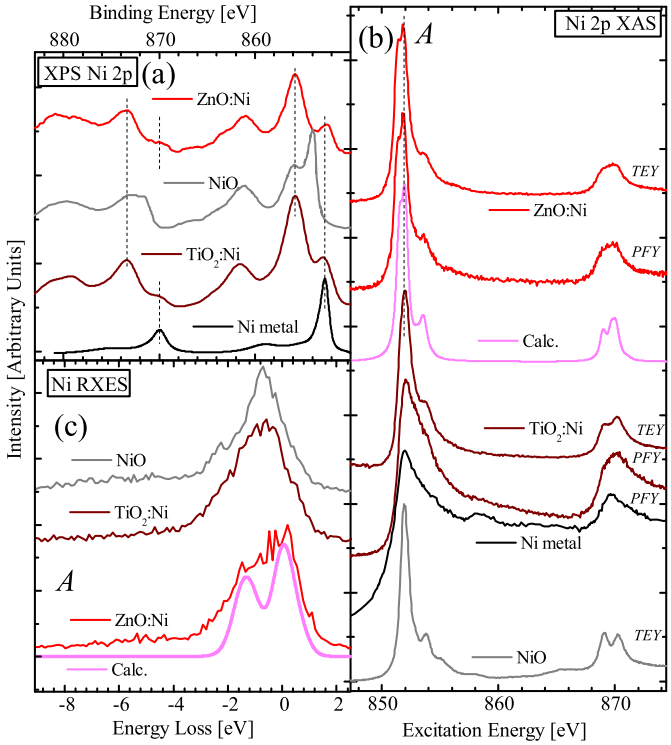

Figure 6.7: (Color online.) Ni dopant in TiO_2 and ZnO. (a) The binding energies in both doped samples mirror the features of both Ni in a 2+ state and Ni metal, indicating contributions from both. (b) XAS for ZnO:Ni is quite similar to NiO, suggesting Ni^{2+} atoms substitutes directly into Zn site; while in TiO_2 the Ni XAS spectra a much more similar to Ni in a metallic state. (c) Ni L_3 RXES spectra show a large sensitivity to local crystal environment. The shown calculation is for Ni atoms coordinated in a distorted tetrahedron.

6.3.6 Nickel

Spectroscopic data on Ni in ZnO and TiO_2, along with spectra of reference materials are presented in Figure 6.7. Ni, in general, strongly prefers to be in a 2+ oxidation state as seen here in the XPS. Just as in the previous TiO_2 doped samples, the XPS spectrum shows a clear metallic signal; but unlike previous ZnO samples, there is indeed the formation of some metallic Ni near the sample surface.

Panel (b) shows clearly that in the bulk of ZnO:Ni it is similar to that of the NiO reference sample, except that nickel atoms in NiO are octahedrally coordinated, so perfect agreement is not expected. The nickel dopant in ZnO was found to be approximately tetrahedrally

coordinated as confirmed by multiplet calculations (pink) with $10Dq = -0.40$ eV, $Ds = -0.10$, $Dt = 0.05$, and Slater integral scaling down to 65%. With these crystal field splitting value, the actual d orbital energies (relative to a spherical ligand field) are $3d_{x^2-y^2}$, $3d_{z^2}$, $3d_{xy}$, and $3d_{xz}/3d_{yz}$ = -2.65, -2.50, 1.35 and 1.9 eV, respectively. Thus, the t_{2g} orbitals are higher in energy than the e_g orbitals, just as is the case in perfect tetrahedral coordination (recall that pristine ZnO is *not* in exact tetrahedral geometry). Thus, it is $Ni^{2+} \rightarrow Zn^{2+}$ substitution that occurs in the bulk. TiO_2:Ni absorption is something of a mixture of between NiO and Ni metal, and therefore the source of any magnetism would be likely due to (undesirable) clusters of Ni forming somewhere in the TiO_2 host lattice.

Our DFT calculations confirm the trend observed in many of the previous samples: in TiO_2:Ni the formations energies of $S + I$ and $2S + I$ defects are similar and much lower than straight substitution. That is, we observe our criterion for the observation of a large amount of nickel atoms aggregating to produce the metallic signal present in our spectroscopic evidence. In the same vein, ZnO heavily prefers Ni→Zn substitution as indicated by its significantly lower formation energy (see Tables 7.1 and 7.1 for numerical values).

6.3.7 Copper

Copper is somewhat of a unique case as compared to the previously mentioned dopants due to its $3d^{10}$ state when it exists as a neutral atom and its 1+ oxidized state (due to the loss of a $4s$ electron). Because of this, multiplet calculations involving the $2p \rightarrow 3d$ transitions as previously done, are of no use here because most transitions will be $p \rightarrow s$. Additionally, for the 2+ state, we have a full $3d$ shell in the final state, and only two dd excitations appear within the crystal field model (neglecting charge transfer effects), therefore in the case of copper, multiplet calculations will be omitted.

The XPS spectra of Cu $2p$ spectra in ZnO and TiO_2 are displayed in Figure 6.8 (a). The unexpected result is that both doped samples clearly resemble the XPS spectrum of Cu_2O (which is generally easily oxidized to CuO), rather than the more stable form CuO on the surface. Note that the Cu $2p_{3/2}$ electrons in Cu metal have a binding energy of ∼932.7 eV with a narrow FWHM, and in this respect it is nearly identical to that of Cu_2O (932.5 eV).

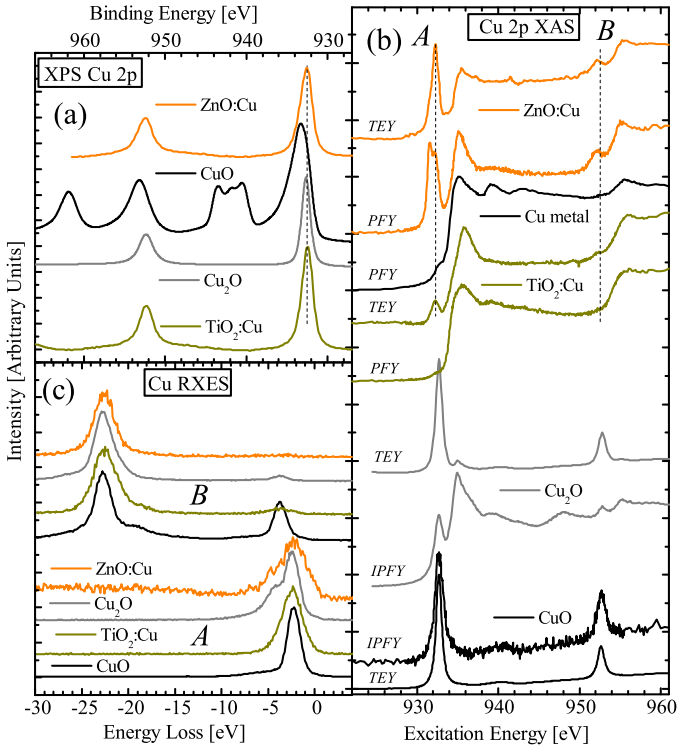

Figure 6.8: (Color online.) Cu dopant in TiO_2 and ZnO. (a) XPS for Cu_2O and Cu metal (not shown) are virtually identical, but the data herein would rule out the possibility of Cu^{2+} on the doped sample's surfaces. (b) XAS suggests primarily $Cu^{1+} \rightarrow Zn^{2+}$ substitution in the bulk of ZnO, with some Cu^{2+} contribution; while the Cu in TiO_2 looks very metallic. (c) XES results confirm the conclusions of XAS.

Because of this, one cannot distinguish between Cu^{1+} substitution or the metallic clustering of Cu atoms in the doped samples from the XPS alone. But in this case DFT calculations performed specially for the surface lend insight into cause of this. Surface defects for S, $S+I$, and $2S+I$ in ZnO have formation energies of 0.44, -2.46, and -0.92 eV; and in TiO_2 these values are 5.33, 2.14, and 2.99 eV. Thus, for ZnO $S+I$ is significantly more favourable and a Cu atom substitutes in a Zn site, while another resides interstitially nearby, and the two together bond the a single oxygen atom. In the case of TiO_2 it is not so straightforward, DFT calculations suggest that $S+I$ defects are slightly more favourable than $2S+I$, and therefore we may expect some combination of metallic Cu and Cu ions, this only becomes clear once our XAS and XES spectra are analyzed.

The absorption spectra of Figure 6.8 (b) confirm that in ZnO the copper dopant is

primarily in a 1+ oxidation state; the enhanced intensity at excitation energy A is due to small contributions from copper in a 2+ oxidation state, a result that was not detectible in our XPS measurements. DFT calculations in Table 6.2 support this claim in the bulk as well: $S + I$ (Cu^{1+}) defects are the most favourable, with substitutional defects coming at a higher energy cost. Moving on to TiO_2, we see that what was only suggested by DFT calculations is now clear, the surface copper dopant atoms are oxidized into a primarily 1+ state, but there is a small contribution from 2+ states as well, as seen in the pre-peak of the TEY. But the bulk data here are very similar to that of Cu metal, in agreement with DFT calculations showing that simple substitution is highly unfavourable, see Table 6.1 for numerical values. This lack of copper ion substitution can also be understood in terms of the large difference between ionic radii of 6-coordinated copper ions and titanium in the host lattice (0.77 and 0.73 Å for Cu^{1+} and Cu^{2+}, respectively, compared to 0.61 Å for Ti). This large mismatch would force significant unfavourable distortions to the TiO_2 crystal structure. On the other hand, these numbers for 4-coordination are 0.60 and 0.57 Å for Cu^{1+} and Cu^{2+}, respectively, compared to 0.60 Å for Zn, and so the same issue does not arise in ZnO.

6.3.8 Valence XPS

XPS measurements of the core levels of TiO_2 doped samples (Figs. 6.3-6.8) are confirmed by x-ray photoelectron spectroscopic measurements of the valence bands (XPS VB), which are displayed in Figures 6.9 and 6.10. The appearance of spectral contributions in the vicinity of the Fermi level for all dopants in TiO_2 can be attributed to the contributions from the clustering of $3d$-states of impurity atoms which are close to that of pure metals.[163, 164] In the case of TiO_2:Mn,Co, the noticeable spectral weight near the Fermi level is due to the clustering of Co atoms, and not Mn atoms. The XPS VB spectra for ZnO show that additional states near the Fermi level are added, but it this case it is due to non-metallic impurities, and clearly narrows the 3.3 eV band gap of pure ZnO as desired.

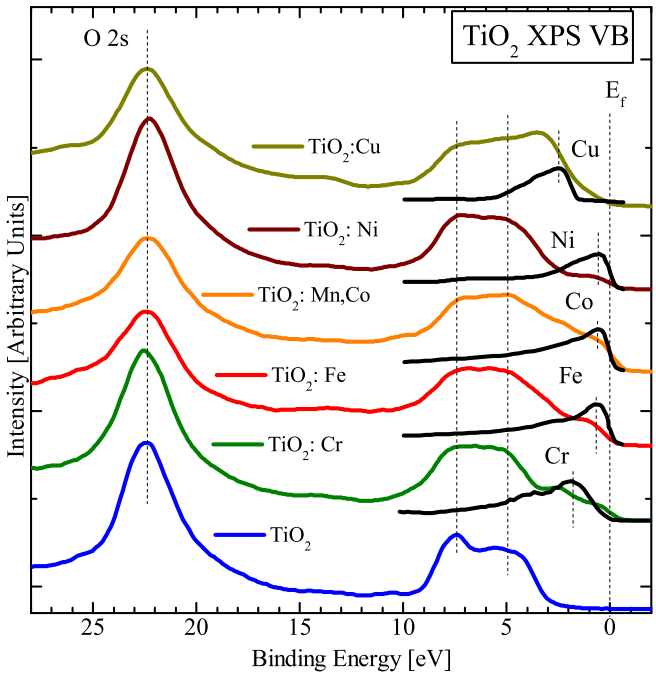

Figure 6.9: (Color online.) XPS valence band measurements show the appearance of spectral features near the Fermi level due to the metallic clustering of 3d impurity atoms. Spectra are offset for clarity.

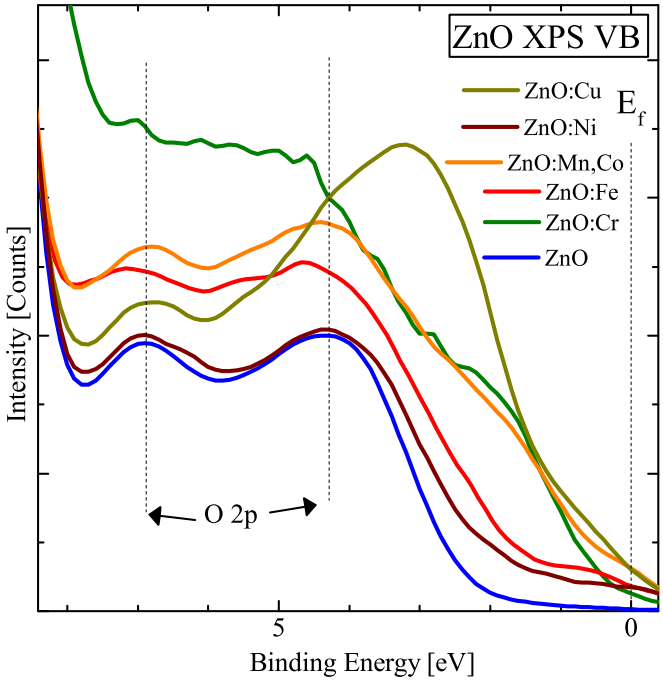

Figure 6.10: (Color online.) XPS valence band measurements of ZnO have spectral contributions near the Fermi level due to dopants in a non-*metallic state, but instead appear because of subtititional impurities. Spectra are shown with no offset, and are therefore representative of counts.*

6.4 Conclusion

In conclusion, we have performed a joint theoretical and experimental study of the local structure of $3d$-dopants in TiO_2(anatase) and ZnO. First-principles density functional theory calculations of formation energies for different configurations of structural defects show that the clustering of impurity atoms is more energetically favourable in TiO_2, while direct cation substitution is more favourable in ZnO. To experimentally confirm these theoretical findings we doped titanium dioxide and zinc oxide thin films with $3d$ transition metals by means of ion implantation, holding fixed both the preparation of the host of material and the parameters of ion implantation ($E = 30$ keV, D=1×10^{17} cm^{-2}).

Our XPS (core and valence), XAS, and RXES results are largely in agreement with DFT calculations of formation energies for structural defects, indicating that DFT calculations are reliable in predicting basic properties of such systems. In TiO_2, the results unambiguously show that in all cases except Mn, the dopant atoms preferred to reside in metal-like clusters. This is undesirable for technological applications as the source of any ferromagnetism would be due to such clusters, or nonexistent in the case of nonmagnetic metals. The promising result for technological applications is present in ZnO doped samples. Using the technique of ion implantation, ZnO thin films nicely incorporate the $3d$ dopants into its host lattice. Using more refined techniques with better control of implantations such as molecular beam epitaxy, one could undoubtedly fabricate reproducible samples which may be applicable for spintronic technologies.

Acknowledgements

We gratefully acknowledge support from the Natural Sciences and Engineering Research Council of Canada (NSERC) and the Canada Research Chair program. This work was done with partial support of Ural Division of Russian Academy of Sciences (Project 12-I-2-2040), Ministry of Science and Education of Russian Federation (GK No.16.513.11.3007) and Russian Foundation for Basic Research (Projects 13-08-00059).

CHAPTER

SEVEN

Background Information

This paper was published in RSC Advances in September 2016. It can be accessed online with doi 10.1039/C6RA16598B . The reference to it is: RSC Advances, 6, 858844-85851 (2016). For this publication I made the following contributions: I performed all x-ray spectroscopy experiments (minus XPS) and did all the corresponding calculations and analysis (including XPS); I undertook the analysis of the magnetic measurements provided by collaborators; I created or heavily revised all figures; lastly, I rewrote the manuscript from the initial draft provided by E. Z. Kurmaev.

Searching for pure iron in nature: the Chelyabinsk meteorite

B. Leedahl,[1] A. V Korolev[2] I. S. Zhidkov,[2,4] S. L. Skornyakov,[2,3] V. I. Anisimov,[2,3] A. S. Belozerov,[2,3] A. I. Kukharenko,[2,4] E. Z. Kurmaev,[2,4] V. I Grokhovskii,[4] S. O. Cholakh,[4] and A. Moewes[1]

[1] Department of Physics and Engineering Physics, University of Saskatchewan, 116 Science Place, Saskatoon, Saskatchewan, Canada, S7N 5E2

[2] M.N. Mikheev Institute of Metal Physics of Ural Branch of Russian Academy of Sciences, S. Kovalevskoi 18 str., 620990 Yekaterinburg, Russia [3] Ural Federal University, 19 Mira Str., 620002 Yekaterinburg, Russia

[4] Institute of Physics and Technology, Ural Federal University, Mira 9 str., 620002 Yekaterinburg, Russia

Abstract

Herein we aimed to use thermomagnetic analysis (TMA) to determine the nature of iron and nickel in the Chelyabinsk meteorite, and their effect on the meteorite's magnetism. Our magnetic measurements show that 3% of the meteorite is metallic and consists of two ferromagnetic phases with Curie temperatures of T_{C1} = 1049 K and T_{C2} = 800 K. Using an Fe-Ni phase diagram, we show that the lower of the two temperatures is due to an Fe-Ni alloy with 51% Ni, while the higher Curie temperature phase is due to a pure or nearly pure (Ni-free) iron phase, for which we can be certain the Ni content is less than 1%. X-ray absorption (XAS) measurements show there are two clearly distinct iron oxidation environments: metallic and 2+, with the 2+ regions differing significantly from the standard FeO phase. We also demonstrate that beneath the immediate surface, iron exists virtually entirely in a metallic state. We are then able to estimate the surface composition using XPS, for which we found that 10% of iron on the surface is still surprisingly unoxidized. Finally, our theoretical calculations show how the density of states for both Fe and Ni atoms is affected for different nickel concentrations.

7.1 Introduction

Pure (impurity-free) iron in nature has never been unambiguously found, and all forms of pure iron we have today are the result of manmade processes. Alloyed iron materials in nature have been the subject of many theories, from meteorite impact to chemical reaction between magma and carbonaceous sediments (decomposed plants turned to rock by heat and pressure

over time).[165] To date, very few measurements suggesting near Ni-free iron have been made. There are, however, many reports regarding the existence of metallic (alloyed) iron in meteorites, which are usually identified with measurements of magnetic susceptibility,[166, 167, 168] x-ray diffraction,[169] photoemission,[170] and Mössbauer spectroscopy.[171] The existence of metallic iron is always discussed in the context of Fe-Ni alloys, with the resistance to oxidation (rusting) being due to the nickel impurities (similar to stainless steel).

The existence of pure iron (without Ni impurities) in *any* type of meteorite has not been well established. Experimental methods such as XPS or Mössbauer spectroscopy are extremely difficult to use to detect pure iron because the charge of iron atoms, as well as the binding energies of core level electrons are nearly identical in pure Fe and Fe-Ni alloy.[172] The only way the distinction can be made between pure Fe-metal and Fe-Ni alloy is with temperature dependent measurements of magnetic susceptibility. That is, pure Fe and Fe-Ni alloys have different Curie temperatures—the temperature at which a material ceases to be ferromagnetic when heated. In the present paper such measurements are performed for the Chelyabinsk meteorite. Specifically, we include the more interesting higher temperatures related to the Curie temperature of pure iron not performed in previous studies. [173, 174]

The well known meteorite entered Earth's atmosphere on February 15th, 2013 after an intense impact event broke it off its parent body millions of years ago—an event that eventually led to a collision path with Earth.[175] Several buildings were damaged, and well over a thousand people were injured by the shockwave, the resulting broken glass, and the thousands of fragments strewn over the area.[176] The largest piece found was 540 kg, recovered from the bottom of Lake Chebarkul; in total, approximately 1000 kg of the meteorite were recovered.[177] It was classified as an LL ordinary chondrite.[178] This type of meteorite is distinguished from others primarily by the abundance of metal present ($\approx$2%), and the average chondrule diameter (0.6 mm); chondrules are small round masses of olivine or pyroxene.[179, 180]

7.2 Experimental Details

For our measurements we used an individual 7 g piece of the Chelyabinsk meteorite. The magnetism of the sample was measured from $T = 2$ to 1300 K with a slowly increasing temperature such that the entirety of the sample was at a uniform temperature. They were performed at the Institute of Metal Physics, Yekaterinburg using *Quantum Design's* MPMS-XL magnetic property measurement system. These measurements were performed last so the sample would not be chemically or magnetically altered for our other measurements.

X-ray photoelectron spectroscopy (XPS) core-level measurements were performed using a spectrometer based on a classic x-ray optic scheme with a hemispherical quartz monochromator and an energy analyzer working in the range of binding energies from 0 to 1400 eV. This apparatus uses electrostatic focusing and magnetic screening to achieve an energy resolution of $\Delta E \leq 0.5$ eV for Al $K\alpha$ radiation (1486.6 eV). The samples were introduced to vacuum (10^{-7} Pa) for 24 hours prior to measurement, and only samples whose surfaces were free from micro-impurities were measured and reported herein. The XPS spectra were recorded using Al $K\alpha$ x-ray emission photons with the spot size on the sample being 100 μm in diameter. An ion neutralizer was used to study the non-conducting samples, and typical signal to noise ratios were greater than 10000:3. Finally, the spectra were processed using ULVAC-PHI MultiPak Software and CasaXPS. The nature of XPS allows for a probing depth of only roughly 3-5 nm, due to the inelastic mean free path of excited electrons, and is thus a very surface sensitive technique.

The x-ray absorption spectroscopy (XAS) measurements were taken at the Resonant Elastic and Inelastic Scattering (REIXS) beamline at the Canadian Light Source. This beamline has an undulator source and the spectrometer uses Rowland circle geometry to disperse the outgoing photons on an energy dispersive microchannel plate detector at an angle of 90^o to the incoming photons. Similarly, the x-ray emission (XES) measurements were performed using Beamline 8.0.1 at the Advanced Light Source (ALS) at the Lawrence Berkeley National Laboratory with the same specifications as above.[122] However, Beamline 8.0.1 offers significantly more flux that allowed us to perform the lower yield XES measurements. The

main difference between beamlines is the spot size: REIXS's beam spot size is 60 $\times 10\mu$m, whereas at Beamline 8.0.1 the spot size is 100 $\times 1000\mu$m. This provides some context for the areas probed with each technique given that the metallic grain sizes on the meteorite are on the order of about 50 $\times 50\mu$m.[181] Linearly polarized light was used at both beamlines and the samples were held at ultra high vacuum of $\sim 10^{-8}$ Torr. All XES and XAS spectra were calibrated on the energy scale by measuring standard oxides with well-known calibrations and adjusting accordingly.

7.3 Magnetic Measurements

7.3.1 Thermomagnetic Analysis

Thermomagnetic analysis (TMA) is a technique that involves the heating of a sample under a magnetic field and observing the temperatures where the ferromagnetism declines rapidly; this decrease is an indication that the Curie temperature was reached.[182, 183, 184]

Fig. 7.1 shows these decreases in magnetization. The meteorite consists of three magnetic phases—signified by sudden decreases in magnetization as temperature increases. The initial drop at low temperatures is due to paramagnetic compounds in the meteorite, such as chromite, which is only ferromagnetic at very low temperatures, and is of little interest for our present purpose.[185]

The Curie temperatures T_C of the two significant drops at higher temperatures correspond to minima of dM/dT [186]. This derivative is shown in the inset in blue; the minima are at $T_{C1} = 800$ K and $T_{C2} = 1049$ K. The 800 K value corresponds to the Curie temperature of taenite—an Fe-Ni alloy with 51% Ni in this case—as shown by a blue dot in the phase diagram of Fe-Ni alloys (Fig. 7.2). The latter value is near the Curie temperature of metallic iron, but also close to the Curie temperature of kamacite (an Fe-Ni alloy with less than 10% Ni).

The phase diagram of Fig. 7.2 was reproduced using the most reliable possible information contained in the aggregate studies of Fe-Ni alloys in Refs. [187, 188, 189, 190]. Although it needs to be noted that all experimental data of Fe-Ni Curie temperatures are over 70 years

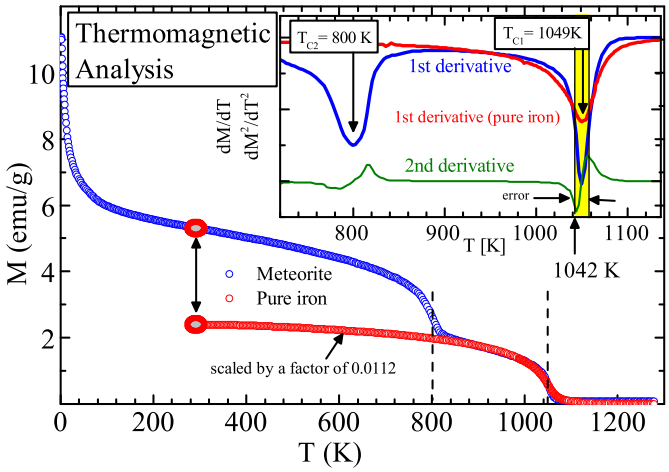

Figure 7.1: Temperature dependence of magnetization of the Chelyabinsk meteorite measured at H =10 kOe. Inset: $\frac{dM}{dT}$ dependence. The yellow block shows the error associated with the measurement, leading to a minimum Curie temperature of 1042 K for the higher of the two Curie temperatures, this temperature is very close to that of pure iron (1043 K). The error also corresponds to the yellow bar in Fig. 7.2.

old today, and the most often cited value of $T_C = 1043$ K [191] for pure iron may be slightly different than our modern measurements.

Indeed, as can be seen from the phase diagram (Fig. 7.2), the Curie temperature of kamacite converges to the Curie temperature of pure iron as the amount of Ni in the kamacite decreases (kamacite may exist at any Ni percentage below $\approx 35\%$). Our experimental value of 1049 K is *higher* than that of often cited pure iron at 1043 K. This may seem troublesome at first, but it can be readily explained as the result of our (and others dated) experiment, as will be discussed in detail in the following paragraph. To test for this we also performed TMA measurements on another extremely pure man-made iron sample (refined carbonyl iron; 99.93% iron). This pure iron magnetization curve is shown overlaid and scaled down by a factor of 0.0112 on the meteorite's curve. They are nearly identical matches, but the most convincing evidence is displayed in the inset. The first derivative minimum of the pure iron is < 0.5 K from the minimum of the meteorite. This is less than any experimental error, so for all intents and purposes they are essentially equal.

To quantify any error in our experiment we have chosen the steepest points in the first derivative (Fig. 7.1 inset), i.e. the maxima of the second derivative. This is where the

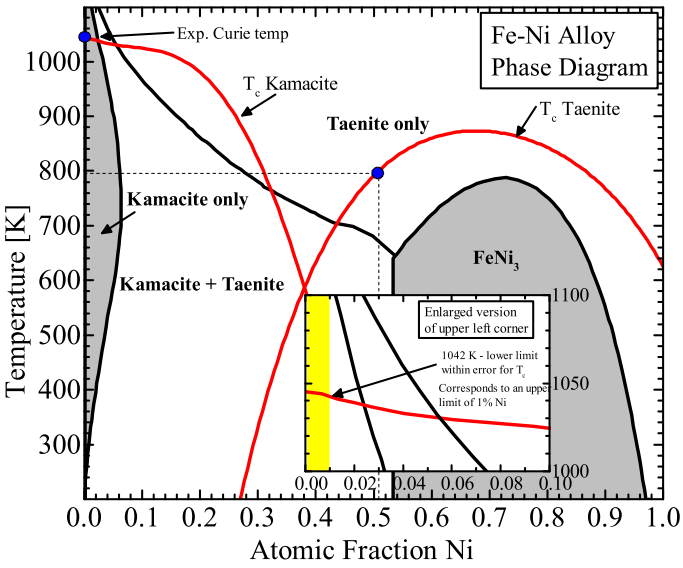

Figure 7.2: Fe-Ni alloy phase diagram. The black lines separate regions of various crystal structures as a function of temperate and Ni content. The red lines show the Curie temperates for the respective temperature and Ni content. The two blue dots correspond to the two phases of iron we find experimentally: the 49% Fe–51% Ni alloy, and the 100% ±1% Fe. Inset: an enlarged version of the very upper left corner to display the error associated with the TMA analysis of Fig. 7.1. Our experiment suggests 0% Ni, but could be as high as 1% including the error.

magnetization begins to drastically decrease, and is shown by the yellow background in the figure. From this analysis we can put the absolute lowest possible Curie temperature at 1042 K. The inset of Fig. 7.2 is an enlarged version of the upper left corner, shown for clarity, it also corresponds to this same error, but converted from Curie temperature to the corresponding Ni percentage. From this inset we can see that the worst possible case is that there may be up to 1% Ni. But of course, as noted by the analysis of Ref. [192], we would not expect the meteorite to have kamacite/iron at a single Ni-concentration, but rather some range in the inhomogeneous sample. Although our experiment is mostly in accordance with the authors of that study, they fail to make the connection to the extremely unique finding of pure, unalloyed iron in the meteorite. Therefore, while our measurements indicate that pure iron (no Ni impurities) is present, the associated error puts a cap on the Ni content at less than 1% in the host Fe metal in *some* regions within the sample.

To discuss this point further: because the meteor is a product of nature, and thus not uniform in composition, we expect it to contain a spectrum of Fe-Ni phases. That is, the 51% Ni phase (taenite) likely consists of several domains hovering around 51%. This is clear from the inset of Fig. 7.1, which does not show an immediate and extremely sharp drop in magnetization, but instead an initial slight decline followed by a drastic decrease. This is the natural shape of a curve indicative of a gaussian spread of inhomogeneities in the sample.[186] Remembering that TMA measures the entire bulk of the sample at once, this means that the meteorite contains regions of taenite between 48% and 54% Ni—corresponding to the temperature range in which the magnetization continues to drop. The temperature with the most significant drop in magnetization (800 K), corresponds to the greatest mass of Ni-content in the taenite regions. In other words, only observing the regions of taenite, the most common concentration of Ni-content is 51%, with regions of Ni concentration existing slightly below and above that value.

The exact same analysis can be performed observing only the more interesting low-Ni-kamacite to pure iron gradient regions of the sample. The magnetization drops between ≈1020 K and 1077 K (Fig. 7.1); this corresponds to a Ni-content between 0% and up to 12%, with the most common being 0% (the minimum of the first derivative). Although in this case, we add error bars using peaks in the second derivative to display the range in which the magnetization drops most drastically. This error was explained to be 1% in the preceding paragraphs. Therefore, our experiment tells us that there are indeed regions of very pure iron ($\ll$1% Ni) surrounded by *smaller* regions of alloyed Ni-Fe.

In addition to the above information, we can also determine the amount of iron by plotting the pure iron curve in Fig. 7.1 of $M(T)$ back to 300 K (red line). The value of M here is 2.4 emu/g. At the same time it is well known that the saturation magnetization value of iron at room temperature is 217 emu/g [193] (we use cgs units where 1 emu/g = 1 $\mathrm{Am}^2/\mathrm{kg}$); this is in accordance with our experiment as the curve in Fig. 7.1 is scaled by 0.0112. From these facts we can conclude that a good estimate for the amount of high Curie temperature very pure iron in the sample is 2.4/217 = 1.1% by mass.

The second ferromagnetic phase at 800 K contributes 2.9 emu/g at 300 K (the difference

between the red dots in Fig. 7.1). The magnetic saturation of an Fe-Ni alloy with roughly the nickel content we see here is ≈140 emu/g.[194] Therefore, the quantity of this second phase can be estimated at $2.9/140 = 2.1\%$ by mass. Hence, the total amount of metal $(1.1 + 2.1 = 3.2\%)$ is within the range of the classifying this meteorite as an LL chondrite.

7.3.2 Curie-Weiss Law

Fig. 7.3 examines of the Chelyabinsk meteorite with respect to the Curie-Weiss law. This describes the magnetic susceptibility of a ferromagnet in the paramagnetic regime above the Curie temperature according to the equation $1/\chi = (T-\Theta)/C$ (where C and Θ are the Curie and Weiss constants, respectively).[195] The linear nature of the law holds very well in the range $T > T_{C1}$. However, the Weiss constant Θ would normally equal the Curie temperature $\Theta \approx T_C$ in pure iron, whereas for the Chelyabinsk meteorite $\Theta = 49$ K $\ll T_{C1}$. This is due to the fact that the measurement probes the entire sample, which contains many other compounds. Thus, we can conclude that the measured susceptibility at high-temperatures is primarily due to other paramagnetic centers in the sample. This is supported by the sharp decline in magnetization at low temperatures in Fig 7.1.

We have found that the vast majority of the sample is paramagnetic with weak exchange interactions (although we cannot totally rule out a ferromagnetic component with a very small Curie temperature). In fact, we can estimate the effective magnetic moment per atom (in the paramagnetic regime) quite easily using $\mu_{eff}^2 = 8Cm$ (where m is the average atomic weight per magnetic atom in the material) [196]. If we assume all the ferromagnetism is due to iron and nickel atoms, then $m \approx 57$ amu and we obtain $\mu_{eff} = 2.19\mu_B$.

As was mentioned earlier, and shown in Fig 7.1, there is a sharp rise in magnetization when going to very low temperatures. For $T < 200\ K \ll T_C$ the magnetization of the ferromagnetic phases remains effectively unchanged, and the sharp increase of $M(T)$ is due to paramagnetic centers. We can then write $\chi = \chi_0 + C/T$, where $\chi_0 = (M_{S1} + M_{S2})/H + \chi_{add} =$ const. (χ_{add} is an additional susceptibility, either diamagnetic or paramagnetic). In this case, we should expect a linear dependence of $\chi \times T$. We observe this experimentally (Fig. 7.3); the χ_0 value (slope) is 5.3×10^{-4} cm^3/g, which is in quite good agreement with our previ-

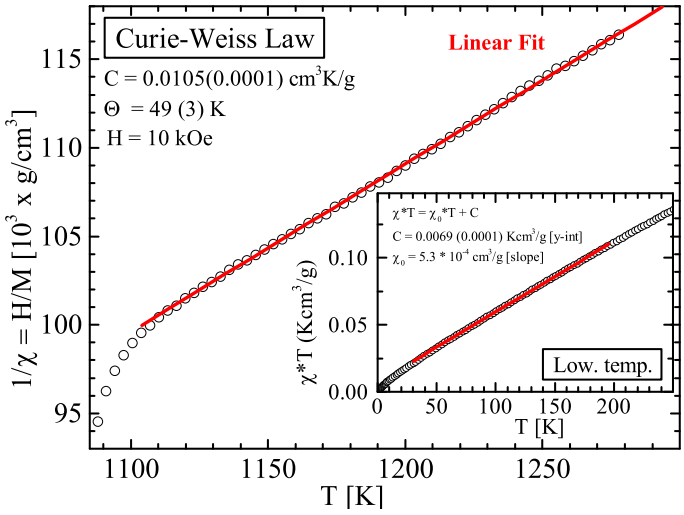

Figure 7.3: The reciprocal of the magnetic susceptibility with temperatures in the paramagnetic regime ($T > T_{C1}$). The linear nature of the law (see text) holds as it should for ferromagnetic materials. Our calculation of magnetic moment per atom from the Curie constant obtained here is $2.19\mu_B$. Inset: The low temperature dependence of $\chi \times T$. The slope χ_0 agrees with the overall magnetization of the sample at room temperature found in Fig. 7.1. The y-intercept value C leads us to the conclusions that the paramagnetic part of the meteorite is saturated with spin 1/2 magnetic centers.

ous experimental value of $M_{S1} + M_{S2} = 5.5$ emu/g (upper red dot in Fig. 7.1), equivalent to $(M_{S1} + M_{S2})/H = 5.5 * 10^{-4}$ cm^3/g. Using the value of the y-intercept from this plot, $C = 0.0069$ Kcm^3/g, we find that for paramagnetic centers $\mu_{eff} = \sqrt{8 * 0.0069 * m} \approx 1.77\mu_B$. This, combined with the fact that in the spin-only approximation $S = 1/2$ and $S = 1$ correspond to $\mu_{eff} = 1.73$ and $2.83\mu_B$, respectively, leads us to conclude that the paramagnetic component of the meteorite contains paramagnetic atoms, each with a magnitude of spin 1/2—that is, each atom contributes one free electron to the magnetic moment.

In summary, we have shown that the Chelyabinsk meteorite has essentially an identical Curie temperature with that of pure iron. Since the Curie temperature decreases as impurities are introduced, we can be certain that there are regions in the meteorite that contain iron phases with an extremely small amount of impurities (mainly nickel at $\ll$1%). This pure phase of iron has be determined to be 1.1% of the meteorite by mass. Such pure iron has never been found naturally occurring and this represents a significant discovery of a

relatively rarely occurring elemental form in our universe.

7.4 Spectroscopic Measurements

7.4.1 X-ray Emission Measurements

The chemical state of Fe-atoms can be determined with Fe $L_{2,3}$ x-ray emission measurements (XES)($3d \rightarrow 2p_{3/2,1/2}$ decay). The depth probed by XES measurements is about ten times deeper than what is probed by XPS measurements, which only probe the sample to a depth of about 20-30 Å due to the much smaller escape depth of electrons compared to that of photons. Since the beam spot size used here was quite large (100 μm x 1000 μm), we are probing all types of surface domains simultaneously.

Firstly, we look at the $I(L_2)/I(L_3)$ intensity ratio (see Fig. 7.4 and Table 7.1 for tabulated integrated intensity ratios). It is related to the probability of radiationless $L_2L_3M_{4,5}$ Coster–Kronig (C–K) transitions, and the ratio of total photoabsorption coefficients (μ_3/μ_2) for excitation energies at the L_2 and L_3 absorption thresholds.[83] Since the ratio of total photoabsorption coefficients depend only on the excitation energy, the $I(L_2)/I(L_3)$ intensity ratio of RXES spectra taken at the same excitation energy is determined by the C–K transitions alone, which are governed by the number of free d-electrons around a target atom. The $I(L_2)/I(L_3)$ ratio of Fe atoms in a conducting (metallic) state (Fe atoms only interact with other Fe atoms) is therefore highly suppressed. On the other hand, the Fe atoms in the insulating state (Fe–O interaction) show a much larger $I(L_2)/I(L_3)$ ratio (Fig. 7.4).

Based on these measurements it can be concluded that the $I(L_2)/I(L_3)$ ratio both in RXES and NXES spectra of Chelyabinsk meteorite are quite similar to those of metallic iron, but very different from the Fe-oxides. This indicates that metallic iron exists in significant proportions beneath the first several atomic layers, and Fe-oxides are in such low concentrations that we cannot even detect them. That is, we expect the phases of taenite and kamacite-pure iron to exist throughout the entire bulk of the meteorite, with extremely low amount of oxidized iron.

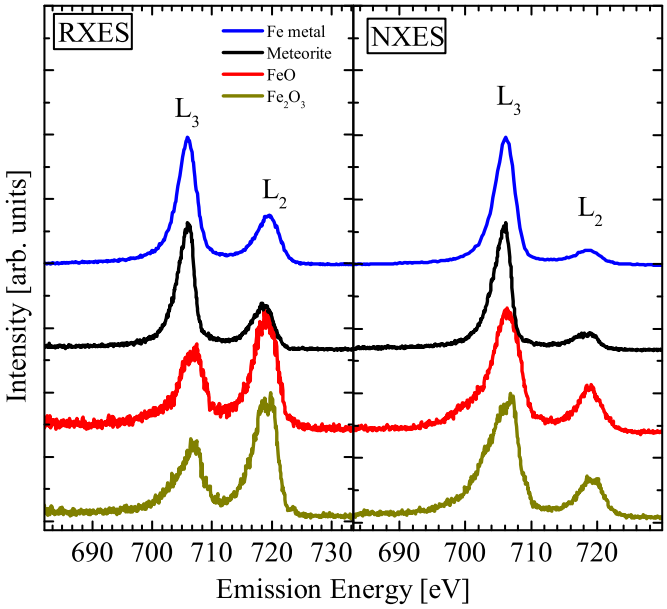

Figure 7.4: Fe $L_{2,3}$ x-ray emission spectra of Chelyabinsk meteorite and reference compounds excited at the L_2-threshold (RXES) and far above the absorption edge (NXES). The ratio of peak heights in the meteorite sample are nearly identical with that of Fe metal. The large beam spot size and bulk sensitivity of this technique, along with the shape of the spectra, demonstrates clearly that beneath the first several atomic layers, the iron is unoxidized in a metallic state.

	RXES	NXES
Fe-metal	0.45	0.17
Meteorite	0.41	0.18
FeO	1.16	0.30
Fe_2O_3	1.39	0.27

Table 7.1: Integrated $I(L_2)/I(L_3)$ ratios for the XES spectra shown in Fig. 7.4. The smaller ratio in metallic iron compared to the Fe-oxides is indicative of a more conducting Fe state (see text for further discussion of this phenomenom). Our meteorite sample also displays this high degree of conductivity, and therefore is largely found in a metallic state as well.

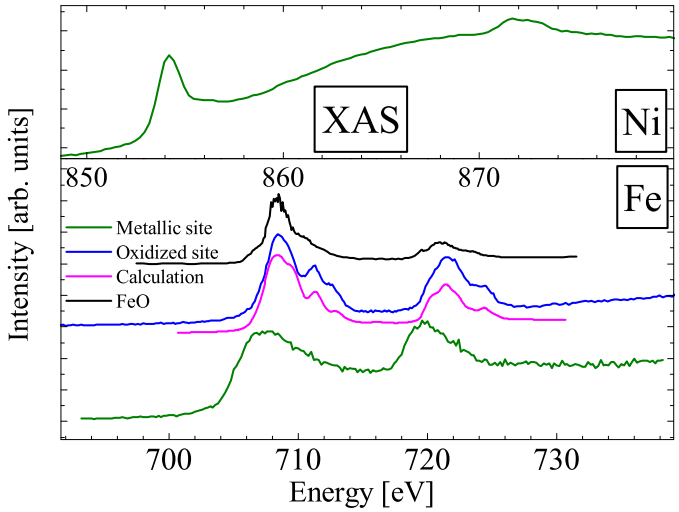

Figure 7.5: Fe and Ni XAS. Two primary signals of Fe were found at different locations: metallic and 2+ sites. Upper panel: Ni was measured at the metallic sites and a small signal on the surface was found, likely due to taenite. The calculation-experimental agreement establishes that the 2+ Fe atoms are not in the standard FeO crystal environment as one might expect. Instead it is in a deformed octahedral envronment, likely due to the many surrounding defects and magnetic interactions.

7.4.2 X-ray Absorption Measurements

Proceeding to x-ray absorption (XAS) measurements, which is a complementary technique to x-ray emission. It supplies us with similar oxidation and chemical information at the same probing depth (when measuring fluorescence yield). Although in this case our beam spot size was at least two orders of magnitude smaller by area (60 $\times 10\mu$m), so we could obtain information from individual domains in the meteorite by moving the beam location around. We found two different environments in which iron atoms were located: metallic and a 2+ oxidation state, with metallic sites being at least ten times less common than oxidized sites, as expected. However, upon probing dozens of sites, a small but detectable nickel signal was always found in the surface sensitive electron yield. It was not observable in the fluorescence yield because the nickel is extremely dilute, and fluorescence yield is roughly two orders of magnitude weaker than electron yield. Even though every metallic iron domain would be impossible to measure given time restraints, this tells us that in the given measured metallic domain there is indeed a small amount of nickel present in the metallic iron, as we would

expect from the taenite regions, which are very spatially near the kamacite regions.[181]

Included in Fig. 7.5 is a crystal field multiplet calculation in agreement with the observed 2+ regions.[45] Interestingly, the experimental spectrum does not appear nearly identical to FeO, which we would expect, although it is clearly in a 2+ state. FeO has its iron atoms nearly perfectly octahedrally coordinated by oxygen atoms, but in order to achieve agreement with calculations, a warped octahedral environment needed to be used. Crystal field parameters used in the calculation were $Dq = 0.08$ eV, $Ds = 0.04$ eV, and $Dt = -0.04$ eV. These values correspond to a stretching of the surrounding octahedral crystal field along one of its axes. This stretching is significant, up to about 20% longer bond lengths along the stretched axis. Although it is still most likely bonded to oxygen atoms, this large distortion of standard FeO is likely a result of the inhomogeneous surroundings and the magnetism inherent to the sample. This new phase of FeO is something unique to this meteorite, such distorted lattices are not seen in iron oxides on Earth.

7.4.3 XPS Measurements

X-ray photoemission measurements probe the binding energies of the elements on the surface (first few nanometers) of a material. This technique is mainly sensitive to the oxidation state of an element. The XPS survey spectrum of the Chelyabinsk meteorite was measured for binding energies in the range of 0-1400 eV (Fig. 7.6 (a)). Clearly present are Mg $1s$, C KLL, O KLL, Fe LMM, Fe $2s$, Fe $2p$, O $1s$, Mg KLL, C $1s$, Si $2s$, and Si $2p$ lines. Where the notation KLL corresponds to the Auger process wherein a $1s$ electron (K) is excited, followed by a $2s$ electron (L_1) decaying to fill the $1s$ hole, with the $2s \rightarrow 1s$ transition energy being imparted to the emission of a $2p$ electron ($L_{2,3}$).

In accordance with these data the surface composition was estimated by multiple authors using both Multipak and CasaXPS software, and the results were very similar, but were averaged, and are shown in the Table 7.2. The carbon signal in the XPS data is completely or nearly completely due to the sample's interaction with Earth, in which carbon is effectively everywhere, and very "sticky", so was not included in the surface composition analysis. Also, chamber the experiment was performed in uses argon as a purging mechanism, and was also

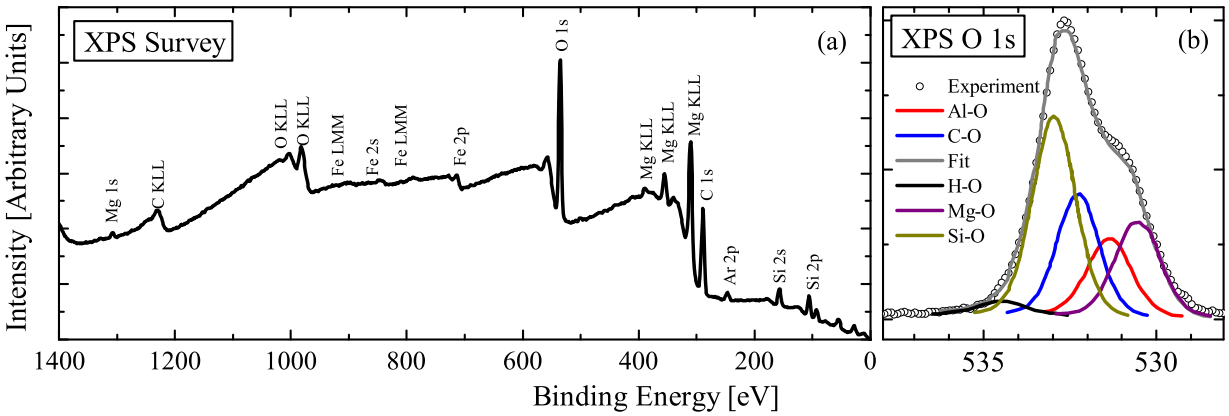

Figure 7.6: (a) XPS survey spectrum showing all the major elements present (b) Oxygen 1s XPS spectrum and component analysis. The areas under the curves represent the relative contributions from each of the elements bonded to oxygen.

not included in the analysis.

The beam spot size used here was 100 μm in diameter, which is relatively large in terms of the grain sizes. Therefore, this gives a reliable composition of the surface of the meteorite as a whole, in agreement with the analysis of Ref. [181]. It is not too dissimilar from the analysis of Ref. [197], but therein a much smaller area was measured ($\approx$7 μm $\times$ 7 μm). Notably, the XPS survey spectrum does not find the presence of nickel. Although, at sufficiently low concentrations (less than 0.1%) this technique is not sensitive enough to detect minute amounts of the metal.[198] So while very small amounts cannot be completely ruled out, it corroborates the magnetic findings above. Note that the carbon contamination is large, and not part of the native composition of the meteorite (anything in contact with the Earth's crust will have lots of carbon on the surface). Nevertheless, the atomic *ratios* of the elements in Table 7.2 (not including carbon) are quite reliable.

The O 1*s* XPS spectrum of Fig. 7.6 has a two peak structure due to the multiple bonding environments of oxygen. The large peak is due to C-O and Si-O bonding, whereas the low energy shoulder is the result of Mg-O and Al-O, and there is a small contribution from H-O bonding at the high energy side. The fit was performed by constraining the binding energy differences of the Mg-O, Al-O, and Si-O to their well-known values in MgO, Al_2O_3, and

Element	O	Si	Mg	Al	Fe	Ni
Atomic %	65.0	17.7	10.3	4.3	2.7	0.0
Error	± 1.6	± 1.5	± 2.1	± 0.2	± 0.6	± 0.1

Table 7.2: Surface composition of Chelyabinsk meteorite determined by XPS survey analysis. Note: carbon and argon signals were not included in the analysis as they are artifacts on the sample surface due to its interaction with Earth's environment.

SiO_2. Their FWHMs were only allowed to vary a small amount from the values known for the binary oxides as well. The contributions from each of the oxygen bonding environments can be seen by the quality of the obtained fit, with the area under each curve representative of the quantity of that bonding environment.

Moving on to detailed Fe 2*p* XPS measurements (Fig. 7.7), we find contributions from Fe-metal, FeO, and Fe_2O_3, with typical charge-transfer satellites ($S1$ and $S2$.[129] The presence of an Fe-metal contribution confirms that some of the iron on the surface has not oxidized after being exposed to ambient atmospheric conditions for over a year. A similar effect was found forty years ago in the XPS measurements of Fe 2*p* spectra of lunar iron.[199]

Using linear combinations of the Fe-metal, FeO, and Fe_2O_3 an approximation of the percentage of each oxidation state on the surface can be made. This best fit linear sum is shown as the black line in Fig. 7.7. It is in good agreement with the maximum entropy treated spectrum (pink) of the meteorite. Thus, on the surface, looking at only the iron, a good estimate is that 10% exists in metallic form, 71% in 2+, and 19% in 3+. The 10% in metallic form is likely mostly taenite, as it is highly alloyed with nickel to resist oxidation. Therefore, the pure (or very near pure) Fe iron that contributes to the high Curie temperature phase is likely buried in the interior of the meteorite in order to resist oxidation. Much of the detected Fe^{3+} is also likely the result of Fe^{2+} oxidizing in our atmosphere. In fact, it is quite surprising that the sample is so rust resistant considering it has been exposed to so much moisture, and relatively harsh conditions since landing on Earth's surface. The exact source of this surface resistance to rusting is something that should be investigated further as rust is the source of degradation of many iron-based products we use every day.

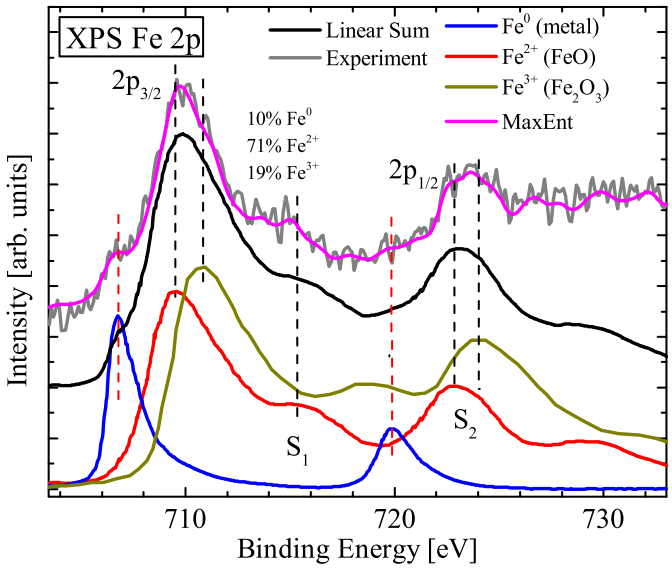

Figure 7.7: Comparison of XPS Fe 2p spectra of Chelyabinsk meteorite (grey = experiment, pink = maximum entropy deconvolution [102]) with spectra of Fe [200] metal, FeO and Fe2O3 [129]. The black line is a linear sum of the three components. The fit with the experimental data suggests that of the iron on the surface, 10% is metallic, 71% is in a 2+ oxidation state, and 19% in 3+.

7.5 Ab-initio Theoretical Analysis

To complete the physical interpretation of our experimental data we complement our magnetic and spectroscopic results with theory. To investigate the effect of Ni on the magnetic properties of Fe_xNi_{1-x} alloy we computed a concentration dependence of the magnetic susceptibility within CPA+DMFT (coherent potential approximation in combination with dynamical mean-field theory)[201]. The susceptibility was calculated as a response to a small external magnetic field. We first assumed that the metallic domain of the meteorite is a solid solution of iron and nickel, and thus should be treated as an alloy. CPA+DMFT accounts for the disorder of atoms and the strong Coulomb interaction between electrons in partially filled shells of Fe and Ni. More details on the methods of dynamic and static mean field theories can be found in Refs. [202, 203].

Herein we consider two characteristic values of Fe concentration (by atomic %) in the alloy: 75% and 95% Fe. Shown in Fig. 7.8 is the comparison of $3d$ spectral functions of pure

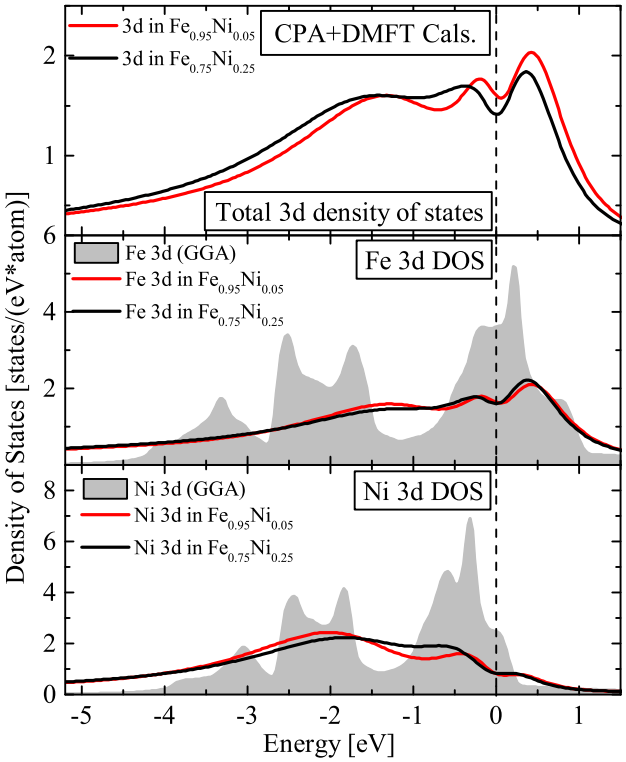

Figure 7.8: (Upper panel): The total 3*d and element-resolved* 3*d (lower and middle panels) spectral functions of* Fe_xNi_{1-x} *(*$x = 0.95, 0.75$*) as obtained in CPA+DMFT, shown by black and red lines (normalized in units of [states/eV*atom]). The GGA results of elemental Fe and Ni are presented as shaded areas. Alloying iron and nickel causes small changes and shifts to the density of states, which could be measured by high resolution XPS.*

metallic Fe and Ni obtained by the standard band technique (GGA – generalized gradient approximation) and those of Fe_xNi_{1-x} computed within CPA+DMFT. According to GGA (Fig. 7.8, shaded regions) the $3d$ spectral functions of Ni and Fe are qualitatively similar in shape and form a common band with a total width of 4 eV for Ni, and 5 eV for Fe.

For the alloys, disorder and correlations smear the fine details of the GGA spectral functions and shift some of their features. In particular, for both Fe and Ni, in both alloy concentrations, the GGA multi-peak structure in the energy window [-4,-1] eV turns into one broad feature in which intensity decreases with increasing Ni content. In the case of Ni (lower panel) the inclusion of disorder and correlation effects severely dampens the features in the [-1, +1] eV range. In contrast, the same region of the Fe spectral function is less sensitive to

disorder and correlations and to a greater degree preserves the form obtained within GGA. The overall form of the total $3d$ spectral functions in the alloy (Fig. 7.8, upper panel) shows a mild concentration dependence, and the position of its features is very similar to those of Fe in the middle panel. Because of the similarity of the curves in the upper panel, we would expect only a very small shift in XPS peaks between quite large differences (5% and 25%) of nickel content. This change has been observed, but it is subtle, and high resolution along with great care in calibrating between spectra would be required.[172, 204] In cases such as the Chelyabinsk meteorite, where the Ni content is minimal, the task becomes even more challenging.

7.6 Conclusion

Whether or not unalloyed iron exists in nature is a crucial question regarding the composition of extra-terrestrial objects. It has been scarcely considered as something to search for despite being one of the most important elements in our daily lives, especially since refining techniques have been developed to manufacture nearly pure iron from iron ores. Notwithstanding, the search for pure iron in our celestial objects could help answer basic questions regarding the formation and relative composition of such rocky objects in our solar system, as well as direct experimental evidence resulting from large objects colliding at extreme speeds in vacuum—a relatively frequent event in space that cannot be reproduced on Earth. Herein we have shown that it is extremely likely that this meteorite (and therefore probably many others) contain domains of pure, or very near pure iron within them. This should garner interest in several fields: cosmology, astronomy, physics, chemistry, and the geosciences; all of which are concerned with the elemental makeup of our universe.

7.7 Acknowledgements

The CPA-DMFT calculations, XPS and magnetic measurements were supported by Russian Science Foundation (Project 14-22-00004). The XAS measurements were performed at the

Canadian Light Source, and XES measurements were performed at the Advanced Light Source, both were supported by the Natural Sciences and Engineering Research Council of Canada (NSERC) and the Canada Research Chair program.

CHAPTER

EIGHT

Background Information

This paper was published in Physical Review B in July 2017. It can be accessed online with doi:10.1103/PhysRevB.96.045202 . The reference to it is: Physical Review B, 96, 045202 (2017). For this manuscript I contributed the following: I did all of the experimental x-ray work after initial measurements performed by K. LeBlanc; all calculations and the complete analysis was performed solely by me; and I wrote the paper after an initial draft by Z. Abooalizadeh.

Tunability of room-temperature ferromagnetism in spintronic semiconductors through nonmagnetic atoms

B. Leedahl,[1] Z. Abooalizadeh,[1] K. LeBlanc,[1] and A. Moewes[1]

[1] Department of Physics and Engineering Physics, University of Saskatchewan, 116 Science Place, Saskatoon, Saskatchewan, Canada, S7N 5E2

Abstract

The implementation and control of room temperature ferromagnetism (RTFM) by adding magnetic atoms to a semiconductor's lattice has been one of the most important problems in solid state state physics in the last decade. Herein we report for the first time, to our knowledge, on the mechanism that allows RTFM to be tuned by the inclusion of *non-magnetic* aluminum in nickel ferrite. This material, $NiFe_{2-x}Al_xO_4$ (x=0, 0.5, 1.5), has already shown much promise for magnetic semiconductor technologies, and we are able to add to its versatile technological viability with our results. The site occupancies and valencies of Fe atoms (Fe^{3+} T_d, Fe^{2+} O_h, and Fe^{3+} O_h) can be methodically controlled by including aluminum. Using the fact that aluminum strongly prefers a 3+ octahedral environment, we can selectively fill iron sites with aluminum atoms, and hence specifically tune the magnetic contributions for each of the iron sites, and therefore the bulk material as well. Interestingly, the influence of the aluminum is weak on the electronic structure (supplemental material), allowing one to retain the desirable electronic properties while achieving desirable magnetic properties.

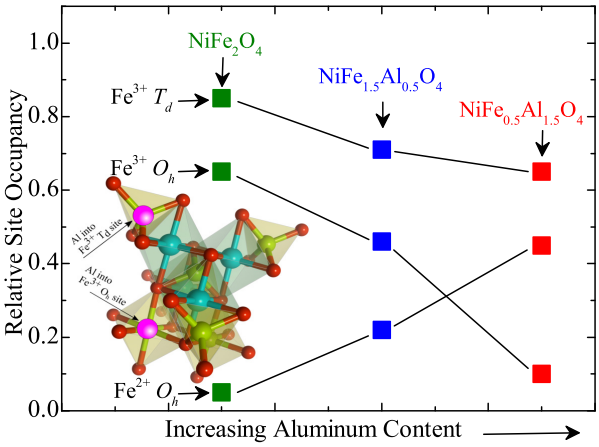

8.1 Introduction

Spinel oxides (AB_2O_4) often have quite unique and highly tunable and versatile functionalities.[205, 206] Among spinel oxides, ferrites are emerging as a viable magnetic material for use in novel technologies; especially in the area of spintronics, wherein magnetic semiconductors play a central role in generating highly spin-polarized currents.[207, 208] Indeed, $NiFe_2O_4$ films have been shown to display spin-polarized currents, and adjustable electrical properties through

varying growth conditions.[209, 210, 211] Currently, nickel ferrites are extensively used in a number of electronic devices because of their high magnetic permeabilities, high electrical resistivity, mechanical hardness, chemical stability, and reasonable cost.[212] Understanding the role of electron correlation effects in these ferrites has been a major challenge.

Theoretical studies have suggested that $NiFe_2O_4$ has Ni ions exclusively on B octahedral (O_h in point group representation) sites, and Fe ions distributed equally among A tetrahedral (T_d in point group representation) and B sites (referring to the AB_2O_4 notation).[213] On one hand, a strength of $NiFe_2O_4$ is that its properties can be tuned based on synthesis conditions, but on the other, measurements of its properties have shown a variety of results. For example, it has been reported to have a magnetic moment in ultra-thin films that is 2.5 times larger than in the bulk.[214] Multiple studies have investigated the properties of $NiFe_2O_4$, but the reported observations lack consistency. [215, 216, 217, 218, 219] These discrepancies make it a worthwhile endeavour to pursue complementary techniques (x-ray, as opposed to optical or theoretical methods) to add to the body of work for such a technologically important material.

The electronic and magnetic effects of alloying different elements (such as Al ions) into nickel ferrite is a topic that warrants further exploration. While the magnetism due to Ni atoms in $NiFe_2O_4$ was thoroughly studied,[220] such non-magnetic alloying provides a promising pathway to tuning its magnetic properties, which is highly desired in the field of spintronics.[47, 221]

Previously, the effect of Al substitution on $NiFe_2O_4$ was shown to cause both the Curie temperature (T_C) and lattice constant to decrease slightly with increasing Al concentration.[222] In the present study the effect that Al doping has on nickel ferrite alloys is explored by using soft x-ray spectroscopy techniques. The x-ray absorption spectroscopy (XAS) at the $L_{2,3}$-edges of Fe and Ni allowed us to examine their element specific electronic and magnetic structures.[54, 223] Finally, through comparison of the experimental spectra and crystal field multiplet calculations of transition metal $L_{2,3}$-edges spectra, we were able to extract the local coordination of these atoms.

8.2 Experiment and Calculation Details

Nanocrystalline powders of $NiFe_{2-x}Al_xO_4$ (x=0.0, 0.5, 1.5) were prepared by the sol-gel method; detailed information regarding the synthesis of these materials can be found in a previous publication [222]. After deposition, the powders were annealed separately in air at different temperatures from 400°C to 1100°C for two hours in order to get the final single phase products. Lastly, x-ray diffraction (XRD) scans were performed to ensure the single phase structure.

The crystal field multiplet calculations in this work use the algorithm initially formulated by Cowan, and the working code subsequently expanded on by Haverkort and Green *et al.*[224, 45, 31, 29] The free parameters include the crystal field strength (from which the local symmetry can be deduced), oxidation state, and the scaling of the intra-atomic Coulomb and exchange (Slater) integrals. The dipole transition matrix elements calculated by this code are then used in the Kramers-Heisenberg equation to simulate spectra.[79] All spectra are broadened by convolutions with a Lorentzian function (to simulate lifetime broadening), and a Gaussian function (to simulate experimental broadening) to match experimental conditions.

Our x-ray magnetic circular dichroism (XMCD) measurements were performed at the REIXS Beamline of the Canadian Light Source mounted on a 0.5 T magnet to saturate the magnetic moments of the sample such that XMCD selection rules are valid. The x-ray photons used were incident at 45° to the sample normal, and maintained greater than 95% circular polarization. A schematic of the XMCD process is shown in Fig. 8.1. Using this technique we were able to decompose the magnetic signal of our samples into different symmetries and oxidation states of iron.

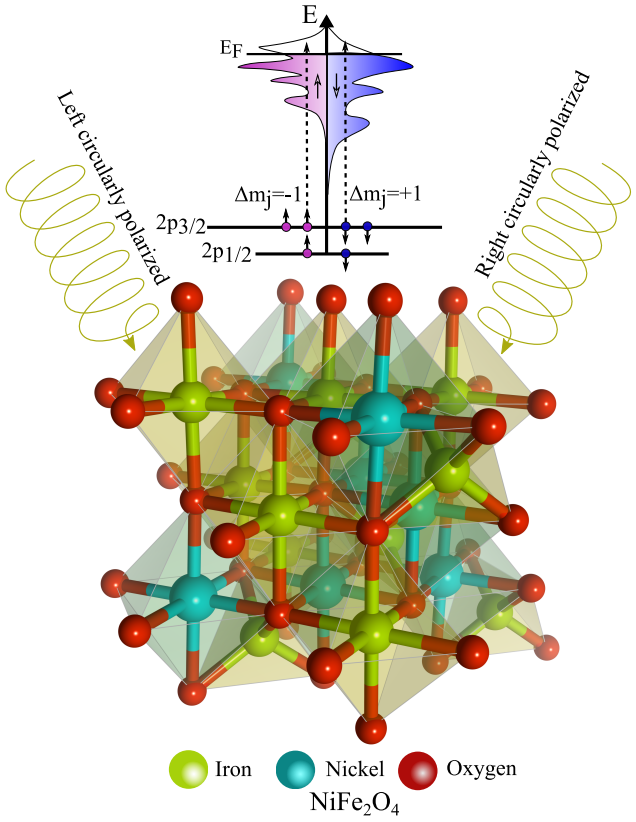

Figure 8.1: XMCD is an element- and orbital-specific technique. It relies upon left and right circularly polarized x-ray to probe exclusively *the Fe 2p electrons. Under a magnetic field the spin-up and spin-down 2p electrons are disproportionately excited into the partially 3d band due to the difference in the unoccupied spin-up and spin-down states. Left and right polarized photons transfer $-\hbar$ and $\hbar$ angular momentum, respectively, to the excited electrons. Dipole selection rules govern the proportion with which spin-up and spin-down electrons are excited. Consequently, this information can be gathered in relatively simple XMCD sum rules,[69] and the difference between left and right polarized absorption spectra determines the orbital and spin magnetic moments per Fe atom.[64]*

8.3 Results and Discussion

The measured XMCD at the Fe $L_{2,3}$-edges for all samples are shown in Fig. 8.2, taken in total electron yield (TEY) mode. The left and right (red and black) polarized XAS spectra are scaled by a factor of 0.25 compared to the XMCD signal (blue) for clarity; this XMCD signal is the difference between the two absorption spectra. In addition to the experimental

spectra, we have included crystal field multiplet calculated spectra for the three individual components (Fe^{3+} T_d, Fe $^{2+}$ O_h, and Fe^{3+} O_h), along with an overall calculated XMCD spectrum, computed as a linear sum of these components.[225] It is also worthy to note that the absorption spectra were also measured in bulk sensitive inverse partial fluorescence yield mode, and hence free of saturation and self-absorption effects that are known to alter feature intensities when using other XAS techniques like fluorescence detection.[60] These spectra agreed with our TEY spectra in Fig. 8.2, however they are inherently substantially noisier and the XMCD sum rules are not possible to use reliably with noisy data.

The Fe XMCD spectra comprises of a superposition of the three main components that are derived from the three sites occupied by iron: Fe^{2+} octahedral (d^6O_h), Fe^{3+} tetrahedral (d^5T_d), and Fe^{3+} octahedral (d^5O_h). The Fe^{3+} ions at the tetrahedral sites are coupled antiferromagnetically to those at the octahedral sites. This antiferromagnetic coupling is clear because in order to achieve agreement with experiment, a sign reversal of the spin operators was required in the calculations.[225]

What we discovered was that an exciting trend emerges among the intensities of the three components. As the Al content increases we observe that both Fe^{3+} signals decrease in magnitude, while the Fe^{2+} XMCD signal increases. This is in accordance with what we would expect from the argument that Al strongly prefers to be in a 3+ oxidation state, and so tends to replace Fe^{3+} atoms. Furthermore, as observed previously,[222] we also concur that the Al^{3+} atoms tend to prefer the octahedral environment of Fe, and therefore the Fe O_h signal is considerably suppressed compared to that of the tetrahedral sites, which are only mildly diminished. As a result of these two strong preferences (Al into O_h and 3+ sites), the Fe^{3+} O_h signal largely dies out, while the Fe^{2+} ions become a large contributor to the magnetism with increasing Al content.

That is to say, as Fe^{3+} O_h sites become filled with Al^{3+} ions, this site's contribution to the overall ferromagnetism is gradually reduced until it is nearly zero. In a similar, but less drastic way, Fe^{3+} T_d sites are filled by Al^{3+} ions. Surprisingly this does not necessarily imply that the overall magnetism of the material must be reduced accordingly. Only by viewing the XMCD signals in Figure 8.2 can we explain this phenomena. The fingerprint XMCD

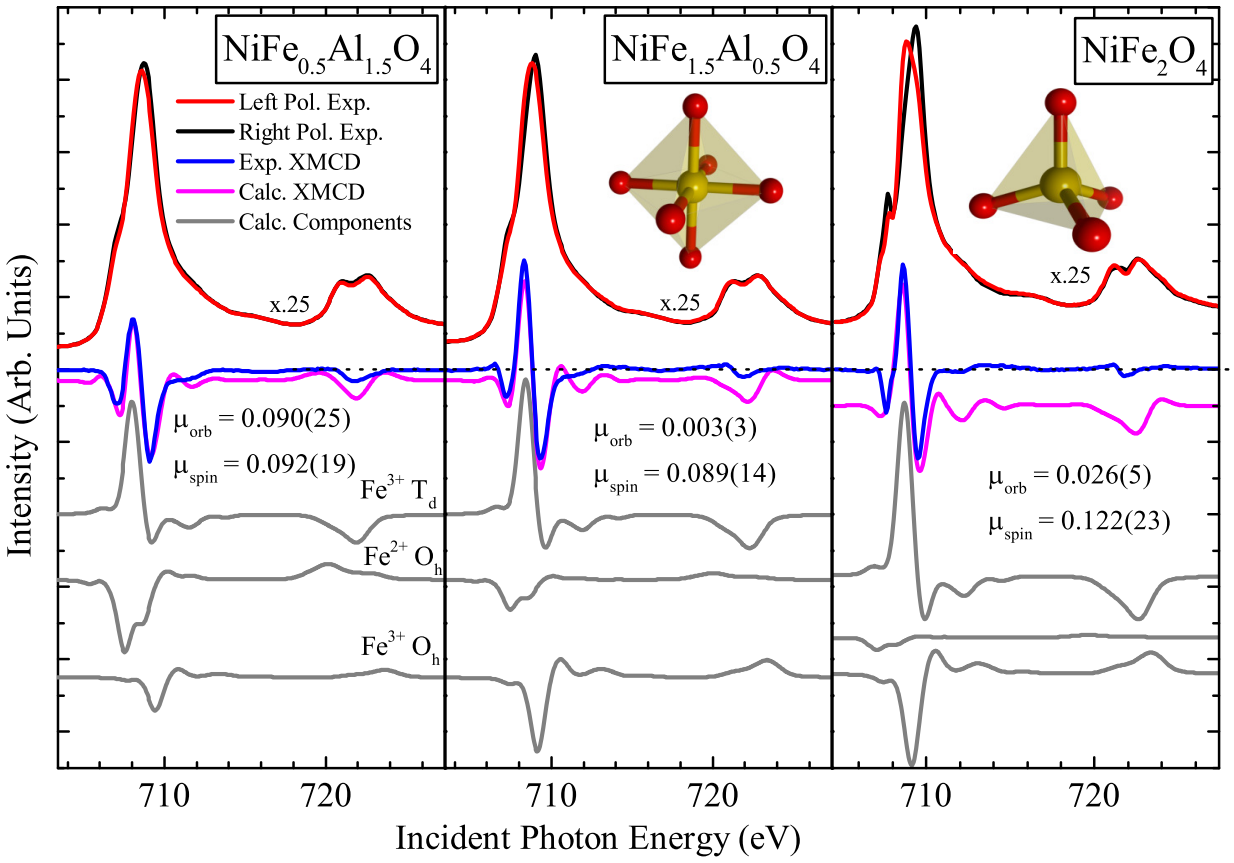

Figure 8.2: Calculated (magenta) and experimental (blue) XMCD spectrum at the Fe $L_{2,3}$-edge with both left and right circularly polarized x-rays. Grey curves (from top to bottom) show calculated Fe^{3+} T_d, Fe^{2+} O_h, and Fe^{3+} O_h components of the XMCD spectra, respectively. With increasing Al content we see the following trends: mildly decreasing Fe^{3+} T_d signal, largely increasing Fe^{2+} O_h signal, and a steadily decreasing Fe^{3+} O_h signal. The experimentally derived spin and orbital magnetic moments for each sample are shown in their respective panels in units of bohr magnetons. The experimental error is also shown in bracket notation; note that this does not account for approximations made within the sum rules themselves.

signals of the two reduced Fe^{3+} sites largely (but by no means completely) cancel one another out. Consequently, their simultaneous reduction does not manifest itself so drastically in the material's bulk magnetic properties. As a matter of fact, what we found is that Fe^{2+} O_h sites emerge as a significant contributor the overall ferromagnetism when the other two sites are reduced. It is this interplay between the three Fe sites and their relative occupancies—which we can *only* discern via XMCD—that gives rise to the bulk magnetic properties. This

finding is validation of the power of XMCD, as well as illustrating an important technique that could be adopted and applied to reach its full potential in the realm of synthesizing spintronic devices, wherein the tuning of magnetic moments is of the utmost importance.

From our experimental XMCD spectra we determined the magnetic moments of the samples using the left and right circularly polarized XAS and XMCD sum rules (orbital and spin moments are shown in Fig. 8.2, with errors due to experiment shown in bracket notation).[65] By adding the orbital μ_{orb} and spin μ_{spin} moment of each sample ($\mu = 0.148\mu_B$ for x = 0, $\mu = 0.092\mu_B$ for x = 0.5, and $\mu = 0.182\mu_B$ for x = 1.5), one can see that the net magnetization decreases when the Al content is increased to x = 0.5, and then increases for x = 1.5. This is consistent with our conclusion that the interplay between the three XMCD signals is what gives rise to the observed bulk magnetic properties. The reduction of some magnetic sites in turn may give rise to the appearance of others, leading to a complicated exchange between them, and not just a simple reduction in magnetism as magnetic atoms are replaced by non-magnetic atoms.

As an additional point it should be noted that there are limitations to using the sum rules in determining precise quantitative values of spin and orbital magnetic moments. (1) Experimental errors such as noise, and the fact that left and right polarized XMCD spectra cannot be taken simultaneously lead to uncertainty in the integrated XMCD spectra (for which small experimental errors can propagate into relatively large absolute quantitative errors, these are the errors shown in Fig. 8.2 brackets). (2) Approximations made within the sum rules themselves such as: assuming the spin-quadrupole coupling term is zero (which is commonly used for transition metal L-edges),[70] and the uncertainty in the number of d-electron holes, which will vary due to some degree of covalency and mixing of oxidation states.[71] For these reasons, the absolute values of our magnetic moments are of secondary importance. What is important for the proper analysis of our data is identifying and explaining the trends and contributions of each of the Fe sites as the amount of Al varies.

Hence, we have found that small changes in the site occupancies can give rise to considerable differences in the relative peak intensities of the XMCD. Using the three calculated components, it is possible to predict the spectral shapes of spinels with different ratios of

Fe^{2+}/Fe^{3+} at the two sites (octahedral/tetrahedral O_h/T_d). This principle can be understood better by considering the *inversion parameter, i*—it tells us the fraction of Fe ions in T_d and O_h sites, and always takes a value between zero and one. It can be written in the following form:

$$[Ni_{1-i}Fe_i]^{T_d}[Ni_iFe_{2-i}]^{O_h}O_4$$

Therefore, a material with an inversion parameter of 1.0 would contain Fe^{3+} in both octahedral and tetrahedral sites in a 1:1 ratio, while a normal spinel ($i = 0$) ferrite of the same formula would contain Fe^{3+} in octahedral sites only. Indeed, in the right panel of Fig. 8.2 we see that the Fe^{2+} is quite negligible, and so $NiFe_2O_4$ has an inversion parameter very close to one, as has been previously found using other methods.[226]

A superposition of the three theoretical components can therefore be fit to the experimental spectra, producing site occupancy ratios of Fe at the three sites. Note that Fe^{2+} at T_d sites have been ignored—if it is included in the fitting process, a small component of < 0.1 atoms per unit formula may be present, but is not significant.[227] The small discrepancies between experiment and calculation can be attributed to the long range effects of the crystal field due non-nearest neighbours and the addition of Al atoms to the host lattice, as well as slight distortions from spectra being taken in TEY mode.

Thus, we can deduce our principal revelation from a few basic tenets. (1) Iron is frequently found in many magnetic compounds in some combination of its four most common environments (Fe^{2+} octahedral, Fe^{2+} tetrahedral, Fe^{3+} octahedral, and Fe^{3+} tetrahedral. (2) Each of these four sites has a unique magnetic signature that can be measured via XMCD. (3) We can then exploit the fact that many elements strongly tend to a given oxidation state and local symmetry. For example, aluminum atoms are found nearly exclusively in a 3+ oxidation state and in octahedral environments. Hence, upon addition of these Al atoms to some host lattice, they will preferentially replace atoms in 3+ octahedral sites, and to a lesser degree 3+ tetrahedral sites. The key point is that the Al atoms *will not* substitute into 2+ sites. Herein, we have shown that it is feasible to exploit this property with the replacement of magnetic Fe atoms by non-magnetic Al atoms in $NiFe_2O_4$. Therefore, by adding aluminum (or other non-magnetic atoms) it is possible to tune the site occupancy

ratios of the ferromagnetic atoms, leading to a tuning of the magnetism of the compound as a whole. What is even more amazing about the fine tuning of the magnetism, is that it is all accomplished while retaining the host material's electronic properties; a full discussion and analysis of the electronic properties is given in the *Supplemental Material*.

8.4 Conclusion

With room temperature ferromagnetic materials becoming a burgeoning area of research in recent years, it is required that substantial advances in the control and understanding of magnetic properties are achieved.[228] The lesser studied idea of using non-magnetic atoms offers a novel avenue of departure from the more customary iron/nickel doping. We have shown that ferromagnetic single-phase nickel ferrite $NiFe_2O_4$ can have the occupancies of the three iron environments adjusted by the inclusion of aluminum atoms, hence altering the spin and orbital magnetic moments of the bulk material. This was shown to be possible only through the use of synchrotron-based XMCD spectroscopy, alongside crystal field multiplet calculations. Our study shows a proof of concept that by decomposing the ferromagnetism into its constituents, we can make substantial advances in understanding the source of the magnetism. In turn this will surely lead to corresponding advances in the tailoring of magnetism that can be achieved with careful synthesis. This ought to garner further interest in the popular field of spintronic devices, wherein controlling electron spin has been one of the most important topics in condensed matter physics in recent decades.

8.5 Acknowledgements

This work was supported by the Natural Sciences and Engineering Research Council of Canada (NSERC) and the Canada Research Chairs program. Measurements were performed at the Canadian Light Source (supported by NSERC, the Canadian Institutes of Health Research, the Province of Saskatchewan, Western Economic Diversification Canada, and the University of Saskatchewan) and the Advanced Light Source (supported by the U.S.

Department of Energy under Contract No. DE-AC02-05CH11231). We are also grateful to Dr. M. Mozaffari and Prof. J. Amighian for their cooperation in the sample synthesis process.

8.6 Supporting Material

8.6.1 Oxygen XAS and XES – The Band Gap of $NiFe_2O_4$

Past experimental studies of the $NiFe_2O_4$ band gap have been somewhat controversial, spanning a range from 1.0 eV to 3.7 eV. The character of the band gap has yet to be agreed upon as well, reporting both direct and indirect band gaps in these studies.[215, 216, 217, 218, 219] Herein, we carried out complementary (x-ray) experiments to study the band gap of $NiFe_2O_4$.

The magnitude of the samples' band gaps can be extracted by taking the energy difference between O K-edge x-ray absorption (XAS) and non-resonant emission spectra (NXES)—where the excitation energy is well above the XAS threshold—which probe the unoccupied and occupied density of states, respectively. We use the second derivative technique to determine the onset of the density of states in each spectrum.[50, 51, 229] The oxygen K-edge XAS and XES and second derivative calculation are shown in Fig. 8.3 for our three samples.

Our findings reveal the semiconducting nature for all three samples with very similar band gaps for all Al concentrations: 0.7 eV for x = 0, 0.8 eV for x = 0.5, and 1.0 eV for x = 1.5. (with an error of ± 0.2 eV). But, because of the core hole left behind in the absorption process, there is a shift in the absorption spectra that can occur, but is usually quite small (<0.2 eV). Therefore, these band gap results are a lower limit, with the actual value likely only slightly larger.

Previous work done by Patange et al. indicated an increase in electrical resistivity with increasing of Al content, consistent with our results of an increasing band gap.[230] However, they did not measure the band gap correlation with this. Our result of only minute change is actually quite significant. It shows that with large differences in Al-content, the host material largely retains its advantageous semiconducting electronic properties. However, as

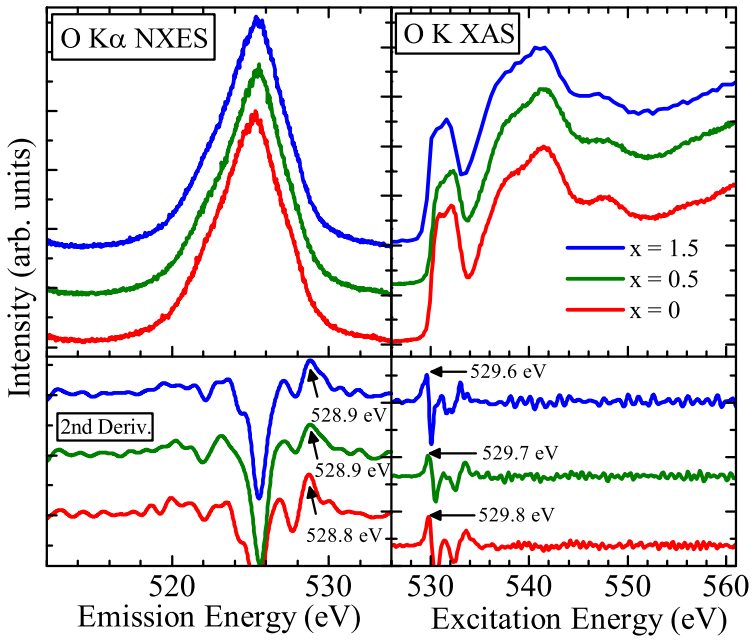

Figure 8.3: Band gap determination from O K-edge spectroscopy. The oxygen K-edge XAS and NXES spectra for our three samples are shown, along with their second derivatives. The peaks in the second derivative allow us to unambiguously determine the onset of the spectra, which are broadened by experimental factors.

desirable, the Al alloying significantly alters the *magnetic* properties.

By exciting resonantly, we are able to probe specific intermediate excited states. We can see that in Fig. 8.4(a), as excitation energy increases, so too does the energy of peak intensity of the emission spectrum. Because resonant x-ray emission (RXES) is a momentum conserving process, and the XES spectra are no longer averaged over all crystal momenta when exciting resonantly, we expect the spectral shape to change. It is indicative of an indirect band gap when it is observed that the peak emission energy increases as excitation energy increases.[54, 231] If there is no change in peak emission energy (as is nearly the case for x = 1.5), then it is a direct band gap, which is what we observe.

8.6.2 Fe and Ni XAS

The x-ray absorption spectra (XAS) for Ni $L_{2,3}$ and Fe $L_{2,3}$-edges along with calculated XAS spectra are displayed in Fig. 8.5(b). For Ni, the crystal field splitting used in the calculation

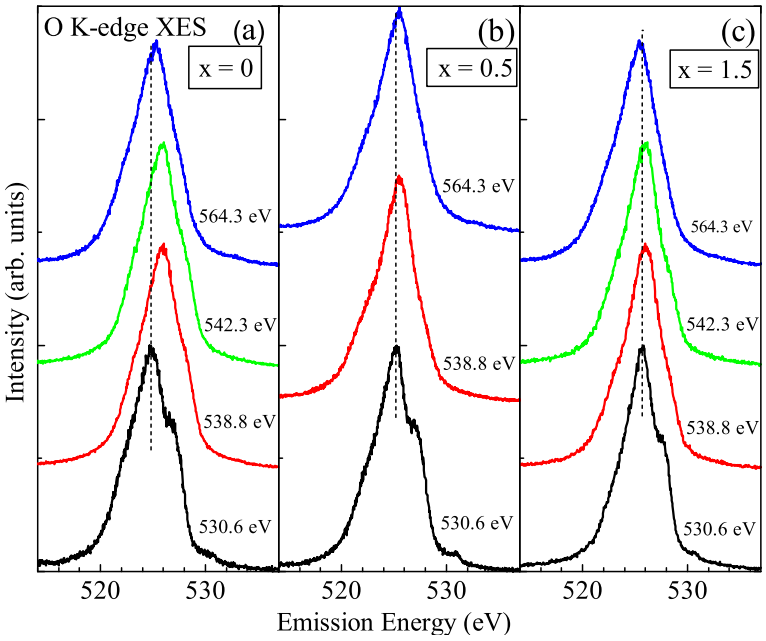

Figure 8.4: The O K-edge RXES spectra of (a) $NiFe_2O_4$, (b) $NiFe_{1.5}Al_{0.5}O_4$, and (c) $NiFe_{0.5}Al_{1.5}O_4$ at different excitation energies. The change in energy of the peak height is indicative of an indirect band gap. However, there is the trend that the band gap becomes nearly direct for $x = 1.5$. The magnitude of the gap is analyzed in Fig. 8.3.

was $10Dq$ = 1.7 eV, and the Slater integrals were scaled to 75% of their Hartree-Fock values. The positive $10Dq$ value indicates O_h coordination for Ni ions. There is effectively no noticeable difference between Ni spectra of the three samples as we would expect as their local coordination remains the same upon Al alloying.

Moving on to Fe in Fig. 8.5(a), the agreement between XAS sspectra of Fe $L_{2,3}$ ions and calculated XAS spectra is very good as well. The similarity of our sample's spectra with that of Fe_2O_3, as well as being confirmed by our multiplet calculations, clearly indicate Fe is primarily (but not entirely) in a 3+ oxidation state ($3d^5$ configuration). We performed calculations for the three different Fe sites and linearly combined them to produce the plotted spectrum in magenta. The crystal field splitting parameters used for the three calculations were $10Dq$ = -0.7 eV, 1.5 eV, and 1.0 eV; and the Slater integrals were scaled to 60%, 70%, and 70% of their Hartree–Fock values, respectively. The weighted contributions for the three sets of parameters were then 50%, 30%, and 20%, which corresponds to the three states in

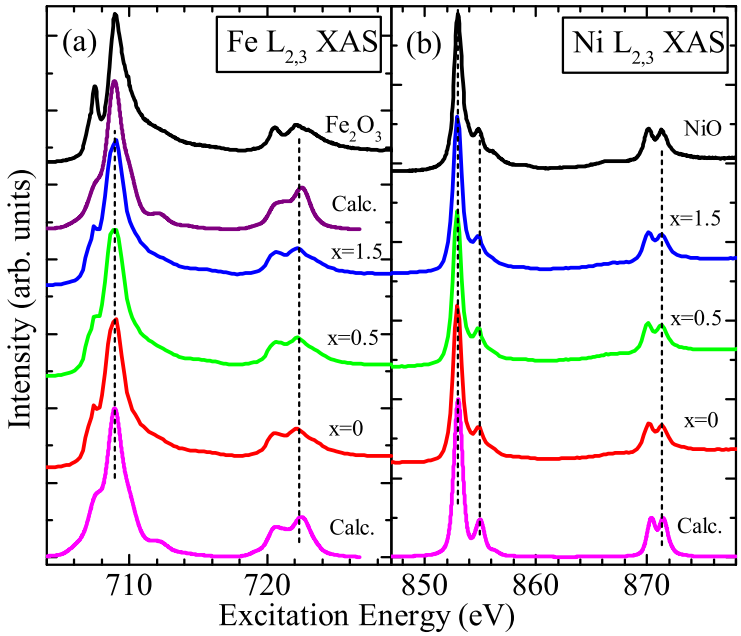

Figure 8.5: Measured and calculated (a) Fe $L_{2,3}$ and (b) Ni $L_{2,3}$ absorption spectra. Ni coordination is not affected by the inclusion of Al atoms, shown by the absence of change in the spectra with increased Al alloying. However, Fe spectra are very subtly altered. The calculation in magenta shows a linear combination of Fe spectra in its three coordination/valency combinations. Then the calculation in purple is similar, but with half the number of O_h Fe atoms. The change is small, but noticeable, and elucidated by our XMCD measurements.

the order Fe^{3+} T_d, Fe^{3+} O_h, and Fe^{2+} O_h.

That is, half the Fe ions are in an octahedral coordination, while the other half are in tetrahedral. Note that another calculation is shown (purple), corresponding to the same parameters except with half the octahedral contribution, as we may expect if Al ions are primarily substituting in these sites. Surprisingly, this has only a small effect on the calculated XAS spectral shape. Therefore, in this case, XAS alone is not as sensitive to the small changes in local symmetry ratios of Fe ions as we would like, hence the need for XMCD analysis to understand the site occupancies.

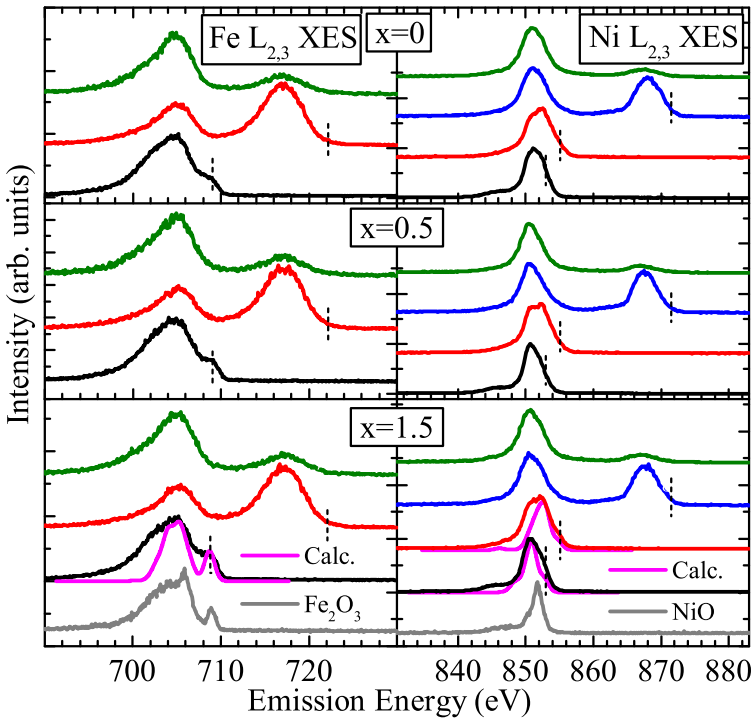

Figure 8.6: Fe and Ni XES. Dashed vertical lines indicate the excitation energy. Nickel emission spectra remain virtually unchanged with Al content, but vary significatly in crystal field splitting from NiO despite their similar ligand environment. The Fe calculation is a sum of Fe^{3+} O_h and T_d sites in a 1:1 ratio as expected from an inverse spinel. Note that charge transfer features at higher loss energies were included in the model.

8.6.3 Fe and Ni XES

To complete our spectroscopic study, RXES measurements of Fe and Ni are shown in Fig. 8.6. The green spectra correspond to the non-resonant emission (NXES) taken at excitation energies well above the absorption edges. Since contributions to the spectra from the three sites are blurred together into a rather featureless peak, it is difficult to observe the small effect of Al content variations on the remaining Fe atoms. Just as in the case with the XAS, the changes between the three samples are then quite difficult to see. This difficulty is even more pronounced with XES due to our energy resolution limitation of ≈1 eV.

In the case of Ni L-edge RXES, all atoms occupy O_h sites, surrounded by oxygen ligands. This is identical to NiO, and since Al atoms do not substitute into these Ni sites, we would

expect very similar spectra to NiO, and to remain unchanged with varying Al content. However, while they do remain unchanged, the crystal field splitting is vastly different from that of NiO. This significantly larger crystal field in our samples is somewhat surprising given their similar coordination and Ni–O bond distances (2.09 Å for NiO and 2.03 Å for $NiFe_2O_4$).[232, 233] This variation is evident from the substantial difference in energy loss features between NiO and our samples (Fig. 8.6 lower right panel). The disparity must result from the second coordination sphere (and beyond), which has twelve Ni atoms at 2.96 Å for NiO, but only three of each Ni and Fe atoms at 2.92 Å (O_h sites), and six more Fe atoms at 3.42 Å (T_d sites) for $NiFe_2O_4$. Thus indicating RXES's sensitivity not only to the first coordination sphere of Ni, but beyond.

Hence, for completeness, the presented supplementary material demonstrates that the overall effect of aluminum alloying on the *electronic* structure of nickel ferrite is quite small. This is actually quite advantageous in this scenario, as it is conducive to practical technological use inasmuch as the magnetic properties can be tweaked while not having to simultaneously compensate for large deviations in the electronic properties.

CHAPTER

NINE

Background Information

This paper was published as an Open Access article in Scientific Reports in June 2017. It can be accessed online with doi:10.1038/s41598-017-06069-3. The reference to it is: Scientific Reports 7, 5758 (2017). My contributions to the final version of this publication were the following: I took all XAS and XES spectra and performed the corresponding calculations; I performed nearly all scientific analysis of the data, including data not taken by me (XPS) and calculations done by collaborators (defect formation energies); and I largely rewrote the paper after an initial draft provided by E. Z. Kurmaev.

Bulk vs. Surface Structure of $3d$ Metal Impurities in Topological Insulator Bi_2Te_3

B. Leedahl,[1] D. W. Boukhvalov,[2,3] E. Z. Kurmaev,[4,5] A. Kukharenko,[5] I. S. Zhidkov,[5] N. V. Gavrilov,[6] S. O. Cholakh,[5] P. Huu Le,[7,8] C. Wei Luo,[7] and A. Moewes[1]

[1] Department of Physics and Engineering Physics, University of Saskatchewan, 116 Science Place, Saskatoon, Saskatchewan, Canada, S7N 5E2

[2] Department of Chemistry, Hanyang University, 222 Wangsimni-Ro, Seoul, 04763, Republic

of Korea.

[3] Theoretical Physics and Applied Mathematics Department, Ural Federal University, Mira Street 19, 620002, Yekaterinburg, Russia

[4] M.N.Mikheev Institute of Metal Physics of Ural Branch of Russian Academy of Sciences, S. Kovalevskoi 18 str., 620990, Yekaterinburg, Russia.

[5] Institute of Physics and Technology, Ural Federal University, Mira 19 St., 620002, Yekaterinburg, Russia. [6] Institute of Electrophysics, Russian Academy of Sciences-Ural Division, 620016 Yekaterinburg, Russia

[7] Department of Electrophysics, National Chiao Tung University, Hsinchu, 30010, Taiwan, ROC.

[8] Faculty of Basic Sciences, Can Tho University of Medicine and Pharmacy, 179 Nguyen Van Cu Street, Can Tho, Vietnam.

Abstract

Topological insulators have become one of the most prominent research topics in materials science in recent years. Specifically, Bi_2Te_3 is one of the most promising for technological applications due to its conductive surface states and insulating bulk properties. Herein, we contrast the bulk and surface structural environments of dopant ions Cr, Mn, Fe, Co, Ni, and Cu in Bi_2Te_3 thin films in order to further elucidate this compound. Our measurements show the preferred oxidation state and surrounding crystal environment of each 3d-metal atomic species, and how they are incorporated into Bi_2Te_3. We show that in each case there is a unique interplay between structural environments, and that it is highly dependant on the dopant atom. Mn impurities in Bi_2Te_3 purely substitute into Bi sites in a 2+ oxidation state. Cr atoms seem only to reside on the surface and are effectively not able to be absorbed into the bulk. Whereas for Co and Ni, an array of substitutional, interstitial, and metallic configurations occur. Considering the relatively heavy Cu atoms, metallic clusters are highly favourable. The situation with Fe is even more complex, displaying a mix of oxidation states

that differ greatly between the surface and bulk environments.

9.1 Introduction

The Bi-chalcogenides such as Bi_2Te_3 and Bi_2Se_3 have long been known for their thermoelectric properties,[234, 235] but recently they have gained a great deal of attention as three-dimensional topological insulators with a large band gap and a single Dirac cone on the surface.[236, 237, 238, 239, 240, 241] Additionally, the introduction of magnetic impurities into Bi-chalcogenides can break time-reversal symmetry and open an energy gap at the Dirac point of the surface states.[242, 243, 244] Recently, Bi_2Te_3 and related systems with dilute doping of 3d-metal atoms (Ti, V, Cr, Mn, and Fe) have been found to have ferromagnetic transitions at low temperatures. $Bi_{2-x}Mn_xTe_3$ was found to have a Curie temperature T_C around 10 K for x = 0.02.[245] For larger doping of thin films of $Sb_{2-x}V_xTe_3$, with x = 0.35, T_C increases to 177 K and for $Sb_{2x}Cr_xTe_3$ with x = 0.59 T_C increases to 189 K [246] which is close to that of more traditional dilute magnetic semiconductors (DMS).[247]

Most DMS materials are crystallized in zinc-blende or wurtzite crystal structures with tetrahedral bonds between atoms. In this respect Bi_2Te_3 is different, its tetradymite-type structure has atoms that form in octahedral coordination. When transition metal atoms are introduced to the tetradymite-type structure, there are various possible oxidation states they may exist in. In addition, the spin-orbit interaction is more complicated due to the expanded octet bonding where not only p-orbitals, but also d-orbitals join the hybridization. The relatively sophisticated tetradymite structure leaves a lot of structural and chemical factors available to be tweaked. This induces even more complicated structural configurations when impurity atoms are introduced, and as a result, create new, unexpected electronic and magnetic properties. In the present paper the local crystal and electronic structure of 3d-impurities (Cr, Mn, Fe, Co, Ni, Cu) in Bi_2Te_3 thin films are studied using x-ray photoelectron spectroscopy (XPS), x-ray ray absorption (XAS), and resonant x-ray emission (RXES) techniques. The experimental spectra are compared with density functional theory (DFT) calculations of formation energies for different configurations of the dopant atoms.

These techniques are powerful in that they are non-invasive *and* able to distinguish between bulk and surface states, key to the study of topological insulators.[248]

9.2 Experiment and Calculation Details

Bi_2Te_3 thin films were grown on an $Al_2O_3(0001)$ substrates via pulsed laser deposition using a stoichiometric Bi_2Te_3 target with a purity of 99.99%.[249] The KrF-pulsed laser fluence and repetition rate were 3.7 J/cm^2 and 4 Hz, respectively. The base pressure of the growth chamber was below 2×10^{-6} Torr. Before loading into the chamber, the substrates were first cleaned using ultrasonication in acetone, methanol, and then deionized water for 30 minutes. The pressure in the chamber was maintained at 0.35 Torr while argon gas was introduced throughout the deposition process. The optimized substrate temperature was 260°C. The deposition times were 5 minutes and 25 minutes to grow the films with thicknesses of approximately 110 and 560 nm, respectively. The orientation and crystallinity of Bi_2Te_3 films were determined using x-ray diffraction (XRD) with Cu $K\alpha$ radiation (8048 eV); the results are displayed in Fig. 9.1.

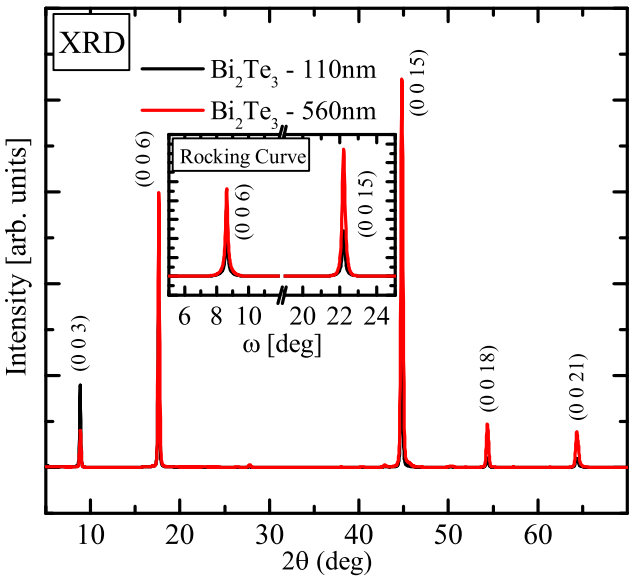

Figure 9.1: X-ray diffraction results show the high quality crystallinity of the Bi_2Te_3 thin films created using pulsed laser deposition.

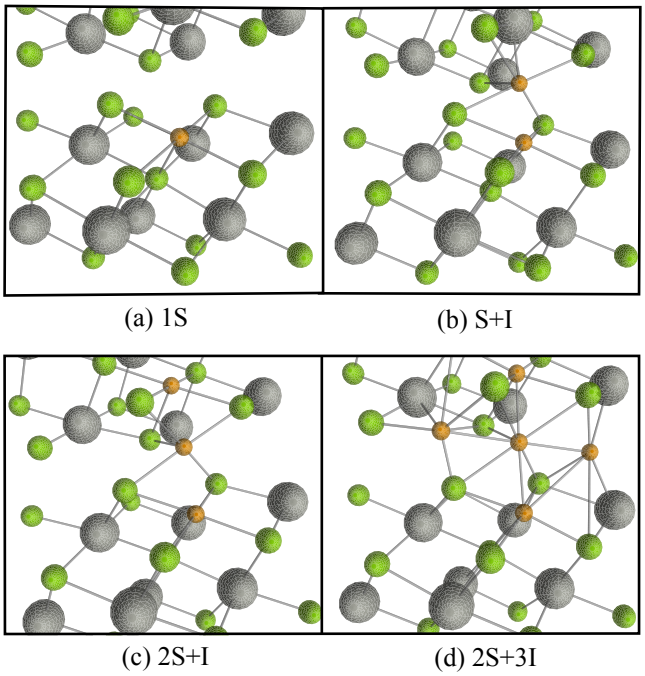

Figure 9.2: The four defect structures for which formation energies were calculated for in the Bi_2Te_3 crystal lattice. (a) $1S$ – a substitutional transition metal dopant residing in a Bi crystal site. (b) $S+I$ – substitutial and interstitial atoms location adjacent to one another. (c) $2S+I$ – further clustering of metallic atoms. (d) $2S+3I$ – this defect corresponds to large amount of metallic atoms clustering together, observed as the formation of metallic bonds. Bismuth atoms are displayed in grey, tellurium in green, and transition metal dopants in orange.

The implantation of ions in Bi_2Te_3 thin film samples was carried out in a vacuum chamber that was evacuated to a residual pressure of 3×10^{-3} Pa. An ion beam with an energy of 30 keV was created at a source cathode by vaporizing the metal with an electric arc. The ions were then used to irradiate the sample in a pulsed mode (25 Hz). After 38 minutes of exposure the sample had an ion fluence (integrated flux over time) of 1×10^{17} cm^{-2}. For ion implantation Cr, Mn, Fe, Ni, Co and Cu metals were used.

X-ray photoelectron spectroscopy (XPS) core-level measurements were performed using a spectrometer with an energy analyzer working in the range of binding energies from 0 to 1400 eV. The samples were introduced to vacuum (10^{-7} Pa) for 24 hours prior to measurement, and only samples whose surfaces were free from micro-impurities were measured and reported herein. The XPS spectra were recorded using Al Kα (1486.6 eV) x-ray emission photons;

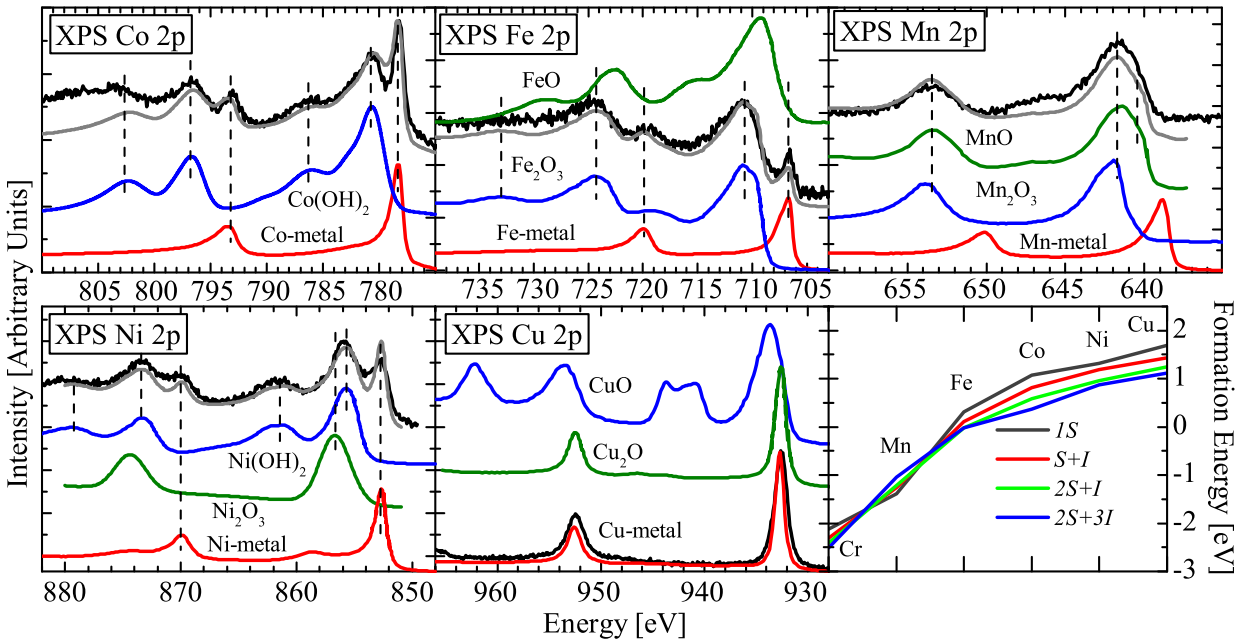

Figure 9.3: XPS spectra for doped samples. Black curves are 2p excitations of the TM dopant atoms in Bi_2Te_3. Grey curves are a linear combination of standard references. Table 9.1 indicates the approximate proportion of each oxidation state the dopants are in. The lower right panel are DFT calculated formation energies for each dopant for four types of defects.

the spot size was 100 μm; the energy resolution is $\Delta E < 0.5$ eV; and typical signal to noise ratios were greater than 10000:3. The x-ray absorption spectroscopy (XAS) measurements were taken at Beamline 8.0.1 at the Advanced Light Source (ALS), and the REIXS and SGM beamlines, the latter two being at the Canadian Light Source. Finally, the x-ray emission (XES) measurements were performed using Beamline 8.0.1.[122]

To simulate 3d-metal impurities in Bi_2Te_3 we applied the pseudo-potential code SIESTA[250] For our purposes a supercell containing 60 atoms ($Bi_{24}Te_{36}$) was adequate; this provides a sufficient distance between embedded impurities. We calculated the formation energies for four possible combinations of impurities: a single substitutional impurity of bismuth ($1S$, Fig. 9.2a), a combination of substitutional impurity and embedded one into the interlayer space ($S + I$, Fig. 9.2b), a combination of two substitutional and one interstitial impurities ($2S + I$, Fig. 9.2c) and a configuration obtained by adding two interstitial atoms to the previous configuration ($2S + 3I$, Fig. 9.2d).

The crystal field multiplet calculations in this work use the algorithm initially formulated by Cowan, and the working code subsequently expanded on by Haverkort and Green *et al.*[224, 45, 31, 29] The free parameters include the crystal field strength (from which the local symmetry can be deduced), oxidation state, and the scaling of the intra-atomic Coulomb and exchange (Slater) integrals. The dipole transition matrix elements calculated by this code are then used in the Kramers-Heisenberg equation to simulate spectra.[79] All spectra are broadened by convolutions of a Lorentzian function (to simulate lifetime broadening), and a Gaussian function (to simulate experimental broadening) to match experimental conditions.

9.3 XPS Measurements

Using Al Kα photons, XPS allows one to probe the binding energies of a transition metal's 2p electrons; this technique is primarily sensitive to the *surface* oxidation state of the atoms. The surface sensitivity is in the range of ≈5 nm, due to the mean free path of escaping electrons. Furthermore, if the metal atoms exist in multiple oxidation states simultaneously, we will observe a superposition of the peaks from the corresponding oxidation states in our sample. Of note is that Cr XPS data was not possible due to the overlap of Cr 2p and Te 3d binding energies, coupled with the dilute nature of Cr atoms, it was not feasible to subtract out the much stronger Te 3d signal.

Shown in Fig. 9.3 are our XPS measurements determining the $2p_{3/2,1/2}$ binding energies of the dopant atoms in Bi_2Te_3. For each dopant atom *except* Mn, there is an obvious contribution from the metallic phase of each element. This corresponds to the peak position in the metallic reference spectra also appearing in the doped Bi_2Te_3 samples (indicated with vertical dashed lines in each plot of Fig. 9.3). This agrees with what we would roughly expect to see when considering our calculations of formations energies (Table 9.1). For each element we see that the clustering of dopant atoms (and hence the formation of metal-like regions, corresponding to $2S + 3I$ and $2S + I$ defects), are quite favourable (see lower right panel of Fig. 9.3 for formation energies of defects), especially in the cases of the heavier elements Co, Ni, and Cu. These defects can be thought of as the tendency for the transition

	0 (metallic)	2+	3+
Cr	–	–	–
Mn	0	88	12
Fe	25	0	75
Co	46	54	0
Ni	30	68	2
Cu	100	0	0

Table 9.1: The XPS spectra in Fig. 9.3 were decomposed into their component oxidation states through a linear combination of common oxides and metals. The tabulated values in this table indicate the percentage of each oxidation state found for each dopant metal on the Bi_2Te_3 surface. The corresponding linear sum is also plotted in Fig. 9.3 as grey curves.

metal atoms to cluster together (see Fig. 9.2 c-d). On the other hand, each doped sample also contains ionized dopants that reside in the Bi_2Te_3 lattice that do not form metallic clusters.

By normalizing the reference XPS spectra to have equal $2p_{3/2}$ and $2p_{1/2}$ edge jumps, we were able to take a linear combination of these to obtain good approximations for proportion of each oxidation state for each metal in Bi_2Te_3. The grey curves in Fig. 9.3 are the linear combination results; in all cases the match with the experimental spectrum is remarkably good. We have summarized the results and percentages of each oxidation state for each dopant in Table 9.1.

Manganese is specifically of interest because of its unique incorporation into Bi_2Te_3. When component oxidation states were analyzed, we found that there is virtually no metal-like signal, and 91% Mn^{2+}. This means that in the case of Mn doping, the cation substitution $Mn^{2+} \rightarrow Bi^{3+}$) is the primary defect. Our DFT calculations in the lower right panel of Fig. 9.3 support this view for Mn as well. It is the only dopant for which the formation energy of a substitutional impurity is the most favourable. In general our DFT calculations support the observed XPS results for all dopants, with the difference in $1S$ and $2S+3I$ formation energies corresponding to the likelihood of metallic cluster formation. That is, metallic clusters tend

to form when the cluster-like $2S+3I$ defects are sufficiently lower in energy than $1S$ defects, and the reverse is true as well, as shown in the case of manganese.

9.4 X-ray Absorption and Emission

Further x-ray measurements complement our XPS findings, these are displayed in Fig. 9.4. When coupled with crystal field calculations, these measurements can be used to deduce the local symmetry of the dopant ions, as well as their oxidation state. By achieving agreement between calculation and experiment, we can use the parameters used in the calculation to extract real physical results. Another important distinction to consider is that the XAS measurements were performed in both total electron yield (TEY) mode, only sensitive to the first ≈5 nm of the sample surface, and the more bulk sensitive partial fluorescence yield (PFY). XES measurements are inherently bulk sensitive (≈100 nm) similar to PFY, due to the greater escape depth of photons as compared to electrons.

For comparison, we have displayed the absorption spectra of common oxides and metals next to the spectra of each of the dopants in Fig. 9.4. Since each oxidation state for each 3d transition metal atom has a vastly different shape, this comparison alone can determine the ion's valency. In each case the calculation (pink) was performed for the primary oxidation state that was found via the XPS data. In general, they adequately agree with the experimental spectra, despite the fact of the existence of some portion of pure metallic bonding in each sample. This is because metallic absorption spectra are rather broad and featureless, whereas the rich spectra of charged transition metal atoms still shines through on top of this. Below we will discuss each dopant in turn and some slight exceptions to the above general statements.

9.4.1 Cobalt

In the case of cobalt (Fig. 9.4b), which has a high percentage of metallic bonding, the agreement between calculation and experiment is least satisfying (due to a large Co-metal contribution), Despite this, sharp scattering features can still be seen on top of the metallic

signal in both TEY and PFY modes. In fact, the differences between these two spectra illustrate that cobalt in the bulk of the sample tends more towards a metallic state, while on the surface it is still largely found in its 2+ state. This is evident from the much more rich TEY spectrum, and in accordance with our XPS results above, which stated that 54% of Co atoms are in a 2+ state. From the agreement with our calculation we can deduce that cobalt in the the sample that is not metallic is in very nearly a perfect octahedral coordination. The splitting of the e_g and t_{2g} 3d orbital is given by the $10Dq$ parameter, and since $10Dq =$ 0.9 eV; $Ds = Dt = 0$, we can be sure it is octahedrally coordinated.

9.4.2 Chromium

A similar analysis between the topological surface and deeper bulk environments for other dopants can also be done. In the case of chromium, the dopant atoms effectively *only* reside on the surface and are not incorporated into the host lattice at all during the ion implantation process, despite being subject to the same fluence. We have two pieces of evidence to support this: (1) the lack of any meaningful PFY signal; in Fig. 9.4c the PFY is extremely weak; (2) the XES had an order of magnitude less counts per second for Cr as compared to the other samples (hence why only one excitation is shown in Fig. 9.4f; it was not possible to obtain more data due to the time length of the measurements). In both cases it is likely that the emitted photons almost entirely originate from the thin surface layer (in which Cr^{3+} is nicely substituted into Bi_2Te_3). Hence, the bulk of the sample must have been effectively void of Cr ions.

As evidenced by the strong TEY signal, we are certain that the surface contains Cr^{3+} ions in a slightly warped octahedral environment (see Table 9.2 for crystal field parameters). Therefore, we have found a profound difference in the assimilation environments for Cr atoms in Bi_2Te_3. Cr atoms appear completely comfortable in a 3+ octahedral surface environment, but will not form in the bulk of the crystal lattice. The lack of bulk Cr can possibly be explained by its small ionic radius, because it is smaller than the other transition metal dopants used here, it may have difficulty finding a low energy state to reside in, and it is effectively expelled from the lattice.

9.4.3 Nickel

Nickel doping is quite similar to cobalt in that a substantial fraction of the dopant atoms prefer to metallically cluster together. However, in this incidence the TEY and the PFY for Ni (Fig. 9.4h) show nearly identical results, with spectra that are a mix between that of Ni-metal and NiO, in agreement with the XPS data. That is, there is a substantial proportion of metallic Ni clusters present. The main conclusion here is that there is no difference between the surface and bulk Ni incorporation, in both locations effectively identical results were found.

9.4.4 Manganese

The most consistent dopant is manganese. In this case all of the DFT, XPS, TEY, and PFY results support the same conclusion: that Mn^{2+} is integrated into the host crystal in substitutional octahedral positions, but in an environment with a much lower crystal field strength than MnO (which is 1.0 eV),[252] due to the larger spatial environment the Mn ions have in our case. In a past study it was shown that pristine Bi_2Te_3 and Mn doped Bi_2Te_3 have have measurably different conductive properties.[253] This difference must not originate due to metallic Mn, and in accordance with the cited study, there is no need to invoke any special inherent surface states to explain the conductive behaviour in the doped sample. Effectively, when incorporating Mn into Bi_2Te_3, both the surface and the bulk environments react identically, and any topological differences must be a result of the host material itself.

9.4.5 Copper

We found that copper undergoes a large scale transformation with age in Bi_2Te_3. Initially it was found to be in a purely metallic state; this was confirmed by the XPS measurements as well as both TEY and PFY in Fig. 9.4i. However, upon exposure to atmospheric conditions for one year, a substantial fraction of the metallic clusters have converted to 2+ ions. This is evident from the followup absorption spectra taken (shown as "aged"), which show substantial contributions to the signal in the same energetic locations as that of CuO.

We believe we can dismiss simple oxidation and the formation of CuO because the bulk of the sample also shows this same phenomena, and the exposure with air to the bulk of the sample is negligible. Also, surface oxidation generally takes place on the scale of only a few minutes,[254] and the initial XPS and XAS measurements showed no sign of this (after the samples were already exposed to air for months). Hence, we can conclude that the bulk and surface properties of Cu dopants in Bi_2Te_3 are effectively identical, and furthermore they age and change identically, and that no special surface states for Cu ions exist upon ion implantation. Note that copper spectra show no fine multiplet structure because of its full 3d shell (the same holds for d^9 in the case of Cu^{2+}), so calculations offer no extra insight in this specific case.

9.4.6 Iron

Lastly, iron is the most complicated case as it was necessary to use a combination of oxidation states on both the surface and in the bulk. However, the ratio of 2+:3+ Fe ions on the surface and in the bulk of the material is much different. If we first consider the TEY in Fig. 9.4g and compare it to the XPS in Fig. 9.3 we discover that there are some conflicting results. To contrast these, we examine further XAS measurements done a year after the initial ones to reveal that the surface undergoes a slow aging process. Initially, our XPS results showed that the surface contained 75% Fe^{3+} and 25% metallic Fe (Table 9.1). Then upon aging for six months our TEY measurements indicate that this ratio has fallen to about 58% Fe^{3+}, while the remaining 42% can be classified as Fe^{2+}. This is apparent from our linear sum of Fe^{2+} and Fe^{3+} calculations in Fig. 9.4g; one can see that the sum of the calculations is a near perfect fit for the experimental TEY spectrum. To test for reproducibility, further TEY measurements were done another year later (TEY aged), and they unambiguously show that the iron on the surface of the sample has become nearly entirely 3+. Hence, we have shown that the Bi_2Te_3 surface enables a slow transformation of Fe atoms' oxidation state toward 2+, given sufficient time.

What is interesting is how the bulk of Bi_2Te_3 reacts in a manner very contrary to its surface. In this case, bulk sensitive PFY measurements taken 18 months apart show no

	$10Dq$	Ds	Dt	β
Cr	1.65	-0.05	-0.05	0.75
Mn	0.6	0	0	0.72
Fe^{2+}	1.0	0	0	0.7
Fe^{3+}	1.6	-0.02	-0.02	0.6
Co	0.9	0	0	0.75
Ni	1.3	0	0	0.75
Cu	–	–	–	–

Table 9.2: Shown are the crystal field parameters for the calculations in pink in Fig. 9.4. The units for $10Dq$*, Ds, and Dt are eV, while* β *is unitless and corresponds to the scaling of the interatomic Slater integrals.*

change. We also found that contrary to the surface, it is Fe^{2+} ions that are much more inclined to reside in the bulk. To illustrate this, a similar analysis as above was done. The 2+ and 3+ calculations together show that the ratio of 2+:3+ is 60:40 in the bulk. It appears clear that in the case of iron dopants in Bi_2Te_3 the surface states are vastly different from that of those in the bulk, and undergo different incorporation mechanisms, as well as different aging effects.

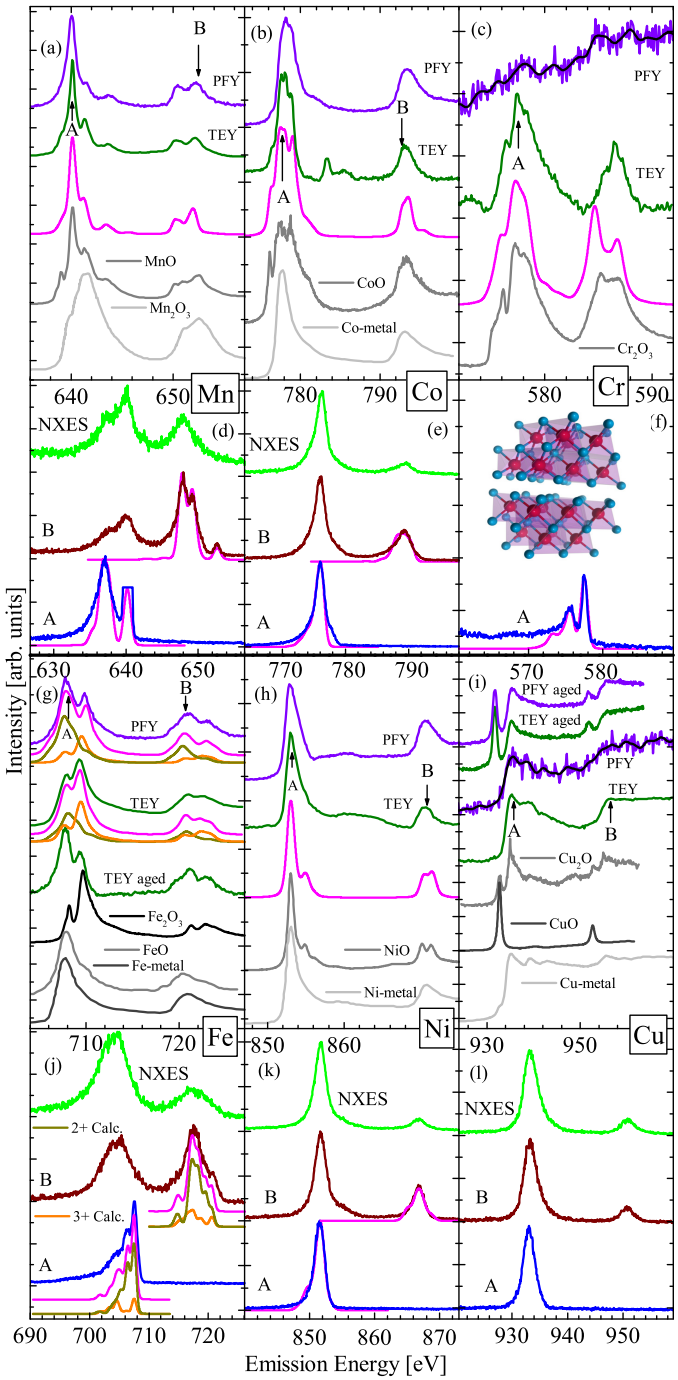

Figure 9.4: X-ray absorption and emission at the transition metal L-edges along with calculated spectra (pink). The Bi_2Te_3:TM XAS spectra are shown in black with standard oxide references in grey for comparison. Panels a–c and g–i contain the XAS spectra, while beneath each is the corresponding element's XES spectra in panels d–f and j–l, respectively. In panel (g), the iron calculations are shown in orange and dark yellow, with the linear sum of the two shown in pink. A thorough discussion of each element's spectra is given separately in the main text. High quality Ni, Co, Fe metal XAS reference spectra were taken from Ref. [251].

9.5 Conclusion

In closure, we have studied the differences between dopant atoms on the surface and in the bulk of what is known to be a promising material for topological technologies. The inherent differences between the bulk and surface structural properties can manifest themselves upon examining how transition metal dopants assimilate into the host lattice. This method of doping with 3d metals is an oft use way of fine-tuning a material's electronic and magnetic properties, and certainly shows favourable evidence to do so here again. Each of our dopants Cr, Mn, Fe, Co, and Ni behaved differently in Bi_2Te_3, facilitating the idea that there is a great deal of freedom in fine-tuning this versatile material. Thus, Bi_2Te_3 may be further honed by exploiting this large degree of freedom via synthesis using other techniques and/or introducing the dopants during synthesis. This would undoubtedly open the door to many other possibilities exploiting this material. By retaining the traditional surface conductivity and bulk insulating properties of this topological insulator, while tweaking its electric and magnetic properties to be better suited for a given technology, one is able to hone this widely heralded material for a tremendous array of technologies.

9.6 Acknowledgements

The XAS measurements were performed at the Canadian Light Source, and XES measurements were performed at the Advanced Light Source; both were supported by the Natural Sciences and Engineering Research Council of Canada (NSERC) and the Canada Research Chair program. XPS measurements were supported by the Ministry of Education and Science of Russian Federation (Project RFMEFI 58714X0002). The ion implantation of Bi_2Te_3 thin films was supported by Act 211 Government of the Russian Federation, agreement No. 02.A03.21.0006.

CHAPTER

TEN

Background Information

This manuscript is currently undergoing review at Physical Review Letters. My contributions to the final version of this manuscript were the following: I took all the experimental data, performed all of the analysis, and wrote the manuscript.

Oxygen Vacancy Induced Structural Distortions in Black Titania - A Unique Approach using Soft X-Ray EXAFS at the O K-Edge

B. Leedahl,[1] T. de Boer,[1] X. Yuan,[2] and A. Moewes[1]

[1] Department of Physics and Engineering Physics, University of Saskatchewan, 116 Science Place, Saskatoon, Saskatchewan, Canada, S7N 5E2

[2] Beijing National Laboratory for Molecular Sciences and State Key Laboratory of Rare Earth Materials Chemistry and Applications College of Chemistry and Molecular Engineering. Peking University, Beijing 100871, China

Abstract

Unknown changes in the crystalline order of regular TiO_2 result in the formation of black titania, which has garnered significant interest as a photocatalytic material due to the accompanying electronic changes. Herein, we determine the nature of the lattice distortion caused by an oxygen vacancy that in turn results in the formation of mid-band gap states. We introduce an innovative technique using a state-of-the-art silicon drift detector, which can be used in conjunction with extended x-ray absorption fine structure (EXAFS) to measure bulk interatomic distances. We illustrate how the energy dispersive nature of such a detector can allow us an unimpeded signal, indefinitely in energy space, thereby sidestepping the hurdles of more conventional EXAFS, which is often impeded by other absorption edges.

10.1 Introduction

Structural information regarding the transformation that takes place in regular "white" titanium dioxide as it transitions to black titania is still not fully understood, despite significant interest.[255] Although we know these crystallographic changes are key in the desirable electronic properties that arise, how the former causes changes the latter is not entirely clear.[210] However, it has been shown that new XRD peaks appear as the white to black transformation occurs, undoubtedly indicating some sort of structural distortion.[29] In addition to this, while the surface-disordered crystalline state of black titania has been documented via high resolution electron microscopy,[256, 12, 257] the bulk character is far less understood.[258] As such, the exact nature of the distortion present has been difficult to determine on account of the complexity and inhomogeneity of the crystal.

Extended x-ray absorption fine structure (EXAFS) is the study of the oscillatory nature of the absorption coefficient as a function of incident photon energy at energies just beyond that of an absorption edge. These oscillations arise from the local atomic structure of a material, and are most frequently used to determine bond distances and vibrational properties of a given element in a material.[259] However, despite being continuously refined ever since its

discovery in the early 1970s,[260] it still has yet to find commonplace use in the soft x-ray energy regime (≈50-1500 eV), despite the technique having contributed to many significant advances.[261, 262, 263] Only a small subset of examples exist in the publication record (all performed by surface sensitive total electron yield), and nothing in the last two decades since the advent of high resolution silicon drift detectors (SDDs).[264, 265, 266, 267, 268, 269]

There are a few reasons for this. (1) There is an abundant number of absorption edges in this energy range. Every element heavier than helium contains electrons with binding energies in this range. This is generally considered a limitation and large problem for EXAFS experiments, as one requires a range of several hundred (> 400) electron-volts of unperturbed absorption data from a single edge to extract meaningful data. (2) Many soft x-ray beamlines at synchrotron facilities do not have a monochromator that can, in a single scan, slew a necessarily large energy range without some combination of changing the mirror and grating of that monochromator. (3) The low probability of fluorescence emission in low-Z elements implies that extremely long count times are required to obtain sufficiently noise-free spectra.

However, using a silicon drift detector, one can achieve very high fluorescence count rates at sufficiently high resolution in the soft x-ray regime.[270, 271] And because silicon drift detectors are energy dispersive, the intrusion of absorption edges impeding our energy range is inconsequential, because we are able to filter out emission photons from other elements and observe only the fluorescence photons from the element of interest. If, however, the sample contains a large enough atomic percentage of some absorption edge energetically above our measured edge (here O), the XAS signal will contain an inverted image of that element as a new decay pathway emerges; fortunately, steps can be taken to disregard this as well. Furthermore, since we are observing emitted photons (as opposed to electrons) in the soft x-ray regime, the technique is bulk sensitive, probing to ≈100 nm in depth.

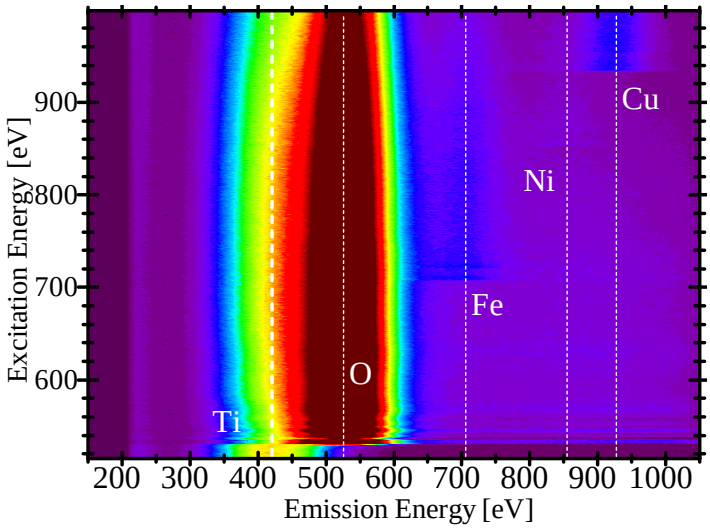

Figure 10.1: Color map of the TiO_2 anatase spectrum. Each horizontal slice corresponds to a single emission spectrum recorded by the SDD. The Ti emission is clearly visible pre-O K-edge. Because of this overlap with the O K-edge emission, one must separate the ≈100 eV wide emission lines by a fitting procedure to isolate the oxygen emission photons. Note the anomalous emission photons at the Fe, Ni, and Cu $L_{2,3}$ edges at 707, 858, and 933 eV, respectively. These are unwanted and are neglected from the data analysis using the procedure described in the text.

10.2 Experiment and Calculation Details

All absorption spectra were measured at the Resonant Elastic and Inelastic X-Ray Scattering (REIXS) beamline at the Canadian Light Source. The spectra were recorded in fluorescence yield mode using an SDD, such that the emission lines from the various elements could be distinguished on an energy scale. The total data set for a spectrum can be visualized in a two dimensional color map plot as shown in Figure 10.1. The energy resolution in this energy range is ≈100 eV, and therefore overlapping emission lines need to be dissociated.[52]

The Fe, Ni, and Cu $L_{2,3}$ emission photons that are observable in Figure 10.1 arise from scattered photons in the sample chamber interacting with the chamber itself. The ultra high vacuum chamber is made of stainless steel, and the arm that holds the sample is largely made of copper. The high intensity synchrotron light that impinges on the sample is scattered in all directions, but the SDD detector will detect only a minute solid angle of the overall emitted

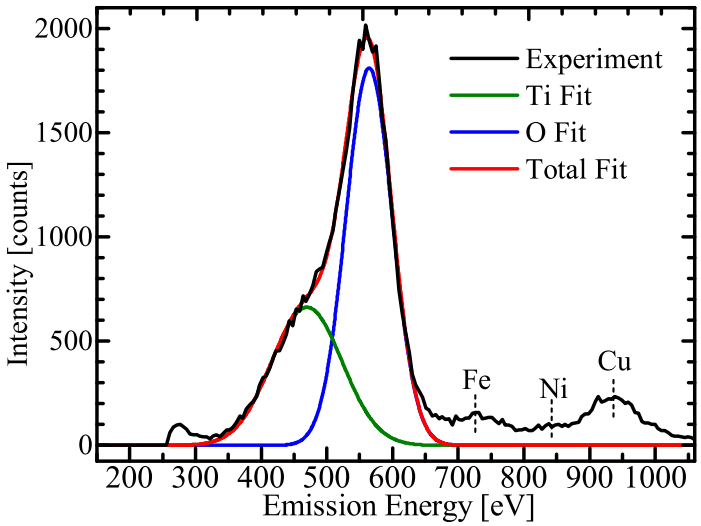

Figure 10.2: The experimental spectrum shown here corresponds to a single horizontal slice in Figure 10.1 taken at 975 eV excitation energy. In order to resolve them we used a fitting algorithm that constrains both the peak energy and FWHM for the Ti and O emission lines. The integrated intensity of the O peak corresponds to a single data point in the partial fluorescence yield XAS spectra shown in the Supplemental Material. Note that unwanted fluorescence from Fe, Ni, and Cu are easily neglected using this method.

and scattered photons. However, these stray photons will excite all constituent materials of the chamber as well. Since an SDD is not an angle resolved detector, it records these secondary photons as well.

While these secondary emissions are generally undesirable, for our present purposes it illuminates our ability to disregard unwanted photons, whether in our sample or otherwise. We can show that in-sample elements such as Ti can be excluded from the analysis, as well as out-of-sample materials that cannot be avoided such as Fe, Ni, and Cu.

The separation of these emission lines can be accomplished with a constrained Gaussian fitting algorithm, wherein the relevant peaks are each fit by a Gaussian curve, and the integrated Gaussian corresponds to the number of photons emitted by a given element for a given incident energy. A Gaussian curve contains three relevant parameters: its center, width (FWHM), and intensity. For the present analysis the Ti and O FWHMs and centers were constrained to remain in a narrow range as to not allow the fitting to stray from reasonable values.

The post-experiment analysis was performed with EXAFSPAK software [272] wherein a spline function was subtracted from the raw spectra (see Supplemental Material for raw experimental spectra) to obtain the EXAFS signal (red lines in Figure 10.3), which has the energy axis converted to wavenumber k. The displayed EXAFS signals are also weighted by their k^2 value, where $k^2 = 2m_eE/\hbar^2$ and m_e, E, and $\hbar$ are the electron mass, incident photon energy, and reduced Planck's constant, respectively. McKale table theoretical phase-shift and amplitude functions of the absorber-backscatter interaction were used for rutile, while full FEFF calculations were run to produce the models for anatase and black titania.[273] To achieve the fits to experiment shown in Figure 10.3(c-f), only the interatomic distances and Debye-Waller factors were allowed to vary.

10.3 Results and Discussion

10.3.1 Rutile and Anatase TiO_2

To demonstrate the reliability of this method, the well-known rutile and anatase TiO_2 powders were measured and compared to the known structures. Generally one wishes to obtain nearest and perhaps second nearest neighbor distances. However, we show that using the high count rates of modern SDD detectors, we can obtain interatomic distances well beyond this threshold in a reasonable amount of time.

Given the Raleigh criterion that the resolution in real space is $\Delta R = \pi/2\Delta k$,[274] we obtained spectra of significant quality to achieve resolutions of 0.19 Å. One should be careful to distinguish these values from the accuracy with which bond lengths can be determined, which is generally on the order of a few hundredths of an angstrom. The real space resolution values only tell us that peaks in the Fourier transform (interatomic distances) that are not separated by more than this distance cannot be distinguished from one another.

Figure 10.3 shows the k^2 weighted EXAFS, and the resulting Fourier transforms. The vertical lines in the Figure 10.3(b) show where the *peaks ought to be located in the nominal crystal structure of rutile*. Given that some coordination spheres will contain both Ti and O atoms at nearly the same distance from the central O atom, and noting our finite energy

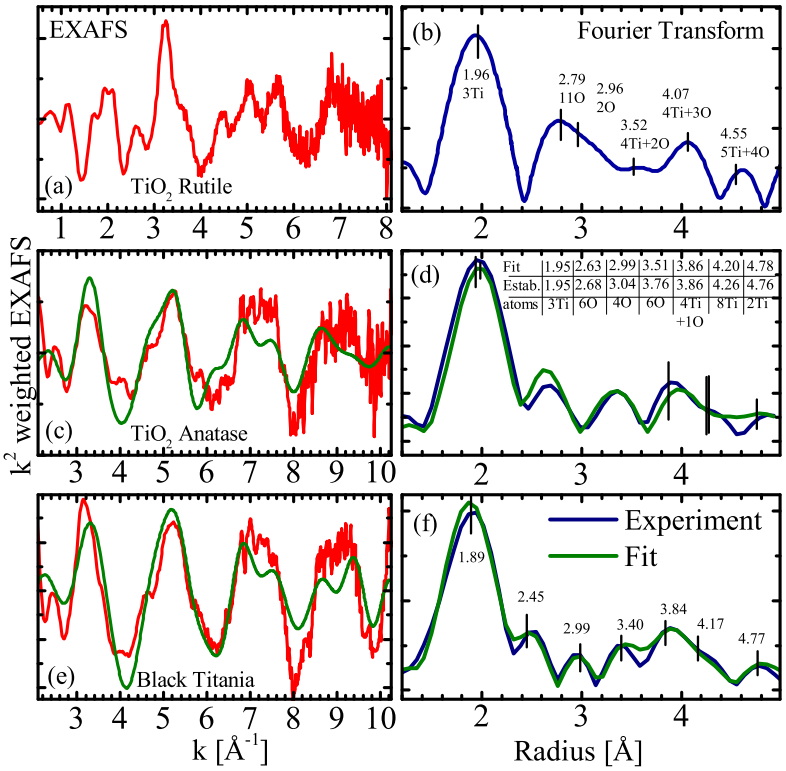

Figure 10.3: (a)(c)(e) EXAFS signal derived from XAS after subtracting a spline curve from the raw spectra. (b)(d)(f) Fourier transforms of EXAFS signals. For rutile, vertical lines represent where one would expect peaks to appear given the well established structure. For anatase, vertical lines were placed at the known Ti-O distances, with the length of line representing Ti degeneracy at that distance. The fit to the anatase experimental EXAFS was obtained using the interatomic distances shown in panel (d), which compare favorably to the established values. For the unknown black titania structure, the vertical lines are located at the interatomic distances that were used to obtain to fit curves.

resolution (ΔR), we would expect some peaks in the Fourier transform to contain a weighted average of the atoms that are at similar distances from the central oxygen atom. This is reflected by the vertical lines for rutile, which makes it visually easy to identify our experimental peak locations in relation to the nominal crystal of rutile, which is well known. The agreement is easily accurate to within the small discrepancies concerning these distances that exist in the literature, which vary by about 2%.[275, 276]

In both rutile and anatase TiO_2 the nearest neighbor Ti atoms can easily be determined to within 0.01 Å of the nominal value. The accuracy in determining this nearest neighbour distance is often all that one expects from EXAFS experiments. However, by comparison of the actual peak locations from our experiment to the nominal values indicated by the vertical lines in Figure 10.3(b) and the comparison of modelled and the established values in panel (d), it can be seen that further coordination shells can also be quite reliably determined with this method. Furthermore, the experiments were repeated and are entirely reproducible, indicating the consistency and reliability of this method.

10.3.2 Black Titania

We have used a model containing oxygen vacancies,[277, 278] which have previously been calculated to be an energetically favorable defect in TiO_2,[279, 280] and is therefore probable to form in the case of black titania.[281] We offer experimental evidence to supplement the theoretical work of this claim. We propose that the relaxation of atomic positions in the vicinity of this vacancy will cause deviations of the nominal bond lengths of anatase. Predictably, this occurs in a quite complex fashion; as one bond angle and/or distance changes, it has the propensity to alter those in its vicinity, and so on to the next nearest neighbours throughout the crystal.

We have formulated a defect that is well supported by the experimental data. This defect, which includes an oxygen vacancy as well as the shift of the nearby atoms, is shown in Figure 10.4. The advantage of using EXAFS in comparison to other techniques often used as evidence of oxygen vacancies such as electron paramagnetic resonance,[282] is that we can determine experimentally the actual crystal distortion on the scale of hundredths of

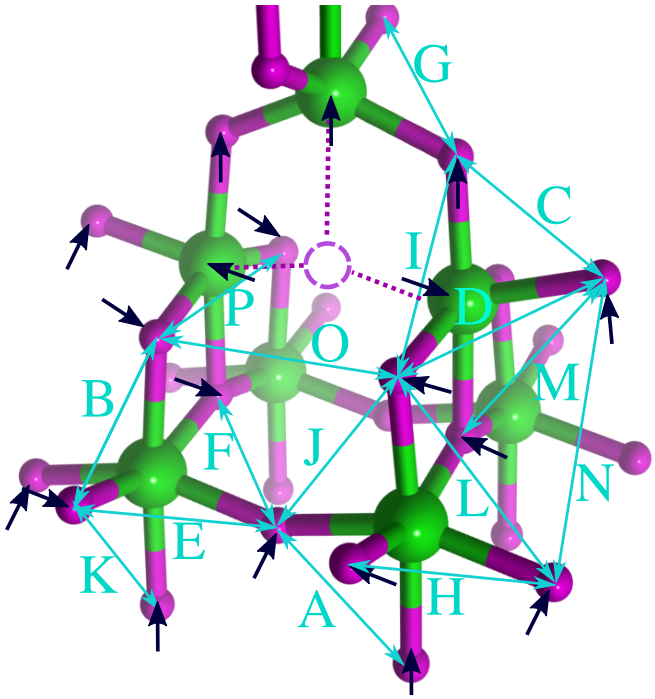

Figure 10.4: Proposed distorted anatase structure that results in black titania and its electronic properties. Arrows indicate the direction of the spatial relaxation of the atoms from their nominal positions. The labeled interatomic distances correspond to those list in Table 10.1.

nanometers.

Black titania is generally synthesized under a hydrogen rich environment and is known to have an enhanced hydrogen mobility thereafter.[256, 283, 284] This is likely to result in bulk oxygen vacancies which give rise to itinerant H_2 molecules and the appearance of OH bonds in the bulk, both of which play a crucial role in forming the mid-band gap states in black titania that make it such an attractive material. These weakly bound hydrogen atoms are able to easily diffuse throughout the crystal via the lattice distortions introduced here. The proclivity towards oxygen vacancy formation in TiO_2, combined with the hydrogenation process allow a subtle alteration to crystal structure, which in turn leads to a drastic alteration of the electronic properties.

Our experimental EXAFS spectrum for black titania, along with its Fourier transform is displayed in Figure 10.3(e-f). The vertical lines in panel (f) are now experimentally determined bond lengths found via the best fit algorithm described above. As a distortion

	Nominal	Degeneracy	Distorted	Multiplicity
	1.96	3 Ti	1.92(avg.)	36 Ti
A	2.46		2.45	8 O
B	2.46	2 O	2.43	8 O
C	2.46		2.50	2 O
D	2.79		2.95	4 O
E	2.79		2.75	8 O
F	2.79	4 O	2.60	4 O
G	2.79		2.76	2 O
H	2.79		2.91	4 O
I	3.04		3.21	4 O
J	3.04		2.73	4 O
K	3.04	4 O	2.88	8 O
L	3.04		2.99	4 O
M	3.04		3.13	2 O
N	3.71	2 O	3.62	4 O
O	3.78		3.48	2 O
P	3.78		3.78	20 O
	3.78	4 O	4.09	4 O
	3.86	4 Ti	3.84(avg.)	16 Ti
	4.26	8 TI	4.20(avg.)	46 Ti
	4.76	2 Ti	4.76(avg.)	10 Ti

Table 10.1: Interatomic distances (in Å) are as labeled in Fig 10.4. The nominal structure corresponds to that of anatase, black titania's parent structure. Degeneracy *refers to the number of atoms in the coordination sphere for every oxygen atom in the nominal structure.* Multiplicity *refers to the number of oxygen-oxygen or oxygen-titanium paths* per oxygen defect site. *The letters correspond to those shown in Figure 10.4.*

is introduced to the lattice, the degeneracy of oxygen-oxygen distances in anatase is broken, and instead of six coordination spheres between 2 Å and 4 Å in anatase, many more will occur in the vicinity of a vacancy (see Table 10.1). In the resulting Fourier transform for black titania, this will lead to smearing of peaks and the appearance of peaks at roughly the average of several of these combined distances. While this degeneracy is also broken in the case of Ti-O distances, it is much more manageable since the resulting Ti-O distances do not stray significantly from their central value (i.e. all the previously 4.26 Å bonds end up closely bunched around 4.17 Å). This, in addition to the fact that the Ti backscattering amplitude is much larger than O backscattering as a consequence of Ti's larger atomic size, implies that the Ti-O derived distances are more reliable than the O-O distances. For these reasons, the Ti-O distances were used as the basis for the proposed structural defect found in Figure 10.4. That is, our proposed black titania distortion was found such that it agrees with the interatomic Ti-O distances found via experiment and fitting. Table 10.1 lists the bond lengths in nominal anatase as well as the degeneracy and type of atom that exists for each coordination sphere, and the equivalent information in the vicinity of a vacancy for our proposed structure. The labeled bonds A to P correspond to those illustrated in Figure 10.4, the unlabeled ones were not shown in the figure as they would significantly obstruct clarity.

The first point to note is the significant reduction that occurs in the bond length to the nearest Ti neighbours: two Ti atoms at 1.94 Å and one at 1.98 Å now become resolved at 1.89 Å in Figure 10.3(f). The next Ti coordination sphere for anatase is at 3.86 Å, which we found at 3.84 Å in black titania, which is effectively identical within experimental error, which is ±0.02 Å for O–Ti distances. However, a noticeable reduction happens for the next Ti coordination sphere at 4.26 Å in anatase, but is found at 4.17 Å in our experiment. Lastly, the 4.78 Å Ti-O distance remains unchanged in the transition to black titania. While the trend is not consistent, this is actually encouraging from the perspective of searching for potential defect structures, as it vastly limits the number of possibilities. Literally hundreds of millions of defect structures were tested wherein the interatomic distances that resulted were compared to those found via experiment and fitting. The conclusion is that the only possible scenario is that shown in Figure 10.4. The Ti atoms, on account of their now

dangling bonds, shift slightly away from the vacancy in order to strengthen their bond with the rest of the lattice, while the nearby O atoms shift slightly inwards toward the vacancy to fill the empty space. This distortion uniquely maintains the above stated trends displayed by the observed shifts (and non-shifts) of Ti-O interatomic distances.

It is necessary to note that we should only expect near perfect agreement if it were the case that this distortion were repeated exactly throughout the entire crystal. However, in real world black titania the defect is not perfectly ordered throughout. And since the EXAFS results are a bulk average of all O atoms in the material, we should expect some influence from non-distorted sites. Despite this, we feel that our result is in fact exceptionally accurate as the model displays the correct trends given by the experimental data, and is indeed a true representation of the crystal structure of black titania.

10.4 Conclusion

Herein, we have shown conclusively that bulk soft x-ray EXAFS at the O K-edge is a valuable tool for systematically determining subtle structural distortions. We have presented very strong evidence that structural changes resulting from vacancies in a crystal can be directly measured. These changes to a parent material often underpin the emergence of novel electronic properties, and are often of the utmost importance to understand. This technique should not be overlooked, and has become feasible with the advent of modern silicon drift detectors, for which one can sidestep some of the difficulties inherent to EXAFS experiments.

10.5 Acknowledgements

This work was supported by the Natural Sciences and Engineering Research Council of Canada (NSERC) and the Canada Research Chairs program. Measurements were performed at the Canadian Light Source (supported by NSERC and the University of Saskatchewan).

10.6 Supplemental Material

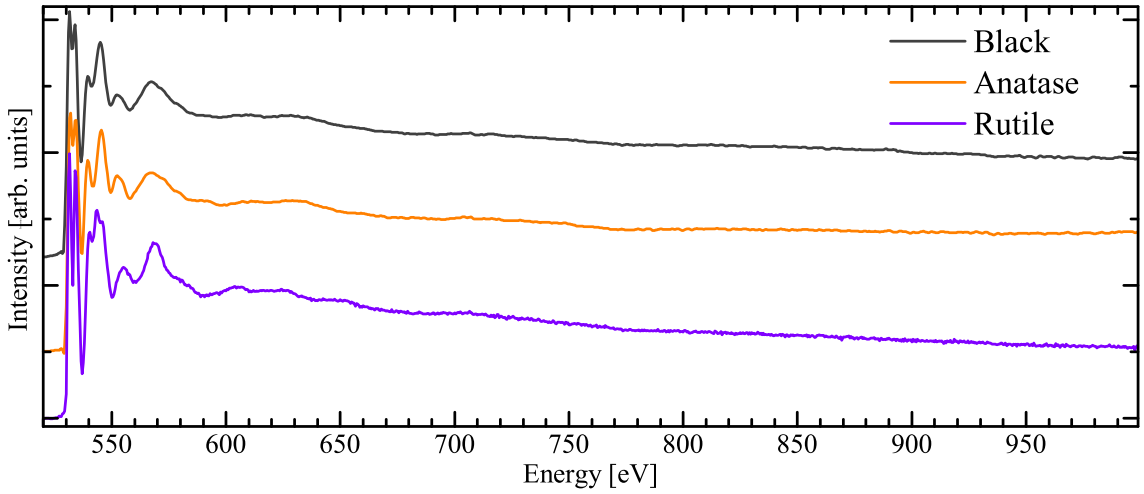

Figure 10.5: Raw partial fluorescence yield (PFY) absorption spectra taken by a silicon drift detector (SDD). Each data point corresponds to the integrated gaussian curve of the oxygen emission as shown in the main text Figure 2. A spline curve is then subtracted from these to produce the EXAFS signals shown in the main text Figure 3.

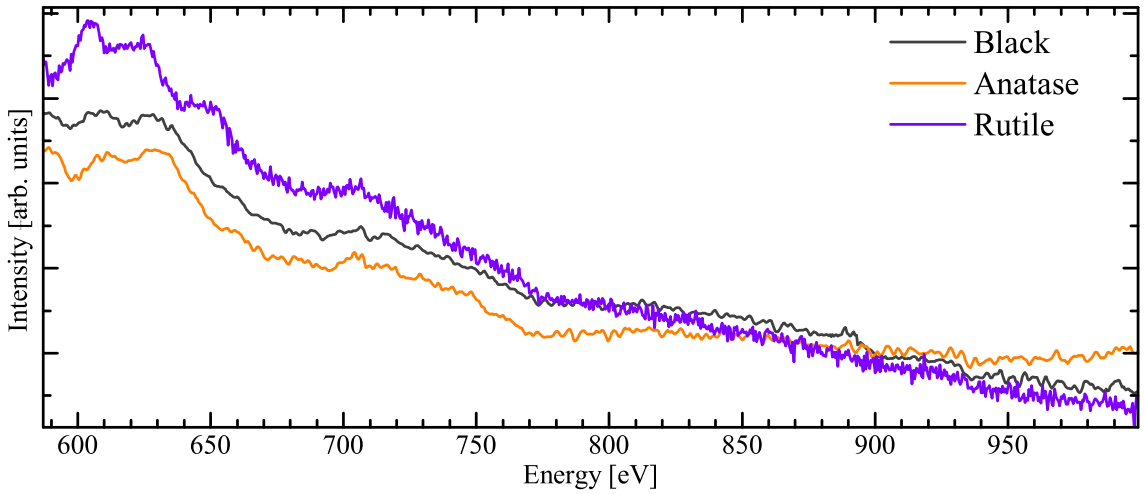

Figure 10.6: Magnified view of the above raw XAS spectra to further clarify the subtle differences between the TiO_2 samples.

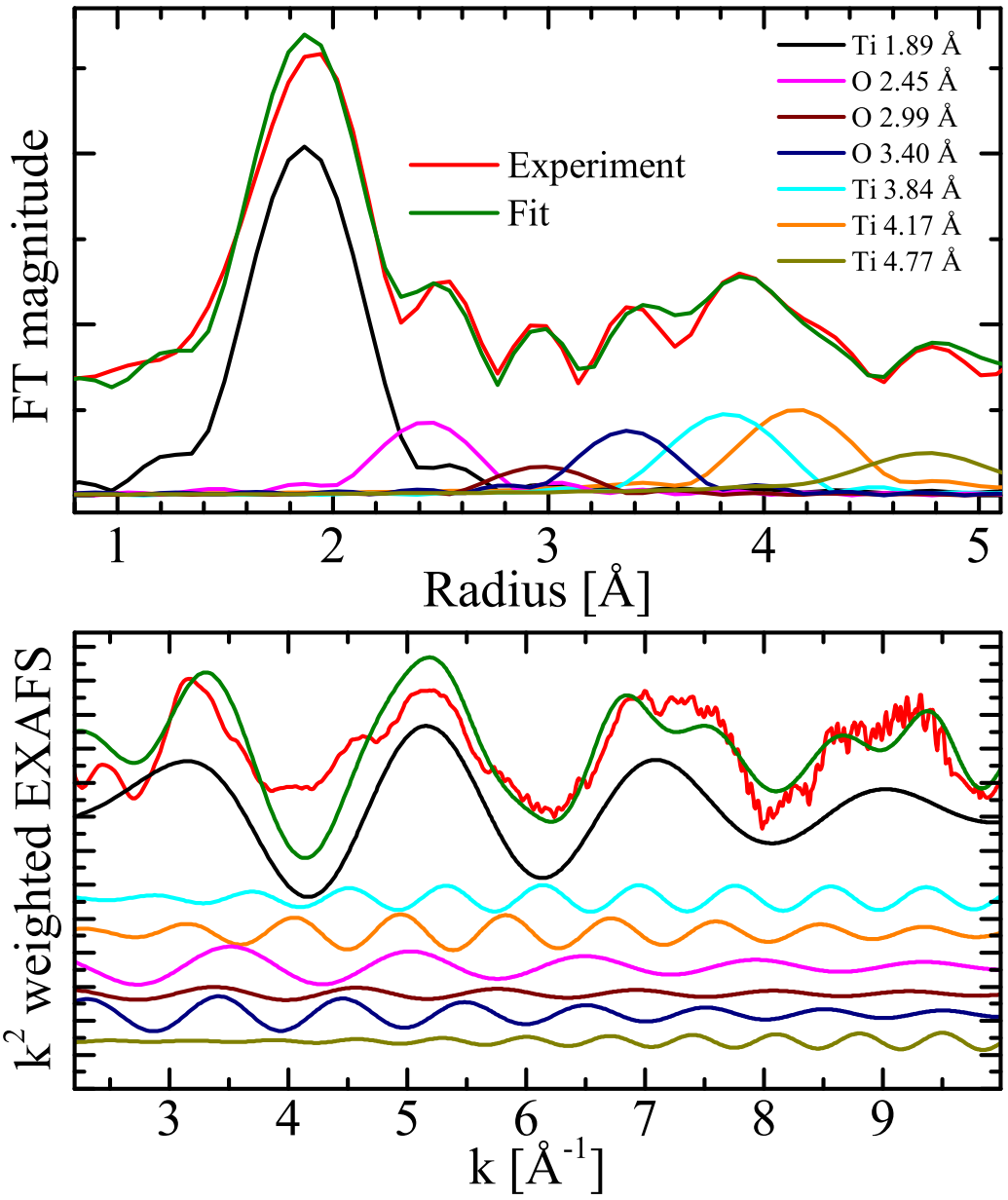

Figure 10.7: Bottom panel: In EXAFS analysis each scattering path (coordination sphere from the central oxygen atom) will contribute to the oscillations in the overall signal. Plotted are the contributions from several coordination spheres, wherein larger frequencies correspond to shorter interatomic distances after the Fourier transform is performed. One can see how the constructive and destructive interference in the oscillating EXAFS components sum to an overall fit of the experimental EXAFS. The Fourier transforms of the individual components in the bottom panel are color coded and plotted in the upper panel (with a FEFF calculated phase-shift), and the total overall fits are shown in green in both panels.

BIBLIOGRAPHY

[1] K. Rupp, M. Horovitz, F. Labonte, O. Shacham, K. Olukotun, L. Hammond, and C. Batten. Years of microprocessor trend data. *Figure available on webpage karlrupp.net/2018/02/42-years-of-microprocessor-trend-data/*, 2018.

[2] Wikipedia. Largest known prime number. *Data available from en.wikipedia.org/wiki/Largest_known_prime_number*, 2018.

[3] G. E. Moore. Cramming more components onto integrated circuits. *Electronics*, 38(8):1–14, 1965.

[4] G. E. Moore. Progress in digital integrated electronics. *Proc. Technical Digest Intl Electron Devices Meeting*, 21:11–13, 1975.

[5] R. Ananthanarayanan, S. K. Esser, H. D. Simon, and D. S. Modha. The cat is out of the bag: cortical simulations with 109 neurons, 1013 synapses. In *Proceedings of the Conference on High Performance Computing Networking, Storage and Analysis*, pages 1–12, Nov 2009.

[6] T. N. Theis and H. S. P. Wong. The end of Moore's Law: A new beginning for information technology. *Computing in Science Engineering*, 19(2):41–50, 2017.

[7] M. N. Baibich, J. M. Broto, A. Fert, F. Nguyen Van Dau, F. Petroff, P. Etienne, G. Creuzet, A. Friederich, and J. Chazelas. Giant magnetoresistance of (001)Fe/(001)Cr magnetic superlattices. *Phys. Rev. Lett.*, 61:2472–2475, Nov 1988.

[8] S. D. Bader and S. S. P. Parkin. Spintronics. *Annu. Rev. Condens. Matter Phys.*, 1(1):71–88, 2010.

[9] B. K. Kaushik, S. Verma, A. A. Kulkarni, and S. Prajapati. *Next Generation Spin Torque Memories*. Springer, Singapore, 2017.

[10] S. Sugahara and J. Nitta. Spin-transistor electronics: an overview and outlook. *Proceedings of the IEEE*, 98(12):2124–2154, 2010.

[11] Supriyo Datta and Biswajit Das. Electronic analog of the electrooptic modulator. *Appl. Phys. Lett*, 56(7):665–667, 1990.

[12] J.-J. Zhou, W. Feng, Y. Zhang, S. A. Yang, and Y. Yao. Engineering topological surface states and giant rashba spin splitting in BiTeI/Bi_2Te_3 heterostructures. 4:3841EP, 2014.

[13] S. G. Tan, M. B. Jalil, T. Liew, K. L. Teo, G. H. Lai, and T. C. Chong. Magnetoelectric spin-fet for memory, logic, and amplifier applications. *Journal of superconductivity*, 18(3):357–365, 2005.

[14] V. K. Joshi. Spintronics: a contemporary review of emerging electronics devices. *Engineering Science and Technology, an International Journal*, 19(3):1503–1513, 2016.

[15] F. Matsukura, D. Chiba, and H. Ohno. Semiconductors and semimetals. In *Spintronics*, chapter 5, pages 207–240. Elsevier, Oxford, 2008.

[16] F. de Groot. Multiplet effects in x-ray spectroscopy. *Coordination Chemistry Reviews*, 249(1):31 – 63, 2005. Synchrotron Radiation in Inorganic and Bioinorganic Chemistry.

[17] P. Dirac. Quantum mechanics of many-electron systems. In *Proceedings of the Royal Society of London A: Mathematical, Physical and Engineering Sciences*, volume 123, pages 714–733. The Royal Society, 1929.

[18] J. M. Coey. *Magnetism and magnetic materials*. Cambridge University Press, 2010.

[19] P. Weiss. Hypothesis of the molecular field and ferromagnetism. *Journal de Physique*, 6:661–690, 1907.

[20] W. Heisenberg. *Z. Physik*, 49:619, 1928.

[21] J. C. Slater. Atomic shielding constants. *Phys. Rev.*, 36:57–64, Jul 1930.

[22] Vogt E. The origin of ferromagnetism and antiferromagnetism in alloys of transition metals. *Phys. Status Solidi A*, 28(1):11–38, 1975.

[23] R. P. Feynman, R. B. Leighton, and M. Sands. *The Feynman Lectures on Physics*, volume 2. Basic books, 1964.

[24] R. Skomski. *Simple models of magnetism*. Oxford University Press on Demand, 2008.

[25] Y. Kakehashi. *Modern theory of magnetism in metals and alloys*, volume 175. Springer Science & Business Media, 2013.

[26] J. J. Rehr and R. C. Albers. Theoretical approaches to x-ray absorption fine structure. *Rev. Mod. Phys.*, 72:621–654, Jul 2000.

[27] F. de Groot and A. Kotani. *Core level spectroscopy of solids*. CRC press, 2008.

[28] R. J. Green, D. W. Boukhvalov, E. Z. Kurmaev, L. D. Finkelstein, H. W. Ho, K. B. Ruan, L. Wang, and A. Moewes. Room-temperature ferromagnetism via unpaired dopant electrons and $p - p$ coupling in carbon-doped in_2o_3: Experiment and theory. *Phys. Rev. B*, 86:115212, Sep 2012.

[29] Y. Lu, M. Höppner, O. Gunnarsson, and M. W. Haverkort. Efficient real-frequency solver for dynamical mean-field theory. *Phys. Rev. B*, 90:085102, Aug 2014.

[30] M. W. Haverkort, M. Zwierzycki, and O. K. Andersen. Multiplet ligand-field theory using wannier orbitals. *Phys. Rev. B*, 85:165113, Apr 2012.

[31] M. W. Haverkort, G. Sangiovanni, P. Hansmann, A. Toschi, Y. Lu, and S. Macke. Bands, resonances, edge singularities and excitons in core level spectroscopy investigated within the dynamical mean-field theory. *Eur. Phys. Lett.*, 108(5):57004, 2014.

[32] R. D. Cowan. *The theory of atomic structure and spectra*. Number 3. Univ. of California Press, 1981.

[33] O.P. Charkin and M.E. Dyatkina. Calculation of the Slater-Condon parameters from atomic spectra for atoms and ions of the second and third transition periods. *J. Struc. Chem.*, 5(3):406–414, 1964.

[34] G. Herzberg. *Atomic Spectra and Atomic Structure*. Dover Publications, 1945.

[35] H. C. Wolfe. Multiplet splitting and intensities of intercombination lines part i. *Phys. Rev.*, 41:443–458, 1932.

[36] F. M. F. de Groot, J. C. Fuggle, B. T. Thole, and G. A. Sawatzky. L_2. *Phys. Rev. B*, 41:928–937, Jan 1990.

[37] A. Hunt, D. Muir, and A. Moewes. Studying $4d - 4f$ transitions in Er using resonant inelastic scattering. *J. Elec. Spec. Rel. Phen.*, 144:573 – 576, 2005.

[38] F. M. F. de Groot, J. C. Fuggle, B. T. Thole, and G. A. Sawatzky. 2p x-ray absorption of 3d transition-metal compounds: An atomic multiplet description including the crystal field. *Phys. Rev. B*, 42:5459–5468, Sep 1990.

[39] P.H. Butler. *Point Group Symmetry Applications: Methods and Tables*. Plenum Press, 1981.

[40] Y. Kurashige, Garnet K.-L. Chan, and T. Yanai. Entangled quantum electronic wavefunctions of the mn4cao5 cluster in photosystem ii. *Nature Chemistry*, 5(8):660–666, 2013.

[41] C. Bradley and A. Cracknell. *The mathematical theory of symmetry in solids: representation theory for point groups and space groups*. Oxford University Press, 2010.

[42] L. E. Smart and E. A Moore. *Solid state chemistry: an introduction*. CRC press, 2012.

[43] Y. Tanabe and S. Sugano. On the absorption spectra of complex ions .1. *J. Phys. Soc. Jap.*, 9(5):753–766, 1954.

[44] A. Hauser. *Ligand Field Theoretical Considerations*, pages 49–58. Springer Berlin Heidelberg, Berlin, Heidelberg, 2004.

[45] R. J. Green, G. S. Chang, X. Y. Zhang, A. Dinia, E. Z. Kurmaev, and A. Moewes. Identifying local dopant structures and their impact on the magnetic properties of spintronic materials. *Phys. Rev. B*, 83:115207, Mar 2011.

[46] M . W. Haverkort. Spin and orbital degrees of freedom in transition metal oxides and oxide thin films studied by soft x-ray absorption spectroscopy. page 161, 2005. PhD Thesis.

[47] R. J. Green, T. Z. Regier, B. Leedahl, J. A. McLeod, X. H. Xu, G. S. Chang, E. Z. Kurmaev, and A. Moewes. Adjacent fe-vacancy interactions as the origin of room temperature ferromagnetism in $(in_{1-x}fe_x)_2o_3$. *Phys. Rev. Lett.*, 115:167401, Oct 2015.

[48] C. J. Ballhausen. *Ligand field theory*, volume 256. McGraw-Hill, New York, 1962.

[49] W. T. Hong, K. A. Stoerzinger, B. Moritz, T. P. Devereaux, W. Yang, and Yang S.-H. Probing $lamo_3$ metal and oxygen partial density of states using x-ray emission, absorption, and photoelectron spectroscopy. *J. Phys. Chem. C*, 119(4):2063–2072, 2015.

[50] E. Z. Kurmaev, R. G. Wilks, A. Moewes, L. D. Finkelstein, S. N. Shamin, and J. Kuneš. Oxygen x-ray emission and absorption spectra as a probe of the electronic structure of strongly correlated oxides. *Phys. Rev. B*, 77:165127, Apr 2008.

[51] T. M. Tolhurst, B. Leedahl, J. L. Andrews, P. M. Marley, S. Banerjee, and A. Moewes. Contrasting 1D tunnel-structured and 2D layered polymorphs of V_2O_5: relating crystal structure and bonding to band gaps and electronic structure. *Phys. Chem. Chem. Phys.*, 18:15798–15806, 2016.

[52] T. M. Tolhurst, J. L. Andrews, B. Leedahl, P. M. Marley, S. Banerjee, and A. Moewes. Structure-induced switching of the band gap, charge order, and correlation strength in ternary vanadium oxide bronzes. *Chem.-Eur. J.*, 23(41):9846–9856, 2017.

[53] J. A. McLeod, D. W. Boukhvalov, D. A. Zatsepin, R. J. Green, B. Leedahl, L. Cui, E. Z. Kurmaev, I. S. Zhidkov, L. D. Finkelstein, N. V. Gavrilov, S. O. Cholakh, and A. Moewes. Local structure of Fe impurity atoms in ZnO: Bulk versus surface. *J. Phys. Chem. C*, 118(10):5336, 2014.

[54] T. D. Boyko, R. J. Green, R. Dronskowski, and A. Moewes. Electronic band gap reduction in manganese carbodiimide: MnNCN. *J. Phys. Chem. C*, 117(24):12754–12761, 2013.

[55] J. L. Andrews, L. R. De Jesus, T. M. Tolhurst, P. M. Marley, A. Moewes, and S. Banerjee. Intercalation-induced exfoliation and thickness-modulated electronic structure of a layered ternary vanadium oxide. *Chem. Mater.*, 29(7):3285–3294, 2017.

[56] R. J. O. Mossanek, A. Mocellin, M. Abbate, B. G. Searle, P. T. Fonseca, and E. Morikawa. Cluster model and band structure calculations of v_2o_5: Reduced v^{5+} symmetry and many-body effects. *Phys. Rev. B*, 77:075118, Feb 2008.

[57] J. E. Penner-Hahn. X-ray absorption spectroscopy in coordination chemistry. *Coordination Chemistry Reviews*, 190-192:1101 – 1123, 1999.

[58] J.J. Yeh and I. Lindau. Atomic subshell photoionization cross sections and asymmetry parameters: 1 z 103. *At. Data Nucl. Data Tables*, 32(1):1 – 155, 1985.

[59] W. Błachucki, J. Szlachetko, J. Hoszowska, J.-Cl. Dousse, Y. Kayser, M. Nachtegaal, and J. Sá. High energy resolution off-resonant spectroscopy for x-ray absorption spectra free of self-absorption effects. *Phys. Rev. Lett.*, 112:173003, Apr 2014.

[60] A. J. Achkar, T. Z. Regier, H. Wadati, Y.-J. Kim, H. Zhang, and D. G. Hawthorn. Bulk sensitive x-ray absorption spectroscopy free of self-absorption effects. *Phys. Rev. B*, 83:081106, Feb 2011.

[61] L. Tröger, D. Arvanitis, K. Baberschke, H. Michaelis, U. Grimm, and E. Zschech. Full correction of the self-absorption in soft-fluorescence extended x-ray-absorption fine structure. *Phys. Rev. B*, 46:3283–3289, Aug 1992.

[62] G. van der Laan, B.T. Thole, G. A. Sawatzky, J. B. Goedkoop, J. C. Fuggle, J-M. Esteva, R. Karnatak, J. P. Remeika, and H. A. Dabkowska. Experimental proof of magnetic x-ray dichroism. *Phys. Rev. B*, 34:6529–6531, Nov 1986.

[63] B. T. Thole, G. van der Laan, and G. A. Sawatzky. Strong magnetic dichroism predicted in the $M_{4,5}$ x-ray absorption spectra of magnetic rare-earth materials. *Phys. Rev. Lett.*, 55:2086–2088, Nov 1985.

[64] B. T. Thole, P. Carra, F. Sette, and G. van der Laan. X-ray circular dichroism as a probe of orbital magnetization. *Phys. Rev. Lett.*, 68:1943–1946, Mar 1992.

[65] G. van der Laan. Applications of soft x-ray magnetic dichroism. *J. Phys.: Conf. Ser.*, 430(1):012127, 2013.

[66] E. Beaurepaire, H. Bulou, F. Scheurer, and J. P. Kappler. *Magnetism: A synchrotron radiation approach*, volume 697. Springer, 2006.

[67] I. P. Krug. *Magnetic Proximity Effects in Highly-ordered Transition Metal Oxide Heterosystems-a Study by Soft-x-ray Photoemission Microscopy*, volume 2. Forschungszentrum Jülich, 2008.

[68] W. L. O'Brien and B. P. Tonner. Orbital and spin sum rules in x-ray magnetic circular dichroism. *Phys. Rev. B*, 50:12672–12681, Nov 1994.

[69] P. Carra, H. König, B. T. Thole, and M. Altarelli. Magnetic x-ray dichroism: General features of dipolar and quadrupolar spectra. *Phys. B: Cond. Mat.*, 192(1-2):182–190, 1993.

[70] C. Piamonteze, P. Miedema, and F. de Groot. Accuracy of the spin sum rule in xmcd for the transition-metal L edges from manganese to copper. *Phys. Rev. B*, 80:184410, 2009.

[71] E. C. Wasinger, F. De Groot, B. Hedman, K. O. Hodgson, and E. I. Solomon. L-edge x-ray absorption spectroscopy of non-heme iron sites: experimental determination of differential orbital covalency. *J. Amer. Chem. Soci.*, 125(42):12894–12906, 2003.

[72] P. Srivastava, N. Haack, H. Wende, R. Chauvistré, and K. Baberschke. Modifications of the electronic structure of ni/cu(001) as a function of the film thickness. *Phys. Rev. B*, 56:R4398–R4401, Aug 1997.

[73] S. Shi, Z. Sun, A. Bedoya-Pinto, Patrizio Graziosi, Xin L., X. Liu, L. Hueso, V. A. Dediu, Y. Luo, and M. Fahlman. Hybrid interface states and spin polarization at ferromagnetic metal-organic heterojunctions: Interface engineering for efficient spin injection in organic spintronics. *Adv. Funct. Mater.*, 24(30):4812–4821, 2014.

[74] Dale E. Sayers, Edward A. Stern, and Farrel W. Lytle. New technique for investigating noncrystalline structures: Fourier analysis of the extended x-ray¯absorption fine structure. *Phys. Rev. Lett.*, 27:1204–1207, Nov 1971.

[75] M. Newville. EXAFS analysis using FEFF and FEFFIT. *J. Synch. Rad.*, 8(2):96–100, 2001.

[76] W. Bambynek, B. Crasemann, R. W. Fink, H. U. Freund, H. Mark, C. D. Swift, R. E. Price, and P. V. Rao. X-ray fluorescence yields, auger, and coster-kronig transition probabilities. *Rev. Mod. Phys.*, 44:716–813, Oct 1972.

[77] L. J. P. Ament, M. van Veenendaal, T. P. Devereaux, J. P. Hill, and J. van den Brink. Resonant inelastic x-ray scattering studies of elementary excitations. *Rev. Mod. Phys.*, 83:705–767, Jun 2011.

[78] H. A. Kramers and W. Heisenberg. On the dispersal of radiation by atoms. *Z. Phys.*, 31:681–708, 1925.

[79] J. J. Sakurai. *Advanced Quantum Mechanics*. Addison-Wesley Publishing, 1967.

[80] T. D. Boyko, T. Gross, M. Schwarz, H. Fuess, and A. Moewes. The local crystal structure and electronic band gap of β-sialons. *J. Mater. Sci.*, 49(8):3242–3252, Apr 2014.

[81] N. F. Mott. The transition to the metallic state. *Philos. Mag.*, 6(62):287–309, 1961.

[82] John Hubbard. Electron correlations in narrow energy bands iii. an improved solution. *Proc. R. Soc. Lond. A*, 281(1386):401–419, 1964.

[83] E. Z. Kurmaev, A. L. Ankudinov, J. J. Rehr, L. D. Finkelstein, P. F. Karimov, and A. Moewes. The L_2:L_3 intensity ratio in soft x-ray emission spectra of 3d-metals. *J. Electron Spectrosc. Relat. Phenom.*, 148:1, 2005.

[84] J. Kawai. Intensity ratio of transition-metal Lα and Lβ lines. *Rigaku J.*, 18(1):31, 2001.

[85] A. O'Hara, T. N. Nunley, A. B. Posadas, S. Zollner, and A. A. Demkov. Electronic and optical properties of NbO_2. *J. Appl. Phys.*, 116(21):213705, 2014.

[86] A. B. Posadas, A. OHara, S. Rangan, R. A. Bartynski, and A. A. Demkov. Band gap of epitaxial in-plane-dimerized single-phase nbo2 films. *Appl. Phys. Lett.*, 104(9):092901, 2014.

[87] T. L. Tansley and C. P. Foley. Optical band gap of indium nitride. *J. Appl. Phys.*, 59(9):3241–3244, 1986.

[88] V. Kumar, S. Kr. Sharma, T. P. Sharma, and V. Singh. Band gap determination in thick films from reflectance measurements. *Optical Materials*, 12(1):115 – 119, 1999.

[89] V. Srikant and D. R. Clarke. On the optical band gap of zinc oxide. *J. Appl. Phys.*, 83(10):5447–5451, 1998.

[90] C. J. Powell and A. Jablonski. Surface sensitivity of x-ray photoelectron spectroscopy. *Nucl. Instrum. Methods. Phys. Res. A*, 601(1):54 – 65, 2009. Special issue in honour of Prof. Kai Siegbahn.

[91] G. G. Fuentes, E. Elizalde, F. Yubero, and J. M. Sanz. Electron inelastic mean free path for ti, tic, tin and tio2 as determined by quantitative reflection electron energy-loss spectroscopy. *Surface and Interface Analysis*, 33(3):230–237, MAR 2002.

[92] M. P. Seah, I. S. Gilmore, and S. J. Spencer. Quantitative XPS: I. Analysis of x-ray photoelectron intensities from elemental data in a digital photoelectron database. *J. Electron Spectrosc. Relat. Phenom.*, 120(1):93 – 111, 2001.

[93] D. Briggs and G. Beamson. XPS studies of the oxygen 1s and 2s levels in a wide range of functional polymers. *Anal. Chem.*, 65(11):1517–1523, 1993.

[94] C. D. Wagner, L. E. Davis, M. V. Zeller, J. A. Taylor, R. H. Raymond, and L. H. Gale. Empirical atomic sensitivity factors for quantitative analysis by electron spectroscopy for chemical analysis. *Surf. Interf. Anal.*, 3(5):211–225.

[95] J. F. Ziegler, M.D. Ziegler, and J.P. Biersack. Srim - the stopping and range of ions in matter. *Nucl. Instr. Meth. Phys. Res. B*, 268(11):1818 – 1823, 2010.

[96] B. Gilbert, B. H. Frazer, A. Belz, P. G. Conrad, K. H. Nealson, D. Haskel, J. C. Lang, G. Srajer, and G. De Stasio. Multiple scattering calculations of bonding and x-ray absorption spectroscopy of manganese oxides. *J. Phys. Chem. A*, 107(16):2839–2847, 2003.

[97] C. Mitra, Z. Hu, P. Raychaudhuri, S. Wirth, S. I. Csiszar, H. H. Hsieh, H.-J. Lin, C. T. Chen, and L. H. Tjeng. Direct observation of electron doping in $la_{0.7}ce_{0.3}mno_3$ using x-ray absorption spectroscopy. *Phys. Rev. B*, 67:092404, Mar 2003.

[98] C. E. Shannon. A mathematical theory of communication (parts i and ii). *Bell System Tech. J.*, 27:379–423, 1948.

[99] E. T. Jaynes. On the rationale of maximum-entropy methods. *Proc. IEEE*, 70(9):939–952, 1982.

[100] Z. V. Pchelkina, A. L. Pitman, A. Moewes, E. Z. Kurmaev, Teck-Yee Tan, D. C. Peets, Je-Geun Park, and S. V. Streltsov. Electronic structure of li_2ruo_3 studied by lda and lda+dmft calculations and soft x-ray spectroscopy. *Phys. Rev. B*, 91:115138, Mar 2015.

[101] J. Skilling and R. K. Bryan. Maximum entropy image reconstruction: general algorithm. *Mon. Notices Royal Astron. Soc.*, 211(1):111–124, 1984.

[102] J. Laverock, A. R. H. Preston, D. Newby Jr., K. E. Smith, and S. B. Dugdale. Maximum entropy deconvolution of resonant inelastic x-ray scattering spectra. *Phys. Rev. B*, 84:235111, 2011.

[103] A. S. Hamid, A. Uedono, Zs. Major, T. D. Haynes, J. Laverock, M. A. Alam, S. B. Dugdale, and D. Fort. Electronic structure and fermi surface of the weak ferromagnet ni$_3$al. *Phys. Rev. B*, 84:235107, Dec 2011.

[104] S. B. Dugdale, M. A. Alam, H. M. Fretwell, M. Biasini, and D. Wilson. Application of maximum entropy to extract Fermi surface topology from positron annihilation measurement. *J. Phys.: Cond. Matt.*, 6(31):L435, 1994.

[105] H. M. Fretwell, S. B. Dugdale, M. A. Alam, M. Biasini, L. Hoffmann, and A. A. Manuel. Reconstruction of 3D electron-positron momentum densities from 2D projections: Role of maximum-entropy deconvolution prior to reconstruction. *EPL (Europhysics Letters)*, 32(9):771, 1995.

[106] M. Grätzel. Photoelectrochemical cells. *Nature*, 414:338, 2001.

[107] A. Hagfeldt and M. Grätzel. Light-induced redox reactions in nanocrystalline systems. *Chem. Rev.*, 95:49, 1995.

[108] A. L. Linsebigler and J.T. Yates G. Lu. Photocatalysis on TiO_2 surfaces: principles, mechanisms, and selected results. *Chem. Rev.*, 95:735, 1995.

[109] A. Millis and S. Le Hunte. An overview of semiconductor photocatalysis. *J. Photochem. Photobiol.*, A 108:1, 1997.

[110] M. Russo, S. E. J. Rigby, W. Caserid, and N. Stingelin. Pronounced photochromism of titanium oxide hydrates (hydrous TiO_2). *J. Mater. Chem.*, 20:1348, 2010.

[111] A. H. Macdonald, P. Schiffer, and N. Samarth. Ferromagnetic semiconductors: moving beyond (Ga,Mn)As. *Nat. Mater.*, 4:195, 2005.

[112] G. S. Chang, E. Z. Kurmaev, D. W. Boukhvalov, L. D. Finkelstein, D. H. Kim, T. W. Noh, A. Moewes, and T. A. Callcott. Clustering of impurity atoms in co-doped anatase TiO_2 thin films probed with soft x-ray fluorescence. *J. Phys.: Condens. Matter*, 18:4243, 2006.

[113] X. Chen and S. S. Mao. Titanium dioxide nanomaterials: synthesis, properties, modifications, and applications. *Chem. Rev.*, 107:2891, 2007.

[114] T. Ohtsuki, A. Chainani, R. Eguchi, M. Matsunami, Y. Takata, M. Taguchi, Y. Nishino, K. Tamasaku, M. Yabashi, T. Ishikawa, M. Oura, Y. Senba, H. Ohashi, and S. Shin. Role of Ti $3d$ carriers in mediating the ferromagnetism of Co:TiO_2 anatase thin films. *Phys. Rev. Lett.*, 106:047602, Jan 2011.

[115] G. S. Chang, E. Z. Kurmaev, D. W. Boukhvalov, L. D. Finkelstein, A. Moewes, H. Bieber, S. Colis, and A. Dinia. Co and Al co-doping for ferromagnetism in ZnO:Co diluted magnetic semiconductors. *J. Phys.: Condens. Matter*, 21:056002, 2009.

[116] J. Pascual, J. Camassel, and H. Mathieu. Fine structure in the intrinsic absorption edge of tio_2. *Phys. Rev. B*, 18:5606–5614, Nov 1978.

[117] K. Hashimoto, H. Irie, and A. Fujishima. TiO_2 photocatalysis: A historical overview and future prospects. *Jpn. J. Appl. Phys.*, 44:8269, 2005.

[118] A. Katoch, H. Kim, T. Hwang, and S. S. Kim. Preparation of highly stable TiO_2 sols and nanocrystalline TiO_2 films via a low temperature solgel route. *J. Sol-Gel Sci. Technol.*, 61:77, 2012.

[119] Y. A. Kotov. Electric explosion of wires as a method for preparation of nanopowders. *J. of Nanopart. Res.*, 5:539, 2003.

[120] S.Tougaard. Low energy inelastic electron scattering properties of noble and transition metals. *Solid State Communs.*, 61:547, 1987.

[121] J. F. Moulder, W. F. Stickle, P. E. Sobol, and K. D. Bomben. *Handbook of X-ray Photoelectron Spectroscopy*. Perkin-Elmer Corporation, 1992.

[122] J. Jia, T. Callcott, J. Yurkas, A. Ellis, F. Himpsel, M. Samant, J. Stöhr, D. Ederer, J. Carlisle, E. Hudson, L. Terminello, D. Shuh, and R. Perera. First experimental results from IBM/TENN/TULANE/LLNL/LBL undulator beamline at the Advanced Light Source. *Rev. Sci. Instrum.*, 66:1394, 1995.

[123] T. Regier, J. Krochak, T. K. Sham, Y. F. Hu, J. Thompson, and R. I. R. Blyth. Performance and capabilities of the Canadian Dragon: The SGM beamline at the Canadian Light Source. *Nucl. Instrum. Meth. A*, 582:93, 2007.

[124] M. Strange, I. S. Kristensen, and K. S. Thygesen. Benchmark density functional theory calculations for nanoscale conductance. *J. Chem. Phys.*, 128:114714, 2008.

[125] G. S. Chang, E. Z. Kurmaev, D. W. Boukhvalov, L. D. Finkelstein, S. Colis, T. M. Pedersen, A. Moewes, and A. Dinia. Effect of Co and O defects on the magnetism in Co-doped ZnO: Experiment and theory. *Phys. Rev. B*, 75:195215, 2007.

[126] J. P. Perdew, K. Burke, and M. Ernzerhof. Generalized gradient approximation made simple. *Phys. Rev. Lett.*, 77:3865–3868, Oct 1996.

[127] M. García-Mota, A. Vojvodic, F. Abild-Pedersen, and J. K. Nørskov. Electronic origin of the surface reactivity of transition-metal-doped TiO_2(110). *J. Phys. Chem. C*, 114:460, 2012.

[128] K. Sato, L. Bergqvist, J. Kudrnovsky, P. H. Dederichs, O. Eriksson, I. Turek, B. Sanyal, G. Bouzerar, H. Katayama-Yoshida, V. a. Dinh aand T. Fukushima, H. Kizaki, and R. Zeller. First-principles theory of dilute magnetic semiconductors. *Rev. Mod. Phys.*, 82:1633, 2010.

[129] R. Zimmermann, P. Steiner, R. Claessen, F. Reinert, S. Hfner, P. Blaha, and P. Dufek. Electronic structure of 3d-transition-metal oxides: on-site coulomb repulsion versus covalency. *J. Phys.: Condens. Matter*, 11:1657, 1999.

[130] X. Gao, D. Qi, S.C. Tan, A. T. S. Wee, X. Yu, and H. O. Moser. Thickness dependence of x-ray absorption and photoemission in fe thin films on si(001). *J. Electr. Spectr. Relat. Phenom.*, 151:199, 2006.

[131] N. A. Skorikov, M. A. Korotin, E. Z. Kurmaev, and S. O. Cholakh. Computer simulation of the energy gap in ZnO- and TiO_2-based semiconductor photocatalysts. *J. Exp. Theor. Phys.*, 142:1196, 2012.

[132] K. Potzger, S. Zhou, H. Reuther, A. Mcklich, F. Eichhorn, M. Helm N. Schell, W. Skorupa, and J. Fassbender. Fe implanted ferromagnetic zno. *Appl. Phys. Lett.*, 88:052208, 2006.

[133] J. P. Crocombette, M. Pollak, F. Jollet, N. Thromat, and M. Gautier-Soyer. X-ray-absorption spectroscopy at the fe $l_{2,3}$ threshold in iron oxides. *Phys. Rev. B*, 52:3143–3150, Aug 1995.

[134] D .A. Zatsepin, A. Hunt, A. Moewes, E. Z. Kurmaev, N. V. Gavrilov, I. S. Zhidkov, and S. O. Cholakh. Pb^+ implanted SiO_2 probed by soft x-ray emission and absorption spectroscopy. *J. Non-Cryst. Solids*, 357:3381, 2011.

[135] J. A. McLeod, A. Moewes, D. A. Zatsepin, E. Z. Kurmaev, A. Wypych, I. Bobowska, A. Opasinska, and S. O. Cholakh. Predicting the band gap of ternary oxides containing $3d^{10}$ and $3d^0$ metals. *Phys. Rev. B*, 86:195207, Nov 2012.

[136] R. J. Green, A. Hunt, D. A. Zatsepin, D. W. Boukhvalov, J. A. McLeod, E. Z. Kurmaev, N. A. Skorikov, N. V. Gavrilov, and A. Moewes. Interplay of ballistic and chemical effects in the formation of structural defects for Sn and Pb implanted silica. *J. Non-Cryst. Sol.*, 358:3187, 2012.

[137] J. A. McLeod, D. W. Boukhvalov, D. A. Zatsepin, R. J. Green, B. Leedahl, L. Cui, E. Z. Kurmaev, I. S. Zhidkov, L. D. Finkelstein, N. V. Gavrilov, S. O. Cholakh, and A. Moewes. Local structure of fe impurity atoms in ZnO: Bulk versus surface. *J. Phys. Chem. C*, 118(10):5336–5345, 2014.

[138] K. Nagaveni, M. S. Hegde, and G. Madras. Structure and photocatalytic activity of $Ti_{1-x}M_xO_{2\pm\delta}$ (M = W, V, Ce, Zr, Fe, and Cu) synthesized by solution combustion method. *J. Phys. Chem. B*, 108:20204, 2004.

[139] A. N. Mangham, N. Govind, M. E. Bowden, V. Shutthanandan, A. G. Joly, M. A. Henderson, and S. A. Chambers. Photochemical properties, composition, and structure in molecular beam epitaxy grown Fe doped and (Fe,N) codoped rutile TiO_2(110). *J. Phys. Chem. C*, 115:15416, 2011.

[140] Y. Zhang, S. G. Ebbinghaus, A. Weidenkaff, T. Kurz, H.-A. Krug von Nidda, P. J. Klar, M. Gngerich, and A. Reller. Controlled iron-doping of macrotextured nanocrystalline titania. *Chem. Mater.*, 15:4028, 2003.

[141] X. Zhang, M. Zhou, and L. Lei. Co-deposition of photocatalytic Fe doped TiO_2 coatings by MOCVD. *Catal. Commun.*, 7:427, 2006.

[142] T. Dietl, H. Ohno, F. Matsukura, J. Cibert, and D. Ferrand. Zener model description of ferromagnetism in zinc-blende magnetic semiconductors. *Science*, 287:1019, 2000.

[143] Y. Matsumoto, M. Murakami, T. Shono, T. Hasegawa, T. Fukumura, M. Kawasaki, P. Ahmet, T. Chikyow, S. Koshihara, and H. Koinuma. Room-temperature ferromagnetism in transparent transition metal-doped titanium dioxide. *Science*, 291:854, 2001.

[144] J.M.D. Coey and S.A. Chambers. Oxide dilute magnetic semiconductors—fact or fiction? *Mrs. Bull.*, 33:1053, 2008.

[145] J. Y. Kim, J. H. Park, B. G. Park, H. J. Noh, S. J. Oh, J. S.Yang, D. H. Kim, S. D. Bu, T.W. Noh, H.J. Lin, H.H. Hsieh, and C.T. Chen. Ferromagnetism induced by clustered co in co-doped anatase TiO_2 thin films. *Phys. Rev. Lett.*, 90:017401, 2003.

[146] K. A. Griffin, A. B. Pakhomov, C. M. Wang, S. M. Heald, and Kannan M. Krishnan. Intrinsic ferromagnetism in insulating cobalt doped anatase TiO_2. *Phys. Rev. Lett.*, 94:157204, 2005.

[147] B. K. Roberts, A. B. Pakhomov, P. Voll, and K. M. Krishnan. Surface scaling of magnetism in Cr:ZnO dilute magnetic dielectric thin films. *Appl. Phys. Lett.*, 92:162511, 2008.

[148] T. Dietl. Origin and control of ferromagnetism in dilute magnetic semiconductors and oxides. *J. Appl. Phys.*, 103:07D111, 2008.

[149] K. Kikoin. Ferromagnetic ordering in dilute magnetic dielectrics with and without free carriers. *J. Magn. Magn. Mater.*, 321:702, 2009.

[150] L. Cui, H. Y. Zhang, G. G.Wang, F. X. Yang, X. P. Kuang, R. Sun, and J. C. Han. Effect of annealing temperature and annealing atmosphere on the structure and optical properties of ZnO thin films on sapphire (0 0 0 1) substrates by magnetron sputtering. *Appl. Surf. Sci.*, 258:2479, 2012.

[151] T. Regier, J. Krochak, T. K. Sham, Y. F. Hu, J. Thompson, and R. I. R. Blyth. Performance and capabilities of the Canadian Dragon: The SGM beamline at the Canadian Light Source. *Nucl. Instrum. Methods Phys. Res., Sect. A*, 582:3, 2007.

[152] Ordejón, P. and Artacho, E. and Soler, J. M. Self-consistent order-N density-functional calculations for very large systems. *Phys. Rev. B*, 53:R10441–R10444, 1996.

[153] J. M. Soler, E. Artacho, J. D. Gale, A. García, J. Junquera, P. Ordejón, and D. Sánchez-Portal. The SIESTA method for ab initio order- N materials simulation. *J. Phys.: Condens. Matter*, 14(11):2745, 2002.

[154] W. M. Haynes, Thomas J. Bruno, and David R. Lide, editors. *CRC Handbook of Chemistry and Physics* . Taylor and Francis Group, LLC, 95 edition, 2014.

[155] D. J. Singh. Electronic structure, disconnected fermi surfaces and antiferromagnetism in the layered pnictide superconductor $Na_xBa_{1x}Ti_2Sb_2O$. *New J. Phys*, 12:123003, 2012.

[156] G. van der Laan, B. T. Thole, G. A. Sawatzky, and M. Verdaguer. Multiplet structure in the $L_{2,3}$ x-ray-absorption spectra: A fingerprint for high- and low-spin Ni^{2+}*compounds*. *Phys.Rev.B*.

[157] M. C. Biesinger, B. P. Payne, L. W. M. Lau, A. R. Gerson, and R. St. C. Smart. Xray photoelectron spectroscopic chemical state quantification of mixed nickel metal, oxide and hydroxide systems. *Surf. Interface Anal.*, 31:324, 2009.

[158] M. C. Biesinger, L. W. M. Lau, A. R. Gerson, and R. St. C. Smart. Resolving surface chemical states in XPS analysis of first row transition metals, oxides and hydroxides: Sc, Ti, V, Cu and Zn. *Appl. Surf. Sci.*, 257:887, 2010.

[159] M. C. Biesinger, B. P. Payne, A. P. Grosvenor, L. W. M. Lau, A. R. Gerson, and R. St. C. Smart. Resolving surface chemical states in XPS analysis of first row transition metals, oxides and hydroxides: Cr, Mn, Fe, Co and Ni. *Appl. Surf. Sci.*, 257:2717, 2011.

[160] N. N. Greenwood and A. Earnshaw. *Chemistry of the Elements*. Butterworth-Heinemann, 2 edition, 1997.

[161] D. Iusan, M. Kabir, O. Granas, O. Eriksson, and B. Sanyal. Microscopic picture of Co clustering in ZnO. *Phys. Rev. B*, 79:125202, 2009.

[162] B. Sanyal, R. Knut, O. Grnäs, D. M. Iuan, O. Karis, and O. Eriksson. Electronic structure of Co doped ZnO: Theory and experiment. *J. Appl. Phys.*, 103:07D310, 2008.

[163] D. Kelly and D. R. Jung. Elemental chromium by XPS. *Surf. Sci. Spectra*, 5:130, 1998.

[164] T. Hofmann, T. H. Yu, M. Folse, L. Weinhardt, M. Baer, Y. Zhang, B. V. Merinov, D. J. Myers, W. A. Goddard III, and C. Heske. Using photoelectron spectroscopy and quantum mechanics to determine d-band energies of metals for catalytic applications. *J. Phys. Chem. C*, 116:24016, 2012.

[165] U. Chandra and G. Parthasarathy. Study of naturally occuring pre-cambrian native iron through high-pressure Mössbauer spectroscopy up to 10 GPa. *AIP Conf. Proc.*, 1195:886, 2009.

[166] R. K. Verma and S. N. Prasad. Probable existence of native iron in newer dolerites from Singbhum, Bihar, India. *J. Geophys. Res.*, 80:3755, 1975.

[167] D. Abbott, R. Mazumder, and D. Breger. Native iron in the Chaibasa shales: result of pre 1.6 Ga impact. *Lunar and Planet. Sc. XXXVII Conf.*, 37:1889, 2006.

[168] P. Rochette, L. Sagnotti, M. Bourot-Denise, G. Consolmagno, L. Folco, J. Gattacceca, M. L. Osete, and L. Pesonen. Magnetic classification of stony meteorites: 1. ordinary chondrites. *Meteorit. Planet. Sci.*, 38:251–268, 2003.

[169] R. R. Jaeger and M. E. Lipschutz. X-ray diffraction study of kamacite from iron meteorites. *Geochim. Cosmochim. Ac.*, 32:773, 1968.

[170] M. Kotsugi, T. Wakita, T. Taniuchi, H. Maruyama, C. Mitsumata, K. Ono, M. Suzuki, N. Kawamura, N. Ishimatsu, M. Oshima, Y. Watanabe, and M. Taniguchi. Direct metallographic analysis of an iron meteorite using hard x-ray photoelectron emission microscopy. *IBM Journal of Research and Development*, 55(4):13:1–13:5, 2011.

[171] U. Chandra, P. Sharma, G. Parthasarathy, and B. Sreedhar. Mössbauer spectroscopy and electrical resistivity studies on naturally occurring native iron under high pressures up to 9.1 GPa. *Am. Mineral.*, 95:870, 2010.

[172] Y. Nagai, M. Senda, and T. Toshima. XPS investigations of Ni-Fe alloy and Fe films. *Jpn. J. Appl. Phys.*, 26:L1131, 1987.

[173] N. S. Bezaeva, D. D. Badyukov, M. A. Nazarov, P. Rochette, and J. Feinberg. Magnetic properties of the Chelyabinsk meteorite: Preliminary results. *Geochem. Int.*, 51:568–574, 2013.

[174] L. Nabelek, M. Mazanec, S. Kdyr, and G. Kletetschka. Magnetic, in situ, mineral characterization of Chelyabinsk meteorite thin section. *Meteorit. Planet. Sci.*, 50:1112–1121, 2015.

[175] S. Ozawa, M. Miyahara, E. Ohtani, O. N. Koroleva, Y. Ito, K. D. Litasov, and N. P. Pokhilenko. Jadeite in Chelyabinsk meteorite and the nature of an impact event on its parent body. *Sci. Rep.*, 4:5033, 2014.

[176] J. Borovicka, P. Spurny, P. Wiegert, P. Kalenda, D. Clark, and L. Shrbeny. The trajectory, structure and origin of the Chelyabinsk asteroidal impactor. *Nature*, 503:235–237, 2013.

[177] M. A. Nazarov, D. D. Badyukov, N. N. Kononkova, and I. V. Kubrakova. Chelyabinsk. *Meteorit. Bull.*, 102:1662, 2013.

[178] O. P. Popova, P. Jenniskens, V. Emel'yanenko, A. Kartashova, E. Biryukov, S. Khaibrakhmanov, V. Shuvalov, Y. Rybnov, A. Dudorov, and V. I. Grokhovsky. Chelyabinsk airburst, damage assessment, meteorite recovery, and characterization. *Science*, 342:3132, 2013.

[179] D. W. Mittlefehldt. Meteorites - A Brief Tutorial. *Rev. Mineral. Geochem.*, 68:571, 2008.

[180] E. R. D. Scott and A. N. Krot. Chondritic meteorites and the high-temperature nebular origins of their components. pages 15–53, 2005.

[181] V. A. Koroteev, S. V. Berzin, Yu. V. Erokhin, K. S. Ivanov, and V. V. Khiller. Composition and structure of the Chelyabinsk meteorite. *Dokl. Earth Sci.*, 451:831, 2013.

[182] E. Petrovsky and A. Kapicka. On determination of the curie point from thermomagnetic curves. *J. Geophys. Res.*, 111:B12S27, 2006.

[183] R. F. Butler. Natural remanent magnetization and thermomagnetic properties of the Allende meteorite. *Earth. Planet. Sci. Lett.*, 17:120–128, 1972.

[184] D. E. Watson, E. E. Larson, J. M. Herndon, and M. W. Rowe. Thermomagnetic analysis of meteorites, C2 chondrites. *Earth. Planet. Sci. Lett.*, 27:101–107, 1975.

[185] J. Gattacceca, P. Rochette, F. Lagroix, P.E. Mathe, and B. Zanda. Low temperature magnetic transition of chromite in ordinary chondrites. *Geophys. Res. Lett.*, 38:L10203, 2011.

[186] K. Fabian, V. P. Shcherbakov, and S. A. McEnroe. Measuring the curie temperature. *Geochem. Geophys. Geosyst.*, 14:947–961, 2013.

[187] G. Cacciamani, A. Dinsdale, M. Palumbo, and A. Pasturel. The Fe-Ni system: Thermodynamic modelling assisted by atomistic calculations. *Intermetallics*, 18:1148–1162, 2010.

[188] L. J. Swartzendruber, V. P. Itkin, and C. B. Alcock. The Fe-Ni (iron-nickel) system. *J. Phase Equilib.*, 12(3):288–312, 1991.

[189] W. Xiong, H. Zhang, L. Vitos, and M. Selleby. Magnetic phase diagram of the Fe-Ni system. *Acta Mater.*, 59:521–530, 2011.

[190] I. Garrick-Bethell and B. P. Weiss. Kamacite blocking temperatures and applications to lunar magnetism. *Earth. Planet. Sci. Lett.*, 294:1–7, 2010.

[191] W. M. Haynes, Thomas J. Bruno, and David R. Lide, editors. *CRC Handbook of Chemistry and Physics*. Taylor and Francis Group, LLC, 95 edition, 2014.

[192] N. S. Bezaeva, D. D. Badyukov, M. A. Nazarov, P. Rochette, and J. Feinberg. Magnetic properties of the ll5 ordinary chondrite Chelyabinsk (fall of february 15, 2013). *Meteorit. Planet. Sci.*, 49:958–977, 2014.

[193] J. Crangle and G. M. Goodman. The magnetization of pure iron and nickel. *Proc. Roy. Soc. Lond. A*, 321:477–491, 1971.

[194] K. H. Gheisari, S. Javadpour, and J. T. Oh. The effect of milling speed on the magnetic properties of mechanically alloyed Fe-45% Ni powders. *J. Phys. Conf. Ser*, 153:012051, 2009.

[195] N. N. Lubinskii, L. A. Bashkirov, A. I. Galyas, S. V. Shevchenko, G. S. Petrov, and I. M. Sirota. Magnetic susceptibility and effective magnetic moment of the Nd^{3+} and Co^{3+} ions in $NdCo_{1-x}Ga_xO_3$. *Inorgan. Chem.*, 44:1015–1021, 2008.

[196] V. Kusigerski, V. Spasojevic, and M. Mitric. Synthesis and some physical properties of the diluted magnetic semiconductor $Cd_{1-x}Mn_xO$. *J. Phys.: Condens. Matt.*, 8:10581, 1996.

[197] D. A. Pavlov, A. I. Bobrov, N. V. Malekhonova, A. V. Pirogov, and A. V. Nezhdanov. Self-assembled nanocrystals discovered in Chelyabinsk meteorite. *Sci. Rep.*, 4:4280, 2014.

[198] A. G. Shard. Detection limits in xps for more than 6000 binary systems using al and mg k x-rays. *Surface and Interface Analysis*, 46(3):175–185, 2014. SIA-13-0416.R1.

[199] A. P. Vinogradov, V. I. Nefedov, V. S. Urusov, and N. M. Zhavoronkov. ESCA investigation of lunar regolith from seas fertility and tranquility. *Proceedings of the Third Lunar Science Conference*, 2:1421, 1972.

[200] A. N. Hattori, K. Hattori, and H. Daimon. X-ray photoelectron spectroscopy of spegrown bcc-Fe, polycrystal and -$FeSi_2$ phases on si(111) surfaces. *Surf. Interface Anal.*, 40:988, 2008.

[201] A. S. Belozerov, A. I. Poteryaev, S. L. Skornyakov, and V. I. Anisimov. Structural gamma-epsilon phase transition in fe-mn alloys from a cpa plus dmft approach. *J. Phys.: Condens. Matt.*, 27:465601, 2015.

[202] M. A. Korotin, N. A. Skorikov, V. M. Zainullina, E. Z. Kurmaev, A. V. Lukoyanov, and V. I. Anisimov. Electronic structure of nonstoichiometric compounds in the coherent potential approximation. *JETP Lett.*, 94:806, 2012.

[203] A. I. Poteryaev, S. L. Skornyakov, A. S. Belozerov, and V. I. Anisimov. Specific heat of a binary alloy within the CPA+DMFT method. *Phys. Rev. B*, 91:195141, 2015.

[204] K. Berndt, O. Brummer, and U. Marx. Study of the Fe 2p states by means of photoelectron spectroscopy in iron and iron alloys. *Phys. Stat. Sol. b*, 86:K93–K95, 1978.

[205] V. O. Garlea, R. Jin, D. Mandrus, B. Roessli, Q. Huang, M. Miller, A. J. Schultz, and S. E. Nagler. Magnetic and orbital ordering in the spinel mnv_2o_4. *Phys. Rev. Lett.*, 100:066404, Feb 2008.

[206] Y. Liu and L. Gao. A study of the electrical properties of carbon nanotube-$NiFe_2O_4$ composites: Effect of the surface treatment of the carbon nanotubes. *Carbon*, 43(1):47 – 52, 2005.

[207] Y. Kajiwara, K. Harii, S. Takahashi, J. Ohe, K. Uchida, M. Mizuguchi, H. Umezawa, H. Kawai, K. Ando, K. Takanashi, S. Maekawa, and E. Saitoh. Transmission of electrical signals by spin-wave interconversion in a magnetic insulator. *Nature*, 464(7286):262–266, 03 2010.

[208] J. Li, L. R. Shelford, P. Shafer, A. Tan, J. X. Deng, P. S. Keatley, C. Hwang, E. Arenholz, G. van der Laan, R. J. Hicken, and Z. Q. Qiu. Direct detection of pure ac spin current by x-ray pump-probe measurements. *Phys. Rev. Lett.*, 117:076602, Aug 2016.

[209] U. Luders, A. Barthelemy, M. Bibes, K. Bouzehouane, S. Fusil, E. Jacquet, J.-P. Contour, J.-F. Bobo, J. Fontcuberta, and A. Fert. $Nife_2o_4$: A versatile spinel material brings new opportunities for spintronics. *Adv. Mater.*, 18(13):1733–1736, 2006.

[210] Yanqing Liu, Yuhan Wu, Dan Li, Yongjun Zhang, Jing Zhang, and Jinghai Yang. A study of structural, ferroelectric, ferromagnetic, dielectric properties of $NiFe_2O_4$-$BaTiO_3$ multiferroic composites. *J. Mater. Sci.-Mater. El.*, 24(6):1900–1904, 2013.

[211] J. Ma, J. Hu, Z. Li, and C.-W. Nan. Recent progress in multiferroic magnetoelectric composites: from bulk to thin films. *Adv. Mater.*, 23(9):1062–1087, 2011.

[212] K. Haneda. Recent advances in the magnetism of fine particles. *Can. J. Phys.*, 65(10):1233–1244, 1987.

[213] B. D. Cullity and C. D. Graham. *Introduction to Magnetic Materials*. Wiley-IEEE Press, 2 edition, 2009.

[214] U. Luders, M. Bibes, J.-F. Bobo, M. Cantoni, R. Bertacco, and J. Fontcuberta. Enhanced magnetic moment and conductive behavior in $NiFe_2O_4$ spinel ultrathin films. *Phys. Rev. B*, 71:134419, Apr 2005.

[215] Q. C. Sun, H. Sims, D. Mazumdar, J. X. Ma, B. S. Holinsworth, K. R. O'Neal, G. Kim, W. H. Butler, A. Gupta, and J. L. Musfeldt. Optical band gap hierarchy in a magnetic oxide: Electronic structure of $nife_2o_4$. *Phys. Rev. B*, 86:205106, Nov 2012.

[216] S. N. Dolia, R. Sharma, M. P. Sharma, and N. S. Saxena. Synthesis, x-ray diffraction and optical band gap study of nanoparticles of $NiFe_2O_4$. *Indian J. Pure Appl. Phys*, 447:774–776, 2006.

[217] J. Haetge, C. Suchomski, and T. Brezesinski. Ordered mesoporous MFe_2O_4 (M = Co, Cu, Mg, Ni, Zn) thin films with nanocrystalline walls, uniform 16 nm diameter pores and high thermal stability: Template-directed synthesis and characterization of redox active trevorite. *Inorgan. Chem.*, 49(24):11619–11626, 2010.

[218] S. Balaji, R. Kalai Selvan, L. John Berchmans, S. Angappan, K. Subramanian, and C.O. Augustin. Combustion synthesis and characterization of sn^{4+} substituted nanocrystalline $NiFe_2O_4$. *Mater. Sci. Eng. B*, 119(2):119 – 124, 2005.

[219] Z. Szotek, W. M. Temmerman, D. Ködderitzsch, A. Svane, L. Petit, and H. Winter. Electronic structures of normal and inverse spinel ferrites from first principles. *Phys. Rev. B*, 74:174431, Nov 2006.

[220] G. van der Laan, C. M. B. Henderson, R. A. D. Pattrick, S. S. Dhesi, P. F. Schofield, E. Dudzik, and D. J. Vaughan. Orbital polarization in $nife_2o_4$ measured by $Ni - 2p$ x-ray magnetic circular dichroism. *Phys. Rev. B*, 59:4314–4321, Feb 1999.

[221] J. Wang, B. Lian, and S.-C. Zhang. Electrically tunable magnetism in magnetic topological insulators. *Phys. Rev. Lett.*, 115:036805, Jul 2015.

[222] M. Mozaffari, Z. Abooalizadeh, and J. Amighian. Investigation of magnetic properties of al substituted nickel ferrite nanopowders, synthesized by the sol-gel method. *J. Magn. Magn. Mater.*, 323(23):2997–3000, 2011.

[223] I. Perez, J. A. McLeod, R. J. Green, R. Escamilla, V. Ortiz, and A. Moewes. Electronic structure of co-substituted fese superconductor probed by soft x-ray spectroscopy and density functional theory. *Phys. Rev. B*, 90:014510, Jul 2014.

[224] Robert D. Cowan. Theoretical calculation of atomic spectra using digital computers. *J. Opt. Soc. Am.*, 58(6):808–818, Jun 1968.

[225] R. A. D. Pattrick, G. van der Laan, M. B C. Henerson, P. Kuiper, E. Dudzik, and D. J. Vaughan. Cation site occupancy in spinel ferrites studied by x-ray magnetic circular dichroism. *Eur. J. Miner.*, 14(6):1095–1102, 2002.

[226] D. Carta, M. F. Casula, A. Falqui, D. Loche, G. Mountjoy, C. Sangregorio, and A. Corrias. A structural and magnetic investigation of the inversion degree in ferrite nanocrystals MFe_2O_4 (M = Mn, Co, Ni). *J. Phys. Chem. C*, 113(20):8606–8615, 2009.

[227] C. M. Richter, J.-M. Mariot, O. Heckmann, L. Kjeldgaard, S. B. Mun, S. C. Fadley, U. Lüders, J.-F. Bobo, P. De Padova, A. Taleb-Ibrahimi, and K. Hricovini. $NiFe_2O_4$ and Fe_3O_4 studied by xmcd and resonant photoemission. *Eur. Phys. J-Spec. Top.*, 169(1):175–180, 2009.

[228] R. H. Kodama, A. E. Berkowitz, E. J. McNiff, Jr., and S. Foner. Surface spin disorder in nife$_2O_4$ nanoparticles. *Phys. Rev. Lett.*, 77:394–397, Jul 1996.

[229] R. J. Green, D. A. Zatsepin, A. Hunt, E. Z. Kurmaev, N. V. Gavrilov, and A. Moewes. The formation of ti-o tetrahedra and band gap reduction in SiO_2 via pulsed ion implantation. *J. Appl. Phys.*, 113(10), 2013.

[230] S.M. Patange, Sagar E. Shirsath, K.S. Lohar, S.S. Jadhav, Nilesh Kulkarni, and K.M. Jadhav. Electrical and switching properties of nialxfe2xo4 ferrites synthesized by chemical method. *Physica B*, 406(3):663 – 668, 2011.

[231] S. Eisebitt and W. Eberhardt. Band structure information and resonant inelastic soft x-ray scattering in broad band solids. *J. Electron. Spectrosc. Relat. Phenom.*, 110-111:335 – 358, 2000. Soft X Ray Emission Spectroscopy.

[232] A. Anspoks, A. Kalinko, R. Kalendarev, and A. Kuzmin. Atomic structure relaxation in nanocrystalline NiO studied by EXAFS spectroscopy: Role of nickel vacancies. *Phys. Rev. B*, 86:174114, Nov 2012.

[233] T. Tangcharoen, W. Klysubun, C. Kongmark, and W. Pecharapa. Synchrotron x-ray absorption spectroscopy and magnetic characteristics studies of metal ferrites (metal=Ni, Mn, Cu) synthesized by solgel auto-combustion method. *Phys. Status Solidi A*, 211(8):1903–1911, 2014.

[234] G. J. Snyder and E. S. Tobere. Complex thermoelectric materials. *Nat. Mater.*, 7:105–114, 2008.

[235] R. Venkatasubramanian, E. Siivola, T. Colpitts, and B. O'Quinn. Thin-film thermoelectric devices with high room-temperature figures of merit. *Nature*, 413(6856):597–602, 10 2001.

[236] Y. Xia, D. Qian, D. Hsieh, L. Wray, A. Pal, H. Lin, A. Bansil, D. Grauer, Y. S. Hor, R. J. Cava, and M. Z. Hasan. Observation of a large-gap topological-insulator class with a single dirac cone on the surface. *Nat. Phys.*, 5:398–402, 2009.

[237] H. J. Zhang, C. X. Liu, X. L. Qi, X. Dai, Z. Fang, and S. C. Zhang. Topological insulators in Bi_2Se_3, Bi_2Te_3 and Sb_2Te_3 with a single dirac cone on the surface. *Nature*, 5:438–442, 2009.

[238] Y. Zhang, K. He, C.-Z. Chang, C.-L. Song, L.-L. Wang, X. Chen, J.-F. Jia, Z. Fang, X. Dai, W.-Y. Shan, S.-Q. Shen, Q. Niu, X.-L. Qi, S.-C. Zhang, and X.-C. Ma Q.-

K. Xue. Crossover of the three-dimensional topological insulator Bi_2Se_3 to the two-dimensional limit. *Nat. Phys.*, 6:584–588, 2010.

[239] D. Hsieh, Y. Xia, D. Qian, L. Wray, J. H. Dil, F. Meier, J. Osterwalder, L. Patthey, J. G. Checkelsky, N. P. Ong, A. V. Fedorov, H. Lin, A. Bansil, D. Grauer, Y. S. Hor, R. J. Cava, and M. Z. Hasan. A tunable topological insulator in the spin helical dirac transport regime. *Nature*, 460:1101–1105, 2009.

[240] Y. L. Chen, J. G. Analytis, J.-H. Chu, Z. K. Liu, S.-K. Mo, X. L. Qi, H. J. Zhang, D. H. Lu, X. Dai, Z. Fang, S. C. Zhang, I. R. Fisher, Z. Hussain, and Z.-X. Shen. Experimental realization of a three-dimensional topological insulator, Bi_2Te_3. *Science*, 325:178–181, 2009.

[241] P. Ngabonziza, M. P. Stehno, H. Myoren, V. A. Neumann, G. Koster, and A. Brinkman. Gate-tunable transport properties of in situ capped Bi_2Te_3 topological insulator thin films. *Adv. Electro. Mater.*, 2(8):1600157, 2016. 1600157.

[242] Y. L. Chen, J.-H. Chu, J. G. Analytis, Z. K. Liu, K. Igarashi, H.-H. Kuo, X. L. Qi, S. K. Mo, R. G. Moore, D. H. Lu, M. Hashimoto, T. Sasagawa, S. C. Zhang, I. R. Fisher, Z. Hussain, and Z. X. Shen. Massive dirac fermion on the surface of a magnetically doped topological insulator. *Science*, 329:659–662, 2010.

[243] L. Zhao, P. Z. Tang, B.-L. Gu, and W. H. Duan. Field-effect birefringent spin lens in ultrathin film of magnetically doped topological insulators. *Phys. Rev. Lett.*, 111:116601, 2013.

[244] Y. Takagaki, A. Papadogianni, and O. Bierwagen. Seebeck effect and giant linear magnetoresistance affected by conflicting n- and p-type defect-induced doping in epitaxial Bi_2Te_3 layers. *Adv. Electro. Mater.*, 1(4):1400007, 2015.

[245] J. Choi, S. Choi, J. Choi, Y. Park, H.-M. Park, H.-W. Lee, B.-C. Woo, and S. Cho. Magnetic properties of mn-doped Bi_2Te_3 and Sb_2Te_3. *Phys. Status Solidi B*, 241:1541–1544, 2004.

[246] J. S. Dyck, C. Drašar, P. Lošt'ák, and C. Uher. Low-temperature ferromagnetic properties of the diluted magnetic semiconductor $Sb_{2x}Cr_xTe_3$. *Phys. Rev. B*, 71:115214, 2005.

[247] H. Ohno. Properties of ferromagnetic III-V semiconductors. *J. Magn. Magn. Mater.*, 200(1-3):110–129, 1999.

[248] J. E. Moore. The birth of topological insulators. *Nature*, 464(7286):194–198, 2010.

[249] P. Huu Le, K. H. Wu, C. W. Luo, and J. Leu. Growth and characterization of topological insulator Bi_2Te_3 thin films on $SrTiO_3$ using pulsed laser deposition. *Thin Solid Films*, 534:659 – 665, 2013.

[250] J.M. Soler, E. Artacho, J.D. Gale, A. Garca, J. Junquera, P. Ordejon, and D. Sanchez-Portal. The SIESTA method for ab initio order-N materials simulation. *J. Phys.: Condens. Matter*, 14:2745, 2002.

[251] T. J. Regan, H. Ohldag, C. Stamm, F. Nolting, J. Lüning, J. Stöhr, and R. L. White. Chemical effects at metal/oxide interfaces studied by x-ray-absorption spectroscopy. *Phys. Rev. B*, 64:214422, 2001.

[252] G. Ghiringhelli, M. Matsubara, C. Dallera, F. Fracassi, A. Tagliaferri, N. B. Brookes, A. Kotani, and L. Braicovich. Resonant inelastic x-ray scattering of MnO: $L_{2,3}$ edge measurements and assessment of their interpretation. *Phys. Rev. B*, 73:035111, Jan 2006.

[253] B. C. Chapler, K. W. Post, A. R. Richardella, J. S. Lee, J. Tao, N. Samarth, and D. N. Basov. Infrared electrodynamics and ferromagnetism in the topological semiconductors Bi_2Te_3 and mn-doped Bi_2Te_3. *Phys. Rev. B*, 89:235308, Jun 2014.

[254] S.-K. Lee, H.-C. Hsu, and W.-H. Tuan. Oxidation Behavior of Copper at a Temperature below 300°C and the Methodology for Passivation. *Materials Research*, 19:51 – 56, 02 2016.

[255] S. Coh, P. Y. Yu, Y. Aoki, S. Saito, S. G. Louie, and M. L. Cohen. Alternative structure of tio$_2$ with higher energy valence band edge. *Phys. Rev. B*, 95:085422, Feb 2017.

[256] X. Chen, L. Liu, Z. Liu, M. A. Marcus, W.-C. Wang, N. A. Oyler, M. E. Grass, B. Mao, P.-A. Glans, and P. Y. Yu. Properties of disorder-engineered black titanium dioxide nanoparticles through hydrogenation. *Sci. Rep.*, 3, 2013.

[257] C. M. Yim, C. L. Pang, and G. Thornton. Oxygen vacancy origin of the surface band-gap state of tio$_2$(110). *Phys. Rev. Lett.*, 104:036806, Jan 2010.

[258] S. Samaneh Ataei, S. Javad Hashemifar, and Mohammad Reza Mohammadizadeh. First-principles insights into role of hydrogen atom in black titania. *Comp. Mater. Sci.*, 139(Supplement C):84 – 88, 2017.

[259] B. K. Teo. *EXAFS: basic principles and data analysis*, volume 9. Springer Science & Business Media, 1986.

[260] E. A. Stern. Theory of the extended x-ray-absorption fine structure. *Phys. Rev. B*, 10:3027–3037, Oct 1974.

[261] D. Popmintchev, B. R. Galloway, M.-C. Chen, F. Dollar, C. A. Mancuso, and A. et. al. Hankla. Near- and extended-edge x-ray-absorption fine-structure spectroscopy using ultrafast coherent high-order harmonic supercontinua. *Phys. Rev. Lett.*, 120:093002, Mar 2018.

[262] Y.-Y. Hu, Z. Liu, K.-W. Nam, O. J. Borkiewicz, J. Cheng, X. Hua, M. T. Dunstan, X. Yu, K. M. Wiaderek, L.-S. Du, K. W. Chapman, P. J. Chupas, X.-Q. Yang, and C. P. Grey. Origin of additional capacities in metal oxide lithium-ion battery electrodes. *Nat. Mater.*, 12:1130 EP –, 11 2013.

[263] H. Zhang, P. An, W. Zhou, B. Yuan Guan, P. Zhang, J. Dong, and X. Wen Lou. Dynamic traction of lattice-confined platinum atoms into mesoporous carbon matrix for hydrogen evolution reaction. *Sci. Adv.*, 4(1), 01 2018.

[264] J. Stöhr, D. Denley, and P. Perfetti. Surface extended x-ray absorption fine structure in the soft-x-ray region: Study of an oxidized Al surface. *Phys. Rev. B*, 18:4132–4135, Oct 1978.

[265] J. Stöhr, L. Johansson, I. Lindau, and P. Pianetta. Extended-x-ray-absorption-fine-structure studies of low-Z atoms in solids and on surfaces: Studies of si_3n_4, sio_2, and oxygen on Si(111). *Phys. Rev. B*, 20:664–680, Jul 1979.

[266] Stöhr, R. S. Bauer, J. C. McMenamin, L. I. Johansson, and S. Brennan. Surface EXAFS investigation of oxygen chemisorption on GaAs(110). *J. Vac. Sci.Tech.*, 16(5):1195–1199, 1979.

[267] L. Tröger, D. Arvanitis, J. J. Rehr, T. Lederer, T. Yokoyama, K. Baberschke, and E. Zschech. Improved distance determination in oxygen EXAFS: Soft x-ray fluorescence measurements versus theoretical standards. *Jap. J. Appl. Phys.*, 32(S2):137, 1993.

[268] C. Dagg, L. Troger, D. Arvanitis, and K. Baberschke. A comparison of low-Z EXAFS experiment and ab initio calculations. *J. Phys.: Condens. Matter*, 5(37):6845, 1993.

[269] K. Amemiya, Y. Kitajima, Y. Yonamoto, S. Terada, H. Tsukabayashi, T. Yokoyama, and T. Ohta. Oxygen K-edge x-ray-absorption fine-structure study of surface methoxy species on Cu(111) and Ni(111). *Phys. Rev. B*, 59:2307–2312, Jan 1999.

[270] P. Lechner, C. Fiorini, R. Hartmann, J. Kemmer, N. Krause, P. Leutenegger, A. Longoni, H. Soltau, D. Stötter, R. Stötter, L. Strüder, and U. Weber. Silicon drift detectors for high count rate x-ray spectroscopy at room temperature. *Nucl. Instrum. Methods Phys. Res. A.*, 458(1):281 – 287, 2001.

[271] P. Lechner, A. Pahlke, and H. Soltau. Novel high-resolution silicon drift detectors. *X-Ray Spectrom.*, 33(4):256–261, 2004.

[272] G. N. George and I. J. Pickering. EXAFSPAK: A suite of computer programs for analysis of x-ray absorption spectra. *SSRL, Stanford*, 1995.

[273] A. G. McKale, B. W. Veal, A. P. Paulikas, S. K. Chan, and G. S. Knapp. Improved ab initio calculations of amplitude and phase functions for extended x-ray absorption fine structure spectroscopy. *J. Am. Chem. Soc.*, 110(12):3763–3768, 1988.

[274] S. Calvin. *XAFS for Everyone.* CRC press, 2013.

[275] E. P. Meagher and George A Lager. Polyhedral thermal expansion in the TiO_2 polymorphs; refinement of the crystal structures of rutile and brookite at high temperature. *Canad. Mineral.*, 17(1):77–85, 1979.

[276] J.R. Smyth, R. J. Swope, and A. R. Pawley. H in rutile-type compounds; II, crystal chemistry of Al substitution in H-bearing stishovite. *Am. Mineral.*, 80(5-6):454, 1995.

[277] Q. Maqbool and A. Srivastava. Benign synthesis of black microspheres of anatase TiO_2 with paramagnetic oxygen vacancies through NH_3 treatment. *Chem. Eur. J.*, 23(56):13864–13868, 2017.

[278] A. Janotti, J. B. Varley, P. Rinke, N. Umezawa, G. Kresse, and C. G. Van de Walle. Hybrid functional studies of the oxygen vacancy in tio_2. *Phys. Rev. B*, 81:085212, Feb 2010.

[279] P. M. Kowalski, M. F. Camellone, N. N. Nair, B. Meyer, and D. Marx. Charge localization dynamics induced by oxygen vacancies on the tio_2(110) surface. *Phys. Rev. Lett.*, 105:146405, Sep 2010.

[280] X. Pan, M.-Q. Yang, X. Fu, N. Zhang, and Y.-J. Xu. Defective TiO_2 with oxygen vacancies: synthesis, properties and photocatalytic applications. *Nanoscale*, 5:3601–3614, 2013.

[281] S. Na-Phattalung, M. F. Smith, K. Kim, M.-H. Du, S.-H. Wei, S. B. Zhang, and S. Limpijumnong. First-principles study of native defects in anatase Tio_2. *Phys. Rev. B*, 73:125205, Mar 2006.

[282] H. Song, C. Li, Z. Lou, Z. Ye, and L. Zhu. Effective formation of oxygen vacancies in black TiO_2 nanostructures with efficient solar-driven water splitting. *ACS Sustain. Chem. Eng.*, 5(10):8982–8987, 2017.

[283] C. Yang, Z. Wang, T. Lin, H. Yin, X. Lu, D. Wan, T. Xu, C. Zheng, J. Lin, F. Huang, X. Xie, and M. Jiang. Core-shell nanostructured black rutile titania as excellent catalyst for hydrogen production enhanced by sulfur doping. *J. Am. Chem. Soc.*, 135(47):17831–17838, 2013.

[284] Z. Wang, C. Yang, T. Lin, H. Yin, P. Chen, D. Wan, F. Xu, F. Huang, J. Lin, X. Xie, and M. Jiang. H-doped black titania with very high solar absorption and excellent photocatalysis enhanced by localized surface plasmon resonance. *Adv. Func. Mater.*, 23(43):5444–5450, 2013.

APPENDIX

A

AUTHORED PUBLICATIONS

- **B. Leedahl**, Z. Abooalizadeh, K. LeBlanc, and A. Moewes. Tunability of room-temperature ferromagnetism in spintronic semiconductors through nonmagnetic atoms. Physical Review B 96 (4), 045202 (2017).

- **B. Leedahl**, D. W. Boukhvalov, E. Z. Kurmaev, A. Kukharenko, I. S. Zhidkov, N. V. Gavrilov, S. O. Cholakh, P. Huu Le, C. Wei Luo, and A. Moewes. Bulk vs. Surface Structure of $3d$ Metal Impurities in Topological Insulator Bi_2Te_3 Scientific Reports, 7 (1), 5758 (2017).

- N. Ketabi, T. M. Tolhurst, **B. Leedahl**, H. Liu, Y. Li, and A. Moewes How functional groups change the electronic structure of graphdiyne: Theory and experiment. Carbon, (123), 1-6 (2017).

- T. M. Tolhurst, J. L. Andrews, **B. Leedahl**, P. Marley, S. Banerjee, and A. Moewes. Structureinduced switching of the band gap, charge order and correlation strength in ternary vanadium oxide bronzes. Chemistry A European Journal, (23), 9846 (2017).

- T. M. Tolhurst, **B Leedahl**, J. L. Andrews, S Banerjee, and A. Moewes. The electronic structure of ϵ-V_2O_5: an expanded band gap in a double-layered polymorph with increased interlayer separation. Journal of Materials Chemistry A, (5), 23694 (2017).

- **B. Leedahl**, A. V. Korolev, I. S. Zhidkov, S. L. Skornyakov, V. I. Anisimov, A. S. Belozerov, A. I. Kukharenko, E. Z. Kurmaev, V. I. Grokhovskii S. O. Cholakhd and A. Moewes Searching for pure iron in nature: the Chelyabinsk meteorite. RSC Advances, (6), 85844 (2016).

- K. Bouras, G. Schmerber, D. Aureau, H. Rinnert, G. Ferblantier, T. Fix, S. Colis, P. Bazylewski, **B. Leedahl**, A. Etcheberry, G. S. Chang, A. Dinia and A. Slaoui. Insight into photon conversion of Nd^{3+} doped low temperature grown p and n type tin oxide thin films. RSC Advances, (6), 67157 (2016).

- T. M. Tolhurst, **B. Leedahl**, J. L. Andrews, P. M. Marley, S. Banerjeeb and A. Moewes Contrasting 1D tunnel-structured and 2D layered polymorphs of V_2O_5: relating crystal structure and bonding to band gaps and electronic structure. Journal of Physical Chemistry Chemical Physics, (18), 15798 (2016).

- P. Bazylewski, V. L. Nguyen, R. P.C. Bauer, A. H. Hunt, E. J. G. McDermott, **B. Leedahl**, A. I. Kukharenko, S. O. Cholakh, E. Z. Kurmaev, P. Blaha, A. Moewes, Y. H. Lee and G. S. Chang. Selective Area Band Engineering of Graphene using Cobalt-Mediated Oxidation. Scientific Reports, (5), 15380 (2015).

- R.J. Green, T.Z. Regier, **B. Leedahl**, J.A. McLeod, X.H. Xu, G.S. Chang, E.Z. Kurmaev, and A. Moewes. Adjacent Fe-Vacancy Interactions as the Origin of Room Temperature Ferromagnetism in $(In_{1-x}Fe_x)_2O_3$. Physical Review Letters, (115), 167401 (2015).

- **B. Leedahl**, D. A. Zatsepin, D. W. Boukhvalov, E. Z. Kurmaev, R. J. Green, I. S. Zhidkov, S. S. Kim, L. Cui, N. V. Gavrilov, S. O. Cholakh, and A. Moewes. Study of the Structural Characteristics of 3d Metals Cr, Mn, Fe, Co, Ni, and Cu Implanted in ZnO and TiO_2—Experiment and Theory. Journal of Physical Chemistry C, (118), 28143 (2014).

- **B. Leedahl**, D. A. Zatsepin, D. W. Boukhvalov, R. J. Green, J. A. McLeod, S. S. Kim, E. Z. Kurmaev, I. S. Zhidkov, N. V. Gavrilov, S. O. Cholakh, and A. Moewes,

Structural defects induced by Fe-ion implantation in TiO_2. Journal of Applied Physics, (115), 053711 (2014).

- J. A. McLeod, D. W. Boukhvalov, D. A. Zatsepin, R. J. Green, **B. Leedahl**, L. Cui, E. Z. Kurmaev, I. S. Zhidkov, L. Finkelstein, N. V. Gavrilov, S. O. Cholakh, and A. Moewes. Local structure of Fe impurity atoms in ZnO: bulk versus surface. Journal of Physical Chemistry C (118), 5336-5345 (2014).

APPENDIX

B

COPYRIGHT AGREEMENTS

I hereby certify that, if appropriate, I have obtained and attached hereto a written permission statement from the owner of each third party copyrighted matter that is included in my thesis, dissertation, or project report, allowing distribution as specified below. I certify that the version I submitted is the same as that approved by my advisory committee.

B.1 American Physical Society

The following is found on the APS copyright FAQ website, and a copy of the Copyright Agreement is attached below.

As the author of an APS-published article, may I include my article or a portion of my article in my thesis or dissertation? Yes, the author has the right to use the article or a portion of the article in a thesis or dissertation without requesting permission from APS, provided the bibliographic citation and the APS copyright credit line are given on the appropriate pages.

November 2012

Terms and conditions associated with the American Physical Society Transfer of Copyright Agreement

Copyright to the [above-listed] unpublished and original article submitted by the [above] author(s), the abstract forming part thereof, and any subsequent errata (collectively, the "Article") is hereby transferred to the American Physical Society (APS) for the full term thereof throughout the world, subject to the Author Rights (as hereinafter defined) and to acceptance of the Article for publication in a journal of APS. This transfer of copyright includes all material to be published as part of the Article (in any medium), including but not limited to tables, figures, graphs, movies, other multimedia files, and all supplemental materials. APS shall have the right to register copyright to the Article in its name as claimant, whether separately or as part of the journal issue or other medium in which the Article is included.

The author(s), and in the case of a Work Made For Hire, as defined in the U.S. Copyright Act, 17 U.S.C. §101, the employer named [below], shall have the following rights (the "Author Rights"):

1. All proprietary rights other than copyright, such as patent rights.
2. The nonexclusive right, after publication by APS, to give permission to third parties to republish print versions of the Article or a translation thereof, or excerpts therefrom, without obtaining permission from APS, provided the APS-prepared version is not used for this purpose, the Article is not republished in another journal, and the third party does not charge a fee. If the APS version is used, or the third party republishes in a publication or product charging a fee for use, permission from APS must be obtained.
3. The right to use all or part of the Article, including the APS-prepared version without revision or modification, on the author(s)' web home page or employer's website and to make copies of all or part of the Article, including the APS-prepared version without revision or modification, for the author(s)' and/or the employer's use for educational or research purposes.
4. The right to post and update the Article on free-access e-print servers as long as files prepared and/or formatted by APS or its vendors are not used for that purpose. Any such posting made or updated after acceptance of the Article for publication shall include a link to the online abstract in the APS journal or to the entry page of the journal. If the author wishes the APS-prepared version to be used for an online posting other than on the author(s)' or employer's website, APS permission is required; if permission is granted, APS will provide the Article as it was published in the journal, and use will be subject to APS terms and conditions.
5. The right to make, and hold copyright in, works derived from the Article, as long as all of the following conditions are met: (a) at least one author of the derived work is an author of the Article; (b) the derived work includes at least ten (10) percent of new material not covered by APS's copyright in the Article; and (c) the derived work includes no more than fifty (50) percent of the text (including equations) of the Article. If these conditions are met, copyright in the derived work rests with the authors of that work, and APS (and its successors and assigns) will make no claim on that copyright. If these conditions are not met, explicit APS permission must be obtained. Nothing in this Section shall prevent APS (and its successors and assigns) from exercising its rights in the Article.
6. If the Article was prepared under a U.S. Government contract, the government shall have the rights under the copyright to the extent required by the contract.

All copies of part or all of the Article made under any of the Author Rights shall include the appropriate bibliographic citation and notice of the APS copyright.

By signing this Agreement, the author(s), and in the case of a Work Made For Hire, the employer, jointly and severally represent and warrant that the Article is original with the author(s) and does not infringe any copyright or violate any other right of any third parties, and that the Article has not been published elsewhere, and is not being considered for publication elsewhere in any form, except as provided herein. If each author's signature does not appear [below], the signing author(s) represent that they sign this Agreement as authorized agents for and on behalf of all authors who have the legal right to transfer copyright and that this Agreement and authorization is made on behalf of the same. The signing author(s) (and, in the case of a Work Made For Hire, the signing employer) also represent and warrant that they have the full power to enter into this Agreement and to make the grants contained herein.

B.2 American Chemical Society

The following is found on the ACS copyright FAQ website, and a copy of their Policy on Theses and Dissertations is attached below.

I am a student writing my thesis. May I use papers I have authored in ACS journals, or material from them, in my thesis without obtaining explicit permission? You may reuse all or part of the Submitted, Accepted, or Published versions of your ACS papers in your thesis or dissertation. Such reuse is permitted subject to the ACS' Ethical Guidelines to Publication of Chemical Research and you should secure confirmation from the respective ACS journal editor(s) to avoid potential conflicts with journal prior publication policies. The ACS copyright credit line should be noted on the appropriate pages and appropriate citation of any Published versions. If the thesis or dissertation to be published is in electronic format, a direct link to the Published Work must be included using the ACS Articles on Request link. Although ACS grants students automatic permission to use their ACS articles in theses, it is highly likely that the graduate school requires a statement of written permission. Students should use RightsLink to obtain permission, and provide their graduate school with the written document provided by RightsLink.

American Chemical Society's Policy on Theses and Dissertations

If your university requires you to obtain permission, you must use the RightsLink permission system.
See RightsLink instructions at http://pubs.acs.org/page/copyright/permissions.html.

This is regarding request for permission to include **your** paper(s) or portions of text from **your** paper(s) in your thesis. Permission is now automatically granted; please pay special attention to the **implications** paragraph below. The Copyright Subcommittee of the Joint Board/Council Committees on Publications approved the following:

> Copyright permission for published and submitted material from theses and dissertations
> ACS extends blanket permission to students to include in their theses and dissertations their own articles, or portions thereof, that have been published in ACS journals or submitted to ACS journals for publication, provided that the ACS copyright credit line is noted on the appropriate page(s).
>
> Publishing **implications** of electronic publication of theses and dissertation material
> Students and their mentors should be aware that posting of theses and dissertation material on the Web prior to submission of material from that thesis or dissertation to an ACS journal may affect publication in that journal. Whether Web posting is considered prior publication may be evaluated on a case-by-case basis by the journal's editor. If an ACS journal editor considers Web posting to be "prior publication", the paper will not be accepted for publication in that journal. If you intend to submit your unpublished paper to ACS for publication, check with the appropriate editor prior to posting your manuscript electronically.

Reuse/Republication of the Entire Work in Theses or Collections: Authors may reuse all or part of the Submitted, Accepted or Published Work in a thesis or dissertation that the author writes and is required to submit to satisfy the criteria of degree-granting institutions. Such reuse is permitted subject to the ACS' "Ethical Guidelines to Publication of Chemical Research" (http://pubs.acs.org/page/policy/ethics/index.html); the author should secure written confirmation (via letter or email) from the respective ACS journal editor(s) to avoid potential conflicts with journal prior publication*/embargo policies. Appropriate citation of the Published Work must be made. If the thesis or dissertation to be published is in electronic format, a direct link to the Published Work must also be included using the ACS Articles on Request author-directed link − see http://pubs.acs.org/page/policy/articlesonrequest/index.html

* Prior publication policies of ACS journals are posted on the ACS website at
http://pubs.acs.org/page/policy/prior/index.html

If your paper has **not** yet been published by ACS, please print the following credit line on the first page of your article: "Reproduced (or 'Reproduced in part') with permission from [JOURNAL NAME], in press (or 'submitted for publication'). Unpublished work copyright [CURRENT YEAR] American Chemical Society." Include appropriate information.

If your paper has already been published by ACS and you want to include the text or portions of the text in your thesis/dissertation, please print the ACS copyright credit line on the first page of your article: "Reproduced (or 'Reproduced in part') with permission from [FULL REFERENCE CITATION.] Copyright [YEAR] American Chemical Society." Include appropriate information.

Submission to a Dissertation Distributor: If you plan to submit your thesis to UMI or to another dissertation distributor, you should not include the unpublished ACS paper in your thesis if the thesis will be disseminated electronically, until ACS has published your paper. After publication of the paper by ACS, you may release the entire thesis (**not the individual ACS article by itself**) for electronic dissemination through the distributor; ACS's copyright credit line should be printed on the first page of the ACS paper.

10/10/03, 01/15/04, 06/07/06, 04/07/10, 08/24/10, 02/28/11

B.3 American Institute of Physics

The following is found on the AIP copyright FAQ website, and a copy of their License to Publish Agreement is attached below.

May I include my AIP Publishing article in my thesis or dissertation? AIP Publishing permits authors to include their published articles in a thesis or dissertation. It is understood that the thesis or dissertation may be published in print and/or electronic form and offered for sale on demand, as well as included in a universitys repository. Formal permission from AIP Publishing is not needed. If the university requires written permission, however, we are happy to supply it.

LICENSE TO PUBLISH AGREEMENT FOR JOURNALS

This License to Publish must be signed, either electronically within the Peer X-Press manuscript submission system, or as a PDF to be uploaded into Peer X-Press as an alternate form, before the manuscript can be published. If you have questions about how to submit the form, please contact the journal's editorial office. For questions regarding the copyright terms and conditions of this License, please contact AIP Publishing LLC's Office of Rights and Permissions, 1305 Walt Whitman Road, Suite 300, Melville, NY 11747-4300 USA; Phone 516-576-2268; Email: rights@aip.org.

Article Title ("Work"):

_____

_____

(Please indicate the final title of the Work. Any substantive changes made to the title after acceptance of the Work may require the completion of a new agreement.)

All Author(s):

_____

_____

(Please list all the authors' names in order as they will appear in the Work. All listed authors must be fully deserving of authorship and no such authors should be omitted. For large groups of authors, attach a separate list to this form.)

Journal: _____

Manuscript ID# _____

All Copyright Owner(s), if not Author(s):

_____

_____

(Please list all copyright owner(s) by name. In the case of a Work Made for Hire, the employer(s) or commissioning party(ies) are the copyright owner(s). For large groups of copyright owners, attach a separate list to this form.)

Copyright Ownership and Grant of Rights

For the purposes of this License, the "Work" consists of all content within the article itself and made available as part of the article, including but not limited to the abstract, tables, figures, graphs, images, and multimedia files, as well as any subsequent errata. The Work refers to the content contained in both the Accepted Manuscript (AM) and the Version of Record (VOR). "Supplementary Material" consists of material that is associated with the article but linked to or accessed separately (available electronically only), including but not limited to data sets and any additional files.

This Agreement is an Exclusive License to Publish not a Transfer of Copyright. Copyright to the Work remains with the Author(s) or, in the case of a Work Made for Hire, with the Author(s)' employer(s). AIP Publishing LLC shall own and have the right to register in its name the copyright to the journal issue or any other collective work in which the Work is included. Any rights granted under this License are contingent upon acceptance of the Work for publication by AIP Publishing. If for any reason and at its own discretion AIP Publishing decides not to publish the Work, this License is considered void.

Each Copyright Owner hereby grants to AIP Publishing LLC the following irrevocable rights for the full term of United States and foreign copyrights (including any extensions):

1. The exclusive right and license to publish, reproduce, distribute, transmit, display, store, translate, edit, adapt, and create derivative works from the Work (in whole or in part) throughout the world in all formats and media whether now known or later developed, and the nonexclusive right and license to do the same with the Supplementary Material.
2. The right for AIP Publishing to freely transfer and/or sublicense any or all of the exclusive rights listed in #1 above. Sublicensing includes the right to authorize requests for reuse of the Work by third parties.
3. The right for AIP Publishing to take whatever steps it considers necessary to protect and enforce, at its own expense, the exclusive rights granted herein against third parties.

Author Rights and Permitted Uses

Subject to the rights herein granted to AIP Publishing, each Copyright Owner retains ownership of copyright and all other proprietary rights such as patent rights in the Work.

Each Copyright Owner retains the following nonexclusive rights to use the Work, without obtaining permission from AIP Publishing, in keeping with professional publication ethics, and provided clear credit is given to its first publication in an AIP Publishing journal. Any reuse must include a full credit line acknowledging AIP Publishing's publication and a link to the VOR on AIP Publishing's site.

Each Copyright Owner may:

1. Reprint portions of the Work (excerpts, figures, tables) in future works created by the Author, in keeping with professional publication ethics.
2. Post the Accepted Manuscript (AM) to their personal web page or their employer's web page immediately after acceptance by AIP Publishing.
3. Deposit the AM in an institutional or funder-designated repository immediately after acceptance by AIP Publishing.
4. Use the AM for posting within scientific collaboration networks (SCNs). For a detailed description of our policy on posting to SCNs, please see our Web Posting Guidelines (https://publishing.aip.org/authors/web-posting-guidelines).
5. Reprint the Version of Record (VOR) in print collections written by the Author, or in the Author's thesis or dissertation. It is understood and agreed that the thesis or dissertation may be made available electronically on the university's site or in its repository and that copies may be offered for sale on demand.
6. Reproduce copies of the VOR for courses taught by the Author or offered at the institution where the Author is employed, provided no fee is charged for access to the Work.
7. Use the VOR for internal training and noncommercial business purposes by the Author's employer.
8. Use the VOR in oral presentations made by the Author, such as at conferences, meetings, seminars, etc., provided those receiving copies are informed that they may not further copy or distribute the Work.
9. Distribute the VOR to colleagues for noncommercial scholarly use, provided those receiving copies are informed that they may not further copy or distribute the Work.
10. Post the VOR to their personal web page or their employer's web page 12 months after publication by AIP Publishing.
11. Deposit the VOR in an institutional or funder-designated repository 12 months after publication by AIP Publishing.
12. Update a prior posting with the VOR on a noncommercial server such as arXiv, 12 months after publication by AIP Publishing.

Author Warranties

Each Author and Copyright Owner represents and warrants to AIP Publishing the following:

1. The Work is the original independent creation of each Author and does not infringe any copyright or violate any other right of any third party.
2. The Work has not been previously published and is not being considered for publication elsewhere in any form, except as a preprint on a noncommercial server such as arXiv, or in a thesis or dissertation.
3. Written permission has been obtained for any material used from other sources, and copies of the permission grants have been supplied to AIP Publishing to be included in the manuscript file.
4. All third-party material for which permission has been obtained has been properly credited within the manuscript.
5. In the event that an Author is subject to university open access policies or other institutional restrictions that conflict with any of the rights or provisions of this License, such Author has obtained the necessary waiver from his or her university or institution.

This License must be signed by the Author(s) and, in the case of a Work Made for Hire, also by the Copyright Owners. One Author/Copyright Owner may sign on behalf of all the contributors/owners only if they all have authorized the signing, approved of the License, and agreed to be bound by it. The signing Author and, in the case of a Work Made for Hire, the signing Copyright Owner warrants that he/she/it has full authority to enter into this License and to make the grants this License contains.

1. The Author must please sign here (*except* if an Author is a U.S. Government employee, then please sign under #3 below):

Author Signature Print Name Date

2. The Copyright Owner (if different from the Author) must please sign here:

Name of Copyright Owner Authorized Signature and Title Date

3. If an Author is a U.S. Government employee, such Author must please sign below.
The signing Author certifies that the Work was written as part of his/her official duties and is therefore not eligible for copyright protection in the United States.

Name of U.S. Government Institution (e.g., Naval Research Laboratory, NIST)

Author Signature Print Name Date

PLEASE NOTE: NATIONAL LABORATORIES THAT ARE SPONSORED BY U.S. GOVERNMENT AGENCIES BUT ARE INDEPENDENTLY RUN ARE NOT CONSIDERED GOVERNMENT INSTITUTIONS. (For example, Argonne, Brookhaven, Lawrence Livermore, Sandia, and others.) Authors at these types of institutions should sign under #1 or #2 above.

If the Work was authored under a U.S. Government contract, and the U.S. Government wishes to retain for itself and others acting on its behalf, a paid-up, nonexclusive, irrevocable, worldwide license in the Work to reproduce, prepare derivative works from, distribute copies to the public, perform publicly, and display publicly, by or on behalf of the Government, please check the box below and add the relevant Contract numbers.

☐ Contract #(s) _____ [1.16.1]

B.4 Royal Society of Chemisty

The following is found on the RSC copyright website.

Author reusing their own work published by the Royal Society of Chemistry
You do not need to request permission to reuse your own figures, diagrams, etc, that were originally published in a Royal Society of Chemistry publication. However, permission should be requested for use of the whole article or chapter except if reusing it in a thesis. If you are including an article or book chapter published by us in your thesis please ensure that your co-authors are aware of this. Reuse of material that was published originally by the Royal Society of Chemistry must be accompanied by the appropriate acknowledgement of the publication. The form of the acknowledgement is dependent on the journal in which it was published originally, as detailed in 'Acknowledgements'.

Rights retained by authors

When the author accepts the exclusive licence to publish for a journal article, he/she retains certain rights that may be exercised without reference to the Royal Society of Chemistry.

Reproduce/republish portions of the article (including the abstract).

Photocopy the article and distribute such photocopies and distribute copies of the PDF of the article for personal or professional use only (the Royal Society of Chemistry makes this PDF available to the corresponding author of the article upon publication. Any such copies should not be offered for sale. Persons who receive or access the PDF mentioned above must be notified that this may not be made available further or distributed.).

Adapt the article and reproduce adaptations of the article for any purpose other than the commercial exploitation of a work similar to the original.

Reproduce, perform, transmit and otherwise communicate the article to the public in spoken presentations (including those that are accompanied by visual material such as slides, overheads and computer projections).

The author(s) must submit a written request to the Royal Society of Chemistry for any use other than those specified above.

All cases of republication/reproduction must be accompanied by an acknowledgement of first publication of the work by the Royal Society of Chemistry, the wording of which depends on the journal in which the article was published originally. The acknowledgement should also include a hyperlink to the article on the Royal Society of Chemistry website.

The author also has some rights concerning the deposition of the whole article.

B.5 Nature Publishing Group

Note: the following information applies to Open Access articles published in Scientific Reports. The following is reproduced from the Licence to Publish Agreement.

Author Rights

Ownership of the copyright in the Contribution remains with the Author(s).

However, the Author(s)' re-use rights in the Contribution are subject to the rights and restrictions set forth in this Section, and in the Pre- print services and Warranties a) Section. After the Author(s) have submitted the Contribution to NPG hereunder, the Author(s)' rights to re-use the Contribution shall be the same as those set forth in the Creative Commons licence listed above, with the following additional re-use rights:

a. to reproduce the Contribution in whole or in part in any printed volume (book or thesis) of which they are the Author(s); and

b. to reuse figures or tables created by the Author(s) and contained in the Contribution in oral presentations and other works created by them.